QUIKSCAT MEASUREMENTS OF THE WIND FIELD OVER THE BERING AND CHUKCHI SEAS

A

THESIS

Presented to the Faculty

of the University of Alaska Fairbanks

in Partial fulfillment of the Requirements

for the Degree of

MASTER OF SCIENCE

By

Jeremy M. Mull, B.S.

Fairbanks, Alaska

December 2008

Abstract

The purpose of this study is to investigate the dynamic wind field and resulting ocean circulation patterns in the Bering and Chukchi Seas. This region forms an important link in global ocean circulation as Bering Strait is a major conduit for water flowing into the Arctic Ocean. The Arctic has been identified as an area sensitive to climate change; thus it is vital to understand how water and energy flow through this region. We first quantify the differences between the winds measured in this region by the Quik Scatterometer (QuikSCAT) and those modeled by the National Centers for Environmental Prediction (NCEP). Although the data sets are well correlated, we find significant discrepancies between these data sets and use linear regressions to correct the NCEP data. The magnitudes of the NCEP wind components are greater than the magnitudes of the QuikSCAT wind components. This creates directional differences between the two data sets at low wind speeds and NCEP speeds that are greater than QuikSCAT speeds at high wind speeds.

We next challenge the assumption that the wind field is spatially uniform over the Bering and Chukchi shelves. We produce mean monthly maps of the wind field, surface Ekman transport, and wind variance based upon the 12-hourly QuikSCAT data from July 1999 – May 2007. These maps reveal that the winds are spatially and temporally dynamic in this region. There are several areas and times in which surface Ekman transport is onshore or offshore near the coasts and may engender coastal downwelling and upwelling, respectively. There are also several instances when surface Ekman convergence and divergence may lead to Ekman pumping and suction.

We use the entire NCEP record (January 1948 – May 2007) to examine patterns of surface Ekman transport across the shelf break. There was a significant increase in the amount of onshelf surface Ekman transport that coincided with the regime shift that occurred in the Bering Sea in the mid-1970s. We attempt to correlate the time series of surface Ekman cross-shelf transport with several climate indices but find only very weak correlations. The annual surface Ekman freshwater fluxes across the shelf break are

calculated and found to be very small compared to the total annual freshwater fluxes calculated by Aagaard et al. (2006) and Kinney et al. (2008).

To resolve the dominant modes of wind variability we compute hourly, monthly, and annual Complex Empirical Orthogonal Functions (CEOFs) with the QuikSCAT and NCEP data sets. The first modes in each analysis account for more than 60% of the variance. Different aspects of the mode amplitude time series are cross-correlated with climate and indices to produce small but significant correlation coefficients.

Finally we calculate Ekman pumping and suction at four locations in the Bering Sea during the spring and summer months of seven years (2000 – 2006). We identify regions and times when Ekman pumping and suction were particularly strong, and perform several runs of a one-dimensional Price-Weller-Pinkel (PWP) vertical mixing model with the QuikSCAT winds, the QuikSCAT winds and a wind-stress-curl term, and the NCEP winds. The results suggest that Ekman suction might facilitate subsequent vertical mixing while Ekman pumping might inhibit subsequent vertical mixing when the winds are generally weak and wind-stress-curl is moderate or strong. The temporal resolution of the QuikSCAT data set is too low to resolve inertial motions at high latitudes. The NCEP data set has higher temporal resolution and is adequate for running the model within this region. We propose interpolating the hourly NWS data collected at St. Paul Island (station PASN) to the QuikSCAT grid using the complex amplitudes and phases from the complex cross-correlations between the two data sets to produce a data set of high temporal and spatial resolution. This would enable researchers to accurately resolve inertial motions and compute wind-stress-curl.

Table of Contents

List of Figures

Page

List of Tables

Page

List of Appendices

Acknowledgements

Funding for this project was provided by the North Pacific Research Board, Alaska Ocean Observing System, International Arctic Research Center, and the Center for Global Change. I would also like to acknowledge and thank my committee members. Dr. Tom Weingartner acquired funding and developed the direction and scope of this project. His advice and ideas were crucial. Dr. Mark Johnson and Dr. Harper Simmons also were indispensable and guided me through the statistical analyses and numerical model experiments.

I would also like to thank my fellow students and staff who provided support. They include Seth Danielson, Rachel Potter, and Jim Alanko. In particular, Markus Janout provided helpful advice and technical support. Finally I would like to acknowledge Kristin for her endless support and helpfulness in completing late-night edits of this text.

Chapter 1 Introduction

The Bering Sea is a semi-enclosed sea with unique bathymetry and complex circulation features. A broad, shallow shelf comprises the northern and eastern portions of the sea while the deeper Aleutian Basin forms the southwestern part. Relatively fresh surface waters flow westward in the Alaskan Stream, flow northward through 14 different passes in the Aleutian Island Chain, and then flow eastward to form the Aleutian North Slope Current (Stabeno et al., 1999). The Aleutian Basin is characterized by cold, relatively nutrient rich water. Mean surface current flow along the margins of the basin in generally cyclonic with the Bering Slope Current forming the eastern and northern boundary of this gyre (Schumacher and Kinder, 1983; Coachman, 1985; Stabeno et al., 1999; Danielson et al., 2006). At the northwestern edge of the Aleutian Basin, the current splits (Coachman, 1985; Stabeno et al., 1999). Some waters flow southward forming the Kamchatka Current, which completes the gyre. Other waters flow northward into the Gulf of Anadyr Current, which brings relatively salty, nutrient rich waters north along the Russian side of the sea through Bering Strait. The Alaska Coastal Current (ACC) flows northward through Unimak Pass carrying relatively fresh, nutrient poor surface waters from the Gulf of Alaska along the Alaskan coast toward Bering Strait. These features are shown in Figure 1.

The mean interior flow is concentrated in the Aleutian North Slope Current and Bering Slope Current, while eddies also penetrate to mid-depths along the shelf break (Stabeno et al., 1999; Mizobata et al., 2006; Kinney et al., 2008). The shelf and basin waters feed the Arctic Ocean through Bering Strait. (Aagaard et al., 1981; Coachman and Aagaard, 1988). Pacific waters enter the upper layers of the Arctic Ocean and help maintain the pycnocline and ice cover in this basin (Aagaard et al., 1981). The Bering water is fresher than Atlantic water but saltier than the water in the upper mixed layer of the Arctic. Thus the northward transport through the Strait is an important component of global climate (Coachman, 1993; Aagaard et al., 2006).

The eastern Bering Sea shelf is divided into three physically distinct regions separated by fronts. The coastal domain extends from the coastline to approximately the 50 m isobath and the middle domain lies between the 50 m and the 100 m isobaths.

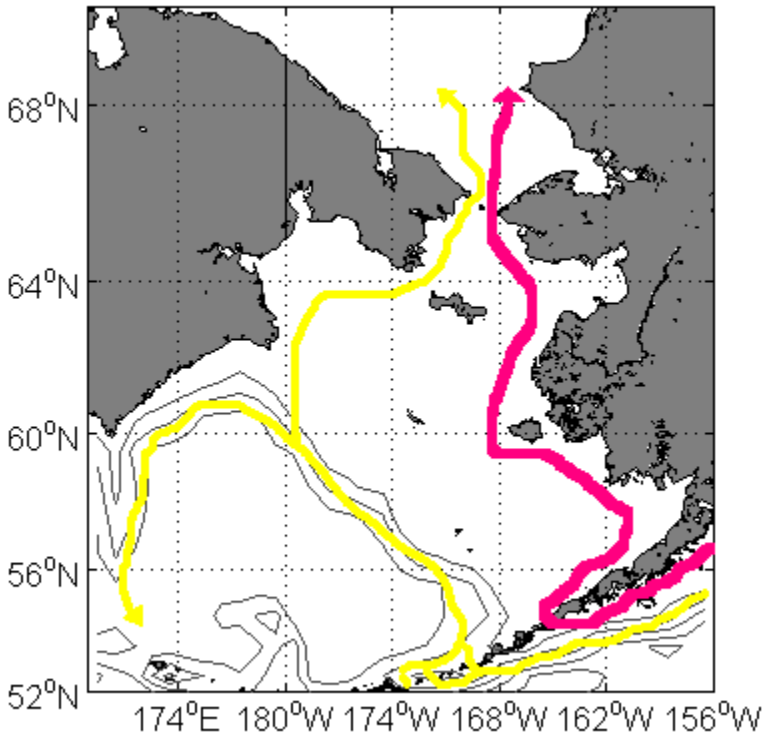

Figure 1. The along-shore flow in the Bering Sea. The red line indicates the Alaska Coastal Current (ACC) and the yellow line indicates the Alaskan Stream, Aleutian North Slope Current, Bering Slope Current, Kamchatka Current, and Gulf of Anadyr waters. The Bering Sea Gyre rotates cyclonically.

Within these domains, tidal energy accounts for about 90% of the kinetic energy in the water column. The remaining 10% of the kinetic energy is dominated by low frequency motions at periods of 2-10 days. The outer domain extends from the 100 m isobath to the shelf break. Here, tidal energy accounts for almost 80% of the total kinetic energy while the rest is energy at sub-tidal frequencies. This implies that wind mixing

and storm events have a greater role to play in the outer domain than close to the coast (Coachman et al., 1975; Schumacher and Kinder, 1983; Coachman 1985).

The Bering Sea supports a relatively rich marine ecosystem including the commercially important walleye pollock (*Theragra chalcogramma*) fishery and large salmon stocks (Stabeno et al., 1999). In general, these fisheries and relatively large populations of birds and mammals are sustained by several regions of upwelling, seasonal ice cover, and the availability of habitat provided by the large width of the shelf (Loughlin et al., 1999; Stabeno et al., 1999). These fisheries are also significant to the economy and culture of Alaska (Stabeno et al., 2006).

It is commonly assumed, for many shelves, that the winds area spatially uniform (Stewart, 2005). This greatly simplifies resolving the wind-driven shelf circulation. However, this assumption may not be appropriate for the relatively broad (~500 km) Bering Sea shelf. Indeed, variability in the along-shore flow is linked with variability in the wind field at meteorological frequencies (Schumacher and Kinder, 1983; Aagaard et al., 1985; Coachman and Aagaard, 1988; Bond et al., 1994; Danielson et al., 2006).

Spatial variability in the winds can also affect vertical mixing. The winds provide mechanical energy for mixing. However, wind-stress-divergence and wind-stress-curl can also lead to vertical displacements in the pycnocline (Stewart, 2005). Chelton et al. (2006) analyzed QuikSCAT data and identified this region as one in which divergence and curl in the wind stress may be significant. Muller et al. (1984) examined a vertical mixing model in which the depth of the pycnocline oscillated in time. They found that this could facilitate or inhibit vertical mixing depending on whether the oscillations in the pycnocline depth were in-phase with wind mixing events. Thus Ekman pumping and suction could stifle or enhance vertical mixing by subsequent storm winds on the Bering Shelf.

The winds also appear to influence biological production. Wilderbuer et al. (2002) found that survival of juvenile flatfish is correlated with winds. When the wind-driven circulation was directed eastward, flathead sole, northern rock sole, and arrowtooth flounder larvae were transported to favorable nursing grounds in Bristol Bay.

However, during the 1990s Ekman transport was generally directed offshore and recruitment of these species was low. They concluded that the larvae were advected to deeper, relatively inhospitable nursery grounds when the winds forced waters offshore.

Our goal is to describe the dominant features of the wind field and wind-driven circulation in this region. We examine the assumption that winds are spatially uniform along the shelf by looking for times and areas in which the winds could cause the along-shore flows to vary, engender Ekman pumping and suction, and potentially impact biological production. For most of this study, data from NASA's Quik Scatterometer (QuikSCAT) is used. The scatterometer measures the backscatter in microwaves that have reflected from the sea surface. This backscatter is caused by sea-surface roughness caused by the wind stress. The scatterometer provides wind velocities and directions at about every 12 hours at locations spaced approximately every 25 km. No measurements are available for areas that are covered by sea ice in the winter months. Rain distorts the measurements and causes the satellite to measure erroneous large zonal wind components (Chelton and Freilich, 2005; Hoffman and Leidner, 2005).

We also use NCEP wind data and compare it to the QuikSCAT data set. Chelton and Freilich (2005) compared QuikSCAT data to winds measured by 15 National Data Buoy Center (NDBC) buoys, including one from the western Bering Sea. Over the entire range of winds speeds, they found that the QuikSCAT data have errors of approximately 0.75 m/s in the along-wind direction and 1.5 m/s in the crosswind direction. However, they found that wind speeds measured by QuikSCAT were essentially the same as those measured by the buoys until the wind speeds exceeded 20 m/s. At greater speeds, the QuikSCAT data diverge from the buoy data but the errors are relatively small. At low speeds wind speeds (< 1 m/s), QuikSCAT data differ directionally from buoy data by as much as 50º. However, these directional differences rapidly decrease as wind speed increases. They hypothesized that the differences could be attributed to differences between wind and wind stress directions with wind stress being guided by surface waves. This interaction is likely much greater at smaller wind speeds. As the buoys measure winds and QuikSCAT measures wind stress, a discrepancy might appear in the data.

However, they concluded that these discrepancies are small and that in general QuikSCAT winds are consistent with the winds measured by NDBC buoys.

This paper is organized as follows. We first compare the modeled NCEP data and QuikSCAT data. We compute the complex correlation coefficients and phase angles between NCEP wind vector time series at certain locations and QuikSCAT wind vector time series at all of the other locations within the domain. This shows that the NCEP and QuikSCAT winds are highly correlated and in phase with one another. The results allow us to substitute NCEP data into QuikSCAT cells that have missing data due to ice or rain contamination. Linear regressions between the meridional and zonal components of NCEP winds and those components of the QuikSCAT winds are constructed for each latitude and longitude within the study region. The regression coefficients are used to augment the entire NCEP data set from January, 1948 to May, 2007.

We present monthly maps of the mean winds, surface Ekman transport, and wind variance based upon the 12-hourly QuikSCAT data. We discuss the seasonal variability in the winds and wind-driven circulation. We also identify times and areas of coastal upwelling and downwelling, and surface Ekman convergence and divergence. The implications for the mean currents, vertical mixing, and biological production in the upper mixed layer are discussed.

We then seek to quantify the annual surface Ekman transport across the shelf break (subsequently referred to as surface Ekman cross-shelf transport). This is important as it can transport salt and nutrients from the Aleutian Basin to the shelf or off of the shelf. We use the NCEP corrected wind components to calculate surface Ekman cross-shelf transport. We calculate the annual wind-driven freshwater flux across the shelf break and find that while there is almost always a flux of freshwater onshore, it is very small and represents ~6% of the onshelf freshwater flux calculated by Aagaard et al. (2006). This suggests other mechanisms are more significant in driving freshwater onto the shelf. We also calculate the annual nitrate flux across the shelf and find that in most years the winds drive an export of nitrate off of the shelf.

We construct Complex Empirical Orthogonal Functions (CEOFs) for QuikSCAT winds within a small domain over the Bering Sea shelf. These reduce the variability in the winds into three significant modes. We compare these modes to those calculated by CEOF analysis of six-hourly, mean monthly, and mean yearly NCEP data. We compare time series of surface Ekman cross-shelf transport and components of the CEOF amplitude series with certain climate indices and find weak correlations.

To examine the variability of Ekman pumping and suction on the shelf, we focus on a small rectangular domain within the study region and examine surface Ekman convergence and divergence within the domain. The NCEP wind data from 1948 to 2007 is used to determine long-term trends. Convergent and divergent patterns appear to vary on seasonal and interannual time scales. We examine the QuikSCAT wind data from four locations within the Bering Sea during the spring and summer months of 2000 – 2006 to look for periods of relatively strong Ekman suction and pumping.

Finally, we present the results of experiments with a version of the Price-Weller-Pinkel (PWP) vertical mixing model developed by Price et al. (1986). This model is chosen because it has been shown to accurately predict the mixed layer depth in several realistic settings at short time scales when there is resonant wind forcing (i.e. the wind oscillates in coherence with the oscillatory motions of the surface layer (Plueddemann and Farrar, 2006). Plueddemann and Farrar (2006) demonstrated that traditional slab models do not produce density profiles similar to those observed in nature.

We force the PWP model with winds and surface fluxes measured and collected at three locations within the Bering Sea. We use QuikSCAT winds, QuikSCAT winds with a wind-stress-curl term, NCEP winds, and National Weather Service (NWS) measured winds to force the model. The results indicate that Ekman suction possibly enhances vertical mixing by raising the pycnocline to a depth where shear develops between the upper mixed layer and deeper waters. Ekman pumping possibly inhibits vertical mixing by depressing the pycnocline to depths where energy from subsequent wind events cannot penetrate. Ekman suction and pumping appear to be most significant when the winds are relatively weak and wind-stress-curl is moderate or strong. The

results also suggest that the temporal resolution of the QuikSCAT data set is too low to accurately resolve inertial motions at these high latitudes. When the 6-houlry NCEP data is used to force the model there is significantly more wind mixing. We propose that the 6-houlry NCEP data, or a hybrid data set with both hourly NWS data and QuikSCAT data, be used to run the PWP model in this region.

Our results suggest that the winds vary on seasonal, interannual, and interdecadal scales, and this variability is correlated with variability in the physics and biology of the system. We also find that the winds vary on spatial scales and that this could contribute to variability in horizontal transport, vertical mixing, and possibly biological production within the region.

Chapter 2 Methods

A map of the region of study is shown in Figure 2. The QuikSCAT grid points are indicated by red dots and the NCEP grid points are indicated by black dots.

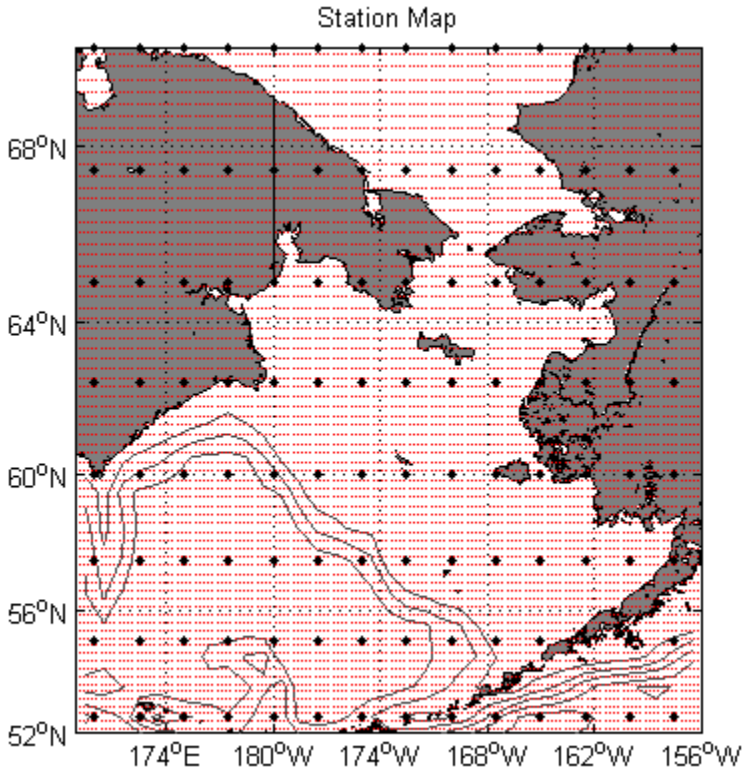

Figure 2. The study region inc**ludes the Bering and Chukchi Seas.** Red dots indicate QuikSCAT data collection points while black dots indicate NCEP model grid points. Note that QuikSCAT cannot measure winds over land and so QuikSCAT data cells over lands contain no data.

Wind data are often spatially and temporally correlated and the degrees of freedom in any statistical analyses must be modified to reflect this. The integral time scale (τ) is the maximum allowable number of lag units over which two time series will be correlated if one expects a significant correlation. τ is computed as

$$\tau = \frac{1}{C(0)} \sum_{k=0}^{m-1} \frac{\Delta\tau}{2} [C(\tau_k + \Delta\tau) + C(\tau_k)]; \quad (1)$$

where $C(\tau)$ is the autocovariance function, m is the number of lag units in the summation, $\Delta\tau$ is the time increment between each data point, and $[C(\tau_k + \Delta\tau) + C(\tau_k)]/2$ is the mean value of the autocovariance function for the midpoint of the interval (τ_k, $\tau_k + \Delta\tau$). The effective degrees of freedom are then

$$N^* = \frac{N\Delta t}{\tau}; \quad (2)$$

where N is the length of the time series and Δt is the time elapsed between each data point (Emery and Thomson, 2001).

To compute τ for the Bering and Chukchi Seas, we analyzed hourly wind data from the meteorological station on St. Paul Island operated by the National Weather Service (Station PASN). We chose this data set as it has a higher temporal resolution than the QuikSCAT data set and it is important to capture high frequency variability (Emery and Thomson, 2001). Wind speeds in excess of 125 knots were considered inaccurate and were removed from the calculation. We calculated τ for each year for the U and V components of the wind and chose 4.26 days as the most conservative estimate of τ.

The National Aeronautics and Space Administration (NASA) Ocean Vector Winds Science Team and Remote Sensing Systems provided the QuikSCAT data and codes for reading the data (Remote Sensing Systems, 2007; http://www.remss.com). They also developed a rain flag, which was used to identify wind measurements that were inaccurate due to rain effects. These data were excluded from all analyses. The NCEP wind data were produced by the National Center for Environmental Prediction/National Center for Atmospheric Research (NCEP/NCAR) (Kalnay et al., 1996; Kistler et al., 2001; http://www.cdc.noaa.gov).

The QuikSCAT satellite makes two passes each day, approximately 12 hours apart. NCEP produces a modeled wind field every six hours. Figure 3 shows how the two data sets are arranged in time. For time series analyses, the ascending passes of

QuikSCAT measurements (green dots) were compared with the NCEP data modeled at 18:00 hrs (GMT) each day and the descending passes of QuikSCAT measurements were compared with the NCEP data modeled at 06:00 hrs (GMT).

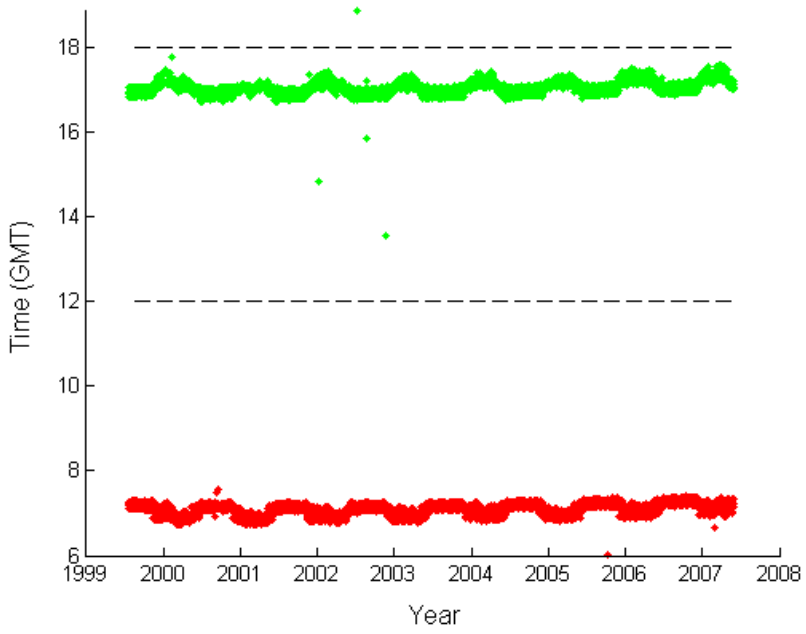

Figure 3. The times of day for QuikSCAT measurements in the Bering Sea. Times for the ascending pass are shown in green. Times for the descending pass are shown in red. NCEP times are indicated by dashed lines. In comparisons, measurements in the ascending passes were compared to NCEP data modeled at 18:00 hrs (GMT), while measurements in the descending passes were compared to NCEP data modeled at 06:00 hrs (GMT).

We next computed the complex correlation coefficients and phase angles between time series at certain NCEP grid points and the time series at all of the QuikSCAT grid points within the region. Missing or erroneous QuikSCAT data points (due to ice, rain, or land effects) were removed from both data sets. We used the procedure outlined by Kundu (1975), in which each vector in both time series is constructed as a complex vector such as

$$w(t) = u(t) + iv(t). \tag{3}$$

The complex correlation coefficient between time series 1 and 2 is then

$$\rho = \frac{\left\langle w_1^*(t) w_2(t) \right\rangle}{\left\langle w_1^*(t) w_1(t) \right\rangle^{1/2} \left\langle w_2^*(t) w_2(t) \right\rangle^{1/2}}, \tag{4}$$

where the '*' indicates complex conjugation and the braces indicate a time average. The phase angle between the two vector time series is then

$$\theta = \tan^{-1} \frac{\left\langle u_1 v_2 - v_1 u_2 \right\rangle}{\left\langle u_1 u_2 + v_1 v_2 \right\rangle}. \tag{5}$$

The data sets were shown to be highly correlated and in phase with one another. This enabled us to substitute NCEP data points for missing QuikSCAT data points in later analyses which required a more extensive data set. Then NCEP data were linearly interpolated onto the QuikSCAT grid points. An example is shown in Figure 4.

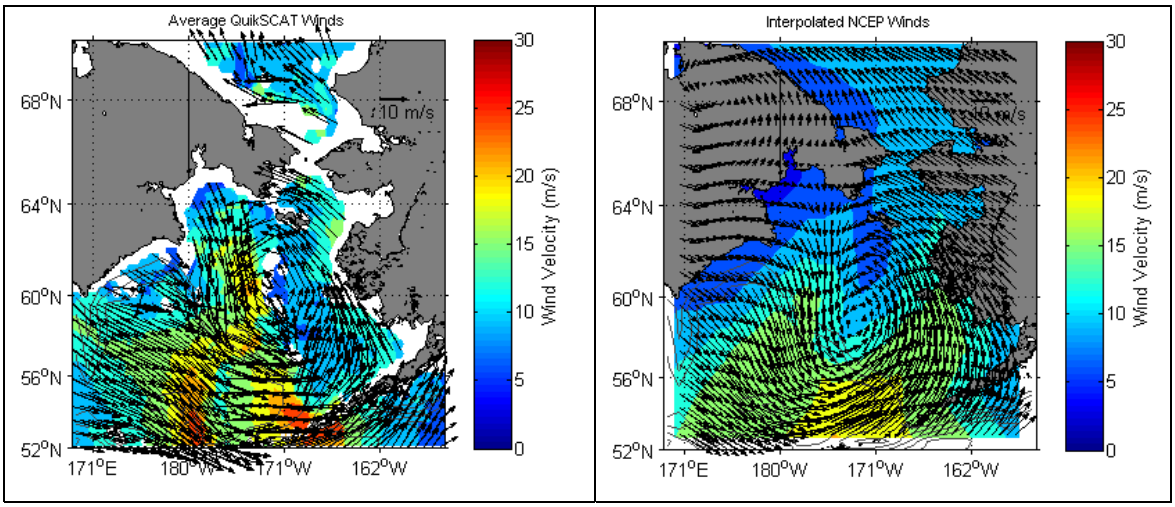

Figure 4. The daily averaged QuikSCAT winds (left side) and daily averaged and interpolated NCEP winds (right side) for November 14, **2004.** Note that NCEP data points can be substituted in for QuikSCAT data points that are missing due to sea ice.

Simple linear regressions were then computed between the zonal and meridional components of QuikSCAT winds and the zonal and meridional components of NCEP

winds. A regression was performed for each wind component at the NCEP grid points over water. The winds at the four closest QuikSCAT grid points were compared to those at each NCEP location. For the most northern NCEP latitude band (70.0º N) only the two closest QuikSCAT grid points south of each station were used as there were no QuikSCAT locations north of this latitude. An example linear regression is shown in Figure 5. The degrees of freedom were modified by τ.

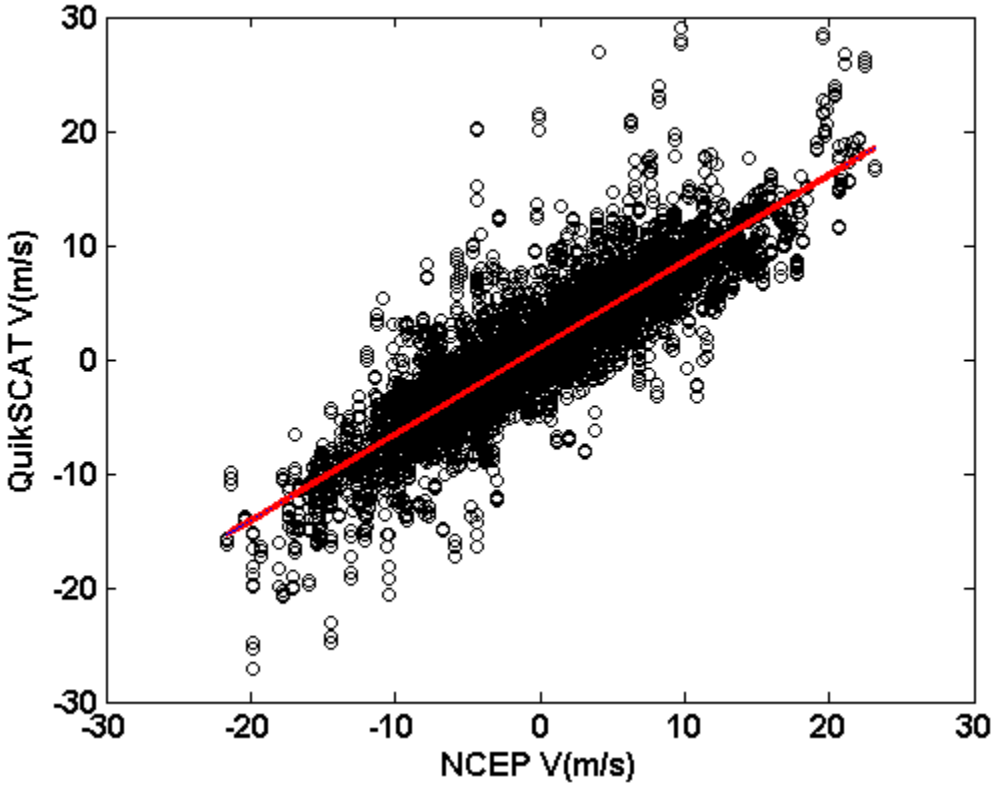

Figure 5. A simple linear regression of the V components of the wind at the NCEP grid point (52.5º N, 175.0º W) and the same components at the four closest QuikSCAT grid points. The equation for the linear regression is: $V_{Quik} = 1.04 + 0.76 * V_{NCEP}$. The R^2 value is 0.76. The regression line is shown in blue and is difficult to distinguish as the confidence bands are relatively tight. The confidence bounds at the 95% confidence level are shown in red.

QuikSCAT measurements were integrated into the NCEP model in the beginning of February 2002 (Chelton and Freilich, 2005; Chelton et al., 2006). We performed regressions before and after this time to determine the improvement of the NCEP model and to provide regression coefficients to augment the NCEP data. This enabled us to quantify the Ekman surface transport across the Bering Sea shelf break. As Chelton and Freilich (2005) had shown that QuikSCAT measurements were consistent with data from meteorological stations and National Data Buoy Center (NDBC) buoys, we considered QuikSCAT data to be accurate. The equations used to correct the NCEP data at each grid point were:

$$U_{actual} = b_0 + b_1 * U_{NCEP} \text{ and} \tag{6}$$

$$V_{actual} = b_0 + b_1 * V_{NCEP}; \tag{7}$$

where b_0 and b_1 were determined by each linear regression. The NCEP data begin in January 1948 and end in May 2007.

We produced maps of the mean monthly wind fields, surface Ekman transport, and wind variances. The winds were averaged for each month in the entire QuikSCAT data set. Wind stress was calculated as:

$$\tau = \rho_{air} C_D \vec{V} \left| \vec{V} \right|; \tag{8}$$

where ρ_{air} is the density of air (approximately 1.29 kg/m^3), C_D is the drag coefficient, $\vec{V}$ is the meridional or zonal component of velocity, and is $\left| \vec{V} \right|$ the speed (Stewart, 2005). Note that τ in this equation is different from τ used in equation 1. Large and Pond (1981) empirically derived formulas for the drag coefficient as:

$$C_D = 1.2/1000 \text{ if } 4 \leq U10 < 11 \text{ m/s; or}$$

$$C_D = (0.49 + 0.065 * U10)/1000 \text{ if } 11 \leq U10 \leq 25 \text{ m/s.} \tag{9}$$

For simplicity, we distinguished between wind speeds less than 11 m/s and greater than or equal to 11 m/s. Surface Ekman transports were:

$$M_x = \frac{-\tau_y}{f}$$

$$M_y = \frac{\tau_x}{f} \; ; \tag{10}$$

where τ_y is the *V* component of the wind stress, τ_x is the *U* component of the wind stress, and *f* is the Coriolis frequency at each latitude (Stewart, 2005).

The complex cross-correlation analysis indicated that the winds at the shelf break were correlated over relatively large spatial scales. Thus we used data from three NCEP grid points along the shelf break with coordinates 60.0º N, 180.0º; 57.5º N, 175.0º W; and 55º N, 170.0º N to estimate Ekman transport as shown in Figure 6.

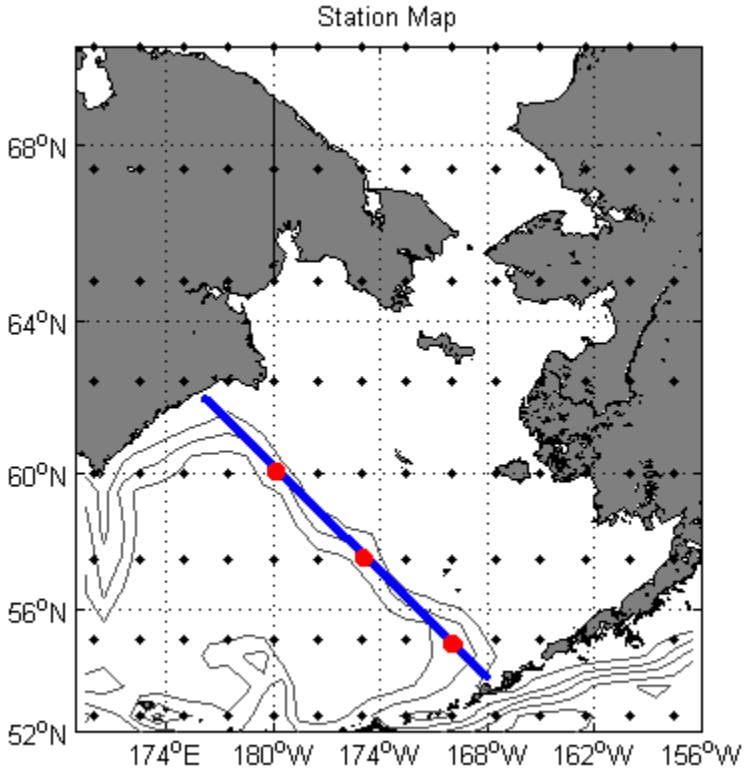

Figure 6. The NCEP grid points wi**thin the study region.** The three NCEP grid points used to calculate surface Ekman cross-shelf transport are shown in red. The straight line used to approximate the shelf break is shown in blue.

The shelf break was approximated by a straight line oriented towards 315º T. The wind vectors at each of these points were rotated to a new Cartesian coordinate system by

$$u' = u\cos 135° + v\sin 135° \text{ and} \tag{11}$$

$$v' = -u\sin 135° + v\cos 135°; \tag{12}$$

where 135º is the angle measured counterclockwise between true east and the approximate shelf break line (Emery and Thomson, 2001). The along-shelf break component of the wind stress (*v*') was assumed to drive Ekman transport across the shelf break. Surface Ekman cross-shelf transport was then calculated by equation10.

The shelf break is approximately 1,175 km long. The three NCEP grid points are roughly 400 km apart. The complex correlations decay to 0.5 over a distance of approximately 686 km in most cases (refer to Appendix A, Figs A-1 through A-16). As this distance exceeds the distance between the NCEP grid points, we were able to use only the three grid points to estimate the winds along the entire shelf break. The shelf break was divided into three segments of equal length and wind stress measurements at each grid point were integrated over these distances. We assumed that the wind blew consistently for 12 hour periods so that each wind measurement was accurate for 12 hours. We also assumed that transport in the surface Ekman layer was balanced by flow in the opposite direction in the bottom layer. This implies that surface Ekman cross-shelf transport onto the shelf would be balanced by an equal transport off of the shelf in the bottom layer (a strictly two-dimensional assumption). These assumptions enabled us to calculate the freshwater flux due to cross-shelf Ekman transport. This flux is calculated as

$$FWE_1 = \int_0^{L_x} M_E(x)\frac{(S_B - S_{Ek})}{S_{\mathrm{Re}f}}dx; \tag{13}$$

where FWE_1 is the freshwater flux, L_x is the length of the shelf break, $M_E(x)$ is the Ekman mass transport calculated at each grid point, S_B is a measurement of bottom salinity, S_{Ek} is the mean salinity in the surface Ekman layer, and S_{Ref} is a reference salinity. Salinity measurements were taken from the vertical profiles in the National Oceanographic Data Center's (NODC) World Ocean Database (NODC, 2005; http://www.nodc.noaa.gov/). Salinity measurements near the shelf break began in 1950, although there are long periods of time when sampling was infrequent. We used salinity measurements taken

along the 150 m isobath. For each wind measurement, the Ekman depth was roughly approximated as:

$$D_E = \frac{7.6}{\sqrt{\sin\phi}} U10\,; \tag{14}$$

where φ indicates latitude and *U10* is the wind speed (Stewart, 2005). Salinity measurements were averaged for each month. The mean salinities shallower than each Ekman depth, and collected within the same month as each wind measurement, were averaged to produce a mean surface layer salinity. In the same manner, salinities between 140m and 160m depth were averaged to yield a mean bottom salinity. Months for which there were no monthly mean salinities were assigned an overall mean salinity profile. The freshwater quantity was then divided by a reference salinity of 34.8 following Aagaard and Carmack (1989). This is slightly saltier than the highest salinity measurements beneath the halocline in the Arctic Ocean (Aagaard et al., 1981). We chose this reference salinity in order to compare the surface Ekman cross-shelf freshwater flux to the Bering Sea freshwater fluxes calculated by Aagaard et al. (2006). Aagaard et al. (2006) developed a salinity budget for the Bering shelf by calculating the annual transport of seawater across the shelf break, through Bering Strait, and through Unimak Pass. They also calculated the mean salinities of these annual transports. We converted their total annual transports to freshwater fluxes by:

$$FWE_2 = T \times \left(\frac{34.8 - \overline{S}}{34.8} \right); \tag{15}$$

where '*T*' refers to the calculated total annual transport, and $\overline{S}$ refers to the calculated mean salinity. In addition, we integrated the salinity fluxes over each month and year in the NCEP data set to determine seasonal and interannual variability.

Nitrate fluxes were calculated accordingly:

$$N_{flux} = \int_0^{L_x} M_E(x)\left(N_B - N_{Ek}\right)dx\,; \tag{16}$$

where N_B and N_{Ek} are the bottom and surface nitrate concentrations, respectively.

The surface Ekman transport calculation revealed that the annual surface Ekman cross-shelf transport might have shifted between 1972 and 1973. To test this, we performed a general non-parametric t-test, which compared the means of the annual surface Ekman cross-shelf transports from 1948 to 1972 and those from 1972 to 2007. We also conducted a Wilcoxon Rank Sum test, which compared the median annual surface Ekman cross-shelf transports during these two time periods. These tests were repeated with mean monthly surface Ekman cross-shelf transports and all tests were conducted at the 95% confidence level.

It is possible that the variability in surface Ekman cross-shelf transport is correlated with climate indices. We performed cross-correlation analyses between mean monthly surface Ekman cross-shelf transport and the Pacific Decadal Oscillation (PDO) index, Pacific-North American (PNA) index, the Arctic Oscillation (AO) Index. All of these data were obtained from the National Climate Data Center database at http://www.ncdc.noaa.gov/. We also attempted to find a significant correlation with the Aleutian Low Pressure Index (ALPI), the North Pacific (NP) index, and the winter and spring values of the Western Pacific (WP), index. The ALPI data were taken from http://www.pac.dfo-mpo.gc.ca. The NP and WP index data were obtained from http://www.beringclimate.noaa.gov/. We followed the cross-correlation technique outlined by Emery and Thomson (2001). All cross-correlation coefficients were computed at the 95% confidence level.

To examine the dominant periods of variability in surface Ekman cross-shelf transport we performed Discrete Fast Fourier Transforms (DFFTs) on the time series as outlined by Emery and Thomson (2001).

CEOFs were compiled for the QuikSCAT winds within a small rectangular region over the Bering Sea shelf and shelf break (Figure 7). The small domain was used because we lacked computer power to calculate the CEOFs for the entire study region.

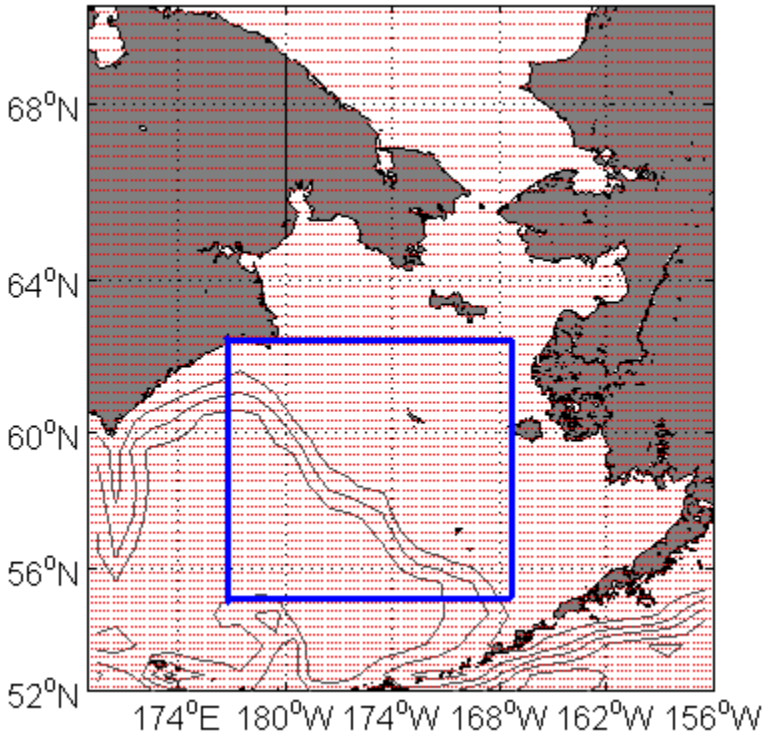

Figure 7. The small domain used to calculate the CEOFs for the QuikSCAT 12-hourly winds from 1999-2007. The domain is indicated by the blue lines while the QuikSCAT grid points are shown in red.

The QuikSCAT 12-hourly data from July 1999 – May 2007 were used with interpolated NCEP winds replacing missing data. The meridional and zonal components of the wind at each grid point were arranged into a complex matrix with grid points along each row and time along each column:

$$U = \left(U_j(t)\right) = \begin{bmatrix} U_{11} & U_{12} & \dots & U_{1P} \\ U_{21} & U_{22} & \dots & U_{2P} \\ \dots & \dots & \dots & \dots \\ U_{N1} & U_{N2} & \dots & U_{NP} \end{bmatrix}. \tag{17}$$

$U_j(t) = u_j(t) + iv_j(t)$, j=1,..,P (the grid point numbers), and t=1,…,N (the sample times). The time series of each grid point were detrended by removing the best fit trend line from

the data. The CEOFs were then computed by solving the eigenvector problem with the complex variance/covariance matrix.

$$([Cov]-\lambda[I])[V]=0; \tag{18}$$

where λ is a vector of eigenvalues, $[I]$ is an identity matrix with the same dimensions as the variance/covariance matrix ([*Cov*]), and $[V]$ are the eigenvectors. The mode amplitudes were then determined by:

$$[Z]=[U][V]^{*}; \tag{19}$$

where '*' indicates complex conjugation (Wallace and Dickinson, 1972; Horel 1984; Kishtawal et al., 2001).

Horel (1984) developed a simple equation to estimate the potential error of each eigenvalue:

$$l_n=\lambda_n\left(\frac{1}{\tau}\right)^{1/2}; \tag{20}$$

where l_n is the width of each error bar (no units), λ_n is the eigenvalue of the *n*'th mode and τ is the number of independent time steps. The eigenvalues were plotted with their error bars and examined to determine which error bars overlapped. If an eigenvalue had error bars that did not overlap with the error bars of another eigenvalue, then the respective mode of that eigenvalue was considered significant (Horel, 1984).

To use equation 20, one must first verify that the variance/covariance matrix follows a complex Wishart distribution. This proved exceedingly difficult so we checked this assumption with a much simpler and cruder technique. If a variance/covariance matrix displays a complex Wishart distribution, then the original data are randomly distributed (Srivastava, 1965; Conradsen et al., 2003). Histograms were made for each wind component and the data appeared to be randomly distributed.

The original data were reconstructed by multiplying the modes by their respective mode amplitudes, weighting each mode by its eigenvalue, and then summing all of the modes. Often, the first few modes will describe a large portion of the variance and only these will be used to examine the variability of the system (Wallace and Dickinson, 1972; Horel 1984; Kishtawal et al., 2001). To ascertain how each mode is rotating throughout

time, we analyzed rotary spectra of the time series of complex amplitudes. This was done following a technique outlined by Mooers (1973) and Emery and Thomson (2001), in which the complex components are separated into clockwise and counter-clockwise rotating components.

We computed CEOFs for the NCEP six-hourly data within the same small domain (Figure 7). Monthly and annual CEOFs were also constructed from monthly and annual means of the NCEP six-hourly data and the leading modes were compared to one another. We tested for correlations between the CEOFs and time series of the climate indices.

It was somewhat difficult to detect temporal and spatial patterns in wind-driven upwelling and downwelling in the monthly climatologies so we computed the surface Ekman transport divergence within a small region of the study domain shown in Figure 8.

Surface Ekman transport was determined at the NCEP grid points in a similar manner to that used to determine surface Ekman cross-shelf transport. We used the six-hourly NCEP data from 1948 – 2007. Surface Ekman convergence and divergence were calculated by summing surface Ekman transports at each side of the box. We calculated the mean surface Ekman convergence and divergence and error at the 95% confidence level for each month within the time period. We also calculated the overall mean and error at the 95% confidence level for each month within the period.

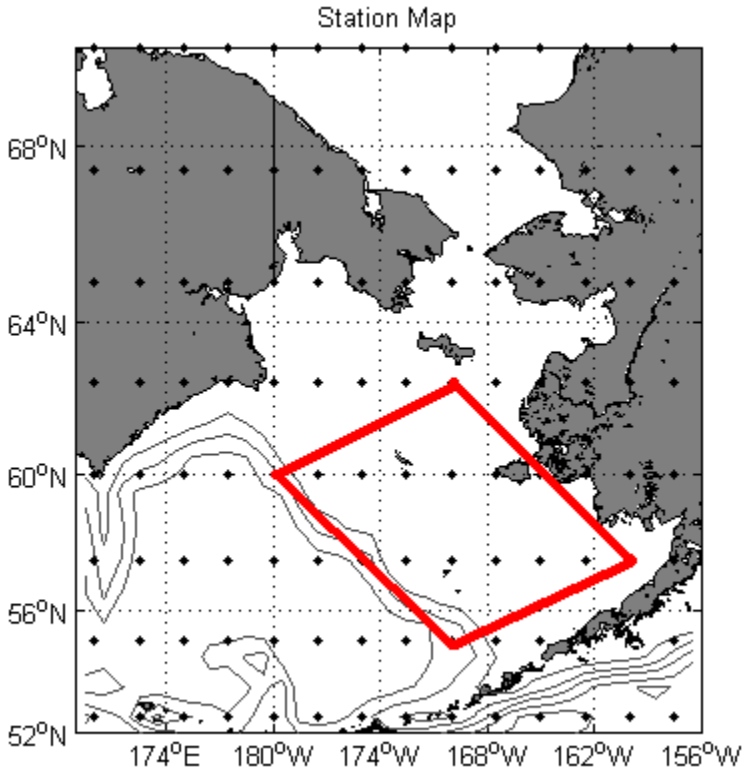

Figure 8. The small rectangular domain used to examine surface Ekman convergence and divergence. The domain is shown in red and NCEP grid points are shown in black.

We calculated the pycnocline displacement due to Ekman pumping and suction at four locations throughout the Bering Sea: near St. Paul Island (54.1250 ºN, 168.8750 ºW), the northwest shelf (62.1250 ºN, 175.8750 ºW), the central shelf (58.1250 ºN, 172.8750 ºW), and the southeast shelf (57.1250 ºN, 167.8750 ºW). These locations are shown in Figure 9.

The curl of the wind stress was calculated at each location using the difference in wind stress measured between the two closest QuikSCAT grid points immediately north and south of the location, and the difference in wind stress measured between the two closest QuikSCAT grid points immediately east and west of the location. The 12-hourly QuikSCAT wind data were used but these were interpolated to one hour intervals to

match the time step of the PWP model. The vertical velocities of the pycnocline were integrated over time to determine the vertical displacements in the pycnocline as follows:

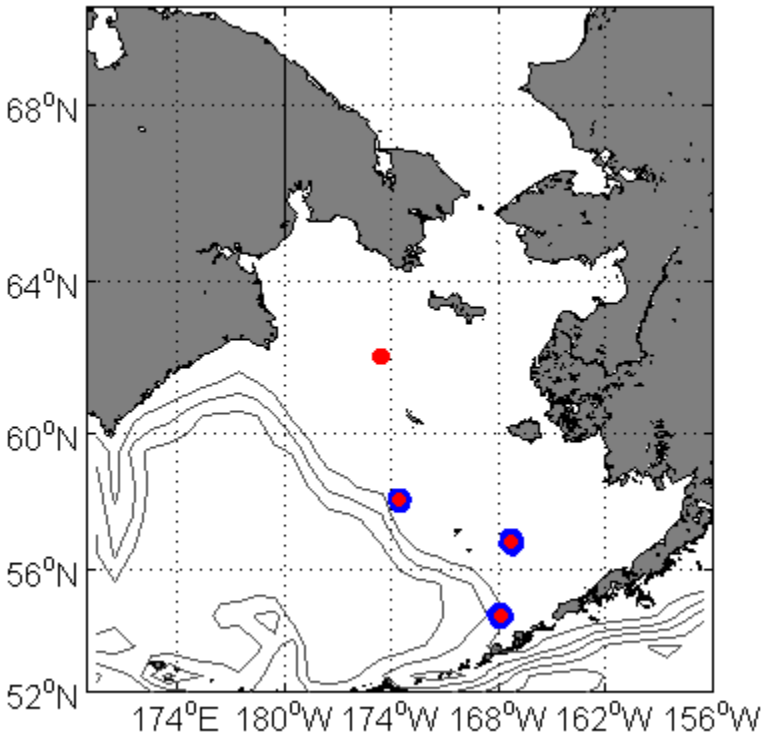

Figure 9. The locations at which displacements in the pycnocline due to wind-stress-curl were calculated**.** The locations are indicated by red circles. Pycnocline displacements were calculated for the summers of 2000 – 2006. The locations at which the PWP model was run are outlined in blue.

$$\Delta\eta = \int W_{Ek}\,dt = \frac{-1}{\rho}\int_{1}^{t}\frac{\partial(\tau^{y}/f)}{\partial x} - \frac{\partial(\tau^{x}/f)}{\partial y}\,dt\,; \tag{21}$$

where $\Delta\eta$ is the vertical displacement in the pycnocline, W_{Ek} is the Ekman pumping/suction, ρ is the reference density of sea water (1,025 kg/m^3), t is time, τ^y is the meridional wind stress, τ^x is the zonal wind stress, x is the zonal distance, and y is the meridional distance. We focused on the spring and summer months (April – August) as

this is the time period when phytoplankton production is maximized (Stabeno et al., 2006). The calculations were made for the years 2000 through 2006.

The PWP vertical mixing model assumes that wind mixing eases shear flow instabilities that arise between the surface mixed layer and the lower stratified layers. The model is driven by changes in temperature, salinity, and momentum in the upper mixed layer. Temperature changes are governed by the equation:

$$\frac{\partial T}{\partial t} = \frac{-1}{\rho_0}\frac{\partial F}{\partial z}; \tag{22}$$

in which T is temperature, t is time, ρ_0 is the reference density for seawater, F is the heat flux (so that $F(0) = Q$, the air-sea heat flux), and z is depth. Salinity is governed by the equation:

$$\frac{\partial S}{\partial t} = -\frac{\partial E}{\partial z}; \tag{23}$$

in which S is salinity, and E is the freshwater flux times salinity (so $E(0) = S(P\text{-}E)$; where P is precipitation and E is evaporation). Wind stress is applied to the surface layers in the momentum balance equation:

$$\frac{\partial \vec{V}}{\partial t} = -\vec{f} \times \vec{V} - \frac{1}{\rho_0}\frac{\partial \vec{G}}{\partial z}; \tag{24}$$

where $\vec{V}$ is the wind driven velocity in the upper mixed layer, $\vec{f}$ is the Coriolis acceleration, and $\vec{G}$ is the stress.

At each model step, the solar insolation is initially added to the surface layers by the equation:

$$I(z) = I(0)\left[I_1 \exp(-z/\lambda_1) + I_2 \exp(-z/\lambda_2)\right]; \tag{25}$$

where I_1 and I_2 are the shortwave and long-wave components of solar insolation and λ_1 and λ_2 are the shortwave and long-wave extinction coefficients which equal 0.6 m and 20 m respectively. The surface is at $z = 0$ and z increased positively with increasing depth. Heat loss due to evaporation and long-wave radiation, and the freshwater flux (precipitation - evaporation) are then calculated at the surface grid point. The density

profile is calculated and if $\frac{\partial \rho}{\partial z} < 0$, denser water sinks. The heat flux profile is then calculated as:

$$F(z) = F(0)[1 - z/h]; \tag{26}$$

where F is the heat flux and h is the mixed layer depth. The mixed-layer Richardson number (R_b) is then calculated as

$$R_b = \frac{g\Delta\rho h}{\rho_0 (\Delta \vec{V})^2}. \tag{27}$$

This dimensionless number is the ratio of the removal of energy due to buoyancy forces to the production of energy due to shear flow. When R_b <0.65, the mixed layer entrains denser waters until $R_b \geq 0.65$.

Price et al. (1986) concluded that there is a relatively smooth pycnocline at the bottom of the mixed layer rather than an abrupt density change within a meter. They proposed calculating the gradient Richardson number (R_θ) in the stratified layer as:

$$R_\theta = \frac{g\,\partial\rho/\partial z}{\rho_0 (\partial \vec{V}/\partial z)^2}. \tag{28}$$

If R_θ <0.25, mixing occurs accordingly:

$$\rho'_j = \rho_j - \left(1 - \frac{R_g}{R'_g}\right)(\rho_j - \rho_{j+1})/2 \text{ ; and} \tag{29}$$

$$\rho'_{j+1} = \rho_{j+1} + \left(1 - \frac{R_g}{R'_g}\right)(\rho_j - \rho_{j+1})/2; \tag{30}$$

in which ρ'_{j+1} is the density after mixing at the depth j+1. R'_g equals 0.3 for numerical convenience. The densities are recalculated until $R_\theta \geq 0.25$. Then the model progresses to the next time step.

Initially, abnormally warm water formed at the surface during certain model runs. This was most likely due to the lack of a sensible heat flux that was dependent upon the changing sea surface temperatures. To account for this, we included the Bulk Aerodynamic Formula for sensible heat flux:

$$Q_S = \rho C_P C_S U_{10} (t_s - t_a); \quad (31)$$

in which Q_S is the sensible heat flux (W/m^2), ρ is the density of air (1.3 kg/m3), C_P is the specific heat capacity of air (1,030 J/(kg C)), C_S is the sensible heat transfer coefficient (0.001), U_{10} is the wind speed, and t_s and t_a are the sea surface and air temperatures respectively (ºC).

There were three groups of model runs. The first group consisted of winds and surface flux variables measured or calculated near St. Paul Island (54.1250 ºN, 168.8750 ºW). Here we ran the model with QuikSCAT winds, QuikSCAT winds and a wind-stress-curl term, NCEP winds, and winds measured at National Weather Service Station PASN on St. Paul Island (57.1667 ºN, 170.2167 ºW). This enabled us to determine the effects of wind-stress-curl on the evolution of the mixed layer and the discrepancies between the different data sets. The first model run used data from April – August 2001.

We next examined the plots of pycnocline displacement to find locations and times for which Ekman pumping or suction were strong. By using data from these grid points and times we were able to model the extent to which wind-stress-curl could contribute to the evolution of the mixed layer. We ran the model for the central shelf location using data from April – August 2005 when relatively strong Ekman suction occurred. We then ran the model for the southeast shelf location using data from April – August 2006, when there was relatively strong Ekman pumping.

The initial salinity and temperature profiles used to start the model were taken from a profile observed on March 11, 2001, at 53.72 ºN, 167.73 ºW. These data were obtained at the NODC World Ocean Database (NODC, 2005; http://www.nodc.noaa.gov/). Calculations of short wave radiation, long wave radiation, latent heat flux, sensible heat flux, precipitation, and air temperature were based on NCEP/NCAR (Kalnay et al., 1996; Kistler et al., 2001; http://www.cdc.noaa.gov/). The table below summarizes the data grid points for each model run.

Table 1. Summary of data grid points for the three model runs.

Model Group	1	2	3
Time	April - August 2001	April - August 2005	April - August 2006
Location	Southeast Aleutian Basin	Middle Shelf	Southeast Shelf
QuikSCAT Data	54.1250 ºN, 168.8750 ºW	58.1250 ºN, 172.8750 ºW	57.1250 ºN, 167.8750 ºW
NCEP Data	55.00 ºN, 167.50 ºW	57.50 ºN, 172.50 ºW	57.50 ºN, 167.50 ºW
Met Station Data	57.1667 ºN, 170.2167 ºW	X	X
NCEP Fluxes	54.2846 ºN, 168.7500 ºW	58.0939 ºN, 172.50 ºW	58.0939 ºN, 168.75 ºW

The inertial period near 54ºN is approximately 14.8 hours. To accurately resolve motions within this period we interpolated the values of all of the surface fluxes and wind stresses to one hour sampling intervals.

Chapter 3 Results

The results of the complex cross-correlation analysis are shown in Appendix A, Figures A-1 through A-16. The maps indicate that the QuikSCAT and NCEP data sets are well correlated and in phase with one another. In the top panel of Figure A-1, the complex correlation coefficient decays to 0.5 over a distance of approximately 690 km. In the bottom panel, the map indicates that the data sets are in phase throughout most of the domain. There is no QuikSCAT data for areas covered by sea ice. This is apparent in Figure A-4, which shows maps for an NCEP grid point at 70º N for the months of January through February. However, the data sets are highly correlated for grid points at lower latitudes during these months (Figures A-1 through A-3) and for this high latitude grid point during ice-free months (Figures A-8, A-12, and A-16). Therefore, we assume that the NCEP winds over ice are reasonably consistent with what QuikSCAT would have measured in the absence of ice. For analyses which require complete data sets, we substitute interpolated NCEP data points for missing QuikSCAT data.

The results of the linear regressions between NCEP and QuikSCAT are shown in Appendix B. Tables B-1 and B-2 show results of the regressions between the zonal (U) and meridional (V) components of winds, respectively, before February 2002. Tables B-3 and B-4 show results of the regressions between the zonal (U) and meridional (V) components of winds, respectively, beginning in February 2002. Only two regressions are not significant at the 95% confidence level. These are the regression for the U components of the data before 2002 at the NCEP grid point 70.0º N and 177.5º W, and the regression for the V components of the data before 2002 at the same NCEP grid point. Both are listed at the beginnings of Tables B-1 and B-2, respectively. The intercept (b_0) and slope (b_1) coefficients are used to correct the NCEP winds records, which begin in 1948.

Tables B-5 through B-8 list the regressions with intercepts that are statistically less than, greater than, or equal to zero and slopes that are statistically less than, greater than, or equal to one at the 95% confidence level. The regressions at many grid points

show that the data sets are statistically different from one another. Table 2 summarizes these findings. Note that there are only 74 total regressions for the wind components before February 1, 2002. Only 74 were counted in these instances because one regression for each of the wind components before 2002 was not significant at the 95% confidence level.

Table 2. The numbers of intercepts and slopes for the linear regressions significant at the 95% confidence level.

Number of Regression Intercepts	<0	0	>0	Totals
U Before Feb. 1, 2002	13	19	42	74
U After Feb. 1, 2002	15	16	44	75
V Before Feb. 1, 2002	7	29	38	74
V After Feb. 1, 2002	22	24	29	75
Number of Regression Slopes	**<1**	**1**	**>1**	**Totals**
U Before Feb. 1, 2002	66	4	4	74
U After Feb. 1, 2002	69	3	3	75
V Before Feb. 1, 2002	69	1	4	74
V After Feb. 1, 2002	69	2	4	75

The monthly climatologies are shown in Appendix C, Figures C-1 through C-24. The wind patterns (Figures C-1 through C-12) seem to have distinct patterns for each season. In January, the winds are primarily northeasterly. In February, the winds are cyclonic, which could lead to Ekman suction. March is dominated by the curl-free northeasterly winds, similar to those in January, except that they are slightly weaker. There is a northeasterly pattern in April with a cyclonic curl. In May, the winds are relatively weak and blow from the north or northeast. In June, the winds are still relatively weak, but an anticyclonic pattern is centered near St. Lawrence Island. This could engender Ekman pumping on the shelf. In addition, a smaller cyclonic pattern characterizes the wind field near Bristol Bay, which could facilitate upwelling. The winds are primarily from the south and southwest over the shelf during July. In the Chukchi Sea the winds come from the north. This seems to create a region of wind convergence near Bering Strait. There is a small degree of positive wind-stress-curl in the Gulf of Anadyr. In August, a large cyclonic pattern dominates the western shelf while a large anticyclonic pattern dominates the northeastern shelf. These are most likely

created by the close proximity of high and low pressure systems. The winds blow from the north and west in September to create a large upwelling feature. This pattern is strengthened in October and November. The December pattern is very similar to the pattern in January.

One can obtain a clearer picture of the how the winds affect circulation by examining the mean monthly Ekman transport maps (Figures C-13 through C-24). In January, surface Ekman transport is primarily directed to the northwest. This creates downwelling along the coast of Russia and upwelling along the western coast of Alaska and the Aleutian Islands. In February, there is still flow into the eastern Russian coastline. There is also a large surface divergence north of the Aleutian Islands centered at approximately 53 ºN, 173 ºW. In March, surface Ekman transport is still directed northwest and offshore along the southern edge of Bristol Bay. This could facilitate upwelling and supply nutrients to the spring phytoplankton bloom. In April, the same general pattern is present although the surface transports are somewhat lower than those in March. There is a zonal band along 55º N where the surface currents diverge. This could also facilitate upwelling during the time when the spring bloom is initiated.

In May Ekman transport remains generally to the west in the southeastern Bering Sea and is generally offshore in Bristol Bay in April - June. There is also a weak divergent zone in the eastern Aleutian Basin, which could facilitate Ekman pumping and phytoplankton growth with increased nutrients at the surface.

June is characterized by a large convergent zone south of St. Lawrence Island, which implies downwelling. Surface Ekman transport near the shelf break during this month is almost entirely onshore. This could impact biological production by transporting nutrients from the deeper waters to the shelf. Surface Ekman cross-shelf transport could also work additively with the summer mesoscale eddies observed by Mizobata et al. (2006) to drive nutrients across the shelf break. Flow in the Chukchi Sea is generally to the north with a small area of southward flow near Bering Strait.

In July and August, surface Ekman transport is generally towards the south and southwest. Upwelling may result as surface waters are pushed offshore along the Russian coast and across the shelf break of the southeast Bering Sea.

In September, surface Ekman transport is almost entirely offshore along the Alaskan coast and shelf break. South of St. Lawrence Island, surface Ekman transport divergence suggests weak upwelling. October, November, and December are characterized by the same pattern but the transports are intensified.

In the spring and summer months, there is often downwelling on one coastline while upwelling on the other. Based solely upon Ekman transport maps, one might conclude that the spring bloom could begin earlier in the year along the Alaskan coast of the Bering Sea. The bloom might be initiated in April and then end in July when surface Ekman transport shifts to the east. Upwelling along the Russian coast of the Bering Sea at this time could supply depleted surface waters with nutrients and facilitate a summer bloom.

The climatologies of wind variability are shown in Figures C-25 through C-26. In general the variances for the *U* wind components, *V* wind components, and the wind speeds are greater in the winter months than in the summer months. In January and February, the variance ellipses are mostly circular indicating that the variances for the zonal and meridional components are approximately equal. The maximum component variances are close to 100 m^2/s^2. In Bristol Bay the zonal variances are slightly larger than the meridional variances.

In March and April the zonal, meridional, and speed variances all decrease compared to the winter months. In April, the zonal wind component variances are slightly larger than the meridional wind component variances in the western Aleutian Basin.

The wind component variances and the speed variances decrease more in May. South of Bering Strait, meridional variability is somewhat greater than zonal variability and this trend persists through October with the ellipses in this area becoming increasingly rectilinear in the summer months. Zonal variability in Bristol Bay is greater

than meridional variability in the summer months (June – August). This implies that the variability in zonal surface Ekman transport (either onshore or offshore in Bristol Bay) is less variable than the variability in meridional surface Ekman. In September, the variances are still relatively small, but these increase in October through December when the variance is isotropic, similar to January and February.

Annual surface Ekman cross-shelf transports at the shelf break are shown in Figure 10. The mean annual net transport (straight red line) is ~ 7,500 km^3/yr. However, the net transport is highly variable and ranges from ~ -1,000 km^3/yr (upwelling) to ~15,000 km^3/yr (downwelling). The annual onshelf transports (blue line) and net transports (red line) appear to be significantly higher after 1972. The results of the non-parametric t-test and Wilcoxon Rank Sum Test (Table 3) indicate a significant difference at the 95% confidence level between the annual net transports and annual onshore transports from 1948–1972 and from 1973-2007. However, no significant difference between the median offshore transports during these two time periods was detected with the Wilcoxon Rank Sum test.

Plots of the anomalies of seasonal surface Ekman cross-shelf break transport are presented in Appendix D, Figures D-1 through D-4. It is difficult to discern if transports during each season shifted after 1972 and the results of the statistics tests, completed for each month, are shown in Table 4. It appears as though the general t-test is more sensitive than the Wilcoxon Rank Sum Test as the t-test indicates significant differences at the 95% confidence level in a few instances where the Rank Sum test does not (March, April, and December). However, both tests detected significant differences for the months of January and July.

The results of the cross-correlation tests between the monthly surface Ekman cross-shelf transports and certain climate indices are shown in Appendix D, Table D-1. There are no strong correlations. Extremely weak correlations exist between the onshore surface Ekman cross-shelf transports along the entire shelf break and the PDO indices (r = 0.36), the offshore surface Ekman cross-shelf transports at 60.0º N, 180.0º W and 57.5º N, 175.0º W and the PNA indices (r = 0.40 and 0.36 respectively), and the offshore

surface Ekman cross-shelf transports along the entire shelf break and the PNA indices (r = 0.35). These correlations are significant at the 95% confidence level.

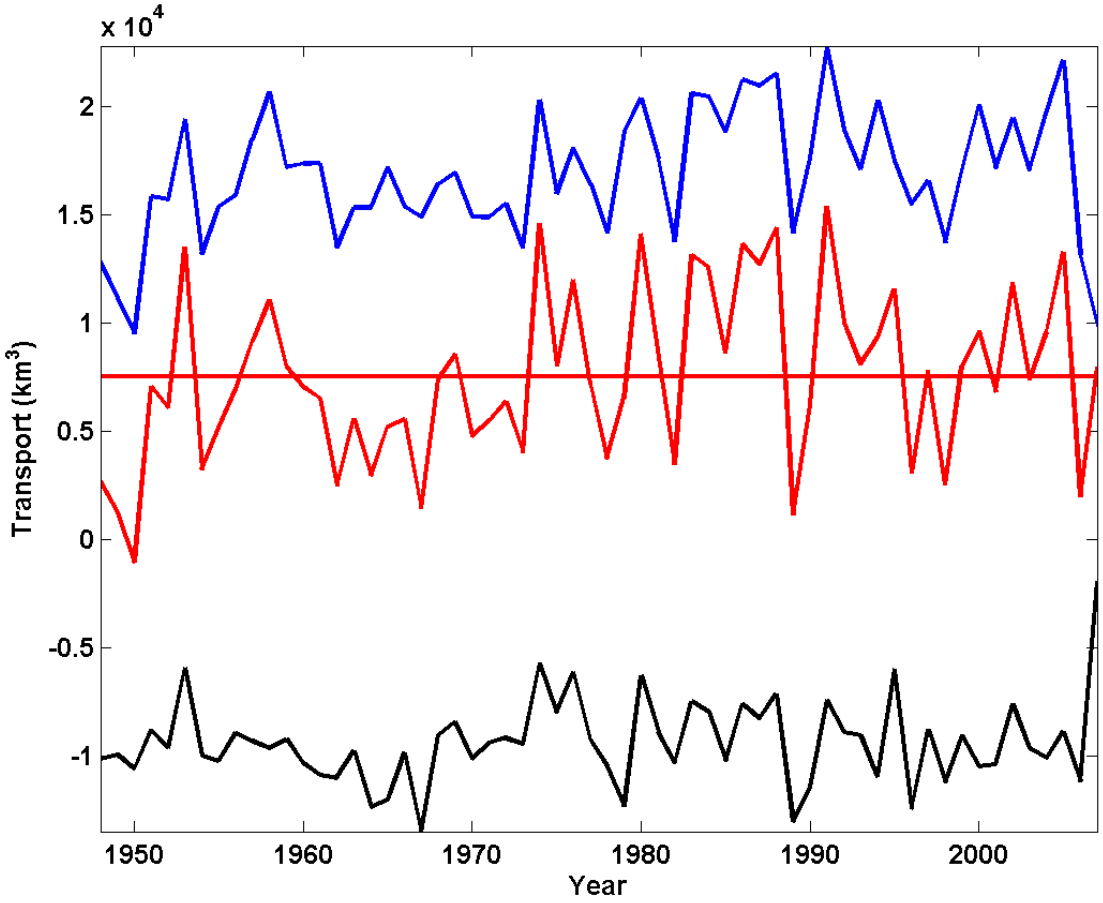

Figure 10. Annual surface Ekman cross-shelf transports. Onshelf transports are shown in blue, offshelf transports are shown in black, and net transports in red. The horizontal red line is the mean net transport. Positive transport indicates that flow is onto the shelf and negative transport indicates that flow is off of the shelf. There is a high degree of interannual variability in the transports.

Table 3. Results of non-parametric t-tests and Wilcoxon rank sum tests for annual surface Ekman cross-shelf transports before and after 1973.

	t-test (p-value)	Wilcoxan Rank Sum Test (p-value)
Net Transport	<<0.05*	<<0.05*
Onshore Transport	<<0.05*	<<0.05*
Offshore Transport	0.02*	0.09

Note: Significant differences are indicated by an asterisk next to each p-value.

Table 4. Results of non-parametric t-tests and Wilcoxon rank sum tests for monthly surface Ekman cross-shelf transports before and after 1973.

	t-test	Wilcoxan Rank Sum Test
Month	**pvalue**	**pvalue**
January	<<0.05*	<<0.05*
February	0.28	0.53
March	0.02*	0.15
April	0.05*	0.08
May	0.58*	0.64
June	0.64	0.37
July	<<0.05*	<<0.05*
August	0.47	0.77
September	0.73	0.49
October	0.14	0.27
November	0.57	0.7
December	0.03*	0.06

Note: Significant differences are indicated by an asterisk next to each p-value.

The annual freshwater fluxes and nitrate fluxes due to surface Ekman cross-shelf transport across the shelf break are shown in Figure 11 and Figure 12, respectively. They show the same change between 1972 and 1973. This indicates that wind-driven freshwater transport onto the shelf and nitrate export off of the shelf both increased after 1972. Figure 11 shows that freshwater has been transported from the basin onto the shelf in all but a few years (1950, 1963, 1965, and 2008). The mean freshwater flux is ~57 km^3/yr. Figure 12 shows that nitrate is mostly exported off the shelf with mean export of ~150 teramoles/yr.

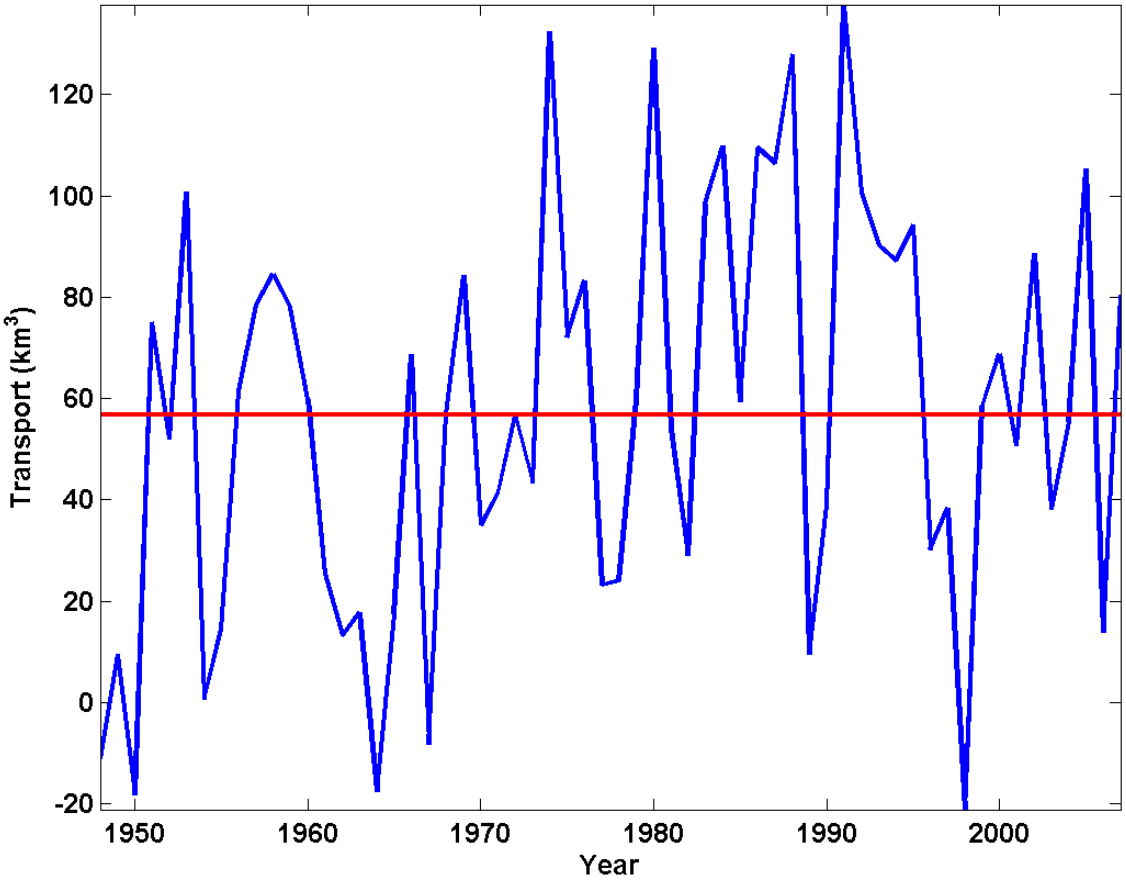

Figure 11. The annual freshwater fluxes across the shelf break due to surface Ekman cross**-shelf transport**. The fluxes are normalized by the reference salinity 34.8 (per Aagaard et al., 1981). Freshwater was transported onto the shelf in all years except 1950, 1963, 1965, and 2008.

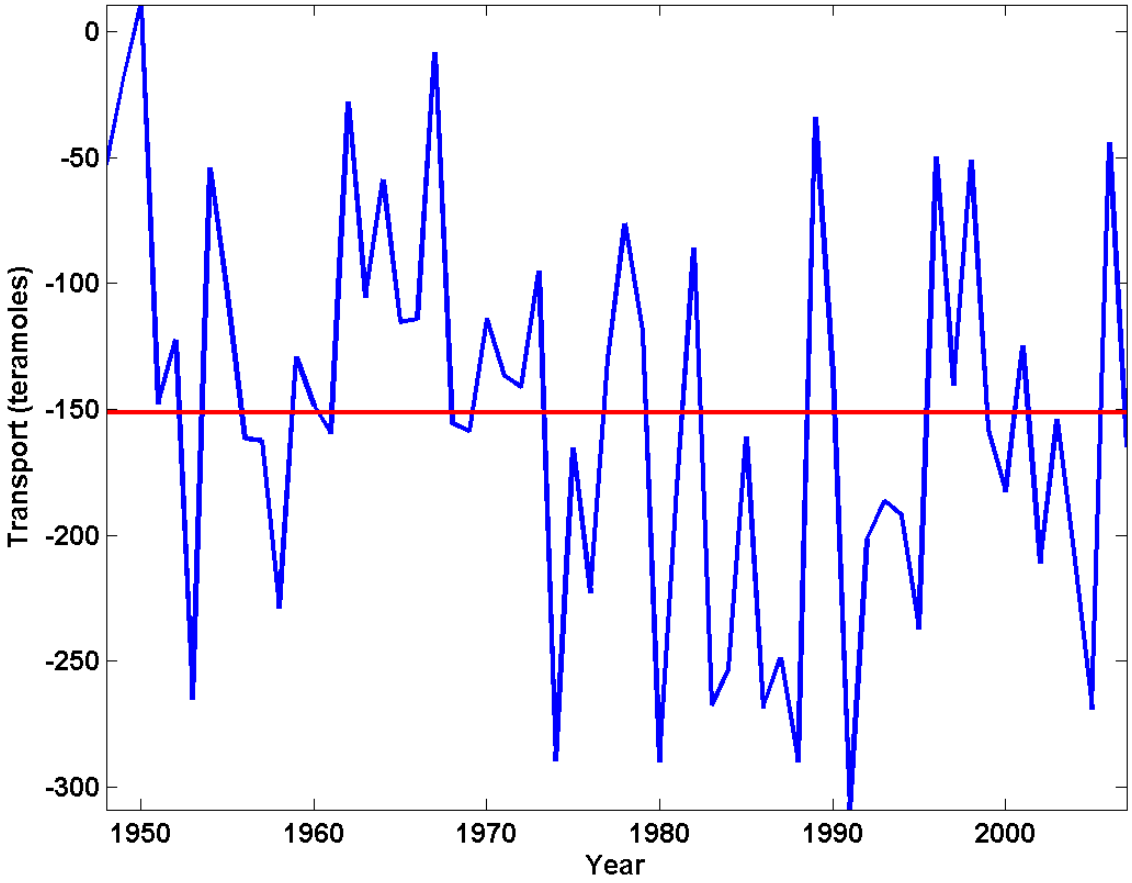

Figure 12. The annual nitrate fluxes across the shelf br**eak** due to surface Ekman cross-shelf transport. Negative values indicate that nitrate was exported off of the shelf. Nitrate was transported onto the shelf only in 1950.

The means and standard deviations for the surface Ekman cross-shelf transports during each month are shown in Figure 13. Winds are downwelling favorable for all months except July and August, when the winds are upwelling favorable. Monthly Ekman transports are highly variable, however, as the standard deviations exceed the means from April through November. Plots of the DFFT of the along-shelf break components of the winds (not shown) indicate that the annual cycle is dominant.

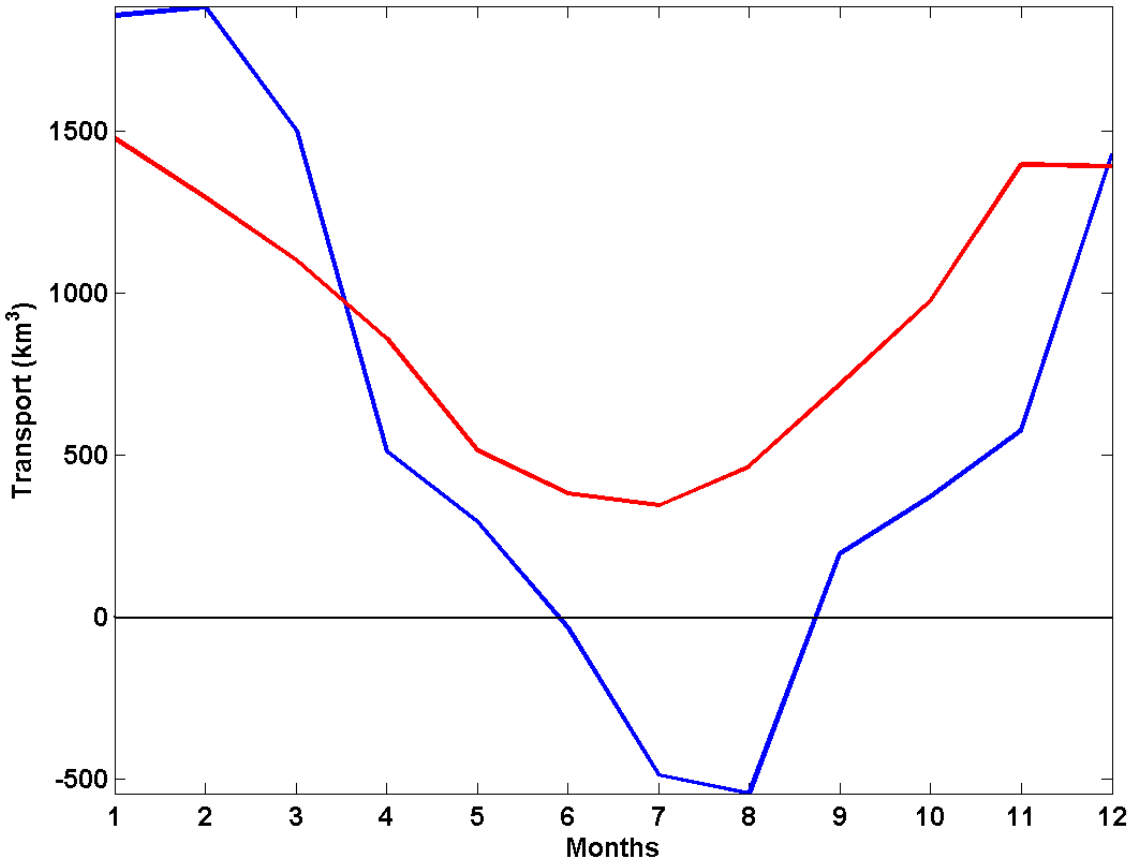

Figure 13. The means (blue line) and standard deviations (red line) of monthly surface Ekman cross-shelf **transport**. Positive values indicate transport onto the shelf while negative values indicate transport off of the shelf.

CEOFs condense the variability of the winds in the region into a few distinct modes. The eigenvalues for the first five modes of the small domain are plotted in Figure 14 and expressed as a percentage of the variance explained by each mode. The plot includes error bars which are calculated by equation 21. Sequentially higher modes express successively smaller amounts of the variance. Eigenvalues that do not have overlapping error bars can be considered significant modes (Horel 1984). Although the first 14 modes are significant, we limit our attention to the first three modes which explain 88.5% of the total variance.

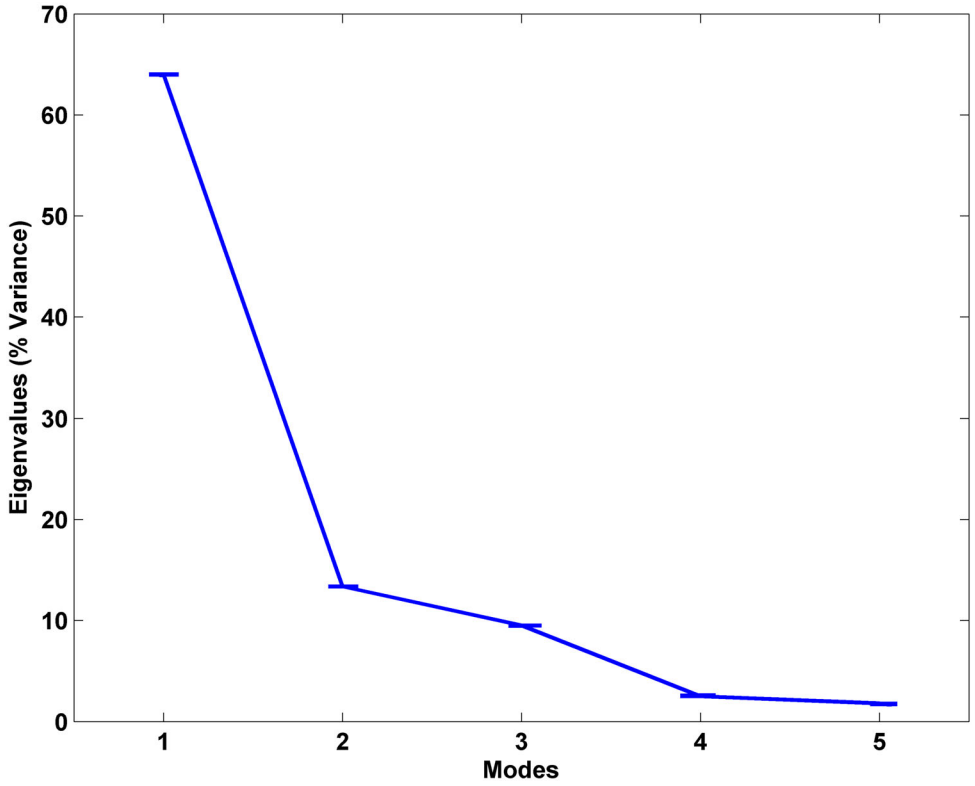

Figure 14. **The eigenvalues of the first five modes.** They are expressed as the percentage of variance that they explain. The first 14 modes are significant (their error bars do not overlap) however only the first five modes are shown here as higher modes explain very small percentages of the total variance. Note that the error bars are close together for each mode.

The first mode accounts primarily for zonal wind variations. The second mode is a cyclonic wind pattern centered near the shelf break at about 59º N, 175º W. The third mode is a convergent wind pattern with winds converging along a north-south axis near 173º W. The wind vectors in each mode are relatively small (Figures 15-17). As the data are reconstructed, the vectors are scaled by relatively large coefficients in the complex principal components matrix. Plots of the principal component matrices and explanations of their implications can be found in the following chapter. In addition, plots of the NCEP 6-hourly, monthly, and annual CEOFs and their correlations with climate indices are presented in Appendix E. These results are also discussed in the next chapter.

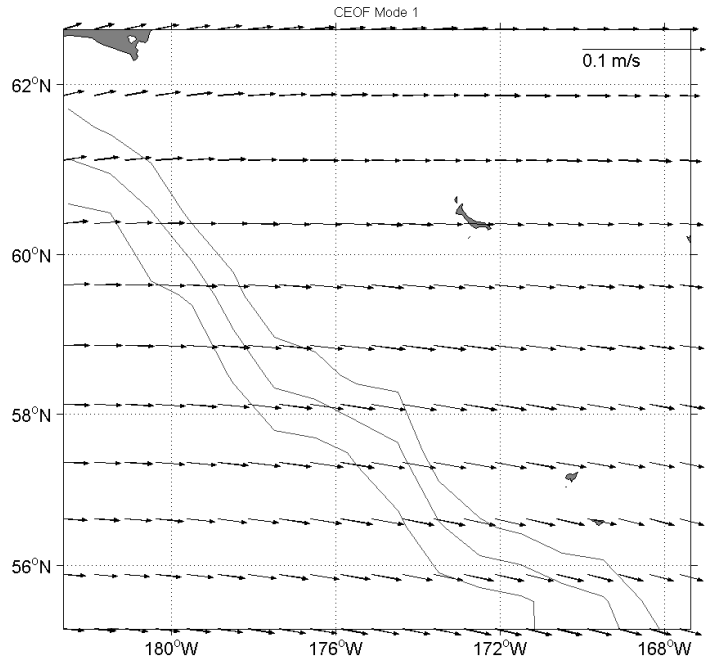

Figure 15. The first CEOF mode, which explains approximately 67.4% of the variance.

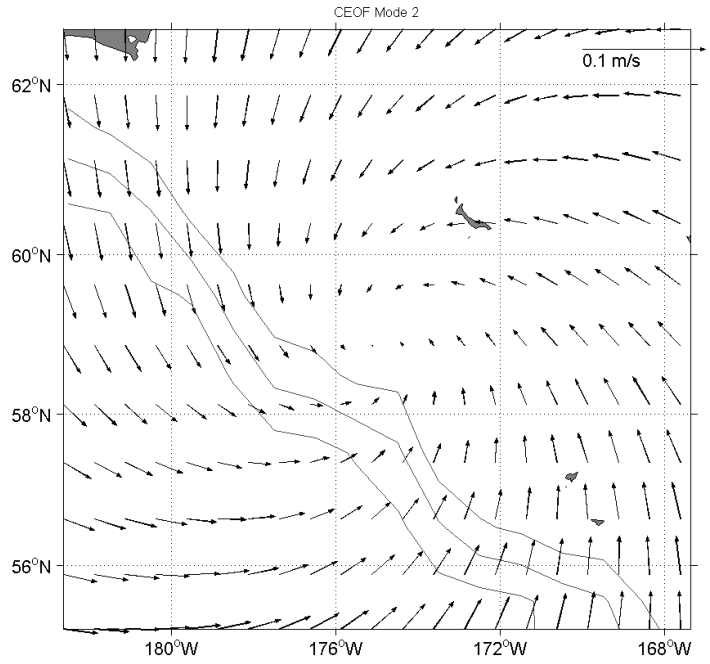

Figure 16. The second CEOF mode, which explains approximately 12.6% of the variance.

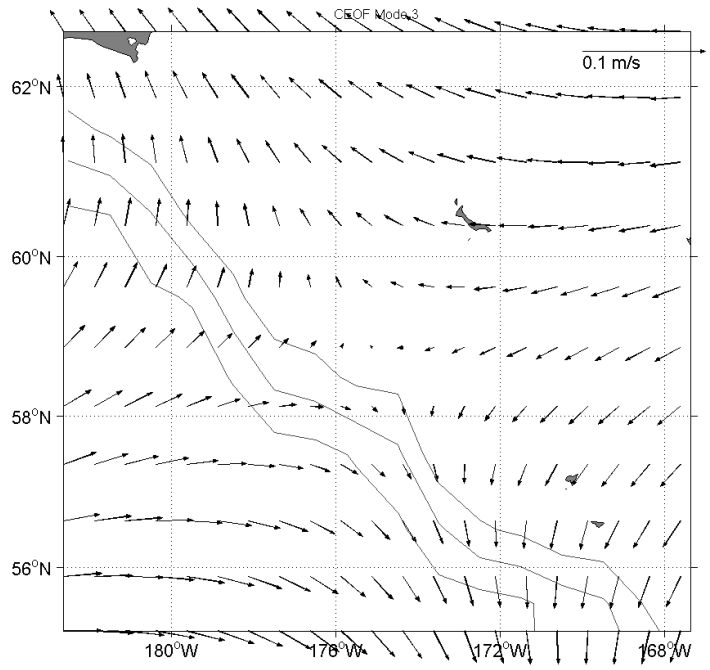

Figure 17. The third CEOF mode, which explains approximately 8.5% of the variance.

Power Spectral Density (PSD) plots of the complex amplitudes for the first three modes (not shown) show large visible peaks in power near the annual period, however, none of the peaks are significant at the 95% confidence level.

A histogram of the Ekman suction and pumping rates within the small domain (Figure 8) over the Bering Sea shelf is shown in Figure 18. The mean is close to zero indicating that winds over in this area generally induce weak Ekman pumping or suction. However, the long tails of the histogram indicate that there are infrequent wind events which may induce relatively large vertical motions in the pycnocline and could be important to vertical mixing. The histogram indicates that some storms could lead to the pycnocline rising or sinking > 3 m/day.

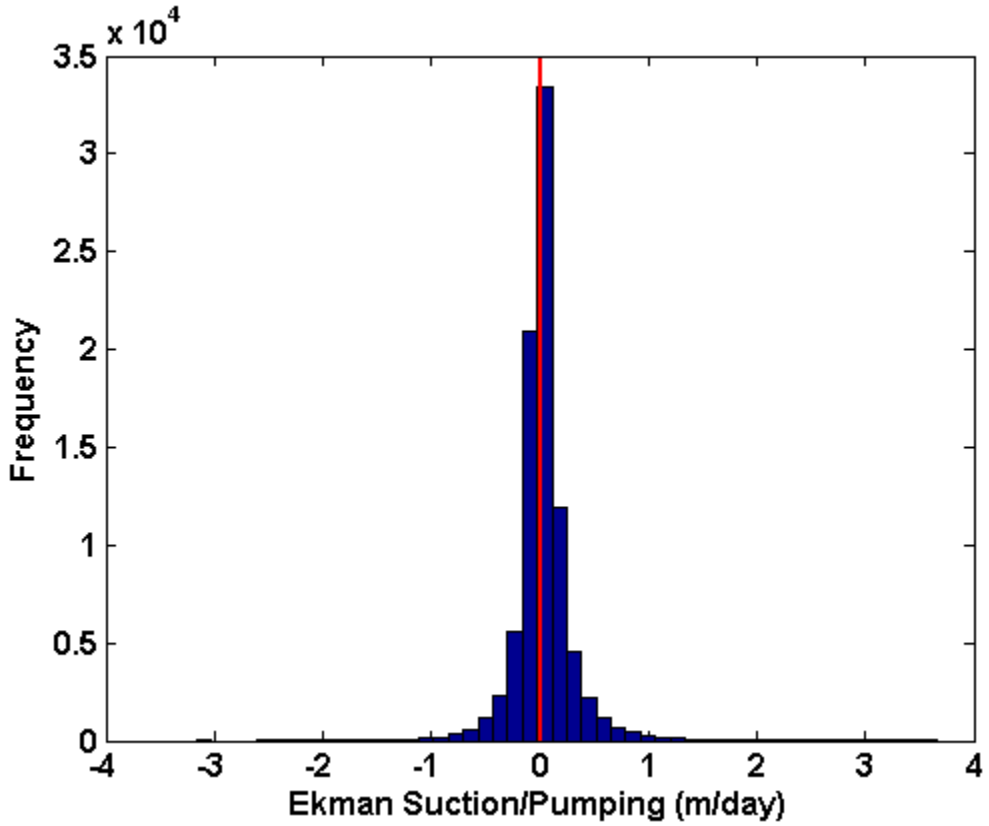

Figure 18. A histogram of the Ekman suction and pumping rates within the small domain over the Bering Sea s**helf** due to NCEP wind forcing from 1948-2007. Positive values indicate Ekman suction and negative values indicate Ekman pumping. The rates are based upon NCEP wind values, which are given every six hours. The wind data was corrected by the linear regression coefficients and then integrated over a six hour period.

The mean rates of Ekman suction and pumping for each month within the small domain over the Bering Sea shelf are shown in Table 5. All of these values are significantly different from zero at the 95% confidence level. These results are discussed in the next chapter. In addition, plots of the mean monthly Ekman pumping and suction rates and their associated errors within the small domain over the Bering Sea shelf are shown in Appendix F.

Table 5. The monthly mean Ekman pumping and suction rates for the rectangular domain over the Bering Sea shelf (1948-2007).

Month	Ekman Pumping/ Suction Rate (m/day)
January	-0.01
February	-0.02
March	0.01
April	0.03
May	0.02
June	0.00
July	0.01
August	0.04
September	0.05
October	0.07
November	0.12
December	0.06

Note: Positive values indicate Ekman suction. Negative values indicate Ekman pumping. The rates are based upon six-hourly NCEP data. None of the values are significantly different from zero at the 95% confidence level.

Figures 19-22 show the cumulative pycnocline displacements due to Ekman pumping and suction in the spring and summer months of seven years (2000–2006) at four locations in the Bering Sea. These figures show the approximate distance that the pycnocline could have been displaced after each hour of wind-stress-curl is applied. Each plot shows results from one of four locations throughout the Bering Sea. The results from seven different years (2000-2006) are shown in each plot. In several different years and locations the pycnocline is significantly displaced due to Ekman pumping and suction.

There is a high degree of interannual variability in pycnocline displacement at these locations. Figure 19 shows that the pycnocline may have been raised a maximum of two meters in 2000 and 2005 at the location near St. Paul Island. It was depressed over four meters at the same location in 2003. Ekman pumping and suction appear to be important over the shelf as well. The pycnocline was raised approximately 3 m in 2005 at the location over the central shelf (Figure 21). The pycnocline was possibly lowered over 4.5 meters at the location over the southeast shelf in 2006 (Figure 22).

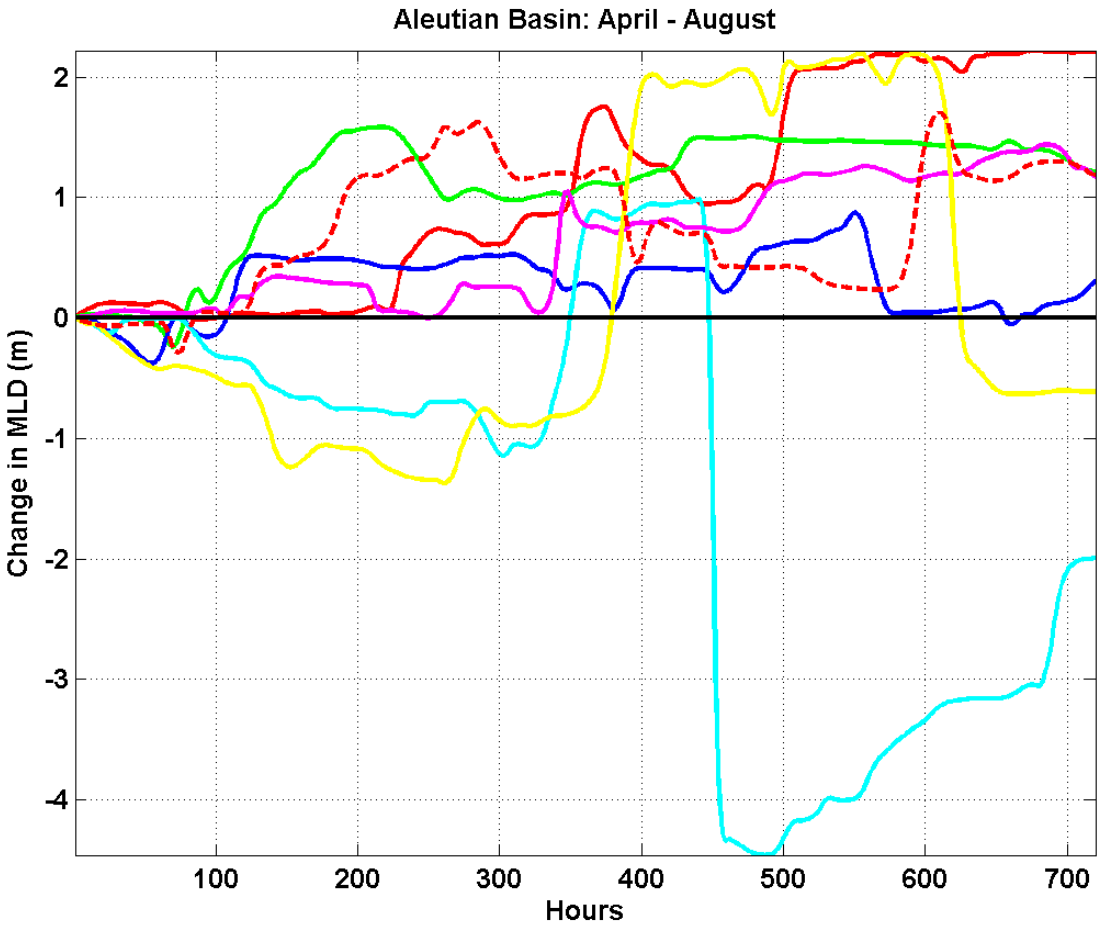

Figure 19. Plots of the integrated Ekman pumping and suction rates for the months of April through August near the Pribilof Islands (54.1250 ºN, 168.8750 ºW). Ekman suction and pumping was calculated using the QuikSCAT winds measured every 12 hours and then interpolated to one hour intervals. The years are indicated as follows: 2000 = red, 2001 = green, 2002 = blue, 2003 = turquoise, 2004 = magenta, 2005 = yellow, and 2006 = dashed red.

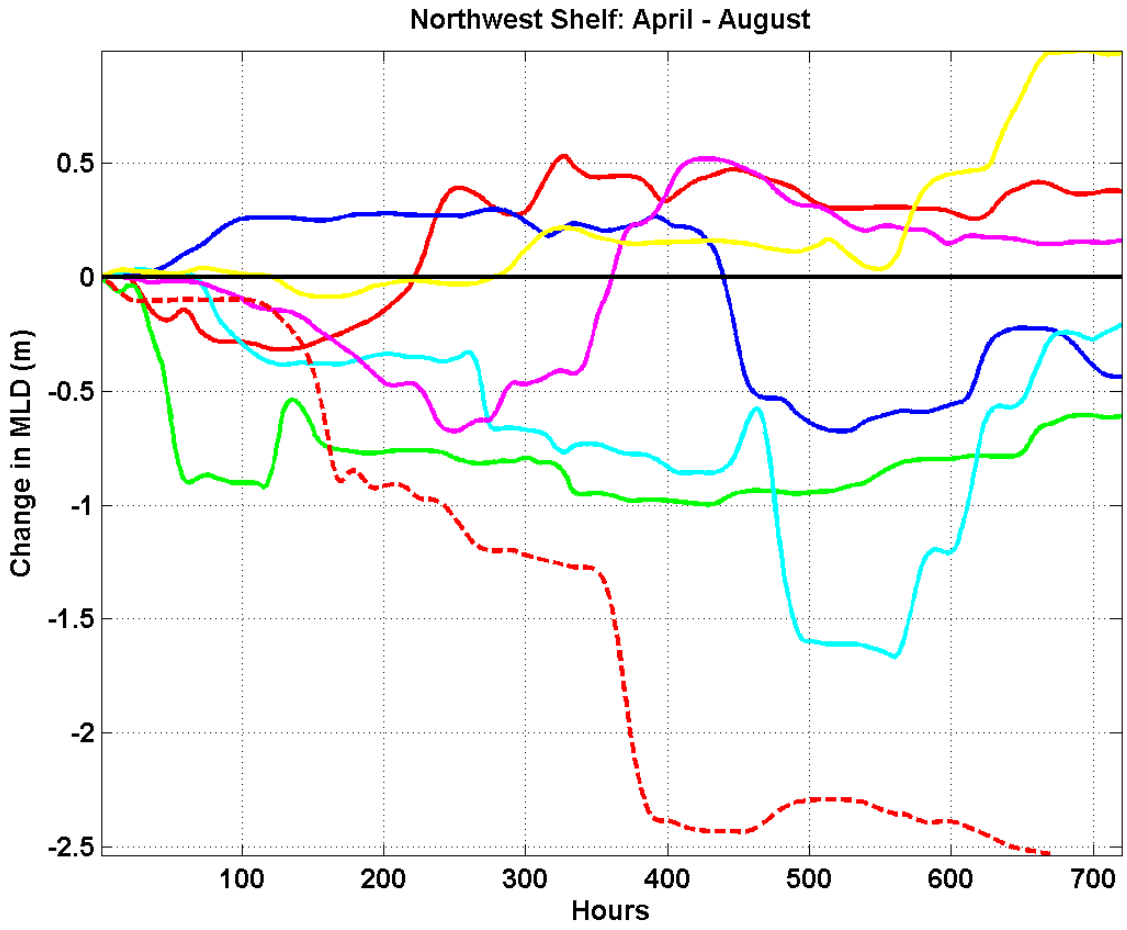

Figure 20. Plots of the inte**grated Ekman pumping and suction rates for the months of April through August in the northwest Bering Sea (62.1250 ºN, 175.8750 ºW).** Ekman suction and pumping was calculated using the QuikSCAT winds measured every 12 hours and then interpolated to one hour intervals. The years are indicated as follows: 2000 = red, 2001 = green, 2002 = blue, 2003 = turquoise, 2004 = magenta, 2005 = yellow, and 2006 = dashed red.

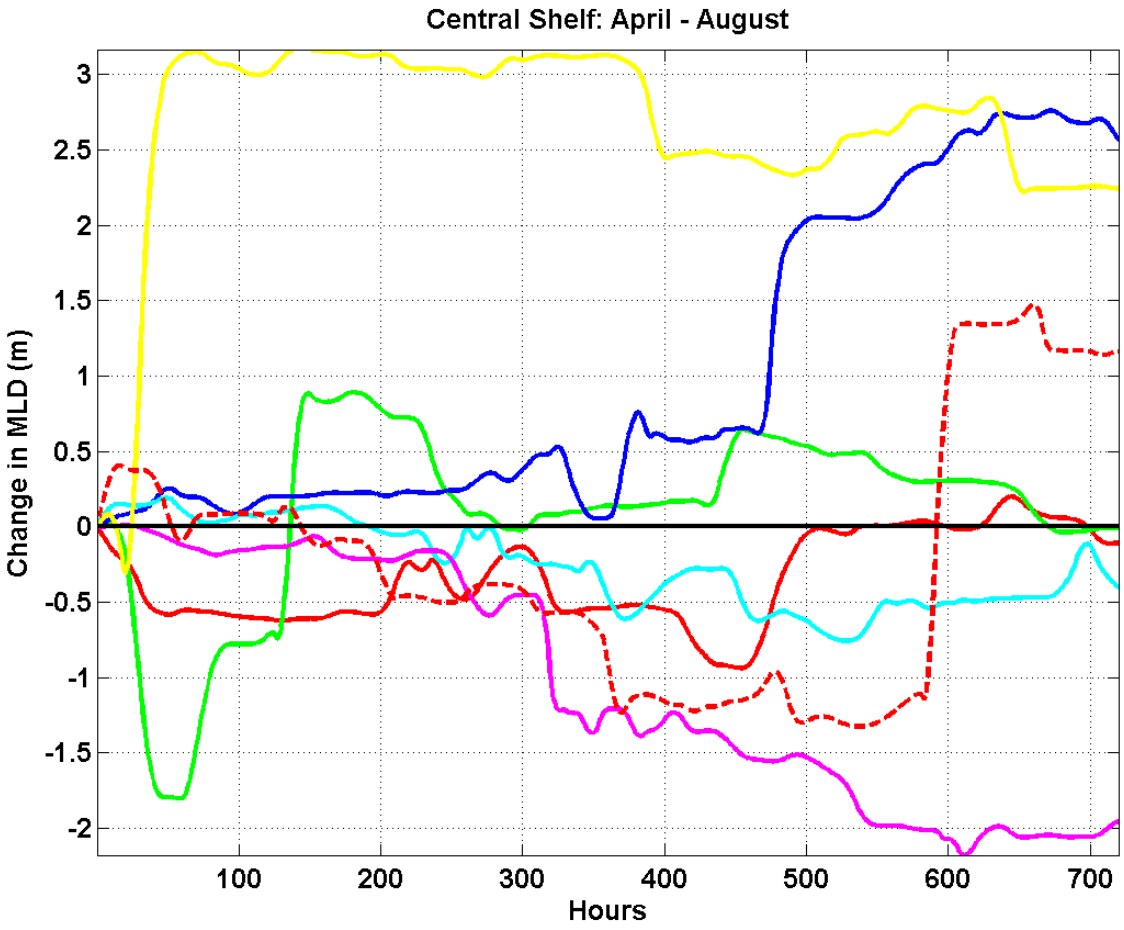

Figure 21. Plots of the integrated Ekman pumping and suction rates for the months of April t**hrough August in the central Bering Sea (58.1250 ºN, 172.8750 ºW).** Ekman suction and pumping was calculated using the QuikSCAT winds measured every 12 hours and then interpolated to one hour intervals. The years are indicated as follows: 2000 = red, 2001 = green, 2002 = blue, 2003 = turquoise, 2004 = magenta, 2005 = yellow, and 2006 = dashed red.

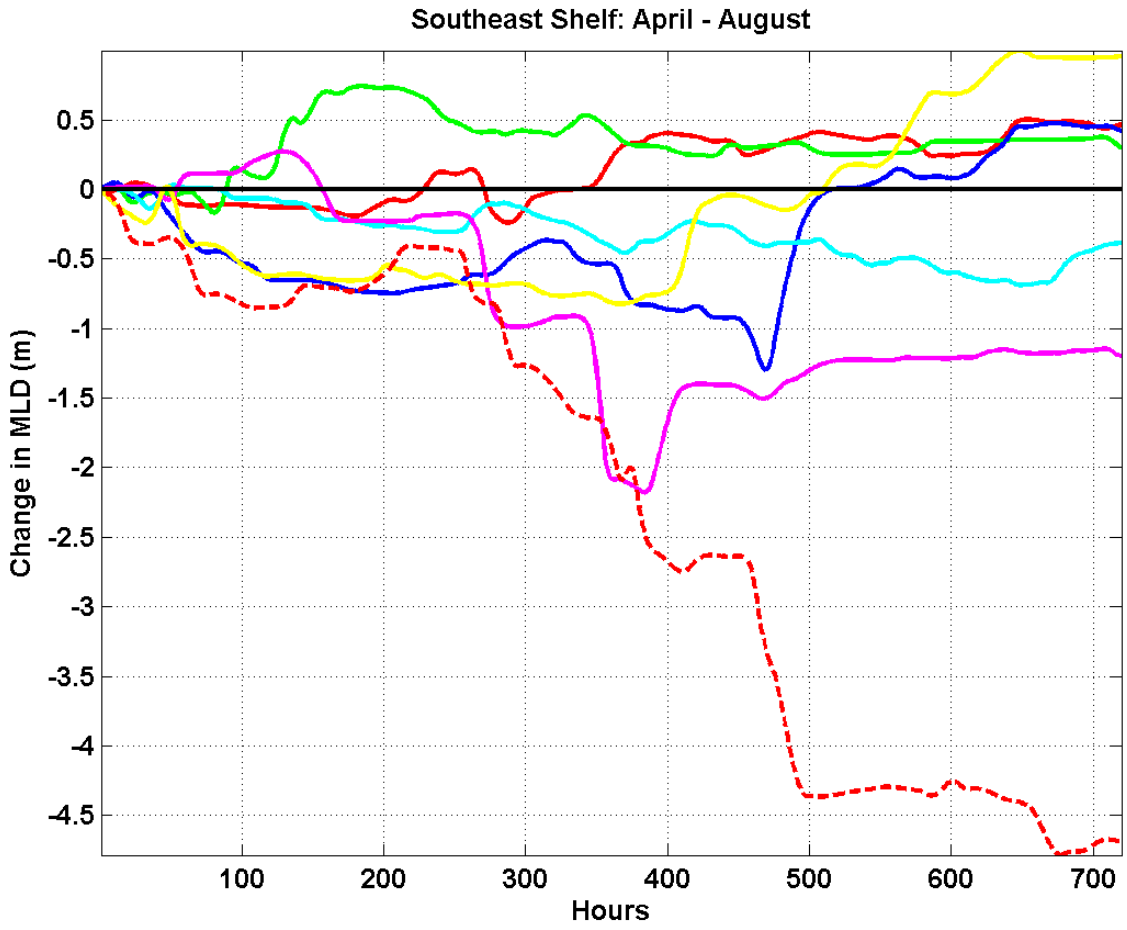

Figure 22. Plots of the integrated Ekman pumping and suction rates for the months of April through August in the southeast Bering Sea (57.1250 ºN, 167.8750 ºW**).** Ekman suction and pumping was calculated using the QuikSCAT winds measured every 12 hours and then interpolated to one hour intervals. The years are indicated as follows: 2000 = red, 2001 = green, 2002 = blue, 2003 = turquoise, 2004 = magenta, 2005 = yellow, and 2006 = dashed red.

The results of the three model runs are also presented in Appendix G. The first model run used data collected off of the shelf near the Pribilof Islands. The vertical profiles that the model computed with QuikSCAT winds, with QuikSCAT winds and wind-stress-curl, with NCEP winds, and with winds measured at station PASN are shown in Figures G-2 through G-8, respectively. The second model run used data from the

central shelf. The third model run used data from the southeast shelf. These results can also be found in Appendix G and are discussed in the Discussion Chapter.

Chapter 4 Discussion

As Chelton and Freilich (2005) determined QuikSCAT measurements to be relatively close to NDBC buoy measurements, we consider QuikSCAT data to be accurate. The complex cross-correlation plots (Appendix A) and linear regression results (Appendix B) suggest that the QuikSCAT and NCEP data sets are well correlated and in-phase with one another. This justifies our substitution of interpolated NCEP winds for missing QuikSCAT wind measurements.

However, there are some discrepancies between the two data sets. A perfect correlation would require that the intercept in each linear regression be zero and the slope be one. However, Table 2 indicates that there are several regression intercepts and slopes that are statistically different from 0 and 1, respectively, at the 95% confidence level. The intercepts for both wind components are generally greater than zero while the slopes for both wind components are generally less than one. This indicates that the NCEP model can produce directional errors for low wind speeds or when one component of the wind is low, such as in an almost purely zonal or meridional wind. At high wind speeds, the model can produce speed errors as it over-predicts the wind speeds.

The mean intercepts listed at the bottom of Tables B-1 through B-4 demonstrate that the NCEP data improved after February 1, 2002 when QuikSCAT was integrated into the model. The mean intercepts decreased from 0.45 to 0.26 for the zonal winds and from 0.22 to 0.06 for the meridional winds. There is little change in the mean regression slopes and mean correlation coefficients. However, Table 2 shows that more regression intercepts became statistically different from zero at the 95% confidence level after February 1, 2002. At the same time, more regression slopes became statistically different from one at the 95% confidence level. Overall, the results improved after incorporating QuikSCAT into the NCEP model. However, there are still differences that suggest that QuikSCAT corrections are appropriate after February 1, 2002.

Figures B-1 and B-2 are histograms of the regression intercepts of zonal (U) wind components before and after February 2002, respectively. In both a clear trend can be

observed. Regression intercepts at high latitudes are generally below zero while those at low latitudes are generally above zero. This indicates a bias that is correlated with latitude. This bias will contribute to the direction discrepancies at low speeds between the two data sets. No spatial trends with the zonal (V) regression intercepts, the regression slopes, or the regression coefficients were detected.

Chelton and Freilich (2005) found differences between the components of the NCEP winds and those of the QuikSCAT winds. They note that the model is calculating actual winds at a grid point while QuikSCAT is measuring the winds relative to the ocean surface. In regions where there are significant ocean currents these two values will diverge. They also explain that the QuikSCAT winds represent the neutral-stability winds at 10 m while the NCEP winds represent the actual winds at 10 m. However, they quantified these discrepancies and concluded that they should not be large (~0.2 m/s). They also compared mean speed differences between the model and QuikSCAT. Over the world's oceans, they found that the two data sets generally agreed with one another. However, they indicate a few areas such as the Chukchi Sea, Bristol Bay, and other parts of the Bering Sea where NCEP speeds were greater than QuikSCAT speeds. Our analysis seems to agree with these findings.

Chelton et al. (2006) also found that the NCEP model underestimated the spatial variability in the wind fields captured by QuikSCAT. This is evident upon comparing the maps in Figure 4. At this time, QuikSCAT captured pockets of high wind that are absent from the NCEP analysis. It is interesting to note that NCEP has under-predicted the wind speeds in this instance.

The mean monthly Ekman transport maps are somewhat consistent with the plot of monthly mean surface Ekman cross-shelf transports in Figure 13. Surface Ekman cross-shelf transport is generally onshore in January through June, although in many areas the transport vectors are oriented parallel to the shelf break. The climatologies suggest that from July through October, surface Ekman cross-shelf transport is directed offshore. It then resumes a direction parallel to the shelf break and somewhat onshore in November. Figure 13 indicates that surface Ekman cross-shelf transport is onshore only

in July and August. This discrepancy may be due to the different time periods that are averaged. The plot in Figure 13 averages data from 1948 to 2007 while the climatologies average data from 1999 to 2007. The plot of annual surface Ekman cross-shelf transports in Figure 10 shows that the annual net surface Ekman cross-shelf transports have been above the 1948 – 2007 mean for the past several years (except 2006). The change was due to an increase in onshore surface Ekman cross-shelf transport (excluding 2006 and 2007) and a decrease in offshore surface Ekman cross-shelf transport. It appears that part of this recent shift in annual net surface Ekman cross-shelf transport is due to an increase in onshore transport and decrease in offshore transport during the months of September and October.

Wilderbuer et al. (2002) concluded that Ekman transport was primarily onshore in Bristol Bay during the1980s and offshore during the 1990s. The QuikSCAT satellite was not operating during these time periods and so we present plots of the mean NCEP winds for the month of June during the 1980s and 1990s in Figures 23 - 24. In Bristol Bay, Ekman transport was generally directed onshore (to the east) during the 1980s. In the 1990s, Ekman transport was generally directed to the south and slightly offshore (to the west). This seems to support the findings of Wilderbuer et al. (2002), who concluded that offshore transport in the Bristol Bay region during the months of April-June advected the larvae of three flatfish species to relatively poor habitat. Our results suggest recruitment numbers for these fish may have been low during the 1999-2007 period.

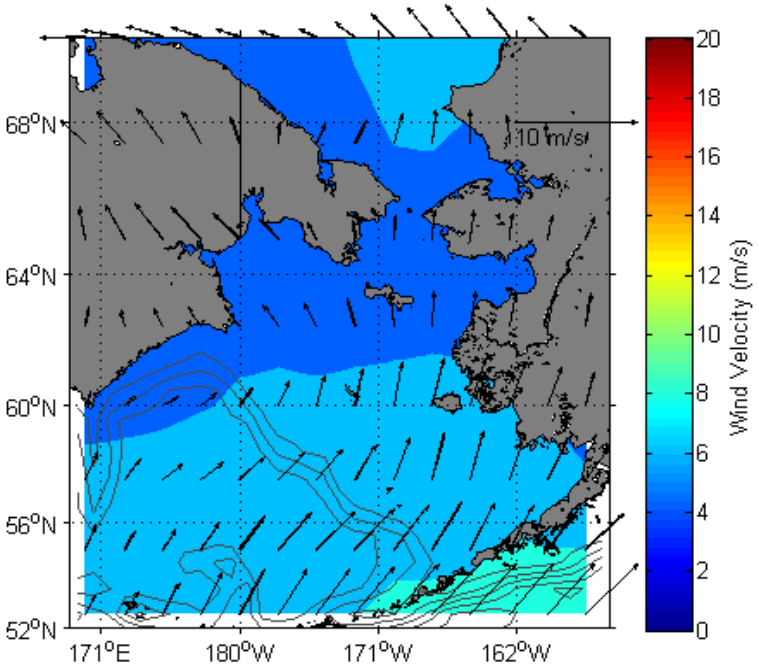

Figure 23. The **mean six-hourly NCEP** winds for June during the 1980s. Ekman transport is primarily onshore in Bristol Bay.

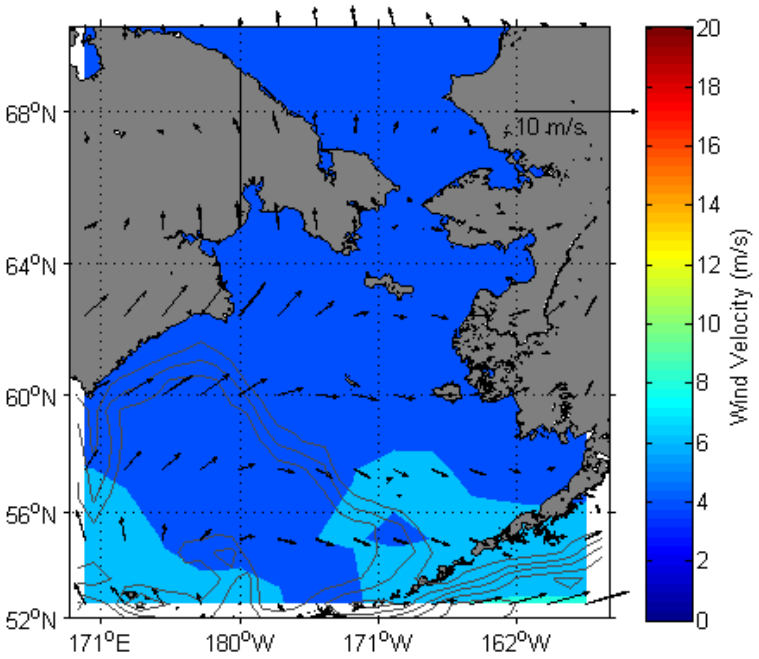

Figure 24. The mean six-hourly NCEP winds for June during the 1990s. Ekman transport is primarily to the south and slightly offshore in Bristol Bay.

Aagaard et al. (2006) calculated that approximately 14,500 km^3/yr of water with mean salinity of 32.6 should flow across the shelf break onto the shelf to maintain the salt flux through Bering Strait. The mean net surface Ekman cross-shelf transport in Figure 10 is approximately 7,500 km^3/yr onto the shelf. However, we assume that this transport is balanced by an equal transport in the opposite direction in the bottom Ekman layer. Using equation 13 with the reference salinity 34.8, we find that Aagaard et al. (2006) predict a net Ekman cross-shelf freshwater transport of 916 km^3/yr. We calculate a net Ekman cross-shelf freshwater transport of 58 km^3/yr, which is 6.3% of their prediction. Our calculations of Ekman cross-shelf freshwater transport range from 20 km^3/yr offshore to 140 km^3/yr onshore (Figure 11). We also find that our calculated mean annual Ekman cross-shelf freshwater transport across the shelf break equals only 2.4% of the freshwater transport through Bering Strait calculated by Aagaard et al. (2006). Thus, surface Ekman cross-shelf transport does not make an important contribution to the freshwater flux into the Arctic Ocean.

This does not resolve the question of how the bulk of the freshwater is transported across the shelf break. Stabeno et al. (1999) estimate that a net transport of 0.5 Sv onto the shelf is required to maintain the flow balance northward between Unimak Pass and Bering Strait. They propose several possible mechanisms for this and cite findings of elevated nutrients on the shelf just east of Unimak Pass, which could be the result of the ANSC interacting with canyon features and depositing deeper, Aleutian Basin water onto the shelf. They also identify a narrow region of the slope located west of the Pribilof Islands. Here the westward flow of the BSC is accelerated along the 100m isobath. The flow turns to the north near Pribilof Canyon and deep water is entrained onto the shelf.

Stabeno et al. (1999) also propose that eddies propagating along the slope could transfer deep waters onto the shelf and shelf waters into the basin. Mizobata et al. (2006) discovered that mesoscale eddies transfer nutrients from the basin to the shelf and facilitate high phytoplankton productivity. They also found that eddies transfer waters with high chlorophyll concentrations off of the shelf and increase the spatial distribution of the spring bloom. Kinney et al. (2008) conducted experiments with a numerical

mixing model and detected several mesoscale eddies propagating along the shelf break within a year. In the experiments, the eddies were formed as the BSC interacted with the deep canyons along the shelf break. Using the same reference salinity, they calculated the freshwater flux across several cross-sections and estimated that the mean freshwater flux across the entire shelf break is approximately 64.0 milliSverdrup (mSV) or 2,019 km^3/yr onto the shelf break. This is much greater than our estimates of surface Ekman cross-shelf transport across the shelf break. These studies indicate that eddies and other turbulent mixing mechanisms along the slope may be more significant than surface Ekman cross-shelf transport.

However, surface Ekman cross-shelf transport could be linked to the physical and ecological variability of the Bering Sea shelf. Figure 10 indicates that the onshore and net annual surface Ekman cross-shelf transports increased between 1972 and 1973. This is supported by the results of the statistics tests in Table 3. This increase in onshore surface Ekman cross-shelf transport coincided with a regime shift in the ecology of the Bering Sea, in which the ecosystem changed from one dominated by large mammals and fish to one dominated by pollock (Stabeno et al., 2006). Based on seasonal surface Ekman cross-shelf transport anomalies (Figures D-1 through D-4) it is difficult to discern if the regime shift in surface Ekman cross-shelf transport was largely the result of any one season. There is a high degree of interannual variability in all of the plots. However, the results of the statistics tests in Table 4 indicate that the surface Ekman cross-shelf transport changed in the months of January and July. The non-parametric t-test is clearly more sensitive than the Wilcoxon Rank Sum Test. If we are cautious, and only accept the significant differences detected by both tests, then a possible change in the along-shelf winds occurred in these two months. An increase in onshore surface Ekman transport in January would most likely mean little to biological productivity as the spring bloom is initiated during the warmer months when stratification takes place (Stabeno et al., 2006). However, an increase in onshore surface Ekman transport in July could influence biological production. Normally, onshore surface Ekman cross-shelf transport advects low-nutrient surface waters onto the shelf. However, Mizobata et al. (2006) found

numerous mesoscale eddies which entrained nutrients into the surface waters near the shelf break. If these eddies upwelled nutrients as surface Ekman cross-shelf transport was directed onshore, primary production could increase over the shelf.

Figure 12 shows the annual nitrate fluxes across the shelf break due to surface Ekman cross-shelf transport. In most years, there is a net flux offshore of nitrate as nitrate concentrations in the surface Ekman layer are lower than concentrations in the bottom layer. This suggests that nitrate renewal from the basin, which drives primary productivity, must come by a mechanism other than surface Ekman cross-shelf transport to maintain the relatively high level of productivity on the shelf.

The CEOF eigenvalues (Figure 14) indicate that most of the variance in the winds is explained within the first three modes. It is unusual that the first mode should represent such a large fraction of the total variance (Wallace and Dickinson, 1972; Horel 1984; Kishtawal et al., 2001). Figure 25 shows a plot of the RMS errors for the zonal and meridional components of the first CEOF mode over time. The RMS errors were calculated as:

$$Error = \frac{\sum_{i=1}^{i=N} \sqrt{\left(Ui_{CEOF}\right)^2 - \left(Ui_{Quik}\right)^2}}{N}; \tag{32}$$

where Ui_{CEOF} is the i^{th} CEOF estimation of the U component of velocity, Ui_{Quik} is the i^{th} QuikSCAT measurement of the U component of velocity, and N is the total number of samples (Emery and Thomson, 2001). For both components, the errors are greater during the winter months indicating that this mode more accurately describes summer wind conditions. The errors are also much larger for the meridional components of the winds. This occurs as the first mode fails to capture any of the north-south variability of the wind field. The errors indicate that meridional components of the winds increase during the winter months and that the winds are relatively zonal in the summer months.

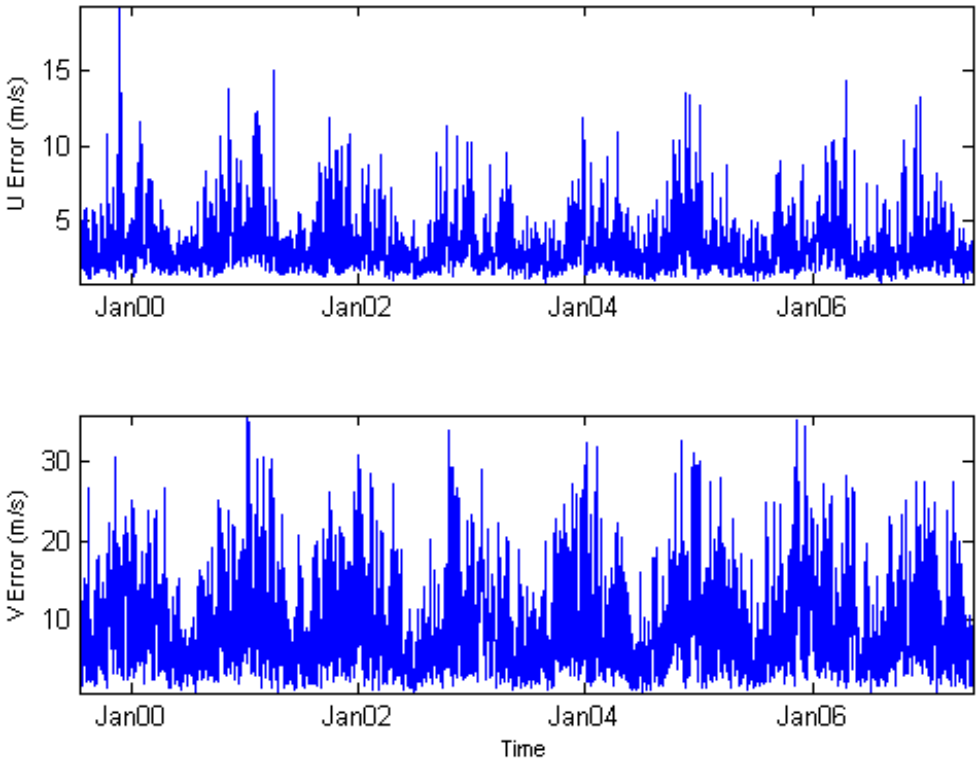

Figure 25. The RMS errors, calculated every 12 hours, of the zonal component (top panel) and meridional component (bottom panel) of the winds for the first CEOF mode. The errors are larger in winter than summer indicating that this is primarily a summer mode.

We can understand how Mode 1 rotates through time by examining the plots of the monthly means and standard deviations of the phase in Figure 26. There is a distinct seasonal cycle to the monthly mean phase while the monthly standard deviation remains somewhat constant at ~$\pi/4$ radians. In the early part of the year the phase is relatively high (between $3\pi/4$ and π radians). This indicates that wind vectors in the first mode are rotated close to 180º in the counterclockwise direction. This would drive surface water onto the shelf. In May, the mean monthly phase decreases to approximately $-\pi/4$ radians. Through August, phase remains between $-\pi/4$ and $-\pi/2$ radians. Rotating the wind vectors

in Mode 1 by this amount would drive surface Ekman transport to the northwest, parallel to the shelf break or slightly offshore. After August, mean monthly phase increase to high positive values again.

This seasonal variability reflects the seasonal variability in surface Ekman cross-shelf transport shown in the monthly climatologies and Figure 10. These show surface Ekman cross-shelf transport onto the shelf in winter months and transport off of the shelf in the summer months.

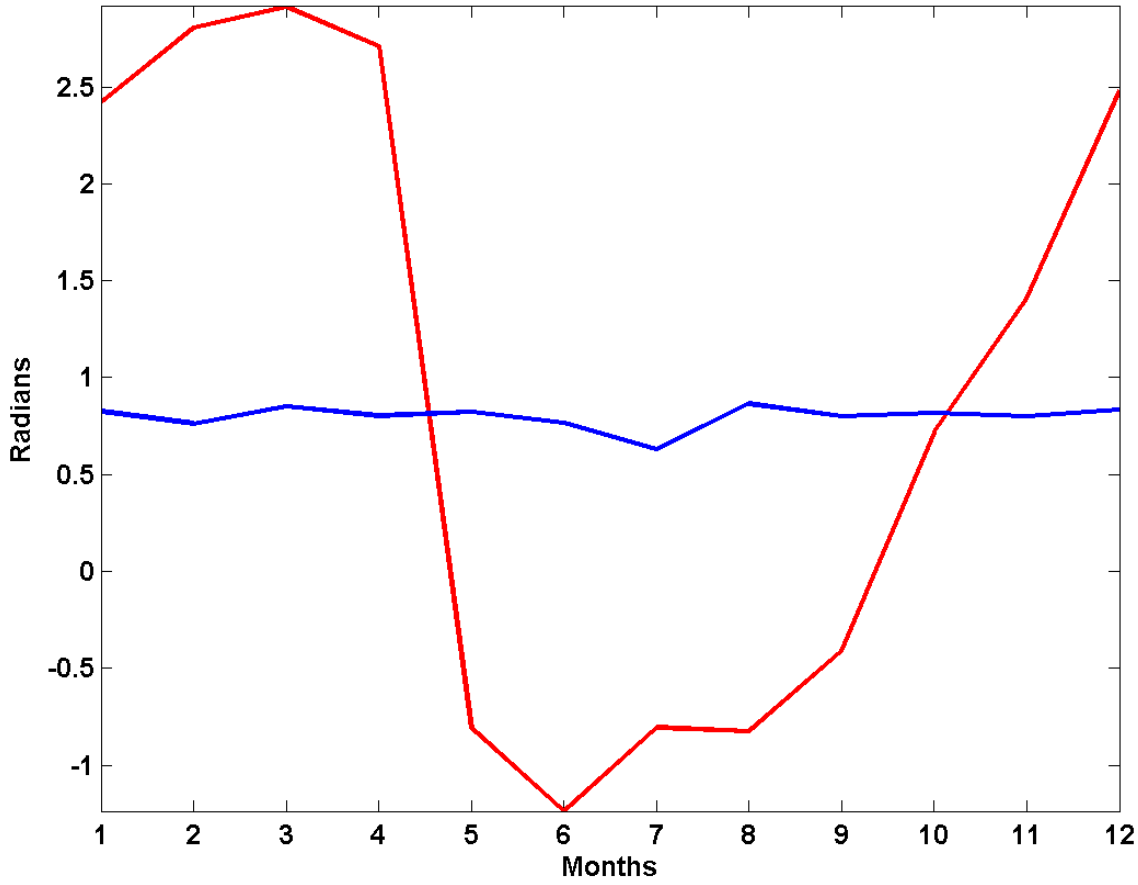

Figure 26. Monthly means (red line) and standard deviations (blue line) of phase for the first CEOF mode.

Mode 2 (Figure 16) describes a cyclonic pattern. The errors for the zonal and meridional components of the Mode 2 patterns are shown in Figure 27. The RMS errors

for the zonal components of the winds are larger than those for the first mode but, the errors for the meridional components of the winds are smaller than those for Mode 1. Thus, this mode captures more of the north-south variability of the winds. The RMS errors are greater in the winter months than in the summer months, which also implies that the second mode describes summer winds better than winter winds.

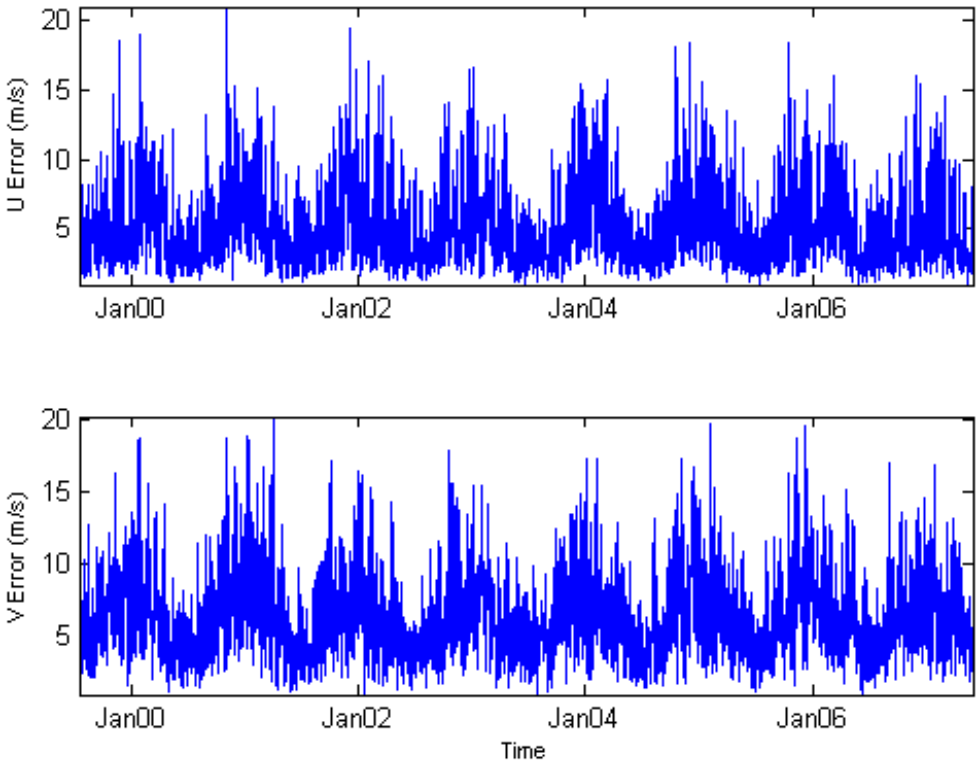

Figure 27. The RMS errors, calculated every 12 hours, of the zonal component (top panel) and meridional component (bottom panel) of the winds for the second CEOF mode.

Plots of the monthly means and standard deviations of phase for Mode 2 are shown in Figure 28. Similar to the analysis of Mode 1, the monthly standard deviations are relatively constant at approximately $\pi/4$ radians. In January and February, the phase exceeds $3\pi/4$ radians, meaning the vectors in Figure 16 are rotated approximately 135º in

a counterclockwise direction. This creates a weak anticyclonic pattern which would facilitate downwelling. In March and April, the phase decreases to approximately $-3\pi/4$ radians, which indicates that the Mode 2 vectors are again rotated 135º but now in a clockwise direction. This also creates a weak anticyclonic pattern which favors downwelling. From May through August the phase becomes small and positive. During these months, the mean monthly QuikSCAT wind vectors are similar to the mode pattern and favor upwelling. After August, the phase decreases creating a divergent wind pattern and then the mode returns to the anticyclonic pattern in the fall. It is difficult to discern if this seasonal variability can be found in the climatologies. For example, the map of the monthly winds for February (Figure C-2) shows a large cyclonic wind field. Within the small domain of the CEOF mode, the winds are generally to the west and southwest. Thus, to accurately represent the winds in February, the winds in the southern area of Mode 2 must be rotated approximately 180º while the winds in the northern area should not be rotated at all. There are similar discrepancies in other months. These most likely arise because the CEOF domain is smaller than the atmospheric features that propagate through this region. CEOF analysis is sensitive to the domain size and to completely describe the spatial variability within a system one must ensure that the domain encompasses the important physics (Horel, 1984). Cyclonic and anticyclonic winds events do occur within this region, however, they cover a relatively large amount of the shelf and basin and often extend into the Chukchi Sea. It is most likely inappropriate to use only Mode 2 to describe the upwelling and downwelling events within the region. One can see from the error plots that this mode does a poor job of representing the zonal winds compared to Mode 1.

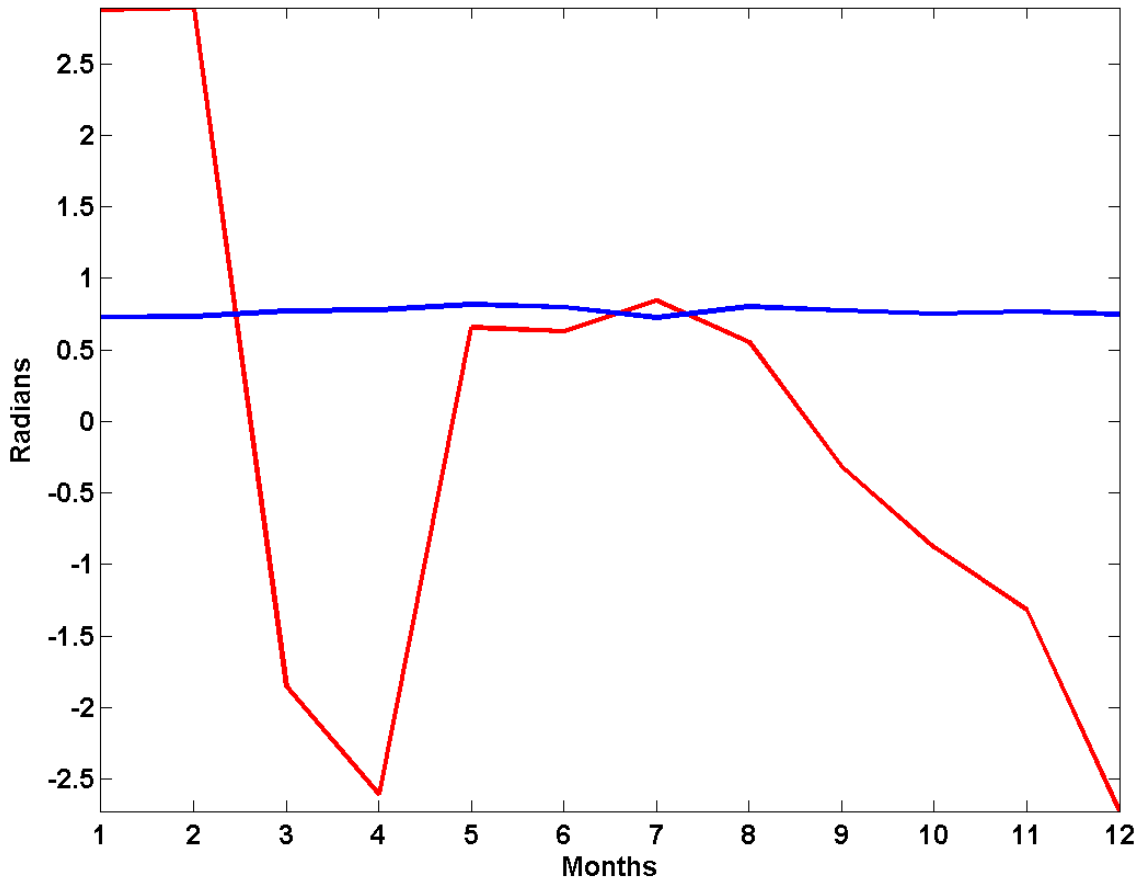

Figure 28. Monthly means (red line) and standard deviations (blue line) of phase for the second CEOF mode.

The RMS errors for the summation of all the modes (weighted by their normalized eigenvalues) are shown in Figure 29. The errors for both components are relatively large. The first mode alone captures the zonal variability of the winds much better than all of the modes combined. The second mode alone captures the meridional variability of the winds better than all of the modes combined. It is evident from this figure that the winds are more variable in the winter months.

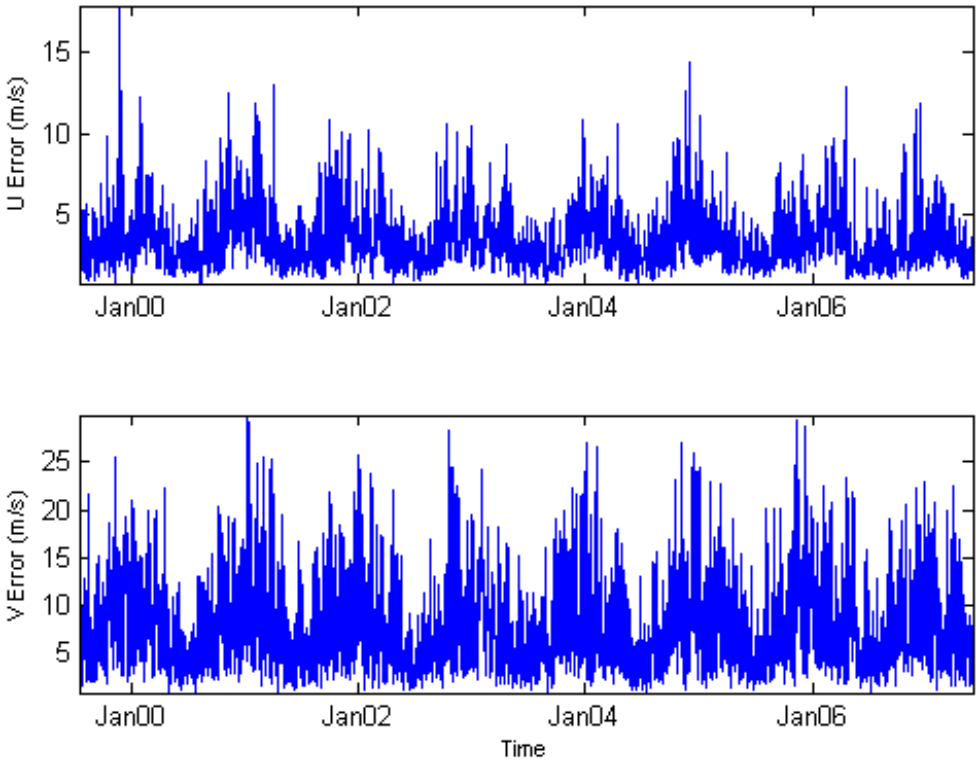

Figure 29. The RMS errors, calculated every 12 hours, of the zonal component (top panel) and meridional component (bottom panel) of the winds for all of the CEOF modes weighted by their normalized eigenvalues.

Horel (1984) found that data reconstructed from CEOFs can vary from the original data. He notes that the correlation coefficients between the reconstructed data and the original data can vary by about 0.2 between time steps. The large errors in Figure 29 may be due to the domain size, which is smaller than the mesoscale wind systems which the CEOFs are trying to describe. To check this we computed the CEOFs for the six-hourly NCEP data from 1948-2007 within the entire study region (Figure 2). The RMS errors for the combined modes are shown in Figure 30 and they are smaller than the errors in Figure 29. This indicates that the small domain size may be contributing to the large RMS errors. Overall, the results suggest that while the QuikSCAT CEOFs capture

most of the variability of the wind field they are missing a significant portion of variability of the wind field in winter.

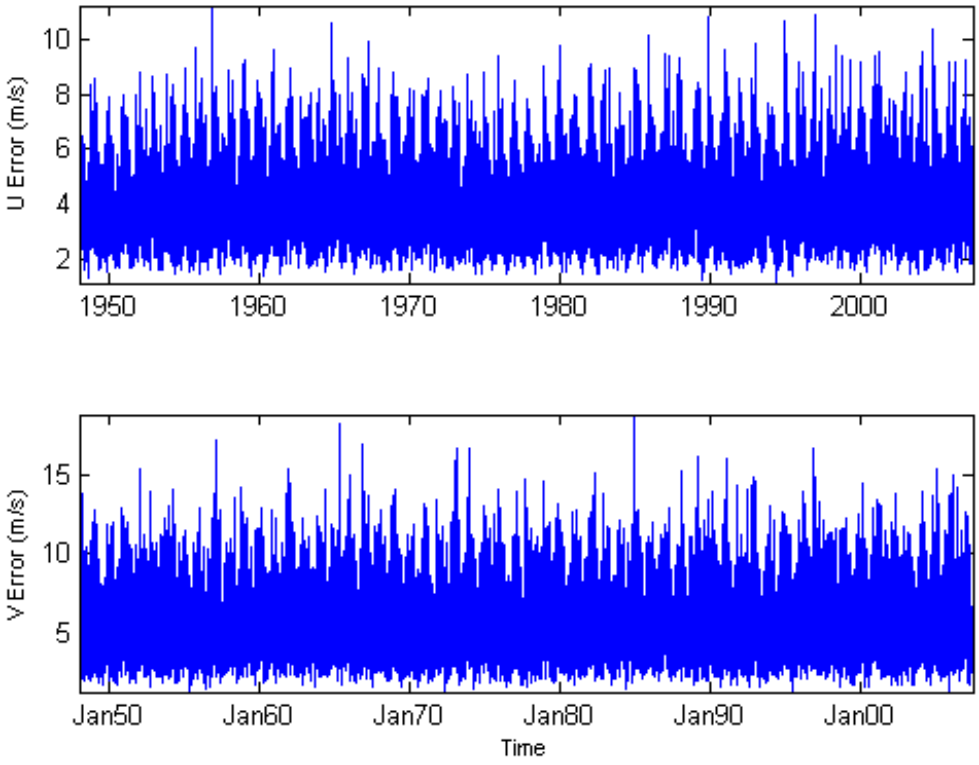

Figure 30. RMS errors, calculated every six hours, of the zonal component (top panel) and meridional component (bottom panel) of the NCEP winds for all of the CEOF modes weighted by their normalized e**igenvalues.** The CEOFs were calculated for the entire study region (Figure 2).

We computed CEOFs of the six-hourly NCEP data from 1948-2007. We used the same method and small domain and the modes are shown in Appendix E, Figures E-1 through E-3. The modes are very similar to those computed for the QuikSCAT data. For example, Mode 1 is primarily a zonal wind pattern with winds blowing from west to east. Mode 2 is a circular pattern although it is anticyclonic and opposite to the Mode 2 pattern

for the QuikSCAT data. This discrepancy is not significant. The principal components matrix determines how each mode rotates through time and a plot of the phase of Mode 2 (not shown) indicates that the NCEP phase is opposite to that of QuikSCAT Mode 2. In essence, they are describing the same wind field as the modes rotate in opposite directions. Mode 3 is the same as the Mode 3 pattern calculated for the satellite data. From Figure E-4 it is evident that the eigenvalues are very similar to those calculated for the QuikSCAT data. Mode 1 accounts for 60.4% of the variance, Mode 2 accounts for 16.4 % of the variance, and Mode 3 accounts for 11.8 % of the variance. The first five modes are significant.

We present plots of the monthly CEOF modes calculated for the NCEP data from 1948 to 2007 in Figures E-5 to E-7. To calculate these CEOFs, mean wind vectors for each month during the time period were produced. The smaller monthly data set enabled us to calculate CEOFs for the entire study region (Figure 2). It is interesting to note that they are similar to the patterns generated previously. The first mode pattern shows primarily zonal winds that blow increasingly to the north as latitude increases. The second pattern is a large anticyclonic pattern centered near St. Lawrence Island. Mode 3 is a convergence and divergence pattern similar to the Mode 3 pattern for the QuikSCAT data except that the pattern is spread over a greater region in this case. The eigenvalues are not presented as they are similar to those for the six-hourly data. These results give us confidence that a high fraction of the variability of the winds can be described by these first three CEOFs.

To further examine the low frequency variability of the winds we present the CEOFs for yearly NCEP data calculated over the entire study region in Figures E-8 through E-10. Mean vectors for each year from 1948 to 2006 were produced and the CEOFs were constructed from this yearly data. The patterns are similar to those for the monthly data except that Mode 2 is a cyclonic pattern, similar to the Mode 2 pattern for the QuikSCAT data. The eigenvalues are not shown as they are similar to the values computed previously.

We compare the different features of the time series of mode amplitudes with important climate indices, and these cross-correlation results are presented in Table E-1. It is important to note that the monthly NCEP CEOF time series were compared with monthly indices of the PDO, PNA, and AO while annual NCEP CEOF time series were compared with the annual indices of the ALPI, NP, and WP. One can see that there are weak correlations in some instances. There are several correlation coefficients greater than 0.3 and only two correlation coefficients greater than 0.4. The imaginary component of the time series for the third annual mode is weakly correlated with the ALPI ($r = 0.42$) and the real component of the time serious for the fourth annual mode is weakly correlated with the NP index ($r = 0.40$). These are not strong correlations although both are significant at the 95% confidence level and have relatively small lags.

These results are realistic. We would expect the time components of the CEOFs to be somewhat correlated with the climate indices as the indices are computed using sea surface temperatures and sea level pressures, which both drive winds. However, it is clear that the variability of the Bering and Chukchi Seas is not completely captured by these indices. The PDO indices utilize sea surface temperatures throughout the Pacific Ocean while the AO indices utilize sea level pressure over the Arctic. The WP indices are compiled from anomalies in the differences between atmospheric 500 mb pressure heights at two points in the west Pacific and the PNA indices utilize several data from the Pacific and North America. The atmospheric processes in these regions affect the sub-Arctic although the connections are complex. Clearly these indices do not completely capture the variability of the Bering and Chukchi Seas.

The weak correlations between the time series components and the ALPI and NP indices are also most likely realistic. The Bering Sea is strongly influenced by the Aleutian Low (Stabeno et al., 2006). The NP indices are computed from the differences between atmospheric pressure heights at two locations in the southern Bering Sea (Brodeur et al., 1999). Niebauer et al. (1999) cross-correlated time series of the wind measurements at the Pribilof Islands with climate indices. They found a strong correlation between the winds and the WP index ($r = 0.55$). They also found a weak

negative correlation between the winds and the NP index (r = -0.33). Although we did not see these relationships our results do not necessarily contradict theirs. Niebauer et al. (1999) were focusing on the winds at the Pribilof Islands, in the southern Bering Sea, which are most likely strongly influenced by the Aleutian Low and the North Pacific. In contrast, we are examining the variability within both the Bering and Chukchi Seas. This region is larger, more complex, and connected to both the Arctic and the Pacific.

The calculations of vertical displacements of the pycnocline due to surface Ekman convergence and divergence within the small box over the Bering Sea shelf (Figure 7) indicate that there are seasonal and interannual variabilities in Ekman pumping and suction. Table 5 shows the mean Ekman pumping and suction rates for this area based upon the six-hourly NCEP data from 1948 – 2007. There is a seasonal cycle to the vertical motions. There is weak Ekman pumping in January and February. From April – August there is weak Ekman suction, which ranges from 0 – 4 cm/day and is most likely not large enough to influence biological production in the euphotic zone. Swift and Aagaard (1976) calculated Ekman suction rates near Samalga Pass and found they ranged from 1.7 – 8.6 cm/day. Our rates seem to agree with these values. September through December are characterized by slightly stronger Ekman suction that ranges between 5 and 12 cm/day.

The plots in Figures F-1 through F-12 suggest that there is a high degree of interannual and seasonal variability in the rates of Ekman suction and pumping. In January 1952 there was a maximum Ekman suction rate of ~35 cm/day and in January 2007 there was a maximum Ekman pumping rate of ~33 cm/day. The range for the month of February is approximately the same. The rates are lower for the spring and summer months. In March, vertical velocities ranged from ~33 cm/day Ekman suction to 23 cm/day Ekman pumping. In April, the velocities ranged between ~27 cm/day Ekman suction and ~15 cm/day Ekman pumping. Stratification and biological production can be initiated in May (Stabeno et al., 2006) and the values for this month ranged between ~20 cm/day Ekman suction and ~10 cm/day Ekman pumping. This could cause a high degree of interannual variability in primary production in the surface layers. If the pycnocline is

raised 20 cm/day and subsequent storms erode the density gradient, nutrients could be injected into the surface layers to facilitate primary production. In contrast, if the pycnocline is depressed for several days subsequent storms may not have enough energy to penetrate to depth and entrain deeper waters. It is important to note that Figure F-5 shows several years for which the month of May was characterized by entirely Ekman suction or pumping.

In the summer the ranges of vertical velocities are smaller. In June, the maximum Ekman suction and pumping rates are ~8 cm/day. In July, the velocities range between ~11 cm/day Ekman suction and ~8 cm/day Ekman pumping. It is important to note that there are several years in the NCEP record for which these months are dominated by either Ekman suction or pumping. This may be linked to interannual variability in phytoplankton production over the shelf. The ranges of vertical velocities increase throughout the late summer, fall, and winter. These values exceed the vertical velocities due to wind-stress-curl calculated by Swift and Aagaard (1976). However, they calculated that the relatively high upwelling rates of ~6 m/day were necessary to maintain the concentrations of dissolved oxygen in the upper mixed layer near Samalga Pass. Our vertical velocities are much smaller than these rates indicating that Ekman suction and pumping on the shelf is weak compared to upwelling and downwelling rates. However, wind-stress-curl could still be important to the evolution of the mixed layer. Figures 22-25 show that the pycnocline could have been displaced several meters over the summer months in different years in the Bering Sea.

Muller et al. (1984) developed a vertical mixing model in which the depth of the pycnocline oscillated throughout time. They determined that the extent to which deeper waters were entrained into the upper mixing layer depended somewhat on whether oscillatory motions of the pycnocline and wind mixing events were in phase or not. If the pycnocline was lowered, subsequent mixing events did not have sufficient energy to penetrate to depth and erode the pycnocline. If the pycnocline was raised, wind mixing events were more effective at eroding the pycnocline and entraining deeper waters. During the spring and summer months, this could alter biological production by injecting

nutrients into the surface mixed layer. If there is Ekman pumping, the pycnocline is depressed and subsequent wind events may be less effective in entraining nutrients. This could inhibit biological production.

In the PWP model, wind mixing occurs as the winds force the surface layer to move and shear develops across the pycnocline. This is a simplified form of mixing and when we refer to wind mixing in this section we are only referring to the mixing due to shear and not to turbulent wind mixing. The results of the model experiments suggest that wind-stress-curl interacts with wind mixing in the Bering Sea as the mixed layer evolves through time. The model outputs for the model runs which used variables from April – August 2001 near St. Paul Island are shown in Figures G-2 through G-8. Figure 19 indicates that there was moderate Ekman suction at this time. The output for the run with QuikSCAT winds and no wind-stress-curl is shown in Figure G-2. The model output for the model run which used QuikSCAT winds in addition to wind-stress-curl is shown in Figure G-3. In both model runs, stratification sets in and increases as the spring and summer progress. However, stratification is initiated late in May for the model without curl and early in June for the model with curl. Ekman suction in early May (Figure 19) mostly likely raises the pycnocline to a depth where shear develops from the winds forcing the surface waters. This may affect the timing of the spring bloom as phytoplankton cannot bloom until they have a stable water column (Stewart, 2005).

The model without curl produces a mixed layer depth that is relatively constant at ~18 m. The model with curl produces a mixed layer with a variable depth throughout the experiment and an MLD of ~15 m at the end of the run. The difference in the final MLDs may seem a small discrepancy but it could be significant when scaled for a large region of the Bering Sea. The model with curl produces a mixing event in mid-August. These results indicate that the Ekman suction increases the amount of vertical mixing in the spring and summer.

Figure G-3 shows the model output for the run using NCEP winds near St. Paul Island from April – August 2001. This model output is similar to the model output using QuikSCAT winds. The figure shows the final MLD as approximately 24 m while it is

shallower in both model runs which used QuikSCAT winds. This implies that there is more wind mixing in the model with NCEP winds. The difference may be due to the different sampling frequencies of the two data sets. The inertial period for 54 ºN is ~14.8 hours and the PWP model is primarily forced by wind stress near the inertial frequency (Plueddemann and Farrar, 2006). The sampling interval for QuikSCAT is ~12 hours and it is possible that these data are missing the wind energy near the inertial frequency band that NCEP data is capturing (sampling interval ~6 hours). To check this, we ran the model with no wind stress to quantify the importance of wind mixing. The output is presented in Figure G-5 and shows a thin upper mixed layer form during the summer. The surface waters are of relatively low density and the final MLD is ~4 m. The surface waters warm to ~20 ºC. This result is different from both of the models with winds, indicating that wind energy is critical to the evolution of the mixed layer in this region.

To further examine the importance of sampling frequencies, we ran the PWP model using NCEP winds collected at 06:00 and 18:00 hrs each day. These are roughly the same times as the measurements of the QuikSCAT winds. The output for this model run is shown in Figure G-6. This model run produced a similar output to the output from the QuikSCAT model with no curl indicating that the QuikSCAT sampling frequency could be too small. The MLD in the under-sampled NCEP model is ~21 m at the end of the run.

We can calculate the work done by the winds to mix the water column by

$$\phi = \int \delta C_D \rho_a U_{10}^3 dt \tag{33}$$

where ϕ is the work per unit done by the winds (W/m^2), C_D is the drag coefficient from equation 9, ρ_a is the density of air (1.29 kg/m3), and U_{10}^3 is the wind speed cubed. δ is a mixing coefficient equal to 0.023 (Simpson and Bowers, 1981). Using equation 33, we calculate that the six-hourly NCEP winds add approximately 4.57 x 10^5 W/m^2 while the QuikSCAT winds add only 2.86 x 10^5 W/m^2 to the water column during the model run. The NCEP winds add ~1.6 times as much energy to promote mixing as the QuikSCAT winds. We have shown that NCEP overestimates the wind speeds in the Bering Sea, however, we calculate that the 12-hourly (under-sampled) NCEP winds add ~4.91 x 10^5

W/m^2 to the water column. The under-sampled NCEP winds add more energy to promote mixing than the six-hourly NCEP winds but produce a shallower mixed layer. This indicates that the under-sampled NCEP winds are missing power at higher frequencies, which deepen the mixed layer and that the sampling interval for the QuikSCAT winds may be too large for this high latitude. It also indicates that the NCEP wind speeds are slightly larger than the QuikSCAT wind speeds.

These results highlight a small discrepancy between the NCEP and QuikSCAT data sets. The difference in MLDs could be significant when scaled for a large region of the Bering Sea. The deeper mixed layer implies that there are more nutrients available for phytoplankton growth in the euphotic zone. Therefore, the NCEP winds could lead one to predict more biological production than the QuikSCAT winds.

The water column profiles for the model with NWS wind measurements (Figure G-7) look similar to the model run with QuikSCAT winds and no curl. Stratification is initiated at approximately the same time in late May. At the end of the plots, the PASN MLD is at ~18 m. However, in June and July the NWS MLD is deeper than 20 m while the QuikSCAT MLD is ~ 17 m. At the end of the model experiments the NWS pycnocline spans a greater depth range (~10 m) than the QuikSCAT pycnocline (~4 m). This suggests a small discrepancy between the QuikSCAT winds and the winds measured at St. Paul Island. The sampling interval for the NWS wind measurements is approximately one hour, far less than the inertial period. We next ran the model with the PASN winds low-pass filtered at 20 hours and the results are shown in Figure G-8. The final MLD for this model run is ~11 m and the winds add ~2.96×10^5 W/m^2 to the water column. This is equal to the power that the QuikSCAT winds supplied to promote vertical mixing. The smoothed winds are missing important high frequency variability and have considerably less power than the other wind data sets. In addition, the smoothed winds have no power at the high frequencies which drive vertical mixing in this model. The results indicate that the large sampling interval for the QuikSCAT data may not be appropriate for this latitude.

Plots G-9 through G-11 show the results for the model runs at the middle station over the shelf for April – August 2005. Figure 21 indicates that Ekman suction was relatively strong at this time and location. The model output for the run with QuikSCAT wind and no curl (Figure G-9) looks different from the model output for the run with QuikSCAT winds and curl (Figure G-10). In both models, stratification is initiated in early May and it increases as progressively lighter water forms near the surface. There are relatively weak mixing events in July and August. However, at the end of the experiments, the MLD formed with no curl is ~18 m and the density of the upper mixed layer is ~1,024.8 kg/m^3. The MLD formed with curl is ~17 m and the density of the upper mixed layer is ~1,024.5 kg/m^3. Figure 21 shows a relatively large Ekman suction event in early April and vertical mixing is produced in both models at this time. Although the pycnocline may have been raised due to wind-stress-curl, the wind energy may have been sufficient to penetrate to the depth at which the pycnocline would have remained in the absence of Ekman suction. Ekman suction may be more critical to mixing if it occurs later in the spring, when the water column is stratified, and if the winds are relatively weak.

The water column evolution predicted with NCEP winds (Figure G-11) is different than that predicted with QuikSCAT winds and no curl. Stratification sets in at approximately the same time in both model runs. Stratification increases in the model with NCEP winds and near the end of the model run the MLD is much deeper than that of the model with QuikSCAT winds. The NCEP MLD is ~27 m and the upper mixed layer has relatively dense water compared to the upper mixed layer formed by QuikSCAT winds. This is similar to the previous model runs with data collected near St. Paul Island and may imply more nutrients in the upper mixed layer and increased biological production. The discrepancy is most likely due to the lower QuikSCAT sampling frequency and higher NCEP wind speeds.

Plots G-12 through G-14 show the results for the model runs at the southeast location over the shelf for April – August 2006. Figure 22 indicates that Ekman pumping was relatively strong at this time and location. Both models show mixing in late May and

early June. The MLD formed with curl is more variable throughout the experiment than the MLD formed without curl. The output for the model with curl shows mixing in late July, which roughly corresponds to a brief period of weak Ekman suction (Figure 22). It is interesting to note that mixing seems to have been enhanced in the presence of Ekman pumping. This could be due to a nonlinear effect of vertical mixing such as cabelling. Despite these differences, the two model outputs are very similar. In this instance, it does not appear that Ekman pumping has a significant effect on the evolution of the mixed layer.

The model output with NCEP winds (Figure G-14) is different from the model output with QuikSCAT winds and no curl. In the NCEP model, stratification increases until late July when there is a wind mixing event which mixes deeper water into the upper mixed layer. This wind mixing event can be seen in the model with QuikSCAT winds wind-stress-curl. However, the NCEP MLD is ~25 m, much deeper than the QuikSCAT MLD. At the end of the model run, the NCEP upper mixed layer has a density of ~1,025.3kg/m^3. This implies relatively large amounts of wind mixing throughout the NCEP model run.

The models using data from the middle and southeast shelf locations were forced with relatively strong values of Ekman suction and pumping. It is possible that the winds were large enough in these cases to generate shear between the mixed layer and lower layers and mix the pycnocline regardless of its depth. This would eliminate any differences between the model outputs with wind-stress-curl and those without curl. To check this we looked for times and locations over the shelf in which wind-stress-curl was more moderate. Figure 23 shows that there was a moderate amount of Ekman suction in the northwest Bering Sea shelf (62.1250 ºN, 175.8750 ºW) in April – August 2005. The PWP model was forced with six-hourly NCEP winds and surface flux data and from this location and time. The results of the model run with NCEP winds and no curl are shown in Figure G-15 and those of the model run with NCEP winds and curl are shown in Figure G-16. The final MLD for the model without curl is ~20 m while the final MLD for the model with curl is ~16 m. Figure 20 indicates that there was strong Ekman

suction near the end of the model experiment. A plot (not shown) of the wind stress during July and August indicates that the winds were relatively light. Although the winds were weak, Ekman suction raised the pycnocline to a depth at which wind-generated momentum was significant and the mixed layer entrained deeper waters.

We can construct a rough criterion to determine if the wind speed, Ekman suction, and mixed layer depth are sufficient to entrain deeper waters into the mixed layer using R_b in equation 27. The velocity at the bottom of the surface mixed layer after the wind stress is applied is

$$V = \frac{\tau \Delta t}{h \rho_s}; \tag{34}$$

where V is the velocity, τ is the wind stress, Δt is the time step (3,600 seconds in this case), h is the depth of the mixed layer, and ρ_s is the density of the upper mixed layer (Price et al., 1986). If Ekman suction is present, then the depth of the mixed layer becomes

$$h_{new} = h - \Delta\eta \tag{35}$$

where h_{new} is the new upper mixed layer depth, h is the upper mixed layer depth without Ekman suction, and $\Delta\eta$ is the displacement in the pycnocline depth due to Ekman suction (equation 21). The model computes the bottom of the mixed layer as the depth at which the change in density is 0.0001 kg/m^3. If we assume that ρ_0 is 1,205 kg/m^3, that ρ_s is 1,204 kg/m^3, that g is 9.8 m/s^2, and that the velocity in the stratified waters is close to 0 m/s, we can rearrange equation 27 so that

$$\frac{(h - \Delta\eta)^3}{\tau^2} \geq 8.4 \times 10^6 . \tag{36}$$

If the term on the right hand side falls below 8.4 x 10^6, the density profile becomes statically unstable and mixing occurs. For a given h, one can get an idea of the relative importance of wind stress and Ekman suction to mixing. Note that if $\Delta\eta$ is large enough and negative (Ekman pumping is significant) and τ remains small, mixing will not occur. This criterion is somewhat sensitive to the choice of surface density as surface densities below 1,024 kg/m^3 will produce a number less than 8.4 x 10^6. However, these low

densities were not generally observed throughout these experiments. In addition, this criterion does account for the strength of stratification such as the Brunt-Väisälä frequency. Thus we can not determine how much mixing will occur, such as if the pycnocline will be completely eroded or not. We can only conclude that shear will facilitate some amount of mixing. This criterion only uses R_b and does not take R_θ into account.

To ameliorate the poor temporal resolution of the QuikSCAT data set we propose combining the NWS data and the QuikSCAT data to produce a data set with high temporal and spatial resolution. This is done by determining the complex correlation between the two data sets. The complex correlation coefficient and phase between the two data sets are shown in Figures 31 and 32, respectively. The figures indicate that the two data sets are highly correlated and in phase with one another. A hybrid data set can be constructed at each QuikSCAT grid point as the PASN winds are scaled by the complex amplitude and rotated by the phase. This would produce a data set that would have the high temporal resolution necessary to resolve inertial motions at this latitude and the high spatial resolution required to calculate wind-stress-curl.

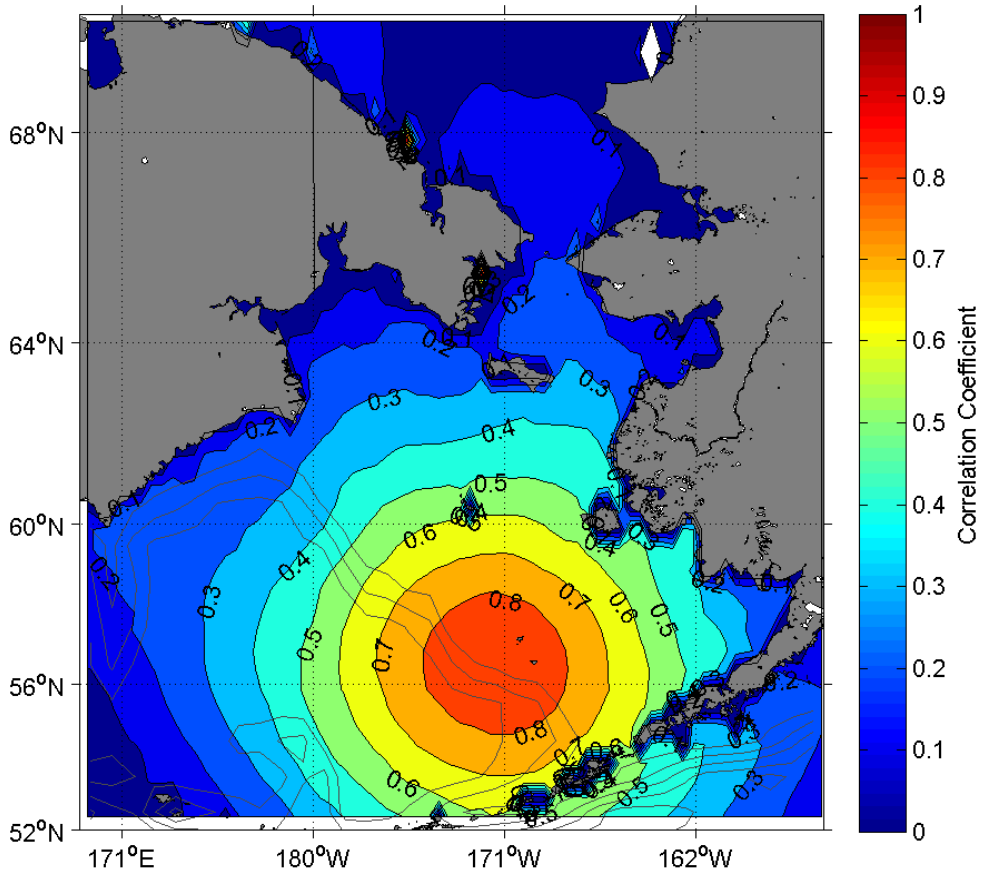

Figure 31. The complex cross-correlation coefficient between a time series of wind data collected from St. Paul Island (station PASN) and time series of QuikSCAT data at all the other grid points within the study region.

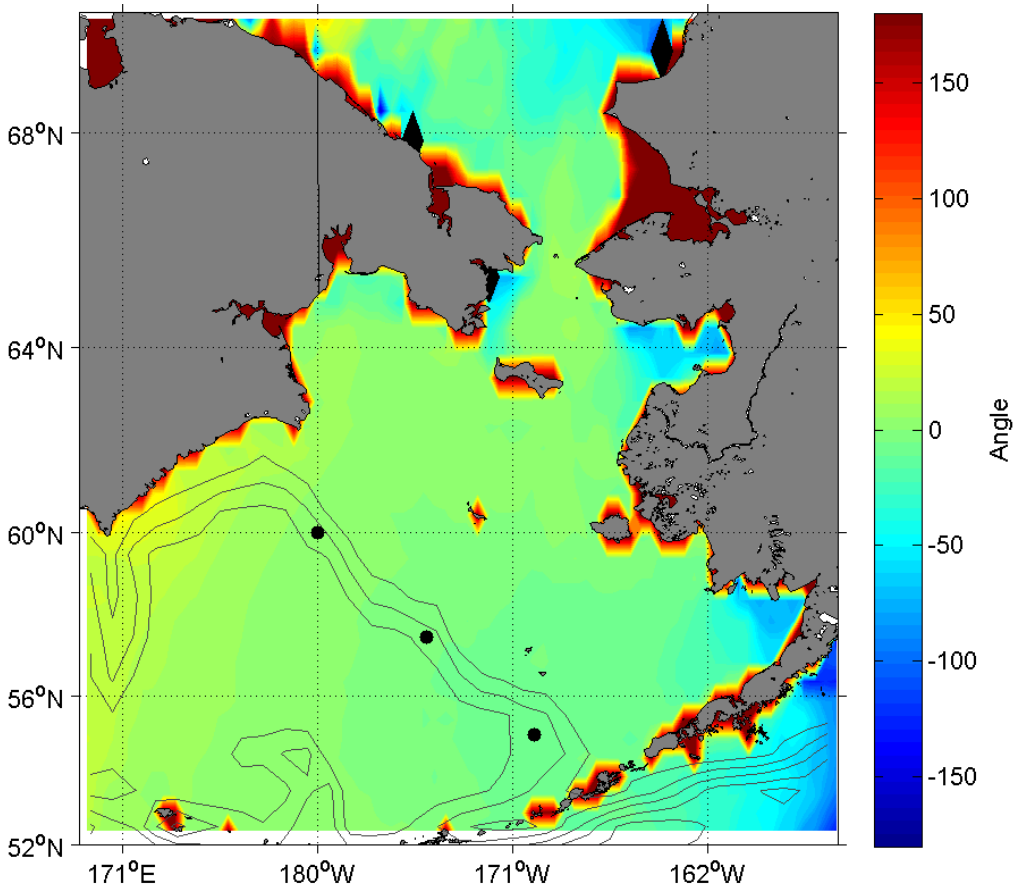

Figure 32. The complex phase angle between a time series of wind data collected from St. Paul Island (station PASN) and time series of QuikSCAT data at all the other grid points within the study region.

Our application of the PWP model to the Bering shelf has limitations. First, the model assumes that there are no spatial variations (Price et al., 1986). Spatial variation is present due to currents and topographic features (Coachman, 1985). Moreover, the model does not include freshwater inputs such as ice melt and river runoff, which are important in facilitating stratification in this region (Stabeno et al., 1999; Stabeno et al., 2006). Second, the model does not include the influence of spatially varying tides and tidal currents, which are critical components in the turbulent kinetic energy budget of the Bering Sea (Coachman, 1985). However, the results of the models, which used data near St. Paul Island imply that wind-stress-curl could be important to vertical mixing when the

winds are relatively weak. In addition, the model highlights important differences between the QuikSCAT and NCEP data sets.

Chapter 5 Conclusions

The QuikSCAT and NCEP data sets are well correlated and in phase with one another. The magnitude of the NCEP wind components tend to be larger than those of the QuikSCAT winds. This creates directional errors between the two data sets at low speeds and speed errors between the two data sets at high speeds. The linear regression between NCEP wind components and QuikSCAT wind components reveal that the regression intercepts for the zonal components of velocity are generally negative at high latitudes and positive at low latitudes.

The monthly climatologies show that there are months and regions in which surface Ekman transport is either onshore or offshore, indicating that coastal upwelling and downwelling may be significant. They also show that there are times and portions of the shelf in which there is wind-stress-divergence and wind-stress-curl. Both of these features could lead to displacements in the pycnocline and possibly affect vertical mixing. These features were apparent in spring and summer and could affect biological production in surface mixed layer and euphotic zone.

Our calculations of surface Ekman cross-shelf transport, and its associated freshwater fluxes, indicate that this transport contributes relatively little to the northward freshwater flow through Bering Strait. Comparisons with other studies indicate that other mechanisms, including mesoscale eddies and transport across the Gulf of Anadyr, are probably more important to the salt flux through Bering Strait. Variability in surface Ekman cross-shelf transport might be linked with variability in the Bering Sea. Annual rates of onshore surface Ekman cross-shelf transport increase at approximately the same time as the region underwent a regime shift between 1972 and 1973. These rates are only weakly correlated with the PDO and PNA indices.

Much of the variability of the wind fields is captured within the first three hourly, monthly, and annual CEOF modes of 12-hourly QuikSCAT data and six-hourly NCEP data. These modes are all significant. The mode amplitudes have cycles which

last several years but are not significant at the 95% confidence level. Only weak correlations were found between the mode amplitudes and climate indices.

Our calculations reveal that Ekman pumping and suction can be significant during the spring and summer when the winds are relatively weak and curl is relatively moderate or strong. The PWP model results indicate that Ekman suction might enhance vertical entrainment of denser, nutrient-rich water into the surface mixed layer while Ekman pumping might inhibit entrainment. In summer, this could have implications for phytoplankton, which require a stratified water column and nutrient replenishment from depth to grow. We also find that NCEP winds predict greater mixing that the QuikSCAT winds because the high temporal resolution of the NCEP data set captures the variability near the inertial frequency which deepens the mixed layer in this model. This indicates that the low temporal resolution of the QuikSCAT data is insufficient to resolve inertial motions at these high latitudes. To remedy this, we propose interpolating the NWS data collected at St. Paul Island (station PASN) to the QuikSCAT grid using the complex amplitudes and phases from the complex cross-correlations between the two data sets.

References

Aagaard, K., L.K. Coachman, and E. Carmack, 1981: On the halocline of the Arctic Ocean, *Deep Sea Research*, 90, 4833–4846.

Aagaard, K., A.T. Roach, and J.D. Schumacher, 1985: On the wind-driven variability of the flow through Bering Strait, *Journal of Geophysical Research*, 90, 7213-7221.

Aagaard, K. and E.C. Carmack, 1989: The role of sea ice and other freshwater in the Arctic circulation, *Journal of Geophysical Research*, 94, 14485-14498.

Aagaard, K., T.J. Weingartner, S.L. Danielson, R.A. Woodgate, G.C. Johnson, and T.E. Whitledge, 2006: Some controls on flow and salinity in Bering Strait, *Geophysical Research Letters*, 33, L19602, doi:10.1029/2006GL026612.

Bond, N.A., J.E. Overland, and P. Turet, 1994: Spatial and temporal characteristics of the wind forcing of the Bering Sea, *Journal of Climate*, 7, 1119-1130.

Brodeur, R.D., C.E. Mills, and J.E. Overland, 1999: Evidence for a substantial increase in gelatinous zooplankton in the Bering Sea, with possible links to climate change. *Fisheries Oceanogr*aphy, 8, 296-306.

Chelton, D.B. and M.H. Freilich, 2005: Scatterometer-based assessment of 10-m wind analyses from the operational ECMWF and NCEP numerical weather prediction models, *Monthly Weather Review*, 133, 409-429.

Chelton, D.B., M.H. Freilich, J.M. Seinkiewcz, and J.M. Von Ahn, 2006: On the use of QuikSCAT Scatterometer Measurements of Surface Winds for Marine Weather Prediction, *Monthly Weather Review*, 134, 2055-2070.

Coachman, L. K., 1985: Circulation, water masses, and fluxes on the southeastern Bering Sea shelf, *Continental Shelf Research*, 5, 23-108.

Coachman, L.K., 1993: On the flow field in the Chirikov Basin, *Continental Shelf Research*, 13, 481-508.

Coachman, L. K. and K. Aagaard, 1988: Transports through Bering Strait: Annual and interannual variability, *Journal of Geophysical Research*, 93: 15,535–15,539

Coachman, L. K., K. Aagaard, and R.B. Tripp, 1975: *Bering Strait: The Regional Physical Oceanography*, 172pp., University of Washington Press, Seattle, Washington.

Conradsen, K., A.A. Nielsen, J. Schou, and H. Skriver, 2003: A test statistic in the complex Wishart distribution and its application to change detection in polarimetric SAR data, *IEEE Transactions on Geoscience and Remote Sensing*, 41: 4-19.

Danielson, S.L., K. Aagaard, T. Weingartner, S. Martin, P. Winsor, G. Gawarkiewicz, D. Quadfasel, and J. Meincke, 2006: The St. Lawrence polynya and the Bering shelf circulation: New observations and a model comparison, *Journal of Geophysical Research*, 111, C09023, doi:10.1029/2005JC003268.

Emery, W.J. and R.E. Thomson, 2001: *Data Analysis Methods in Physical Oceanography*, 638pp., Elsevier Press, Amsterdam.

Hoffman, R.N. and S.M. Leidner, 2005: An introduction to the Near-Real-Time QuikSCAT Data, *Weather and Forecasting*, 20, 476-493.

Horel, J.D., 1984: Complex principal component analysis: theory and examples, *Journal of Climate and Applied Meteorology*, 23: 1660 – 1673.

Kalnay, E., M. Kanimitsu, R. Kistler, W. Collins, D. Deaven, L. Gandin, M. Iredell, S. Saha, G. White, J. Woolen, Y. Zhu, A. Leetmaa, and B. Reynolds, 1996: The NCEP/NCAR 40-year reanalysis project, *Bulletin of the American Meteorological Society*, 77, 437-472.

Kinney, J.C., W. Maslowski, and S. Okkonen, 2008: On the processes controlling shelf-basin exchange and outer shelf dynamics in the Bering Sea, *Deep Sea Research II*, in press.

Kishtawal, C.M., S. Basu, and S. Karthikeyan, 2001: Retrieval of vertical wind profiles during monsoon from satellite observed winds over the Indian Ocean using complex EOF analysis, *Indian Academy of Sciences (Earth Planet Science)*, 110: 77 – 86.

Kistler, R., E. Kalnay, W. Collins, S. Saha, G. White, J. Woollen, M. Chelliah, W. Ebisuzaki, M. Kanamitsu, V. Kousky, H. van den Dool, R. Jenne, and M. Fiorino, 2001: The NCEP-NCAR reanalysis: Monthly means and CD-ROM documentation, http://doc.nprb.org.

Kundu, P.K., 1975: Ekman veering observed near the ocean bottom, *Journal of Physical Oceanography*, 6, 238-242.

Large, W.G. and S. Pond, 1981: Open ocean momentum flux measurements in moderate to strong winds, *Journal of Physical Oceanography*, 11, 324-336.

Loughlin, T.R., I.N. Sukhanova, E.H. Sinclair, and R.C. Ferrero, 1999: Summary of biology and ecosystem dynamics in the Bering Sea, In *Dynamics of the Bering Sea: A*

Summary of Physical, Chemical, and Biological Characteristics, and a Synopsis of Research on the Bering Sea, T.R. Loughlin and K. Ohtani (eds.), North Pacific Marine Science Organization (PICES), Univ. of Alaska Sea Grant, AK-SG-99-03, 387-409.

Mizobata, K., J. Wang, and S. Saitoh, 2006: Eddy-induced cross-slope exchange maintaining summer high productivity of the Bering Sea shelf break, *Journal of Geophysical Research*, 111, C10017.

Mooers, C.N.K., 1973: A technique for the cross spectrum analysis of pairs of complex-valued time series, with emphasis on properties of polarized components and rotational invariants, *Deep-Sea Research*, 20: 1129 – 1141.

Muller, P., R.W. Garwood Jr., and J.P. Garner, 1984: Effect of vertical advection on the dynamics of the oceanic surface mixed layer, *Annales Geophysicae*, 2, 387 – 398.

National Oceanographic Data Center (NODC), 2005: http://www.nodc.noaa.gov/OC5/WOD05/data05geo.html
National Research Council, 1996: *Report of the Committee on the Bering Sea Ecosystem; Polar Research Board; Commission on Geosciences, Environment, and Resources: The Bering Sea Ecosystem*, 307pp, National Academy Press.

Niebauer, H.J., N.A. Bond, L.P. Yakunin, and V.V. Plotnikov, 1999: An update on the climatology and sea ice of the Bering Sea, In *Dynamics of the Bering Sea: A Summary of Physical, Chemical, and Biological Characteristics, and a Synopsis of Research on the Bering Sea*, T.R. Loughlin and K. Ohtani (eds.), North Pacific Marine Science Organization (PICES), Univ. of Alaska Sea Grant, AK-SG-99-03, 29-60.

Plueddemann, A.J. and J.T. Farrar, 2006: Observations and models of the energy flux from the wind to mixed-layer inertial currents, *Deep Sea Research (II)*, 53, 5-30.

Price, J.F., R.A. Weller, and R. Pinkel, 1986: Diurnal cycling: Observations and models of the upper ocean response to diurnal heating, cooling, and wind mixing, *Journal of Geophysical Research*, 91, 8411-8427.

Remote Sensing Systems, 2007: http://www.remss.com

Schumacher, J.D. and T.H. Kinder, 1983: Low-frequency current regimes over the Bering Sea shelf, *Journal of Physical Oceanography,* 13, 607-623.

Simpson, J.H. and J.D. Bowers, 1981: Models of stratification and frontal movement in shelf seas, *Deep Sea Research*, 284, 727-738.

Srivastava, M.S., 1965: On the complex Wishart distribution, *The Annals of Mathematical Science*, 36: 313 – 315.

Stabeno, P.J., J.D. Schumacher, and K. Ohtani, 1999: The physical oceanography of the Bering Sea, In *Dynamics of the Bering Sea: A Summary of Physical, Chemical, and Biological Characteristics, and a Synopsis of Research on the Bering Sea*, T.R. Loughlin and K. Ohtani (eds.), North Pacific Marine Science Organization (PICES), Univ. of Alaska Sea Grant, AK-SG-99-03, 1-28.

Stabeno, P.J., G.L. Hunt, Jr., J.M. Napp, and J.D. Schumacher, 2006: Physical forcing of ecosystem dynamics on the Bering Sea Shelf. Chapter 30 In *The Sea, Vol. 14*, A.R. Robinson and K. Brink (eds.), *The Global Coastal Ocean: Interdisciplinary Regional Studies and Syntheses*, Part B, Harvard University Press, 1177-1212.

Stewart, R.H, 2005: *Introduction to Physical Oceanography*, 344pp, Texas A&M University, Department of Oceanography.

Swift, J.H. and K. Aagaard, 1976: Upwelling near Samalga Pass, *Limnology and Oceanography*, 21, 399 – 408.

Wallace, J.M. and R.E. Dickinson, 1972: Empirical orthogonal representation of time series in the frequency domain: Parts I and II, *Journal of Applied Meteorology*, 11: 887 – 900.

Wilderbuer, T.K., A.B. Hollowed, W.J. Ingraham, Jr., P.D. Spenceer, M.E. Conners, N.A. Bond, and G.E. Walters, 2002: Flatfish recruitment response to decadal climate variability and ocean conditions in the Bering Sea, *Progress in Oceanography*, 55: 235 – 247.

Appendix A

Complex Cross-correlation Results

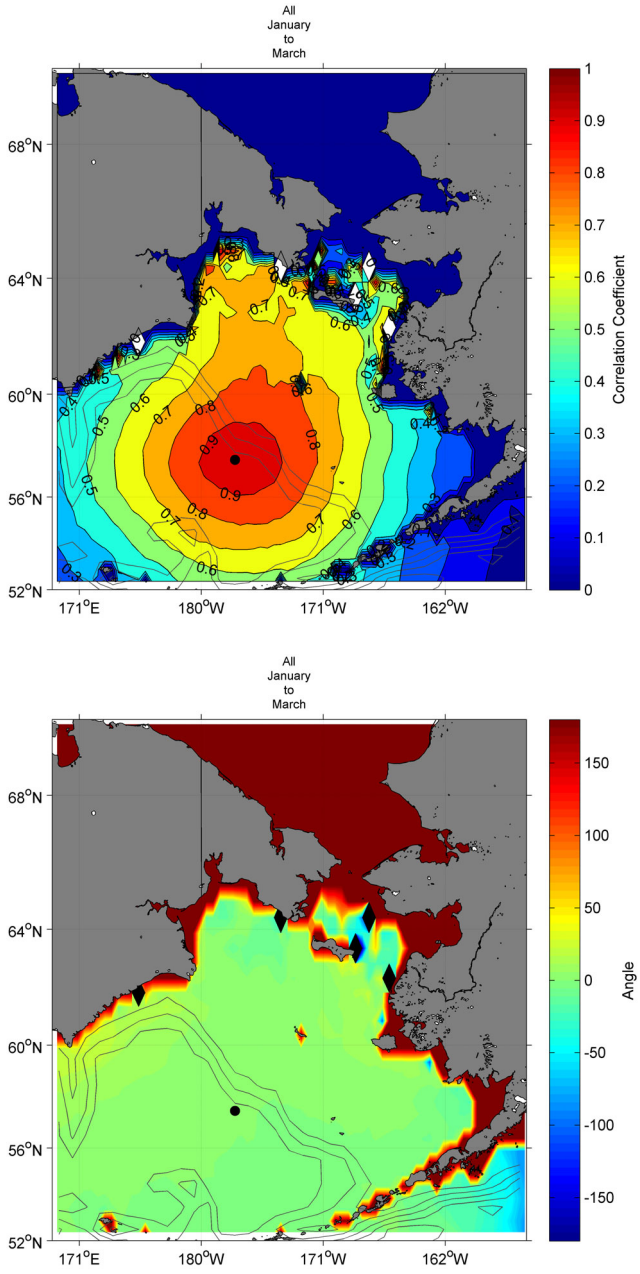

Figure A-1. Complex correlation coefficients (top panel) and phase angles (bottom panel) for the time series a**t one NCEP station with the time series at all QuikSCAT stations within the domain.** The NCEP station is indicated by a black dot. Note that there are no correlations for grid points within areas of sea ice.

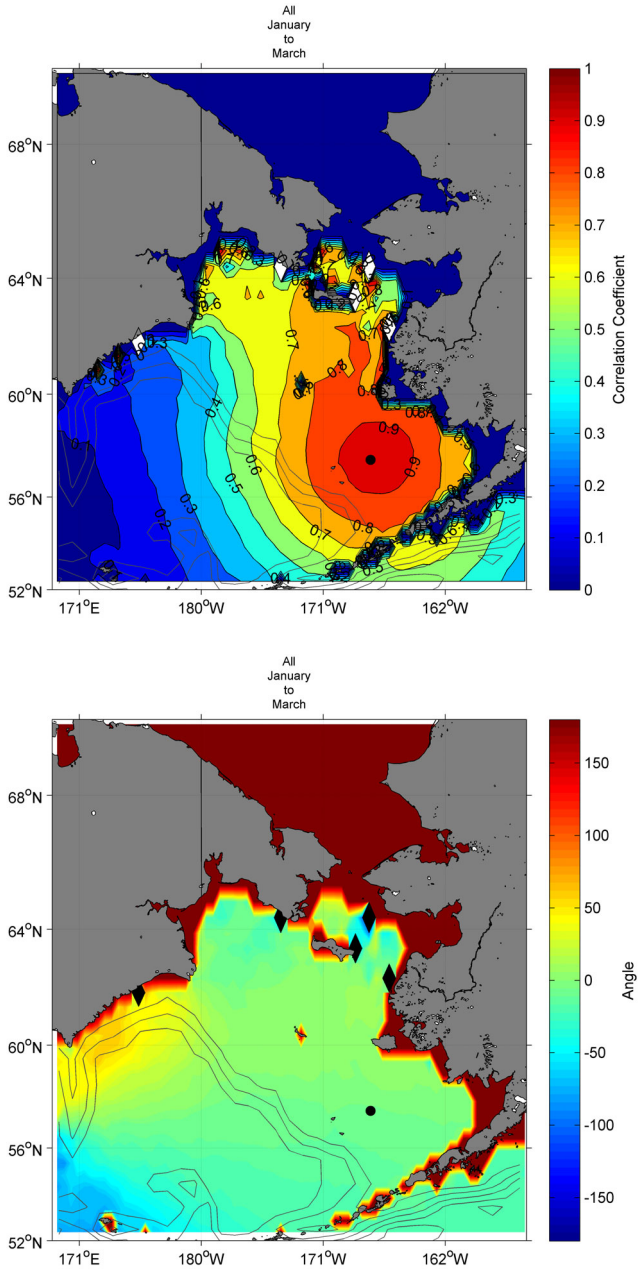

Figure A-2. Complex correlation coeffic**ients (top panel) and phase angles (bottom panel) for the time series at one NCEP station with the time series at all QuikSCAT stations within the domain.** The NCEP station is indicated by a black dot. Note that there are no correlations for grid points within areas of sea ice.

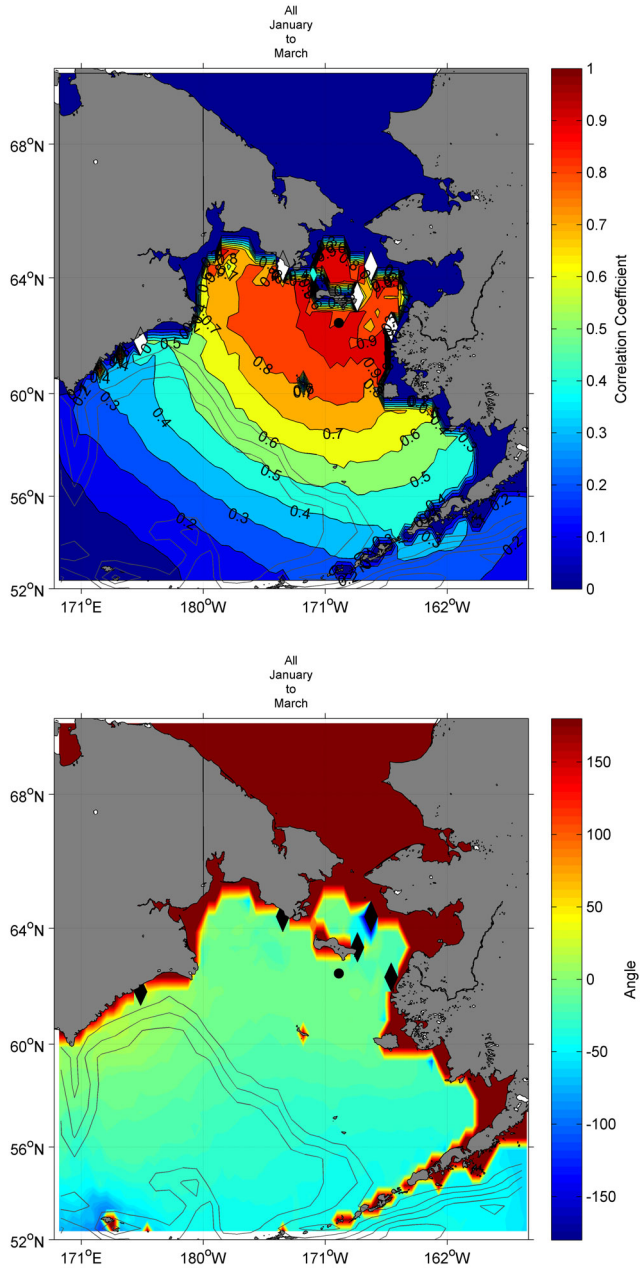

Figure A-3. Complex correlation coefficients (top panel) and phase angles (bottom panel) for the time series at one NCEP station with the time series at all QuikSCAT stations within the domain. The NCEP station is indicated by a black dot. Note that there are no correlations for grid points within areas of sea ice.

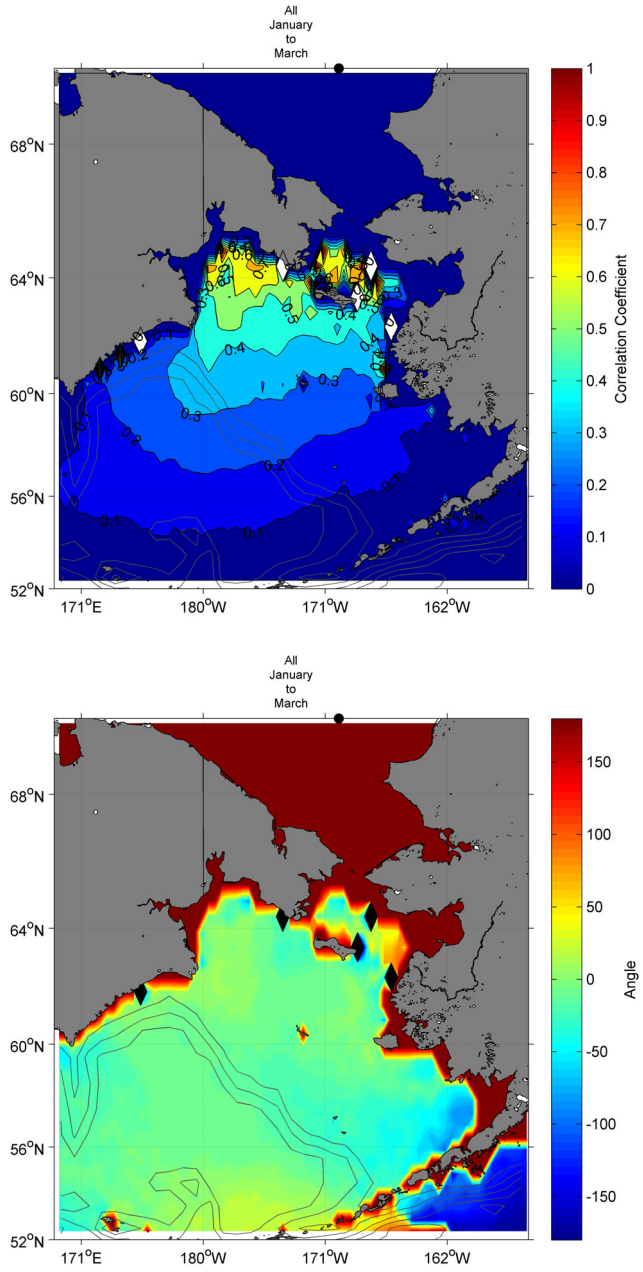

Figure A-4. Complex correlation coefficients (top panel) and phase angles (bottom panel) for the time series at one NCEP station with the time series at all **QuikSCAT stations within the domain.** The NCEP station is indicated by a black dot. Note that there are no correlations for grid points within areas of sea ice.

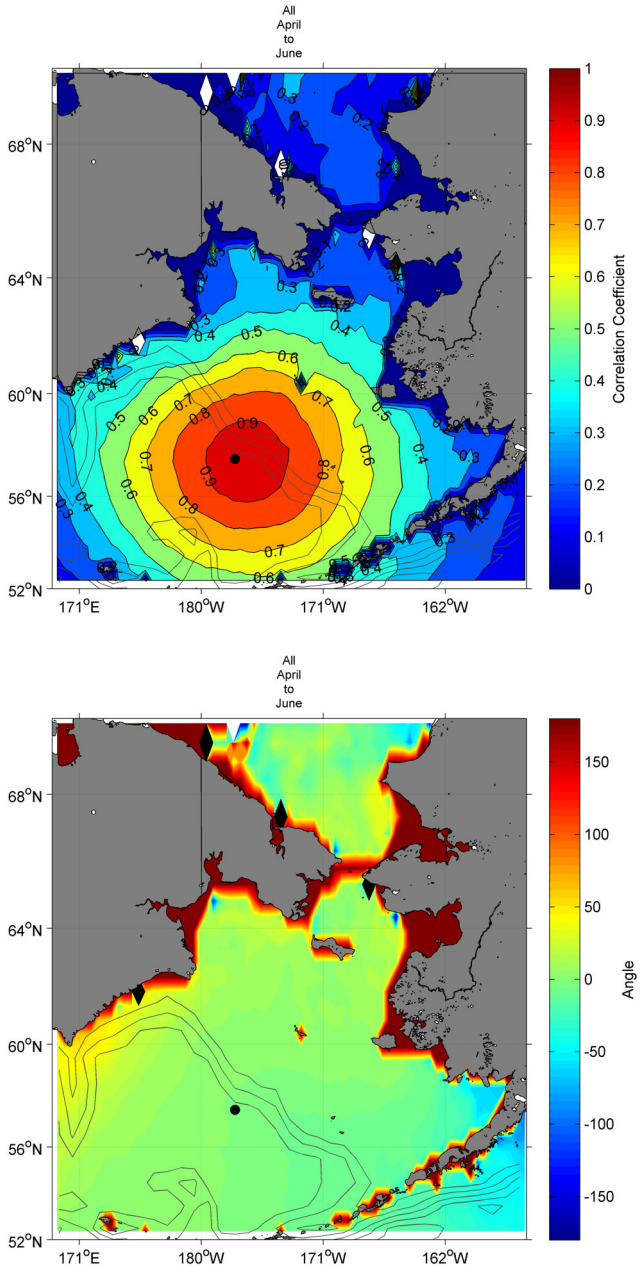

Figure A-5. Complex correlation coefficients (top panel) and phase angles (bottom panel) **for the time series at one NCEP station with the time series at all QuikSCAT stations within the domain.** The NCEP station is indicated by a black dot. Note that there are no correlations for grid points within areas of sea ice.

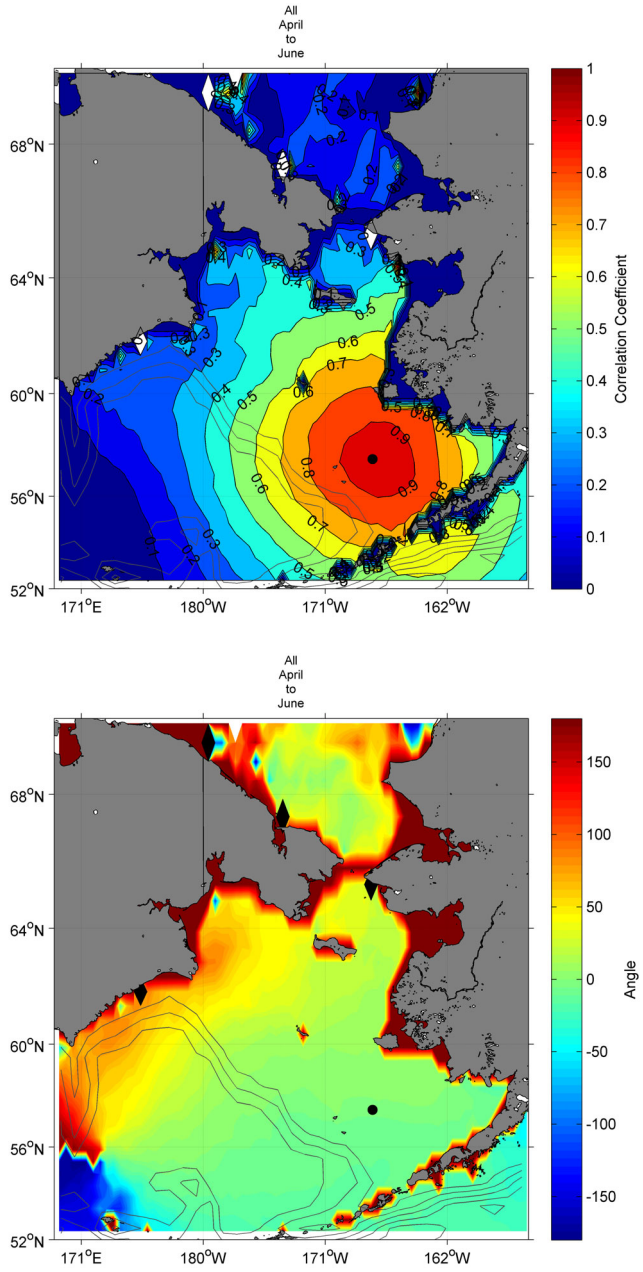

Figure A-6. Complex **correlation coefficients (top panel) and phase angles (bottom panel) for the time series at one NCEP station with the time series at all QuikSCAT stations within the domain.** The NCEP station is indicated by a black dot. Note that there are no correlations for grid points within areas of sea ice.

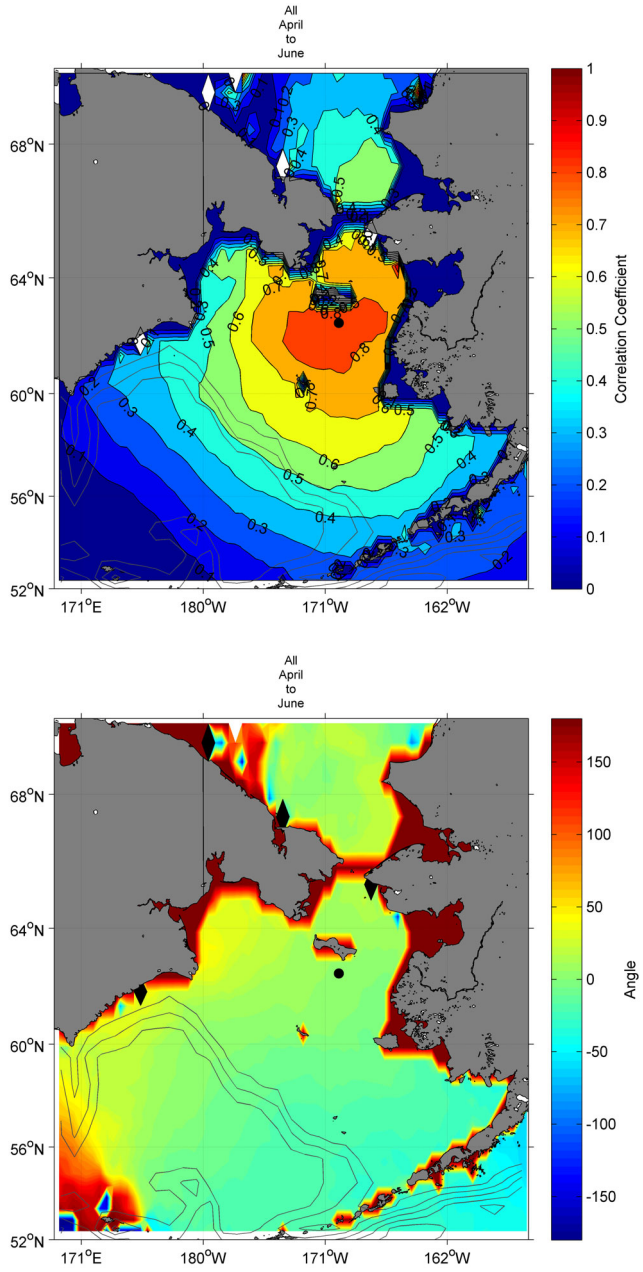

Figure A-7. Complex correlation coefficients (top panel) and phase angles (bottom panel) for the time series at one NCEP station with the time series at all QuikSCAT stations within the domain. The NCEP station is indicated by a black dot. Note that there are no correlations for grid points within areas of sea ice.

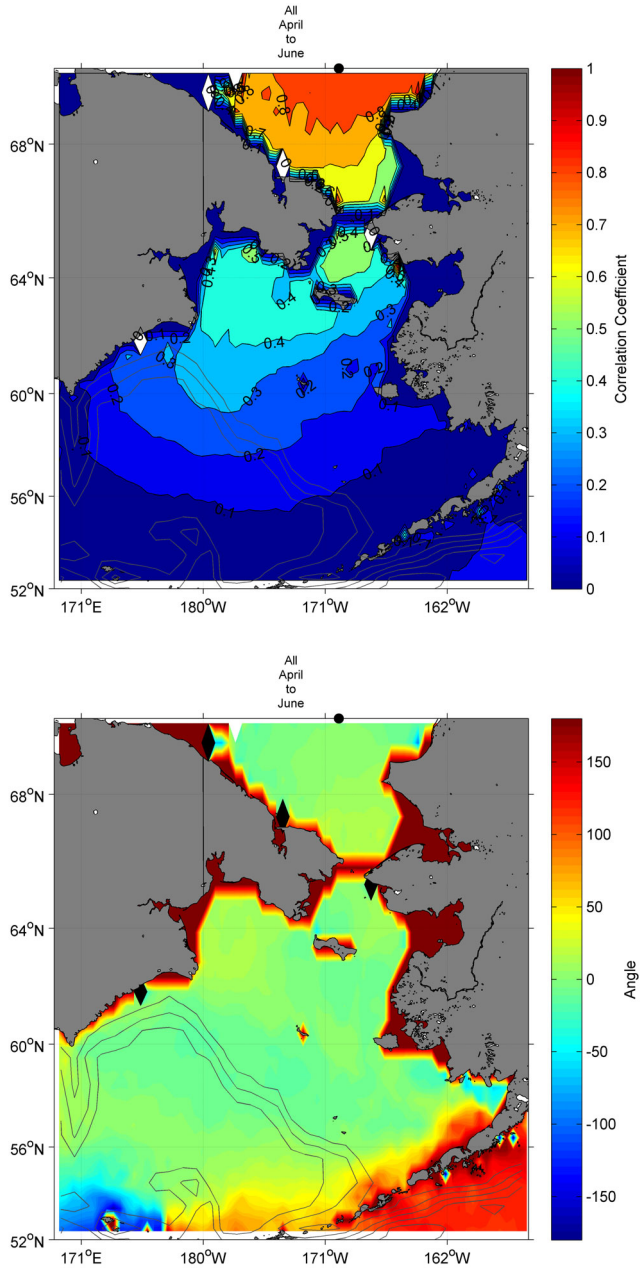

Figure A-8. Complex correlation coefficients (top panel) and phase angles (bottom panel) for the time series at one NCEP station with the **time series at all QuikSCAT stations within the domain.** The NCEP station is indicated by a black dot. Note that there are no correlations for grid points within areas of sea ice.

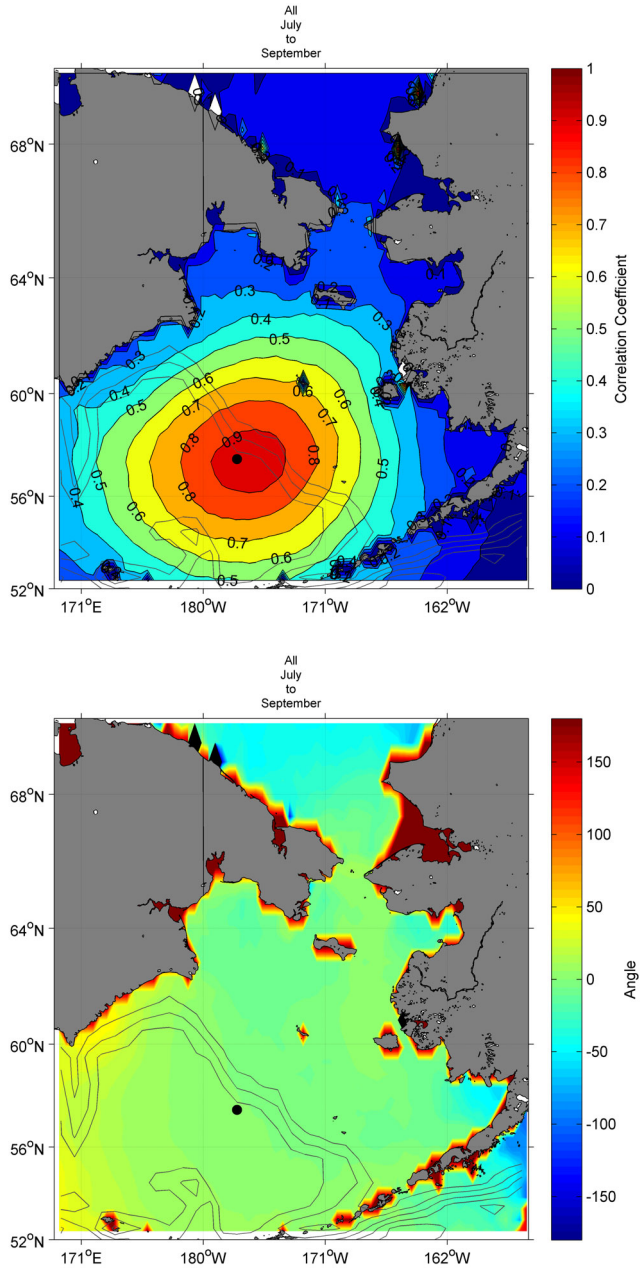

Figure A-9. Complex correlation coefficients (top panel) and phase a**ngles (bottom panel) for the time series at one NCEP station with the time series at all QuikSCAT stations within the domain.** The NCEP station is indicated by a black dot. Note that there are no correlations for grid points within areas of sea ice.

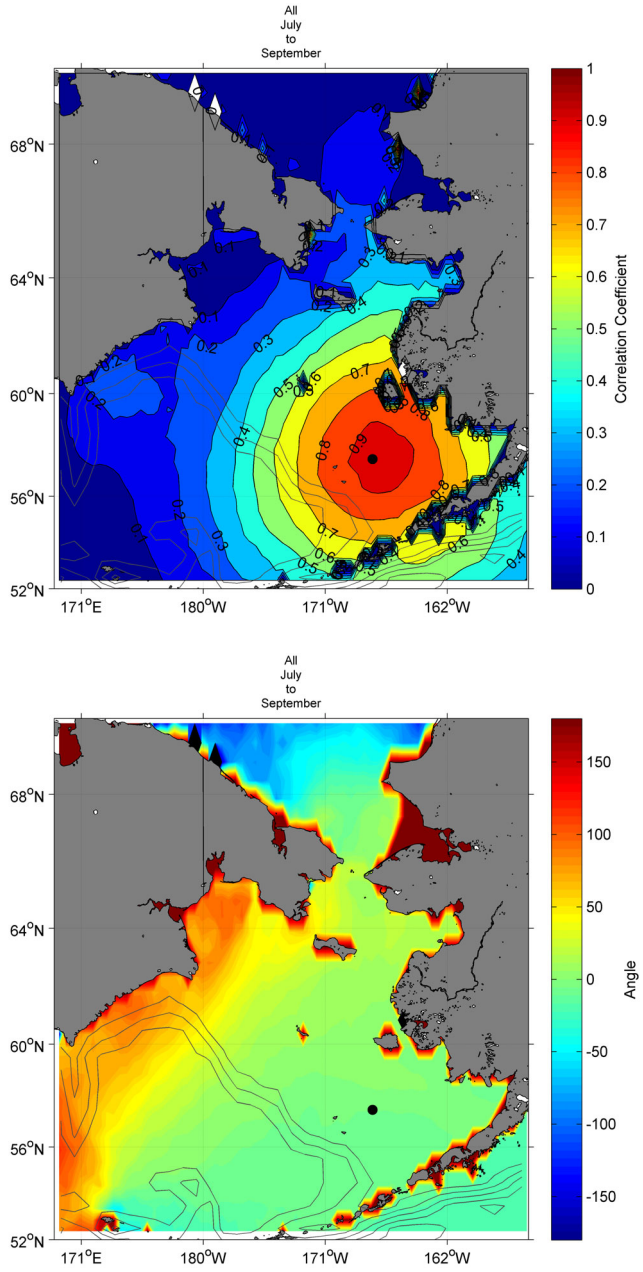

Figure A-10. Complex correlation coefficients (top panel) and phase angles (bottom panel) for the time series at one NCEP station with the time series at all QuikSCAT stations within the domain. The NCEP station is indicated by a black dot. Note that there are no correlations for grid points within areas of sea ice.

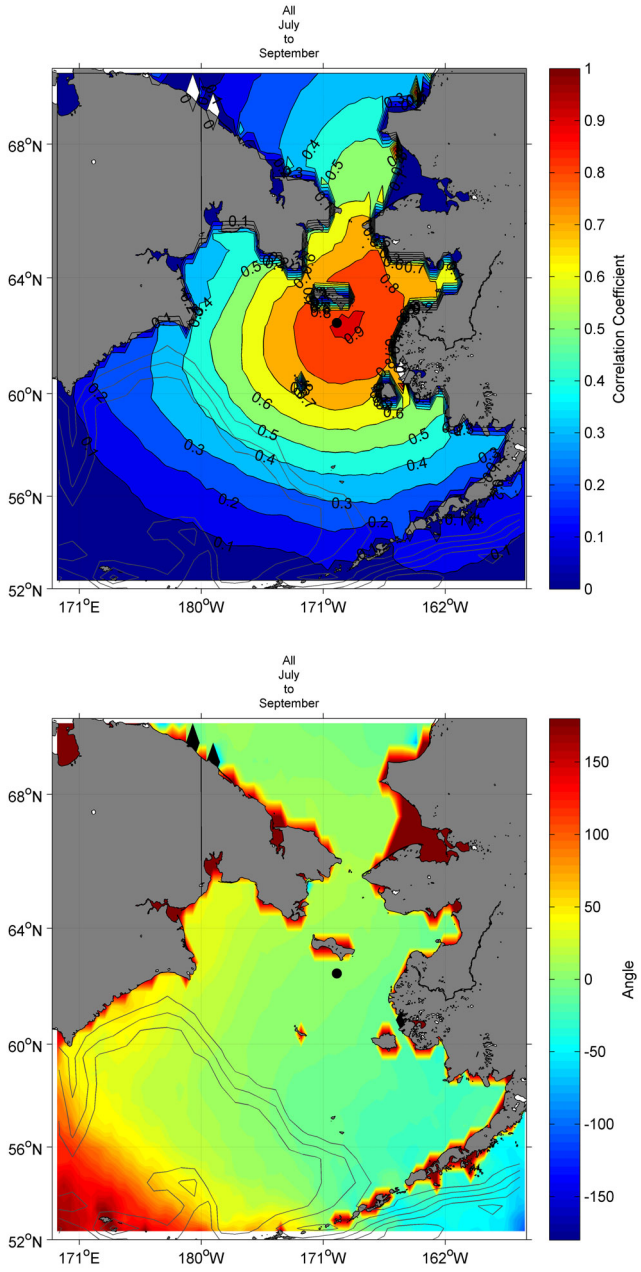

Figure A-11. Complex correlation coefficients (top panel) and phase angles (bottom panel) for the time series at one NCEP station with the time series at all QuikSCAT stations within th**e domain.** The NCEP station is indicated by a black dot. Note that there are no correlations for grid points within areas of sea ice.

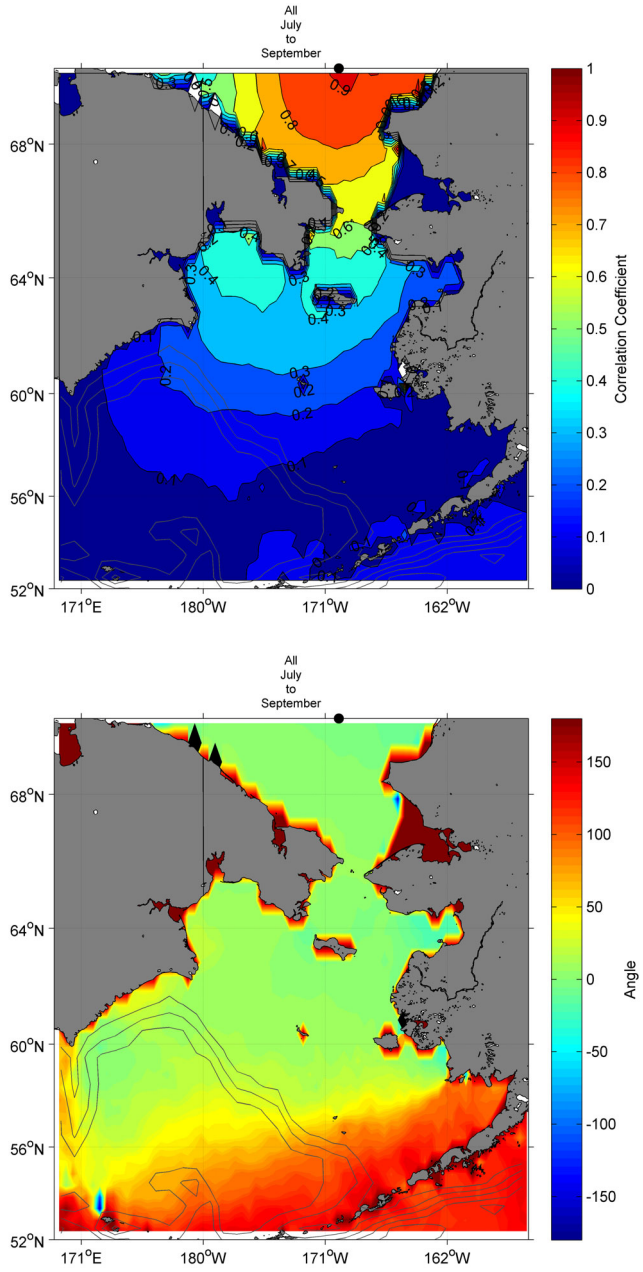

Figure A-12. Complex correlation coefficients (top panel) and phase angles (bottom panel) for the time series at o**ne NCEP station with the time series at all QuikSCAT stations within the domain.** The NCEP station is indicated by a black dot. Note that there are no correlations for grid points within areas of sea ice.

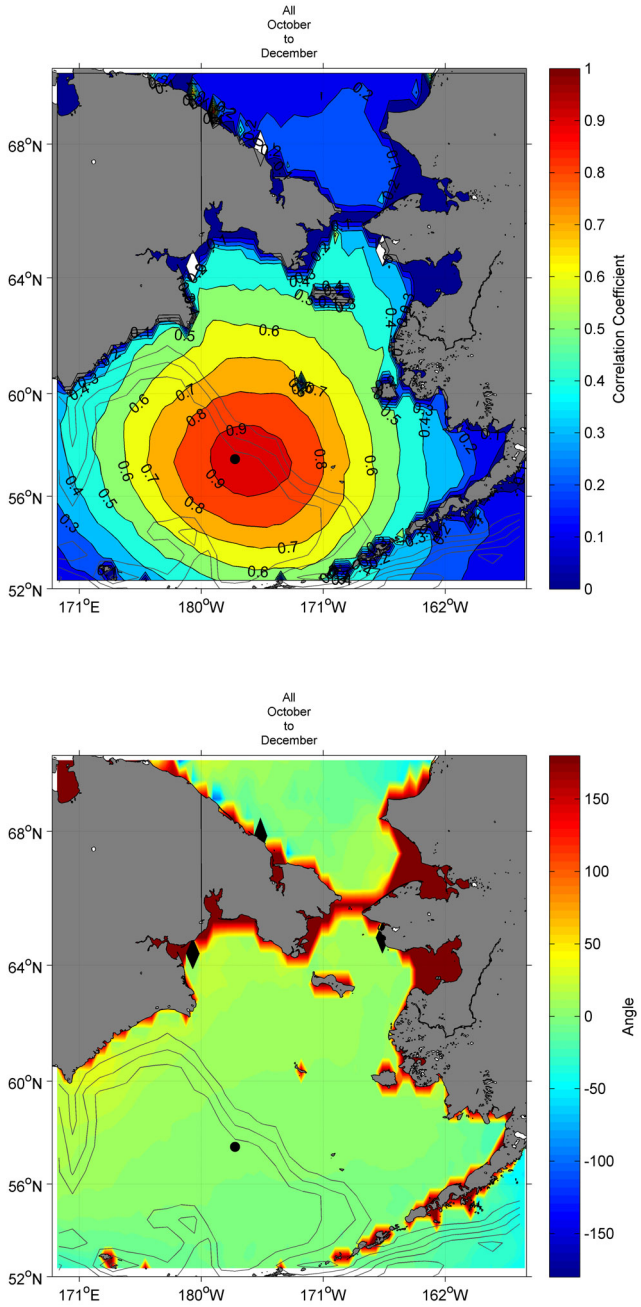

Figure A-13. Complex correlation coefficien**ts (top panel) and phase angles (bottom panel) for the time series at one NCEP station with the time series at all QuikSCAT stations within the domain.** The NCEP station is indicated by a black dot. Note that there are no correlations for grid points within areas of sea ice.

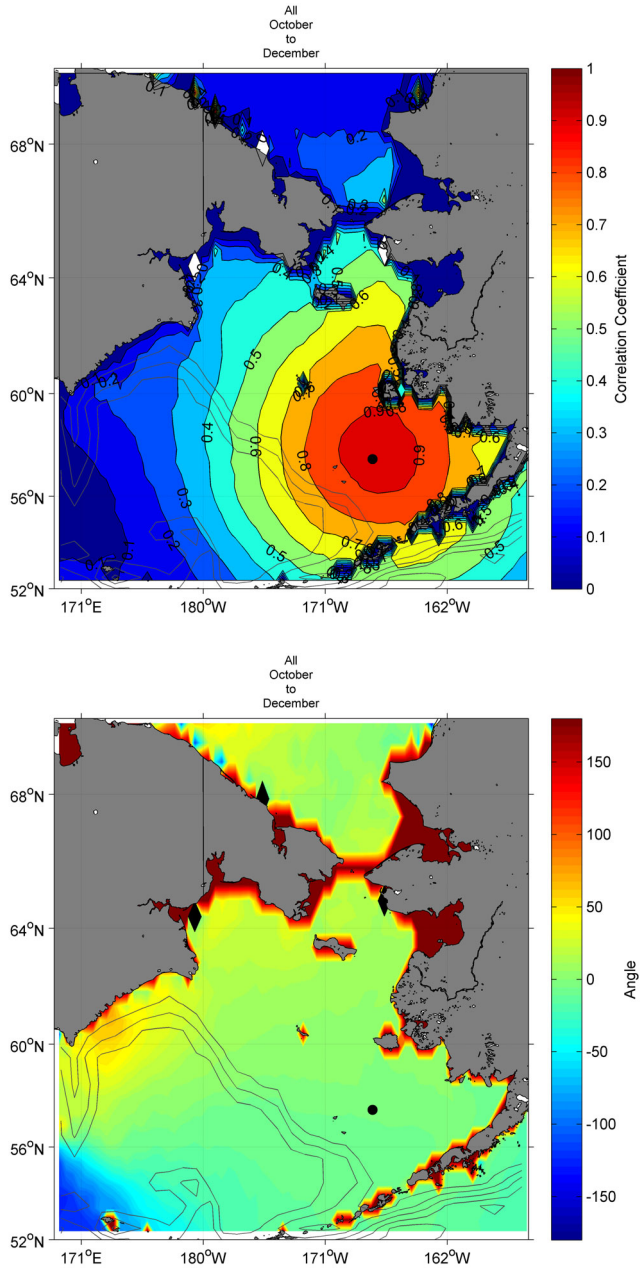

Figure A-14. Complex correlation coefficients (top panel) and phase angles (bottom panel) for the time series at one NCEP station with the time series at all QuikSCAT stations within the domain. The NCEP station is indicated by a black dot. Note that there are no correlations for grid points within areas of sea ice.

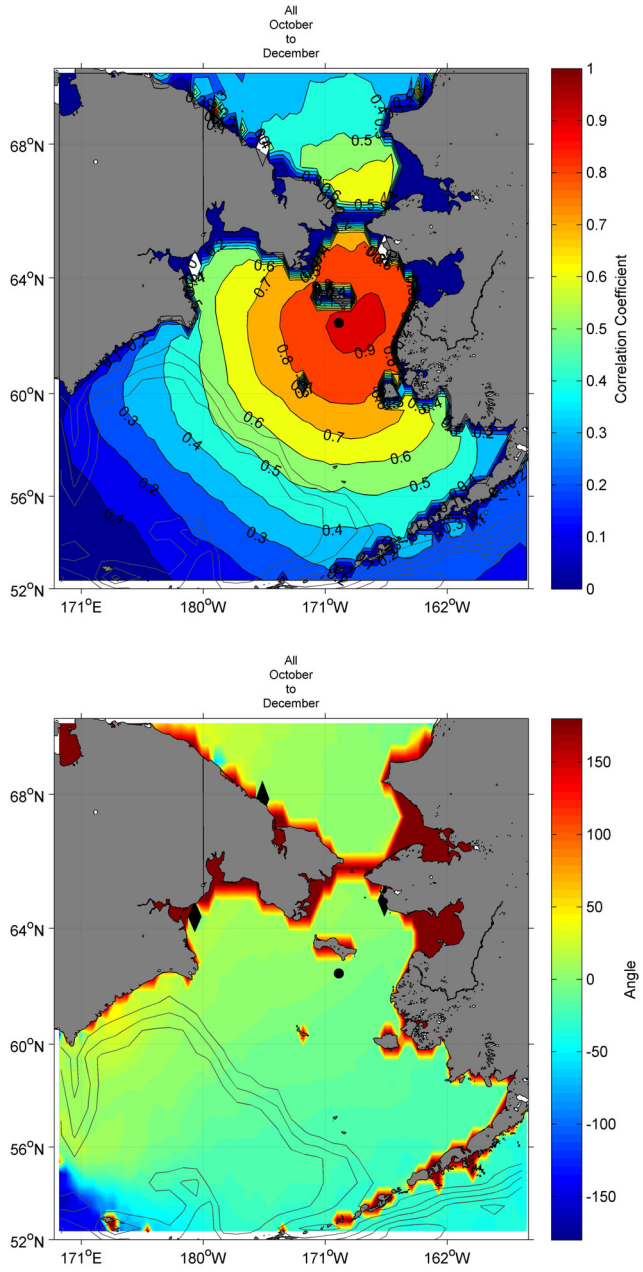

Figure A-15. Complex correlation coefficients (top panel) and phase angles (bottom panel) for the time series at one NCEP station with the time series at all **QuikSCAT stations within the domain.** The NCEP station is indicated by a black dot. Note that there are no correlations for grid points within areas of sea ice.

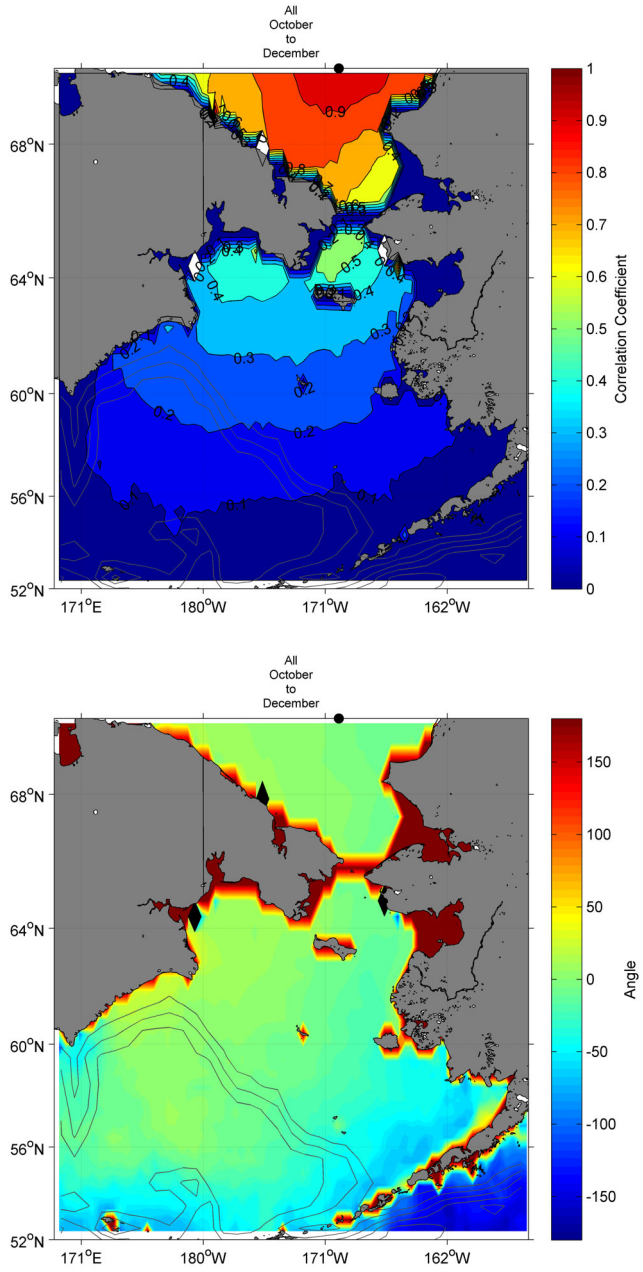

Figure A-16. Complex correlation coefficients (top panel) and phase angles (bottom panel**) for the time series at one NCEP station with the time series at all QuikSCAT stations within the domain.** The NCEP station is indicated by a black dot. Note that there are no correlations for grid points within areas of sea ice.

Appendix B

Linear Regression Results

Table B-1. Results of the linear regressions between the zonal components (U) of QuikSCAT and NCEP data before February 1, 2002.

NCEP Lat	NCEP Lon	r	Rsquared	b0	Upper b0	Lower b0	b1	Upper b1	Lower b1	p-value
70	177.5	0.93	0.87	-0.18	11646.13	-11646.50	1.07	620.33	-618.18	0.21
70	180	0.85	0.72	0.04	0.85	-0.77	0.96	1.01	0.91	<<0.05*
70	182.5	0.85	0.72	-0.57	-0.01	-1.13	0.93	0.97	0.89	<<0.05*
70	185	0.91	0.83	-0.62	-0.28	-0.96	0.94	0.96	0.92	<<0.05*
70	187.5	0.91	0.82	-0.46	-0.15	-0.78	0.92	0.94	0.90	<<0.05*
70	190	0.90	0.81	-0.30	0.03	-0.63	0.91	0.93	0.89	<<0.05*
70	192.5	0.92	0.84	-0.15	0.18	-0.47	0.97	0.99	0.95	<<0.05*
70	195	0.91	0.83	0.01	0.36	-0.34	1.04	1.06	1.01	<<0.05*
67.5	187.5	0.67	0.45	-0.01	0.31	-0.34	0.55	0.57	0.53	<<0.05*
67.5	190	0.63	0.40	0.20	0.49	-0.09	0.48	0.50	0.46	<<0.05*
67.5	192.5	0.61	0.38	0.29	0.61	-0.03	0.50	0.52	0.48	<<0.05*
65	180	0.50	0.25	-1.55	-0.90	-2.21	0.61	0.67	0.55	<<0.05*
65	182.5	0.47	0.22	-2.60	-2.18	-3.01	0.59	0.62	0.55	<<0.05*
65	190	0.60	0.35	-0.55	-0.26	-0.85	0.61	0.63	0.58	<<0.05*
65	192.5	0.59	0.34	-0.08	0.29	-0.44	0.60	0.63	0.57	<<0.05*
62.5	177.5	0.50	0.25	-0.13	0.41	-0.67	0.63	0.68	0.57	<<0.05*
62.5	180	0.68	0.46	0.54	0.91	0.16	0.98	1.01	0.95	<<0.05*
62.5	182.5	0.71	0.50	0.00	0.34	-0.34	0.99	1.01	0.96	<<0.05*
62.5	185	0.72	0.52	-0.42	-0.08	-0.75	0.95	0.98	0.93	<<0.05*
62.5	187.5	0.71	0.51	-0.71	-0.39	-1.03	0.87	0.89	0.85	<<0.05*
62.5	190	0.70	0.50	-0.33	-0.02	-0.65	0.77	0.78	0.75	<<0.05*
62.5	192.5	0.72	0.52	-0.04	0.28	-0.36	0.76	0.78	0.74	<<0.05*
62.5	195	0.68	0.46	0.45	1.34	-0.45	0.82	0.89	0.75	<<0.05*
60	170	0.64	0.41	-0.48	0.15	-1.11	1.40	1.46	1.33	<<0.05*
60	172.5	0.63	0.39	-1.86	-1.49	-2.24	1.37	1.40	1.33	<<0.05*
60	175	0.69	0.47	-1.46	-1.16	-1.76	1.14	1.16	1.11	<<0.05*
60	177.5	0.72	0.51	-0.93	-0.64	-1.23	1.00	1.02	0.98	<<0.05*
60	180	0.71	0.51	-0.54	-0.23	-0.84	0.86	0.88	0.85	<<0.05*
60	182.5	0.72	0.52	-0.03	0.27	-0.32	0.78	0.80	0.77	<<0.05*
60	185	0.72	0.51	0.19	0.49	-0.11	0.75	0.77	0.74	<<0.05*
60	187.5	0.68	0.46	0.30	0.62	-0.01	0.68	0.70	0.67	<<0.05*
60	190	0.71	0.50	0.28	0.58	-0.03	0.71	0.72	0.69	<<0.05*
60	192.5	0.67	0.44	0.12	0.50	-0.26	0.68	0.70	0.66	<<0.05*
60	195	0.60	0.36	0.95	1.38	0.53	0.68	0.71	0.65	<<0.05*
60	197.5	0.51	0.26	0.95	1.53	0.36	0.60	0.65	0.55	<<0.05*
57.5	170	0.75	0.57	0.74	1.01	0.46	0.88	0.89	0.86	<<0.05*
57.5	172.5	0.74	0.54	0.67	0.96	0.39	0.83	0.85	0.82	<<0.05*
57.5	175	0.75	0.56	0.56	0.84	0.28	0.79	0.81	0.78	<<0.05*
57.5	177.5	0.73	0.53	0.57	0.86	0.28	0.74	0.75	0.73	<<0.05*
57.5	180	0.70	0.48	0.65	0.96	0.35	0.69	0.70	0.67	<<0.05*
57.5	182.5	0.70	0.48	0.70	1.01	0.40	0.70	0.71	0.68	<<0.05*
57.5	185	0.69	0.47	0.45	0.77	0.14	0.70	0.72	0.69	<<0.05*
57.5	187.5	0.69	0.47	0.34	0.64	0.04	0.68	0.69	0.67	<<0.05*
57.5	190	0.73	0.54	0.23	0.50	-0.04	0.67	0.68	0.66	<<0.05*
57.5	192.5	0.74	0.55	0.30	0.56	0.04	0.70	0.71	0.69	<<0.05*
57.5	195	0.77	0.60	0.51	0.76	0.26	0.77	0.79	0.76	<<0.05*

Table B-1 (Continued)

NCEP Lat	NCEP Lon	r	Rsquared	b0	Upper b0	Lower b0	b1	Upper b1	Lower b1	p-value
57.5	197.5	0.79	0.62	1.04	1.28	0.80	0.87	0.88	0.85	<<0.05*
57.5	200	0.76	0.58	1.49	1.79	1.20	0.95	0.97	0.93	<<0.05*
55	170	0.69	0.47	0.60	0.89	0.31	0.65	0.66	0.63	<<0.05*
55	172.5	0.70	0.49	0.75	1.05	0.46	0.67	0.69	0.66	<<0.05*
55	175	0.70	0.49	0.75	1.05	0.45	0.68	0.69	0.67	<<0.05*
55	177.5	0.68	0.47	0.77	1.08	0.46	0.68	0.69	0.66	<<0.05*
55	180	0.68	0.47	0.85	1.15	0.54	0.66	0.68	0.65	<<0.05*
55	182.5	0.68	0.46	1.02	1.33	0.70	0.66	0.67	0.64	<<0.05*
55	185	0.70	0.49	1.00	1.30	0.70	0.67	0.68	0.65	<<0.05*
55	187.5	0.70	0.49	1.14	1.44	0.85	0.67	0.68	0.66	<<0.05*
55	190	0.70	0.50	1.21	1.49	0.92	0.66	0.68	0.65	<<0.05*
55	192.5	0.71	0.50	1.23	1.53	0.94	0.68	0.70	0.67	<<0.05*
55	195	0.74	0.54	0.95	1.24	0.67	0.68	0.69	0.67	<<0.05*
55	200	0.66	0.44	2.57	3.40	1.74	0.66	0.71	0.61	<<0.05*
55	202.5	0.73	0.53	2.33	2.63	2.04	0.77	0.78	0.75	<<0.05*
52.5	170	0.67	0.44	0.98	1.31	0.65	0.69	0.71	0.68	<<0.05*
52.5	172.5	0.67	0.44	1.00	1.35	0.65	0.69	0.70	0.67	<<0.05*
52.5	175	0.70	0.49	0.63	0.94	0.31	0.70	0.72	0.69	<<0.05*
52.5	177.5	0.72	0.51	0.60	0.92	0.29	0.73	0.75	0.72	<<0.05*
52.5	180	0.71	0.50	0.86	1.17	0.55	0.70	0.71	0.68	<<0.05*
52.5	182.5	0.71	0.51	1.00	1.30	0.69	0.67	0.68	0.65	<<0.05*
52.5	185	0.72	0.52	1.13	1.41	0.84	0.65	0.66	0.64	<<0.05*
52.5	187.5	0.76	0.58	1.10	1.42	0.77	0.69	0.70	0.68	<<0.05*
52.5	190	0.68	0.46	2.00	2.32	1.69	0.64	0.65	0.63	<<0.05*
52.5	192.5	0.71	0.50	2.16	2.47	1.86	0.69	0.70	0.68	<<0.05*
52.5	195	0.72	0.52	2.02	2.31	1.74	0.69	0.70	0.67	<<0.05*
52.5	197.5	0.75	0.56	2.04	2.31	1.77	0.72	0.73	0.71	<<0.05*
52.5	200	0.76	0.58	2.05	2.32	1.78	0.74	0.75	0.72	<<0.05*
52.5	202.5	0.76	0.57	2.12	2.40	1.84	0.73	0.75	0.72	<<0.05*
Means		0.71	0.51	0.45	0.81	0.10	0.76	0.78	0.74	

Regressions that are significant at the 95% confidence level are indicated by an asterisk.

Table B-2. Results of the linear regressions between the meridional components (V) of QuikSCAT and NCEP data before February 1, 2002.

NCEP Lat	NCEP Lon	r	Rsquared	b0	Upper b0	Lower b0	b1	Upper b1	Lower b1	p-value
70	177.5	0.86	0.74	-1.31	6897.81	-6900.42	0.70	612.08	-610.68	0.24
70	180	0.66	0.44	-0.64	0.07	-1.35	0.60	0.66	0.54	<<0.05*
70	182.5	0.86	0.73	-0.21	0.32	-0.73	0.82	0.86	0.79	<<0.05*
70	185	0.89	0.79	0.26	0.60	-0.08	0.81	0.83	0.79	<<0.05*
70	187.5	0.92	0.85	0.42	0.70	0.15	0.82	0.84	0.81	<<0.05*
70	190	0.93	0.86	0.30	0.57	0.03	0.80	0.82	0.79	<<0.05*
70	192.5	0.91	0.82	0.10	0.40	-0.20	0.82	0.84	0.80	<<0.05*
70	195	0.87	0.75	-0.37	-0.06	-0.69	0.76	0.79	0.74	<<0.05*
67.5	187.5	0.87	0.76	-0.25	0.03	-0.53	0.81	0.83	0.80	<<0.05*
67.5	190	0.85	0.72	-0.17	0.11	-0.45	0.81	0.82	0.79	<<0.05*
67.5	192.5	0.81	0.65	-0.18	0.16	-0.52	0.86	0.88	0.84	<<0.05*
65	180	0.66	0.43	0.23	0.84	-0.37	0.70	0.75	0.66	<<0.05*
65	182.5	0.80	0.64	0.44	0.81	0.08	0.94	0.96	0.91	<<0.05*
65	190	0.84	0.70	-0.63	-0.31	-0.94	0.85	0.86	0.83	<<0.05*
65	192.5	0.83	0.69	-0.11	0.24	-0.47	0.86	0.87	0.84	<<0.05*
62.5	177.5	0.68	0.47	-0.39	0.10	-0.88	0.70	0.74	0.67	<<0.05*
62.5	180	0.83	0.69	0.30	0.65	-0.05	1.07	1.09	1.05	<<0.05*
62.5	182.5	0.86	0.74	1.02	1.28	0.76	0.94	0.96	0.93	<<0.05*
62.5	185	0.86	0.74	1.00	1.25	0.76	0.82	0.83	0.80	<<0.05*
62.5	187.5	0.87	0.75	0.62	0.86	0.38	0.81	0.82	0.80	<<0.05*
62.5	190	0.86	0.74	0.31	0.56	0.06	0.80	0.82	0.79	<<0.05*
62.5	192.5	0.83	0.68	0.21	0.49	-0.08	0.81	0.82	0.79	<<0.05*
62.5	195	0.85	0.72	-0.30	0.40	-0.99	0.92	0.97	0.88	<<0.05*
60	170	0.60	0.35	-0.48	-0.06	-0.90	0.77	0.81	0.73	<<0.05*
60	172.5	0.74	0.55	-0.03	0.28	-0.33	1.21	1.24	1.19	<<0.05*
60	175	0.85	0.72	0.52	0.76	0.28	1.17	1.19	1.16	<<0.05*
60	177.5	0.87	0.75	0.77	0.99	0.55	0.99	1.00	0.98	<<0.05*
60	180	0.85	0.73	0.55	0.79	0.31	0.91	0.92	0.90	<<0.05*
60	182.5	0.87	0.75	0.24	0.46	0.02	0.82	0.83	0.81	<<0.05*
60	185	0.85	0.72	0.35	0.58	0.12	0.78	0.79	0.77	<<0.05*
60	187.5	0.85	0.73	0.18	0.40	-0.05	0.76	0.77	0.75	<<0.05*
60	190	0.86	0.73	0.13	0.37	-0.10	0.82	0.83	0.81	<<0.05*
60	192.5	0.84	0.71	0.01	0.30	-0.27	0.82	0.84	0.81	<<0.05*
60	195	0.80	0.65	0.09	0.47	-0.28	0.93	0.96	0.91	<<0.05*
60	197.5	0.75	0.57	-0.27	0.31	-0.85	1.06	1.10	1.02	<<0.05*
57.5	170	0.85	0.72	0.71	0.90	0.51	0.89	0.90	0.88	<<0.05*
57.5	172.5	0.84	0.71	1.02	1.23	0.82	0.85	0.86	0.84	<<0.05*
57.5	175	0.86	0.74	1.04	1.24	0.84	0.79	0.80	0.78	<<0.05*
57.5	177.5	0.86	0.75	0.97	1.17	0.77	0.77	0.77	0.76	<<0.05*
57.5	180	0.87	0.75	0.76	0.97	0.55	0.77	0.78	0.76	<<0.05*
57.5	182.5	0.87	0.75	0.53	0.74	0.32	0.81	0.82	0.80	<<0.05*
57.5	185	0.87	0.76	0.41	0.62	0.20	0.85	0.86	0.84	<<0.05*
57.5	187.5	0.87	0.76	0.10	0.30	-0.10	0.85	0.86	0.84	<<0.05*
57.5	190	0.88	0.77	-0.12	0.07	-0.32	0.83	0.84	0.82	<<0.05*
57.5	192.5	0.87	0.77	-0.32	-0.13	-0.52	0.85	0.86	0.84	<<0.05*
57.5	195	0.86	0.75	-0.41	-0.21	-0.62	0.89	0.90	0.88	<<0.05*

Table B-2 (Continued)

NCEP Lat	NCEP Lon	r	Rsquared	b0	Upper b0	Lower b0	b1	Upper b1	Lower b1	p-value
57.5	197.5	0.83	0.69	-0.60	-0.38	-0.82	0.94	0.96	0.93	<<0.05*
57.5	200	0.78	0.60	-0.54	-0.31	-0.78	0.87	0.89	0.85	<<0.05*
55	170	0.87	0.76	0.32	0.51	0.13	0.80	0.81	0.79	<<0.05*
55	172.5	0.86	0.74	0.13	0.33	-0.06	0.77	0.78	0.76	<<0.05*
55	175	0.86	0.74	0.25	0.45	0.05	0.78	0.79	0.77	<<0.05*
55	177.5	0.87	0.76	0.30	0.50	0.11	0.81	0.81	0.80	<<0.05*
55	180	0.88	0.78	0.31	0.50	0.13	0.81	0.82	0.81	<<0.05*
55	182.5	0.89	0.78	0.26	0.45	0.07	0.84	0.84	0.83	<<0.05*
55	185	0.88	0.77	0.32	0.51	0.12	0.83	0.84	0.82	<<0.05*
55	187.5	0.87	0.77	0.38	0.57	0.18	0.82	0.83	0.81	<<0.05*
55	190	0.87	0.76	0.34	0.54	0.14	0.83	0.84	0.82	<<0.05*
55	192.5	0.88	0.77	0.28	0.48	0.08	0.82	0.83	0.81	<<0.05*
55	195	0.89	0.79	0.34	0.54	0.13	0.84	0.85	0.83	<<0.05*
55	200	0.83	0.69	0.25	0.89	-0.38	0.82	0.85	0.78	<<0.05*
55	202.5	0.84	0.70	1.62	1.83	1.41	0.88	0.90	0.87	<<0.05*
52.5	170	0.86	0.74	-0.04	0.16	-0.24	0.77	0.78	0.76	<<0.05*
52.5	172.5	0.85	0.73	-0.04	0.17	-0.24	0.75	0.76	0.74	<<0.05*
52.5	175	0.87	0.76	0.26	0.46	0.06	0.79	0.80	0.78	<<0.05*
52.5	177.5	0.89	0.79	0.43	0.61	0.25	0.79	0.80	0.78	<<0.05*
52.5	180	0.88	0.77	0.34	0.54	0.15	0.80	0.81	0.79	<<0.05*
52.5	182.5	0.86	0.75	0.19	0.39	-0.01	0.79	0.79	0.78	<<0.05*
52.5	185	0.85	0.72	0.04	0.24	-0.17	0.76	0.77	0.75	<<0.05*
52.5	187.5	0.88	0.77	0.17	0.40	-0.06	0.79	0.80	0.78	<<0.05*
52.5	190	0.85	0.71	0.21	0.44	-0.01	0.79	0.80	0.78	<<0.05*
52.5	192.5	0.86	0.74	0.49	0.70	0.27	0.82	0.83	0.81	<<0.05*
52.5	195	0.87	0.77	0.68	0.88	0.48	0.80	0.81	0.79	<<0.05*
52.5	197.5	0.89	0.79	0.67	0.86	0.48	0.78	0.79	0.77	<<0.05*
52.5	200	0.88	0.77	0.84	1.03	0.64	0.76	0.77	0.76	<<0.05*
52.5	202.5	0.87	0.76	1.04	1.24	0.85	0.76	0.77	0.75	<<0.05*
Means		0.85	0.72	0.24	0.51	-0.03	0.83	0.85	0.82	

Regressions that are significant at the 95% confidence level are indicated by an asterisk.

Table B-3. Results of the linear regressions between the zonal components (*U*) of QuikSCAT and NCEP data beginning February 1, 2002.

NCEP Lat	NCEP Lon	r	Rsquared	b0	Upper b0	Lower b0	b1	Upper b1	Lower b1	p-value
70	177.5	0.88	0.78	-1.41	-0.19	-2.63	0.99	1.07	0.91	<<0.05*
70	180	0.85	0.72	-0.98	-0.64	-1.32	0.93	0.96	0.91	<<0.05*
70	182.5	0.88	0.77	-0.83	-0.54	-1.11	0.86	0.87	0.84	<<0.05*
70	185	0.88	0.77	-0.63	-0.40	-0.87	0.82	0.84	0.81	<<0.05*
70	187.5	0.89	0.80	-0.41	-0.20	-0.62	0.82	0.83	0.80	<<0.05*
70	190	0.91	0.82	-0.14	0.07	-0.35	0.83	0.84	0.82	<<0.05*
70	192.5	0.92	0.84	0.17	0.38	-0.04	0.90	0.91	0.89	<<0.05*
70	195	0.92	0.84	0.19	0.42	-0.04	0.99	1.01	0.98	<<0.05*
67.5	187.5	0.70	0.49	-0.11	0.09	-0.31	0.55	0.56	0.54	<<0.05*
67.5	190	0.64	0.42	0.36	0.56	0.17	0.48	0.49	0.47	<<0.05*
67.5	192.5	0.60	0.36	0.48	0.69	0.26	0.46	0.48	0.45	<<0.05*
65	180	0.44	0.19	-1.57	-1.13	-2.01	0.53	0.58	0.48	<<0.05*
65	182.5	0.38	0.14	-1.88	-1.58	-2.18	0.47	0.50	0.45	<<0.05*
65	190	0.51	0.26	-0.13	0.09	-0.35	0.49	0.51	0.48	<<0.05*
65	192.5	0.48	0.23	0.34	0.61	0.07	0.49	0.51	0.47	<<0.05*
62.5	177.5	0.54	0.29	0.13	0.47	-0.22	0.60	0.63	0.57	<<0.05*
62.5	180	0.66	0.43	0.74	0.99	0.49	0.95	0.97	0.93	<<0.05*
62.5	182.5	0.71	0.50	0.27	0.50	0.04	0.98	1.00	0.97	<<0.05*
62.5	185	0.69	0.48	0.07	0.30	-0.16	0.92	0.94	0.90	<<0.05*
62.5	187.5	0.66	0.44	0.09	0.32	-0.13	0.82	0.83	0.80	<<0.05*
62.5	190	0.63	0.40	0.23	0.45	0.01	0.71	0.73	0.69	<<0.05*
62.5	192.5	0.64	0.41	0.39	0.61	0.17	0.72	0.74	0.70	<<0.05*
62.5	195	0.69	0.48	0.60	1.26	-0.06	0.82	0.87	0.76	<<0.05*
60	170	0.69	0.48	-1.05	-0.68	-1.42	1.52	1.56	1.48	<<0.05*
60	172.5	0.67	0.45	-2.09	-1.81	-2.36	1.41	1.44	1.38	<<0.05*
60	175	0.70	0.48	-1.76	-1.52	-2.00	1.12	1.14	1.10	<<0.05*
60	177.5	0.72	0.52	-1.47	-1.23	-1.71	0.98	0.99	0.96	<<0.05*
60	180	0.73	0.54	-1.16	-0.93	-1.39	0.85	0.87	0.84	<<0.05*
60	182.5	0.76	0.57	-0.72	-0.51	-0.93	0.80	0.81	0.79	<<0.05*
60	185	0.74	0.55	-0.24	-0.02	-0.45	0.76	0.78	0.75	<<0.05*
60	187.5	0.73	0.53	-0.12	0.08	-0.32	0.70	0.71	0.69	<<0.05*
60	190	0.73	0.53	0.07	0.26	-0.13	0.72	0.73	0.71	<<0.05*
60	192.5	0.66	0.44	0.15	0.40	-0.10	0.70	0.72	0.69	<<0.05*
60	195	0.60	0.35	0.60	0.92	0.27	0.69	0.71	0.66	<<0.05*
60	197.5	0.53	0.29	0.54	0.99	0.08	0.66	0.70	0.62	<<0.05*
57.5	170	0.77	0.59	0.80	1.03	0.58	0.89	0.90	0.88	<<0.05*
57.5	172.5	0.76	0.58	0.60	0.83	0.37	0.85	0.87	0.84	<<0.05*
57.5	175	0.75	0.56	0.43	0.65	0.20	0.79	0.80	0.78	<<0.05*
57.5	177.5	0.75	0.56	0.32	0.55	0.09	0.75	0.76	0.74	<<0.05*
57.5	180	0.75	0.57	0.18	0.40	-0.05	0.73	0.74	0.72	<<0.05*
57.5	182.5	0.75	0.56	0.13	0.36	-0.09	0.73	0.74	0.72	<<0.05*
57.5	185	0.75	0.56	-0.10	0.12	-0.33	0.74	0.75	0.73	<<0.05*
57.5	187.5	0.74	0.55	-0.21	0.01	-0.43	0.73	0.74	0.72	<<0.05*
57.5	190	0.77	0.59	-0.25	-0.05	-0.45	0.73	0.74	0.72	<<0.05*
57.5	192.5	0.76	0.58	-0.12	0.08	-0.31	0.73	0.74	0.72	<<0.05*
57.5	195	0.78	0.61	0.23	0.42	0.04	0.82	0.83	0.81	<<0.05*

Table B-3 (Continued)

NCEP Lat	NCEP Lon	r	Rsquared	b0	Upper b0	Lower b0	b1	Upper b1	Lower b1	p-value
57.5	197.5	0.78	0.60	0.57	0.77	0.38	0.90	0.91	0.89	<<0.05*
57.5	200	0.75	0.56	1.08	1.29	0.87	0.95	0.96	0.93	<<0.05*
55	170	0.71	0.50	0.57	0.81	0.33	0.67	0.68	0.66	<<0.05*
55	172.5	0.73	0.53	0.47	0.71	0.23	0.72	0.73	0.71	<<0.05*
55	175	0.74	0.55	0.49	0.73	0.26	0.74	0.75	0.72	<<0.05*
55	177.5	0.75	0.57	0.61	0.84	0.38	0.74	0.75	0.73	<<0.05*
55	180	0.75	0.57	0.75	0.97	0.52	0.72	0.73	0.71	<<0.05*
55	182.5	0.78	0.60	0.77	0.98	0.55	0.74	0.75	0.73	<<0.05*
55	185	0.79	0.62	0.83	1.04	0.62	0.75	0.76	0.74	<<0.05*
55	187.5	0.78	0.60	0.87	1.09	0.66	0.74	0.75	0.73	<<0.05*
55	190	0.77	0.60	0.89	1.10	0.68	0.72	0.73	0.71	<<0.05*
55	192.5	0.77	0.59	0.86	1.07	0.65	0.72	0.73	0.71	<<0.05*
55	195	0.79	0.63	0.83	1.02	0.63	0.72	0.73	0.71	<<0.05*
55	200	0.70	0.50	1.83	2.46	1.20	0.71	0.74	0.67	<<0.05*
55	202.5	0.75	0.57	1.60	1.82	1.38	0.79	0.80	0.78	<<0.05*
52.5	170	0.72	0.52	0.97	1.23	0.71	0.77	0.78	0.75	<<0.05*
52.5	172.5	0.71	0.50	0.88	1.14	0.61	0.74	0.75	0.72	<<0.05*
52.5	175	0.75	0.57	0.51	0.75	0.27	0.76	0.77	0.75	<<0.05*
52.5	177.5	0.78	0.60	0.64	0.87	0.41	0.76	0.77	0.75	<<0.05*
52.5	180	0.76	0.58	0.80	1.02	0.57	0.72	0.73	0.71	<<0.05*
52.5	182.5	0.78	0.60	0.94	1.16	0.72	0.71	0.72	0.71	<<0.05*
52.5	185	0.79	0.63	0.92	1.12	0.72	0.68	0.68	0.67	<<0.05*
52.5	187.5	0.81	0.65	0.97	1.17	0.77	0.70	0.71	0.69	<<0.05*
52.5	190	0.74	0.55	1.62	1.85	1.39	0.69	0.70	0.68	<<0.05*
52.5	192.5	0.77	0.59	1.73	1.96	1.50	0.75	0.76	0.74	<<0.05*
52.5	195	0.77	0.59	1.49	1.71	1.26	0.74	0.75	0.73	<<0.05*
52.5	197.5	0.79	0.62	1.44	1.65	1.23	0.74	0.75	0.73	<<0.05*
52.5	200	0.79	0.63	1.59	1.80	1.39	0.74	0.75	0.73	<<0.05*
52.5	202.5	0.79	0.62	1.52	1.72	1.31	0.73	0.73	0.72	<<0.05*
Means		0.73	0.54	0.26	0.52	0.00	0.77	0.79	0.76	

Regressions that are significant at the 95% confidence level are indicated by an asterisk.

Table B-4. Results of the linear regressions between the meridional components (V) of QuikSCAT and NCEP data beginning February 1, 2002.

NCEP Lat	NCEP Lon	r	Rsquared	b0	Upper b0	Lower b0	b1	Upper b1	Lower b1	p-value
70	177.5	0.83	0.70	-0.04	1.01	-1.09	0.72	0.80	0.65	<<0.05*
70	180	0.80	0.64	-0.50	-0.19	-0.81	0.68	0.70	0.66	<<0.05*
70	182.5	0.88	0.78	0.09	0.38	-0.20	0.82	0.84	0.81	<<0.05*
70	185	0.91	0.83	0.19	0.42	-0.04	0.85	0.86	0.84	<<0.05*
70	187.5	0.92	0.85	0.25	0.46	0.05	0.83	0.84	0.82	<<0.05*
70	190	0.93	0.87	0.18	0.38	-0.02	0.83	0.84	0.82	<<0.05*
70	192.5	0.91	0.84	-0.11	0.10	-0.31	0.85	0.86	0.84	<<0.05*
70	195	0.87	0.76	-0.55	-0.33	-0.77	0.80	0.81	0.78	<<0.05*
67.5	187.5	0.87	0.76	-0.34	-0.16	-0.53	0.79	0.80	0.78	<<0.05*
67.5	190	0.85	0.72	-0.53	-0.34	-0.72	0.81	0.82	0.80	<<0.05*
67.5	192.5	0.80	0.63	-0.66	-0.42	-0.89	0.83	0.85	0.82	<<0.05*
65	180	0.69	0.47	0.31	0.72	-0.11	0.67	0.70	0.63	<<0.05*
65	182.5	0.83	0.69	0.16	0.41	-0.09	0.94	0.95	0.92	<<0.05*
65	190	0.82	0.67	-0.84	-0.62	-1.07	0.80	0.82	0.79	<<0.05*
65	192.5	0.81	0.65	-0.82	-0.57	-1.08	0.83	0.84	0.81	<<0.05*
62.5	177.5	0.71	0.50	-0.48	-0.16	-0.79	0.61	0.63	0.59	<<0.05*
62.5	180	0.82	0.67	0.19	0.43	-0.06	1.09	1.11	1.08	<<0.05*
62.5	182.5	0.86	0.75	0.78	0.96	0.60	0.92	0.93	0.92	<<0.05*
62.5	185	0.85	0.73	0.49	0.65	0.33	0.79	0.79	0.78	<<0.05*
62.5	187.5	0.85	0.72	-0.03	0.15	-0.20	0.79	0.79	0.78	<<0.05*
62.5	190	0.83	0.69	-0.43	-0.24	-0.61	0.80	0.81	0.79	<<0.05*
62.5	192.5	0.80	0.64	-0.53	-0.33	-0.74	0.86	0.87	0.85	<<0.05*
62.5	195	0.81	0.65	-0.19	0.43	-0.82	1.01	1.06	0.96	<<0.05*
60	170	0.65	0.42	-0.54	-0.29	-0.79	0.80	0.82	0.78	<<0.05*
60	172.5	0.78	0.60	-0.18	0.02	-0.38	1.18	1.20	1.17	<<0.05*
60	175	0.85	0.73	0.44	0.62	0.27	1.11	1.12	1.10	<<0.05*
60	177.5	0.86	0.75	0.69	0.86	0.52	0.94	0.95	0.93	<<0.05*
60	180	0.87	0.75	0.56	0.73	0.39	0.87	0.88	0.87	<<0.05*
60	182.5	0.88	0.77	0.21	0.37	0.05	0.81	0.82	0.81	<<0.05*
60	185	0.87	0.75	-0.11	0.05	-0.27	0.80	0.81	0.80	<<0.05*
60	187.5	0.85	0.73	-0.55	-0.40	-0.71	0.77	0.78	0.77	<<0.05*
60	190	0.86	0.74	-0.66	-0.50	-0.82	0.84	0.85	0.83	<<0.05*
60	192.5	0.83	0.69	-0.59	-0.38	-0.80	0.87	0.89	0.86	<<0.05*
60	195	0.80	0.63	-0.43	-0.12	-0.75	1.00	1.02	0.98	<<0.05*
60	197.5	0.77	0.59	-0.50	-0.06	-0.94	1.07	1.10	1.04	<<0.05*
57.5	170	0.84	0.71	0.54	0.70	0.38	0.87	0.88	0.86	<<0.05*
57.5	172.5	0.85	0.71	0.98	1.14	0.82	0.84	0.85	0.83	<<0.05*
57.5	175	0.86	0.74	1.02	1.17	0.86	0.81	0.81	0.80	<<0.05*
57.5	177.5	0.86	0.74	0.78	0.94	0.62	0.77	0.78	0.76	<<0.05*
57.5	180	0.87	0.75	0.54	0.70	0.38	0.77	0.78	0.76	<<0.05*
57.5	182.5	0.88	0.78	0.27	0.43	0.12	0.82	0.82	0.81	<<0.05*
57.5	185	0.88	0.78	-0.06	0.09	-0.21	0.87	0.87	0.86	<<0.05*
57.5	187.5	0.89	0.79	-0.20	-0.05	-0.35	0.89	0.90	0.88	<<0.05*
57.5	190	0.89	0.79	-0.47	-0.33	-0.62	0.85	0.86	0.84	<<0.05*
57.5	192.5	0.88	0.77	-0.43	-0.28	-0.58	0.84	0.85	0.84	<<0.05*
57.5	195	0.86	0.74	-0.39	-0.24	-0.55	0.86	0.87	0.85	<<0.05*

Table B-4 (Continued)

NCEP Lat	NCEP Lon	r	Rsquared	b0	Upper b0	Lower b0	b1	Upper b1	Lower b1	p-value
57.5	197.5	0.83	0.69	-0.52	-0.36	-0.68	0.88	0.89	0.87	<<0.05*
57.5	200	0.78	0.60	-0.59	-0.43	-0.74	0.81	0.82	0.80	<<0.05*
55	170	0.87	0.75	0.09	0.25	-0.06	0.81	0.82	0.80	<<0.05*
55	172.5	0.87	0.75	0.12	0.28	-0.04	0.82	0.83	0.82	<<0.05*
55	175	0.87	0.76	0.15	0.31	0.00	0.82	0.83	0.81	<<0.05*
55	177.5	0.88	0.78	0.03	0.18	-0.11	0.82	0.83	0.81	<<0.05*
55	180	0.89	0.79	-0.06	0.08	-0.21	0.82	0.83	0.81	<<0.05*
55	182.5	0.90	0.80	-0.03	0.11	-0.18	0.82	0.83	0.82	<<0.05*
55	185	0.90	0.81	0.17	0.31	0.03	0.83	0.84	0.83	<<0.05*
55	187.5	0.90	0.81	0.42	0.57	0.28	0.84	0.85	0.83	<<0.05*
55	190	0.90	0.80	0.43	0.57	0.28	0.82	0.83	0.81	<<0.05*
55	192.5	0.88	0.78	0.39	0.54	0.24	0.79	0.80	0.78	<<0.05*
55	195	0.88	0.78	0.35	0.50	0.20	0.79	0.79	0.78	<<0.05*
55	200	0.80	0.65	0.38	0.83	-0.06	0.75	0.78	0.73	<<0.05*
55	202.5	0.84	0.71	1.17	1.32	1.01	0.89	0.90	0.88	<<0.05*
52.5	170	0.87	0.75	-0.11	0.05	-0.27	0.80	0.81	0.79	<<0.05*
52.5	172.5	0.85	0.72	-0.04	0.12	-0.20	0.74	0.75	0.73	<<0.05*
52.5	175	0.88	0.78	0.25	0.41	0.10	0.80	0.81	0.80	<<0.05*
52.5	177.5	0.90	0.80	0.28	0.42	0.14	0.79	0.80	0.79	<<0.05*
52.5	180	0.89	0.80	0.13	0.28	-0.02	0.80	0.81	0.80	<<0.05*
52.5	182.5	0.88	0.78	0.22	0.37	0.07	0.80	0.81	0.79	<<0.05*
52.5	185	0.89	0.79	0.31	0.45	0.16	0.79	0.80	0.79	<<0.05*
52.5	187.5	0.90	0.80	0.34	0.49	0.20	0.80	0.81	0.79	<<0.05*
52.5	190	0.86	0.75	0.32	0.49	0.16	0.77	0.78	0.76	<<0.05*
52.5	192.5	0.87	0.75	0.24	0.40	0.08	0.79	0.80	0.78	<<0.05*
52.5	195	0.87	0.76	0.39	0.55	0.23	0.79	0.80	0.79	<<0.05*
52.5	197.5	0.88	0.78	0.63	0.78	0.47	0.79	0.79	0.78	<<0.05*
52.5	200	0.87	0.77	0.69	0.84	0.54	0.78	0.79	0.77	<<0.05*
52.5	202.5	0.87	0.75	0.79	0.94	0.64	0.77	0.78	0.76	<<0.05*
Means		0.85	0.73	0.06	0.27	-0.15	0.83	0.85	0.82	

Regressions that are significant at the 95% confidence level are indicated by an asterisk.

Table B-5. The regression slopes and intercepts of the linear regressions between the zonal components (*U*) of QuikSCAT and NCEP data before February 1, 2002.

NCEP Lat	NCEP Lon	Intercept	Slope	NCEP Lat	NCEP Lon	Intercept	Slope
70	177.5	0	0	57.5	197.5	>0*	<1*
70	180	0*	1*	57.5	200	>0*	<1*
70	182.5	<0*	<1*	55	170	>0*	<1*
70	185	<0*	<1*	55	172.5	>0*	<1*
70	187.5	<0*	<1*	55	175	>0*	<1*
70	190	0*	<1*	55	177.5	>0*	<1*
70	192.5	0*	<1*	55	180	>0*	<1*
70	195	0*	>1*	55	182.5	>0*	<1*
67.5	187.5	0*	<1*	55	185	>0*	<1*
67.5	190	0*	<1*	55	187.5	>0*	<1*
67.5	192.5	0*	<1*	55	190	>0*	<1*
65	180	<0*	<1*	55	192.5	>0*	<1*
65	182.5	<0*	<1*	55	195	>0*	<1*
65	190	<0*	<1*	55	200	>0*	<1*
65	192.5	0*	<1*	55	202.5	>0*	<1*
62.5	177.5	0*	<1*	52.5	170	>0*	<1*
62.5	180	>0*	1*	52.5	172.5	>0*	<1*
62.5	182.5	0*	1*	52.5	175	>0*	<1*
62.5	185	<0*	<1*	52.5	177.5	>0*	<1*
62.5	187.5	<0*	<1*	52.5	180	>0*	<1*
62.5	190	<0*	<1*	52.5	182.5	>0*	<1*
62.5	192.5	0*	<1*	52.5	185	>0*	<1*
62.5	195	0*	<1*	52.5	187.5	>0*	<1*
60	170	0*	>1*	52.5	190	>0*	<1*
60	172.5	<0*	>1*	52.5	192.5	>0*	<1*
60	175	<0*	>1*	52.5	195	>0*	<1*
60	177.5	<0*	1*	52.5	197.5	>0*	<1*
60	180	<0*	<1*	52.5	200	>0*	<1*
60	182.5	0*	<1*	52.5	202.5	>0*	<1*
60	185	0*	<1*				
60	187.5	0*	<1*				
60	190	0*	<1*				
60	192.5	0*	<1*				
60	195	>0*	<1*				
60	197.5	>0*	<1*				
57.5	170	>0*	<1*				
57.5	172.5	>0*	<1*				
57.5	175	>0*	<1*				
57.5	177.5	>0*	<1*				
57.5	180	>0*	<1*				
57.5	182.5	>0*	<1*				
57.5	185	>0*	<1*				
57.5	187.5	>0*	<1*				
57.5	190	0*	<1*				
57.5	192.5	>0*	<1*				
57.5	195	>0*	<1*				

Regressions that are significant at the 95% confidence level are indicated by an asterisk.

Table B-6. The regression slopes and intercepts of the linear regressions between the meridional components (*V*) of QuikSCAT and NCEP data before February 1, 2002.

NCEP Lon	Intercept	Slope	NCEP Lat	NCEP Lon	Intercept	Slope
177.5	0	0	57.5	197.5	<0*	<1*
180	0*	<1*	57.5	200	<0*	<1*
182.5	0*	<1*	55	170	>0*	<1*
185	0*	<1*	55	172.5	0*	<1*
187.5	>0*	<1*	55	175	>0*	<1*
190	>0*	<1*	55	177.5	>0*	<1*
192.5	0*	<1*	55	180	>0*	<1*
195	<0*	<1*	55	182.5	>0*	<1*
187.5	0*	<1*	55	185	>0*	<1*
190	0*	<1*	55	187.5	>0*	<1*
192.5	0*	<1*	55	190	>0*	<1*
180	0*	<1*	55	192.5	>0*	<1*
182.5	>0*	<1*	55	195	>0*	<1*
190	<0*	<1*	55	200	0*	<1*
192.5	0*	<1*	55	202.5	>0*	<1*
177.5	0*	<1*	52.5	170	0*	<1*
180	0*	>1*	52.5	172.5	0*	<1*
182.5	>0*	<1*	52.5	175	>0*	<1*
185	>0*	<1*	52.5	177.5	>0*	<1*
187.5	>0*	<1*	52.5	180	>0*	<1*
190	>0*	<1*	52.5	182.5	0*	<1*
192.5	0*	<1*	52.5	185	0*	<1*
195	0*	<1*	52.5	187.5	0*	<1*
170	<0*	<1*	52.5	190	0*	<1*
172.5	0*	>1*	52.5	192.5	>0*	<1*
175	>0*	>1*	52.5	195	>0*	<1*
177.5	>0*	1*	52.5	197.5	>0*	<1*
180	>0*	<1*	52.5	200	>0*	<1*
182.5	>0*	<1*	52.5	202.5	>0*	<1*
185	>0*	<1*				
187.5	0*	<1*				
190	0*	<1*				
192.5	0*	<1*				
195	0*	<1*				
197.5	0*	>1*				
170	>0*	<1*				
172.5	>0*	<1*				
175	>0*	<1*				
177.5	>0*	<1*				
180	>0*	<1*				
182.5	>0*	<1*				
185	>0*	<1*				
187.5	0*	<1*				
190	0*	<1*				
192.5	<0*	<1*				
195	<0*	<1*				

Regressions that are significant at the 95% confidence level are indicated by an asterisk.

Table B-7. The regression slopes and intercepts of the linear regressions between the zonal components (*U*) of QuikSCAT and NCEP data beginning February 1, 2002.

NCEP Lat	NCEP Lon	Intercept	Slope	NCEP Lat	NCEP Lon	Intercept	Slope
70	177.5	<0*	1*	57.5	197.5	>0*	<1*
70	180	<0*	<1*	57.5	200	>0*	<1*
70	182.5	<0*	<1*	55	170	>0*	<1*
70	185	<0*	<1*	55	172.5	>0*	<1*
70	187.5	<0*	<1*	55	175	>0*	<1*
70	190	0*	<1*	55	177.5	>0*	<1*
70	192.5	0*	<1*	55	180	>0*	<1*
70	195	0*	1*	55	182.5	>0*	<1*
67.5	187.5	0*	<1*	55	185	>0*	<1*
67.5	190	>0*	<1*	55	187.5	>0*	<1*
67.5	192.5	>0*	<1*	55	190	>0*	<1*
65	180	<0*	<1*	55	192.5	>0*	<1*
65	182.5	<0*	<1*	55	195	>0*	<1*
65	190	0*	<1*	55	200	>0*	<1*
65	192.5	>0*	<1*	55	202.5	>0*	<1*
62.5	177.5	0*	<1*	52.5	170	>0*	<1*
62.5	180	>0*	<1*	52.5	172.5	>0*	<1*
62.5	182.5	>0*	1*	52.5	175	>0*	<1*
62.5	185	0*	<1*	52.5	177.5	>0*	<1*
62.5	187.5	0*	<1*	52.5	180	>0*	<1*
62.5	190	>0*	<1*	52.5	182.5	>0*	<1*
62.5	192.5	>0*	<1*	52.5	185	>0*	<1*
62.5	195	>0*	<1*	52.5	187.5	>0*	<1*
60	170	<0*	>1*	52.5	190	>0*	<1*
60	172.5	<0*	>1*	52.5	192.5	>0*	<1*
60	175	<0*	>1*	52.5	195	>0*	<1*
60	177.5	<0*	<1*	52.5	197.5	>0*	<1*
60	180	<0*	<1*	52.5	200	>0*	<1*
60	182.5	<0*	<1*	52.5	202.5	>0*	<1*
60	185	<0*	<1*				
60	187.5	0*	<1*				
60	190	0*	<1*				
60	192.5	0*	<1*				
60	195	>0*	<1*				
60	197.5	>0*	<1*				
57.5	170	>0*	<1*				
57.5	172.5	>0*	<1*				
57.5	175	>0*	<1*				
57.5	177.5	>0*	<1*				
57.5	180	0*	<1*				
57.5	182.5	0*	<1*				
57.5	185	0*	<1*				
57.5	187.5	0*	<1*				
57.5	190	<0*	<1*				
57.5	192.5	0*	<1*				
57.5	195	>0*	<1*				

Regressions that are significant at the 95% confidence level are indicated by an asterisk.

Table B-8. The regression slopes and intercepts of the linear regressions between the meridional components (*V*) of QuikSCAT and NCEP beginning February 1, 2002.

NCEP Lon	Intercept	Slope	NCEP Lat	NCEP Lon	Intercept	Slope
177.5	0*	<1*	57.5	197.5	<0*	<1*
180	<0*	<1*	57.5	200	<0*	<1*
182.5	0*	<1*	55	170	0*	<1*
185	0*	<1*	55	172.5	0*	<1*
187.5	0*	<1*	55	175	0*	<1*
190	0*	<1*	55	177.5	0*	<1*
192.5	0*	<1*	55	180	0*	<1*
195	<0*	<1*	55	182.5	0*	<1*
187.5	<0*	<1*	55	185	>0*	<1*
190	<0*	<1*	55	187.5	>0*	<1*
192.5	<0*	<1*	55	190	>0*	<1*
180	0*	<1*	55	192.5	>0*	<1*
182.5	0*	<1*	55	195	>0*	<1*
190	<0*	<1*	55	200	0*	<1*
192.5	<0*	<1*	55	202.5	>0*	<1*
177.5	<0*	<1*	52.5	170	0*	<1*
180	0*	>1*	52.5	172.5	0*	<1*
182.5	>0*	<1*	52.5	175	>0*	<1*
185	>0*	<1*	52.5	177.5	>0*	<1*
187.5	0*	<1*	52.5	180	0*	<1*
190	<0*	<1*	52.5	182.5	>0*	<1*
192.5	<0*	<1*	52.5	185	>0*	<1*
195	0*	1*	52.5	187.5	>0*	<1*
170	<0*	<1*	52.5	190	>0*	<1*
172.5	0*	>1*	52.5	192.5	>0*	<1*
175	>0*	>1*	52.5	195	>0*	<1*
177.5	>0*	<1*	52.5	197.5	>0*	<1*
180	>0*	<1*	52.5	200	>0*	<1*
182.5	>0*	<1*	52.5	202.5	>0*	<1*
185	0*	<1*				
187.5	<0*	<1*				
190	<0*	<1*				
192.5	<0*	<1*				
195	<0*	1*				
197.5	<0*	>1*				
170	>0*	<1*				
172.5	>0*	<1*				
175	>0*	<1*				
177.5	>0*	<1*				
180	>0*	<1*				
182.5	>0*	<1*				
185	0*	<1*				
187.5	<0*	<1*				
190	<0*	<1*				
192.5	<0*	<1*				
195	<0*	<1*				

Regressions that are significant at the 95% confidence level are indicated by an asterisk.

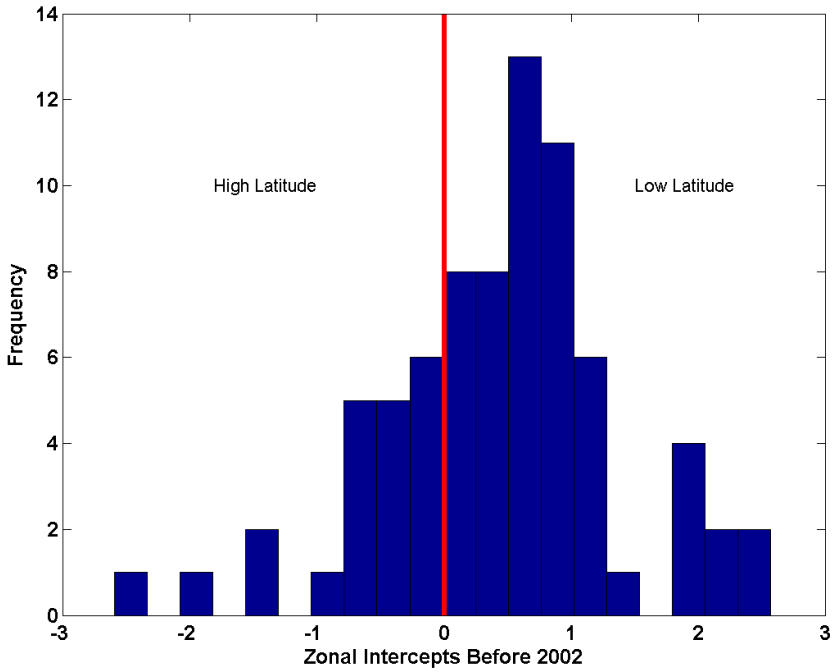

Figure B-1. A histogram of the linear regression intercepts (b0) for the zonal components of the QuikSCAT and NCEP data sets before February 1, 2002.

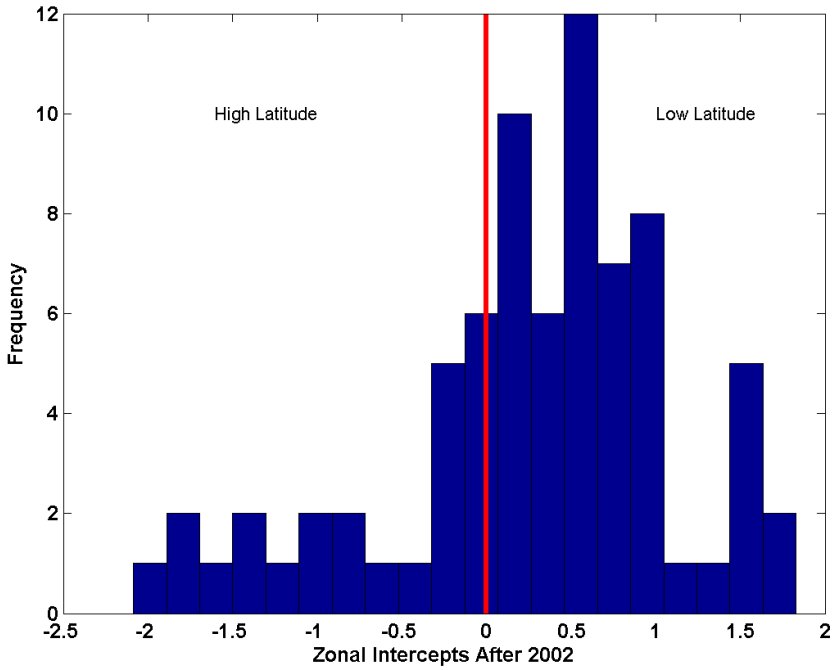

Figure B-2. A histogram of the linear regression intercepts (b_0) for the zonal components of the QuikSCAT and NCEP data sets beginning February 1, 2002.

Appendix C

Monthly Climatologies

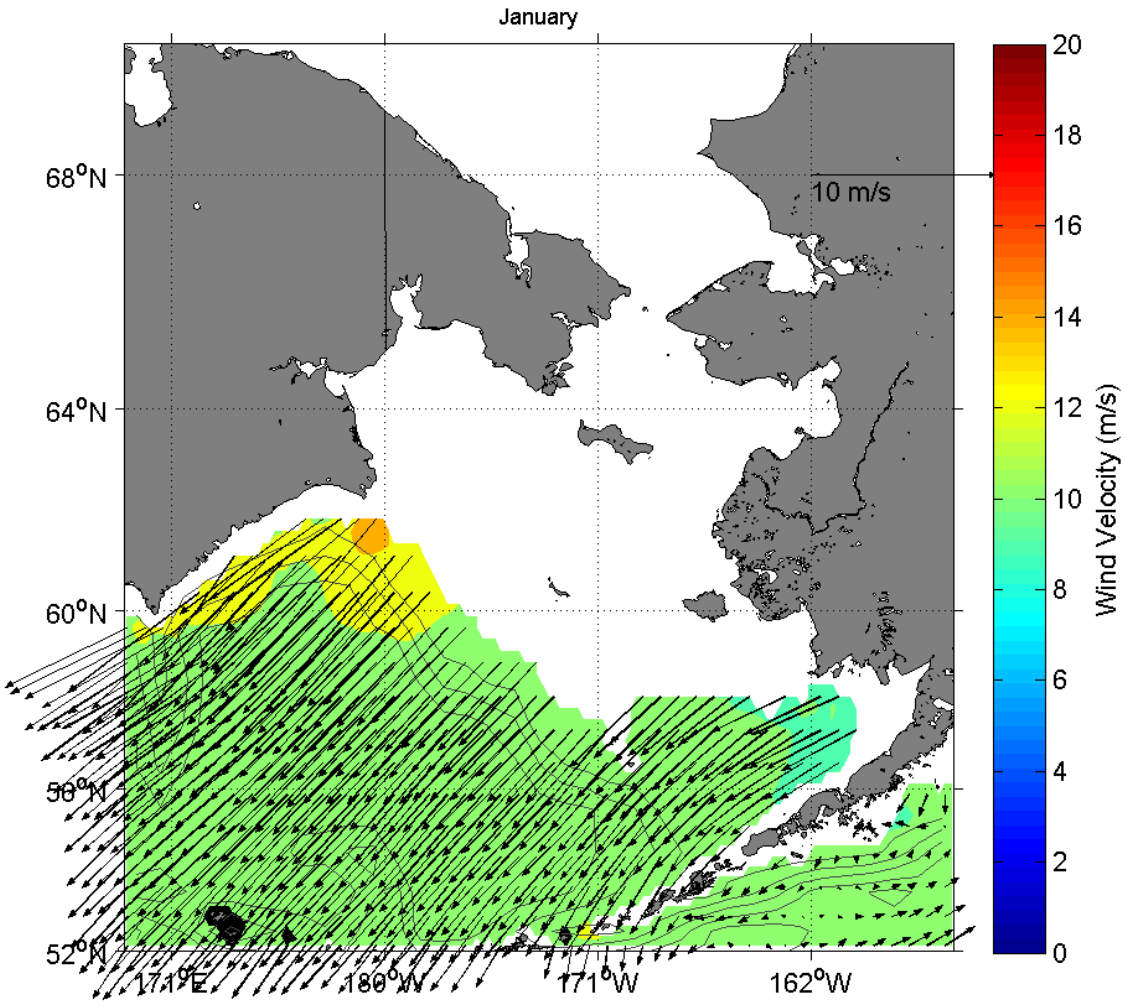

Figure C-1. Monthly mean winds for **January.** Every third vector is plotted. Means are based upon data collected every 12 hours.

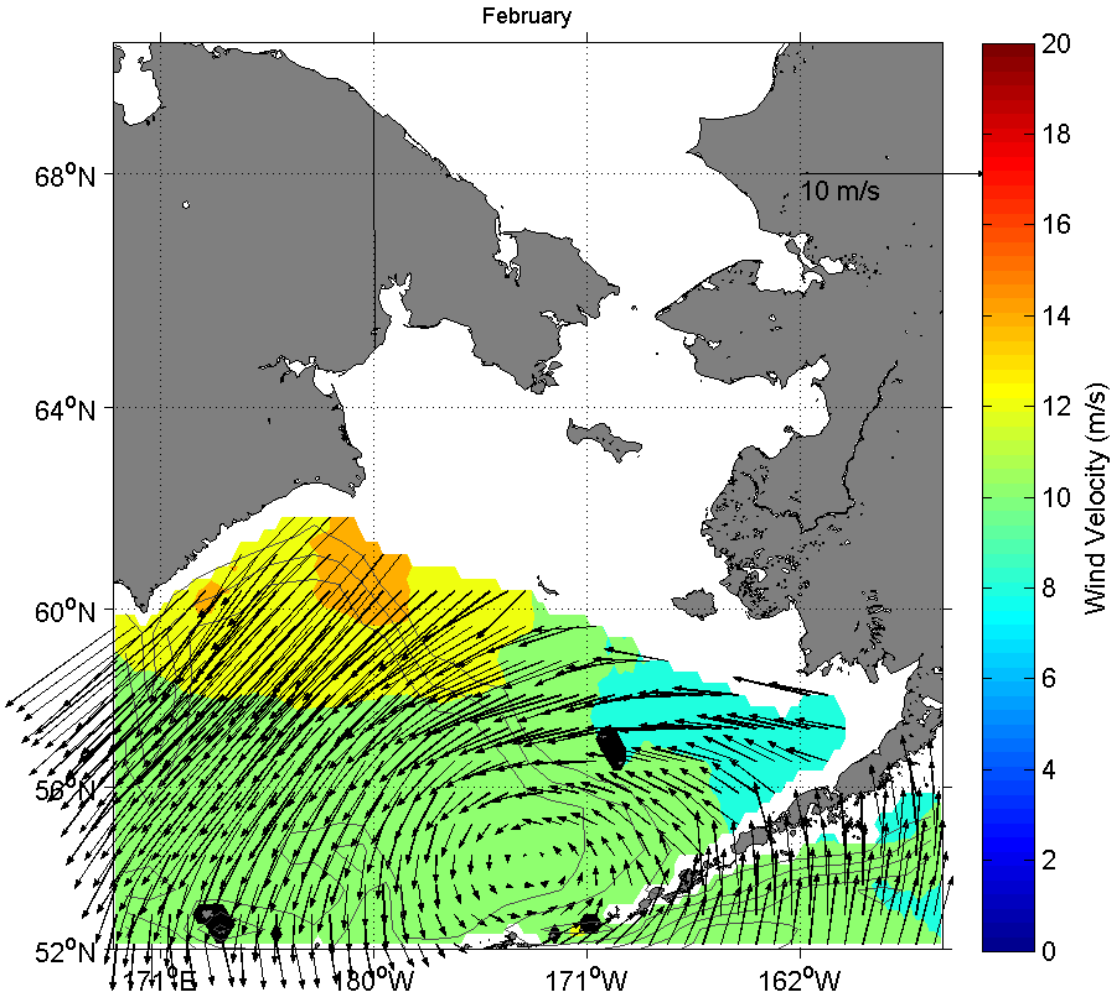

Figure C-2. Monthly mean winds for February. Every third vector is plotted. Means are based upon data collected every 12 hours.

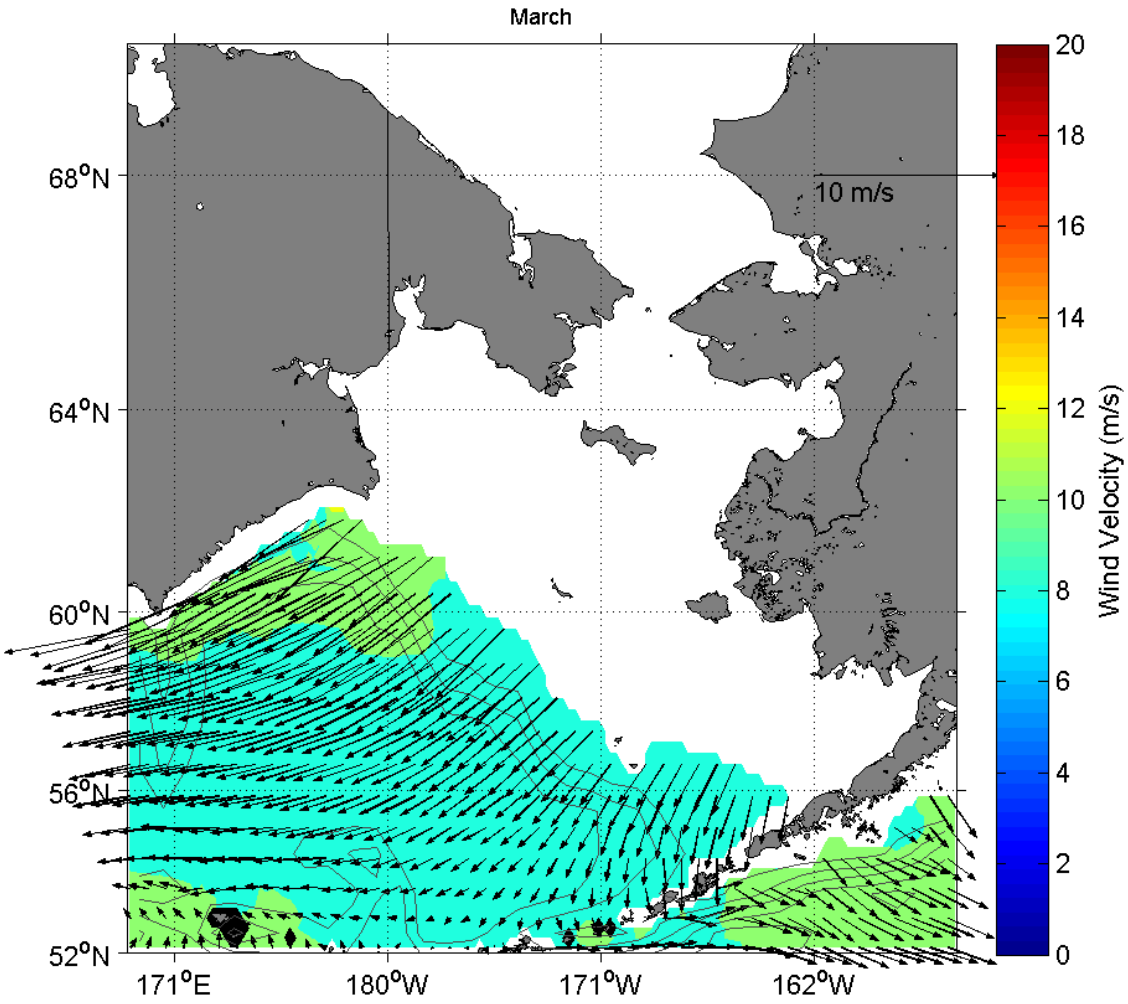

Figure C-3. Monthly mean **winds for March.** Every third vector is plotted. Means are based upon data collected every 12 hours.

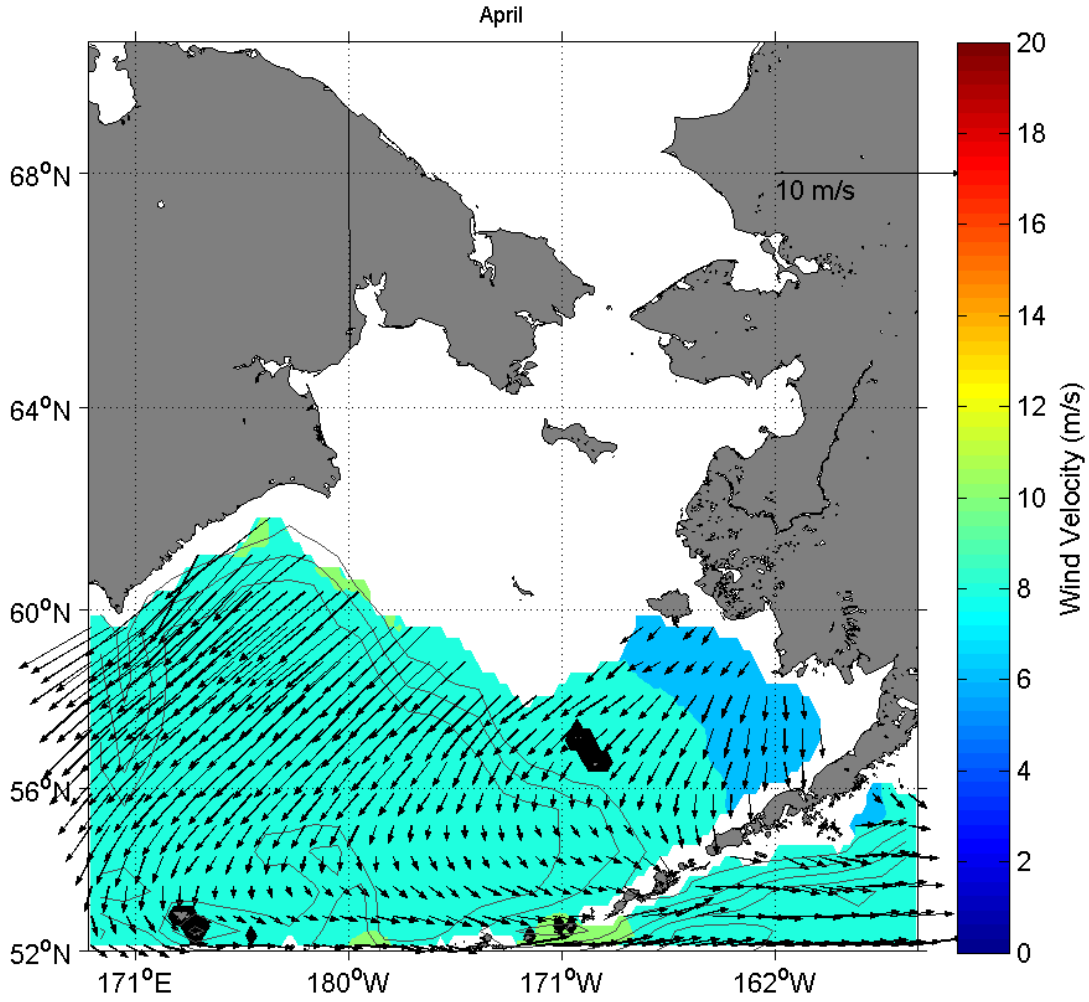

Figure C-4. Monthly mean winds for April. Every third vector is plotted. Means are based upon data collected every 12 hours.

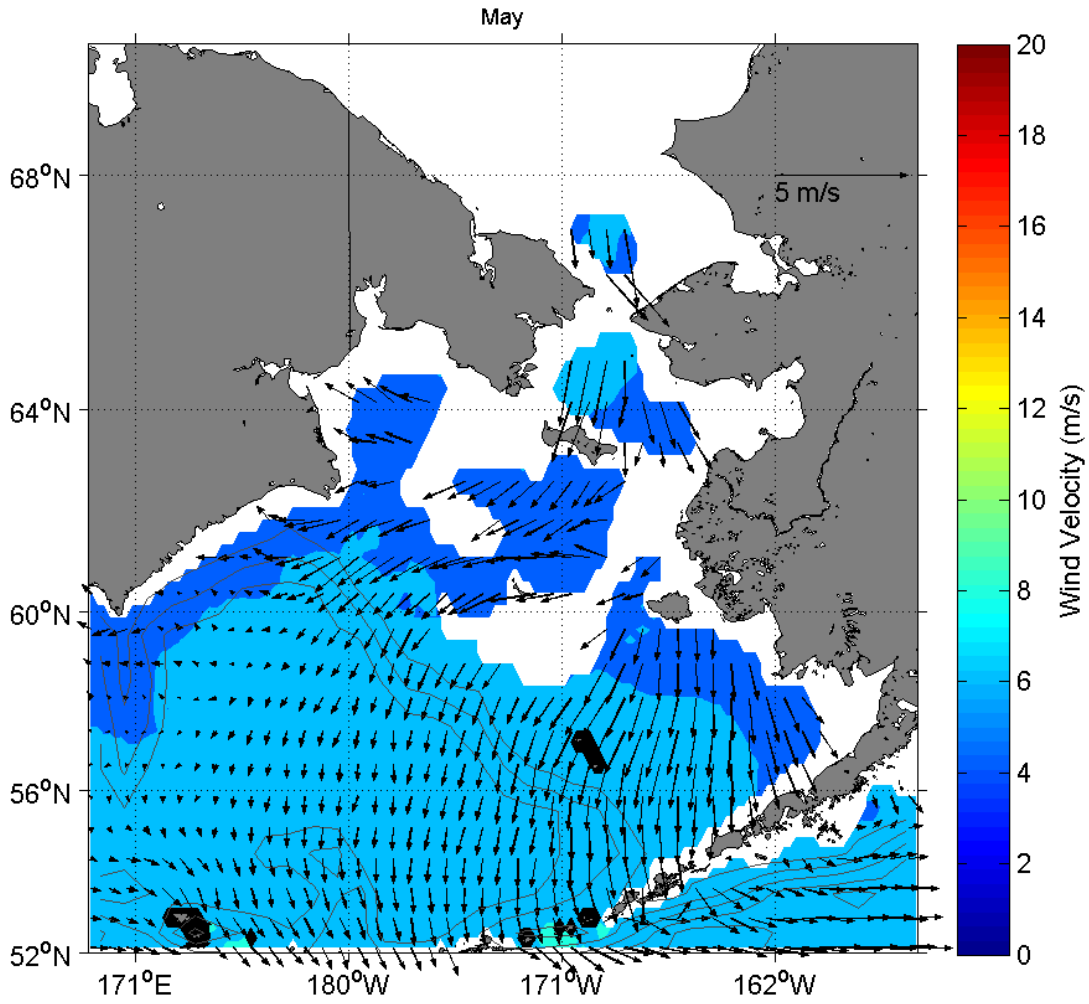

Figure C-5. Monthly **mean winds for May.** Every third vector is plotted. Means are based upon data collected every 12 hours.

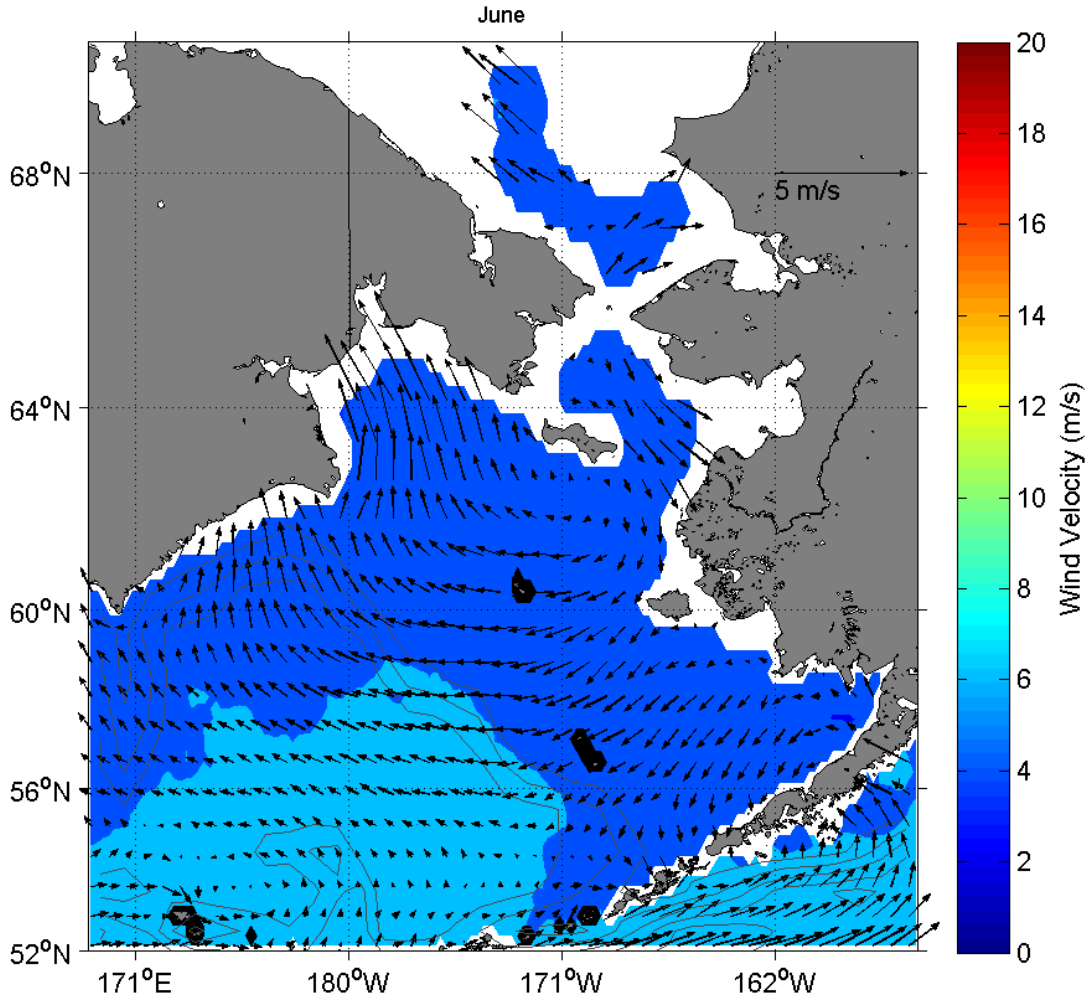

Figure C-6. Monthly mean winds for June. Every third vector is plotted. Means are based upon data collected every 12 hours.

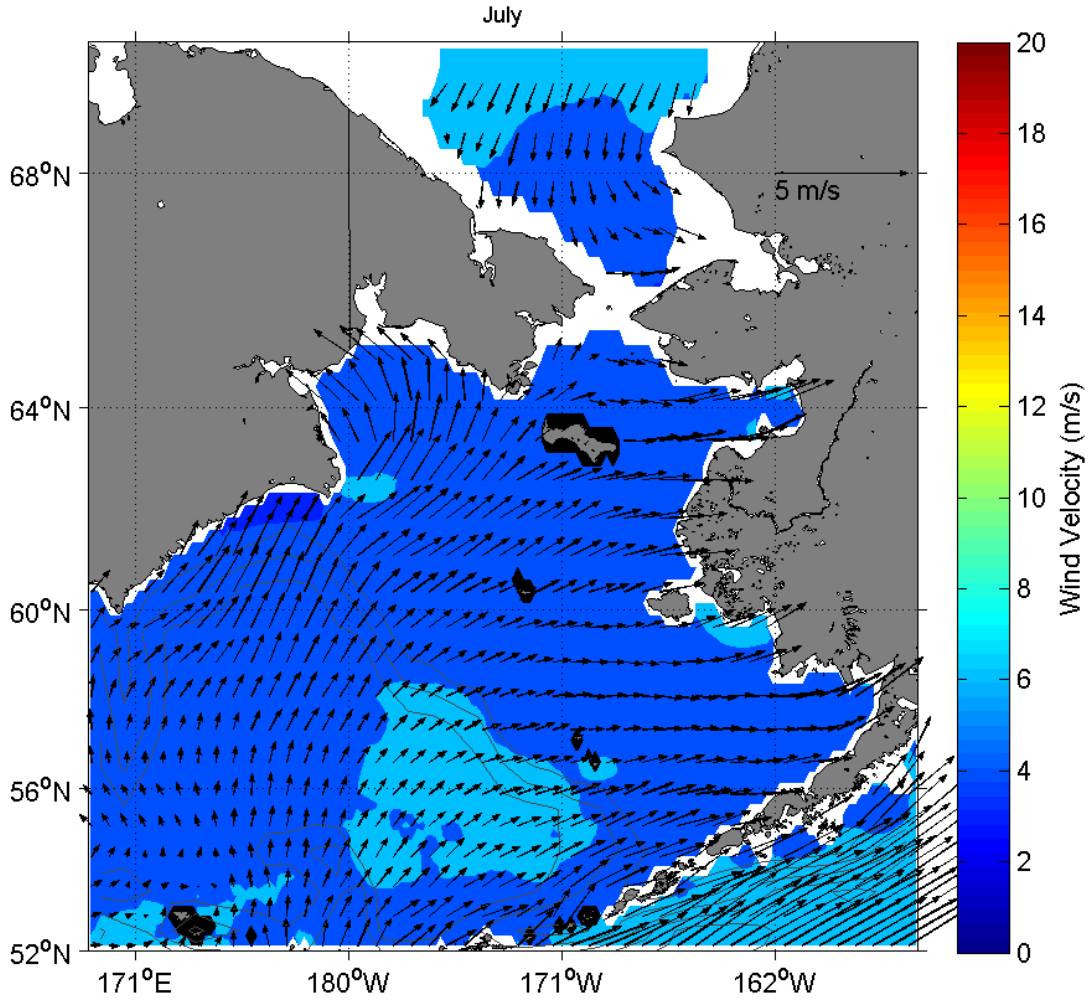

Figure C-7. Mon**thly mean winds for July.** Every third vector is plotted. Means are based upon data collected every 12 hours.

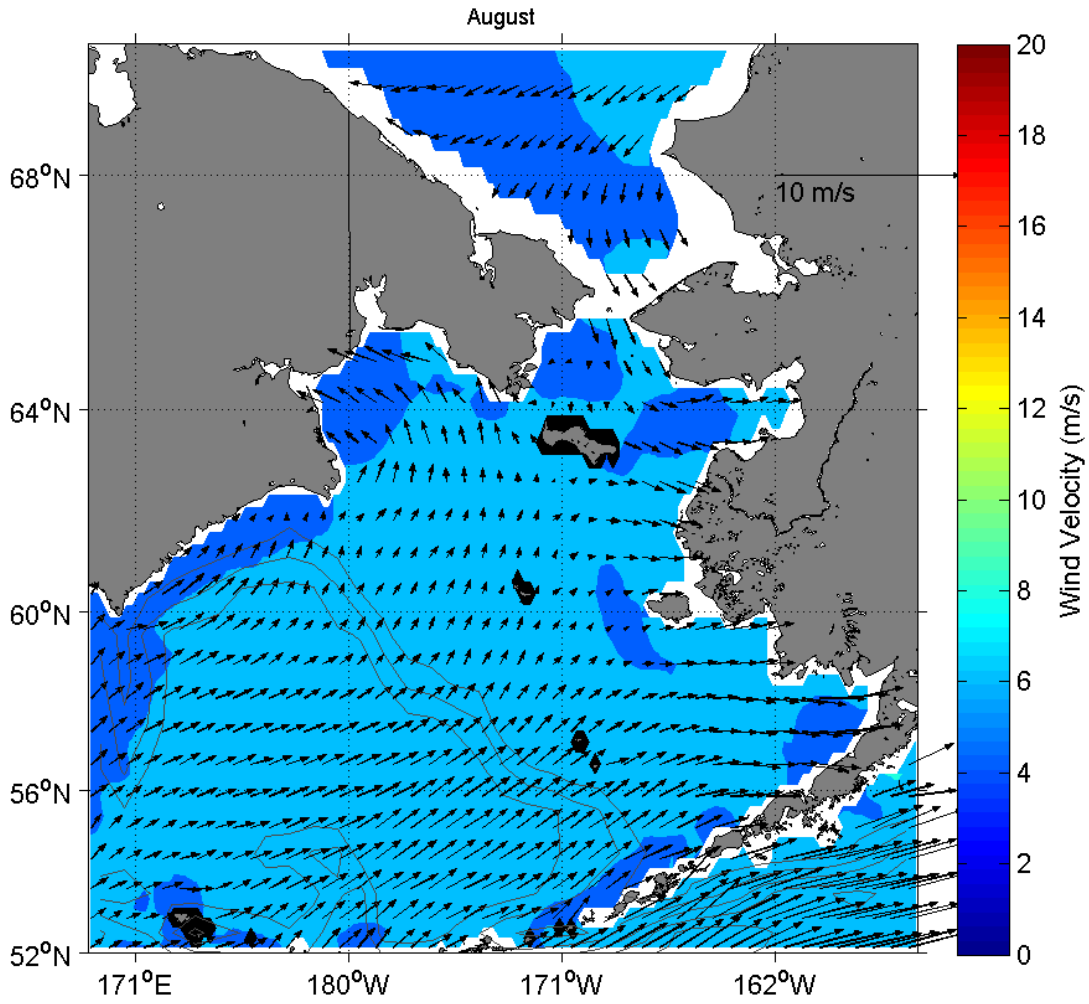

Figure C-8. Monthly mean winds for August. Every third vector is plotted. Means are based upon data collected every 12 hours.

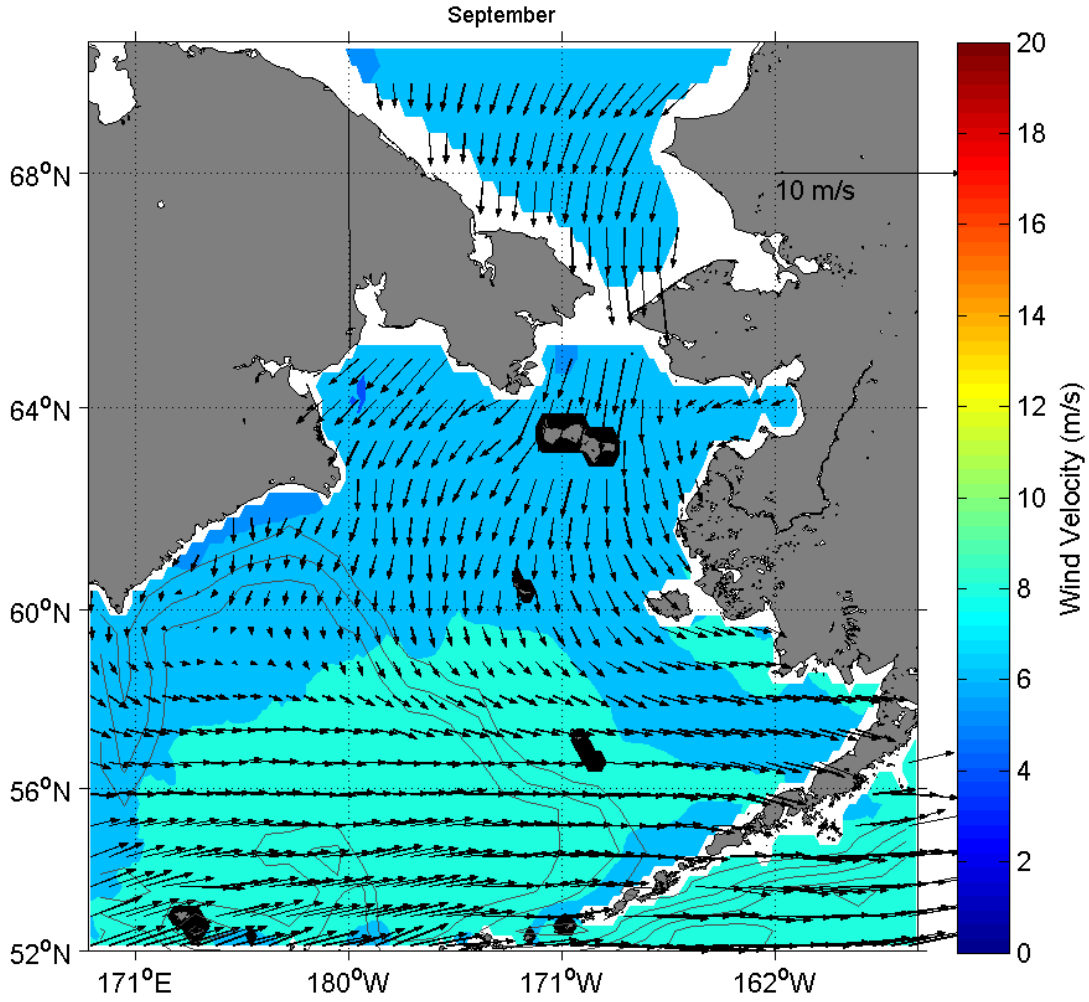

Figure C-9. Monthly mean winds for September. Every third vector is plotted. Means are based upon data collected every 12 hours.

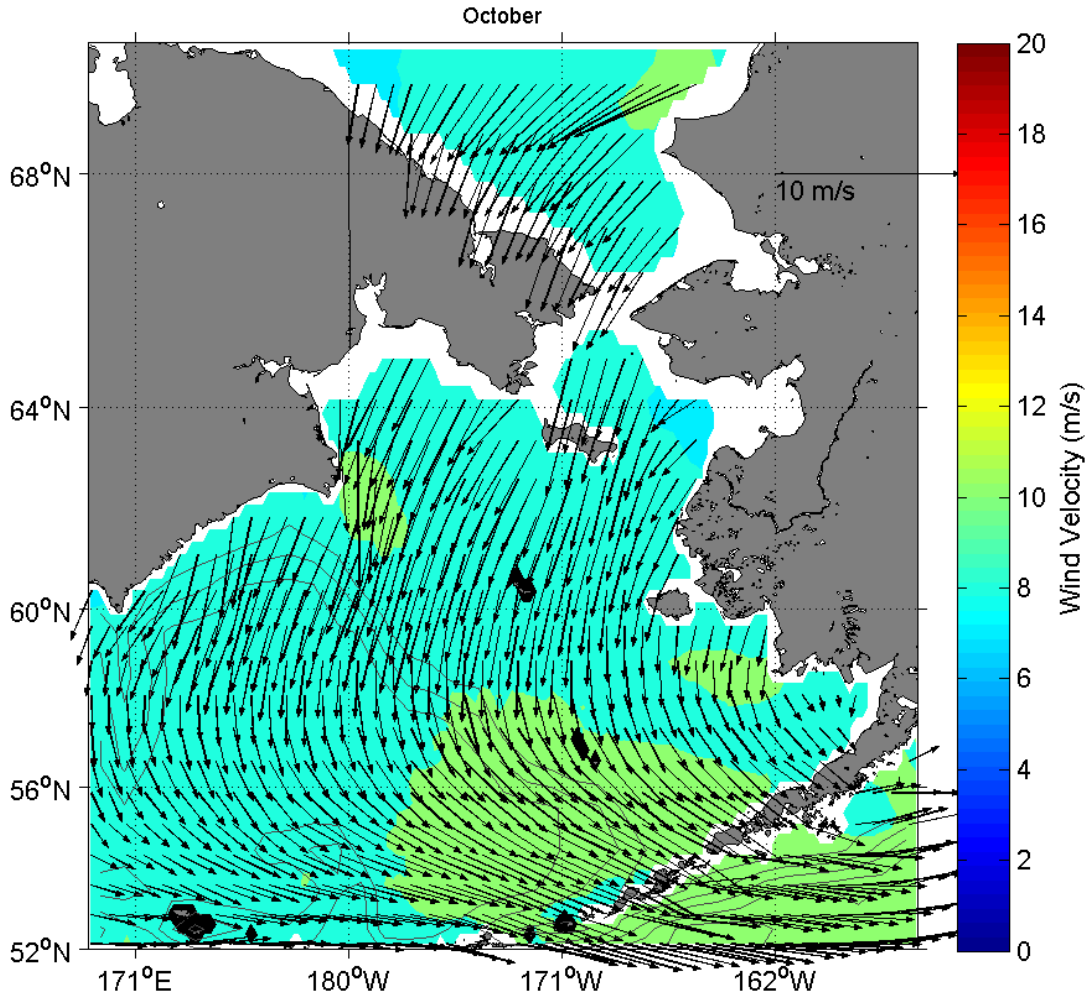

Figure C-10. Monthly mean winds for October. Every third vector is plotted. Means are based upon data collected every 12 hours.

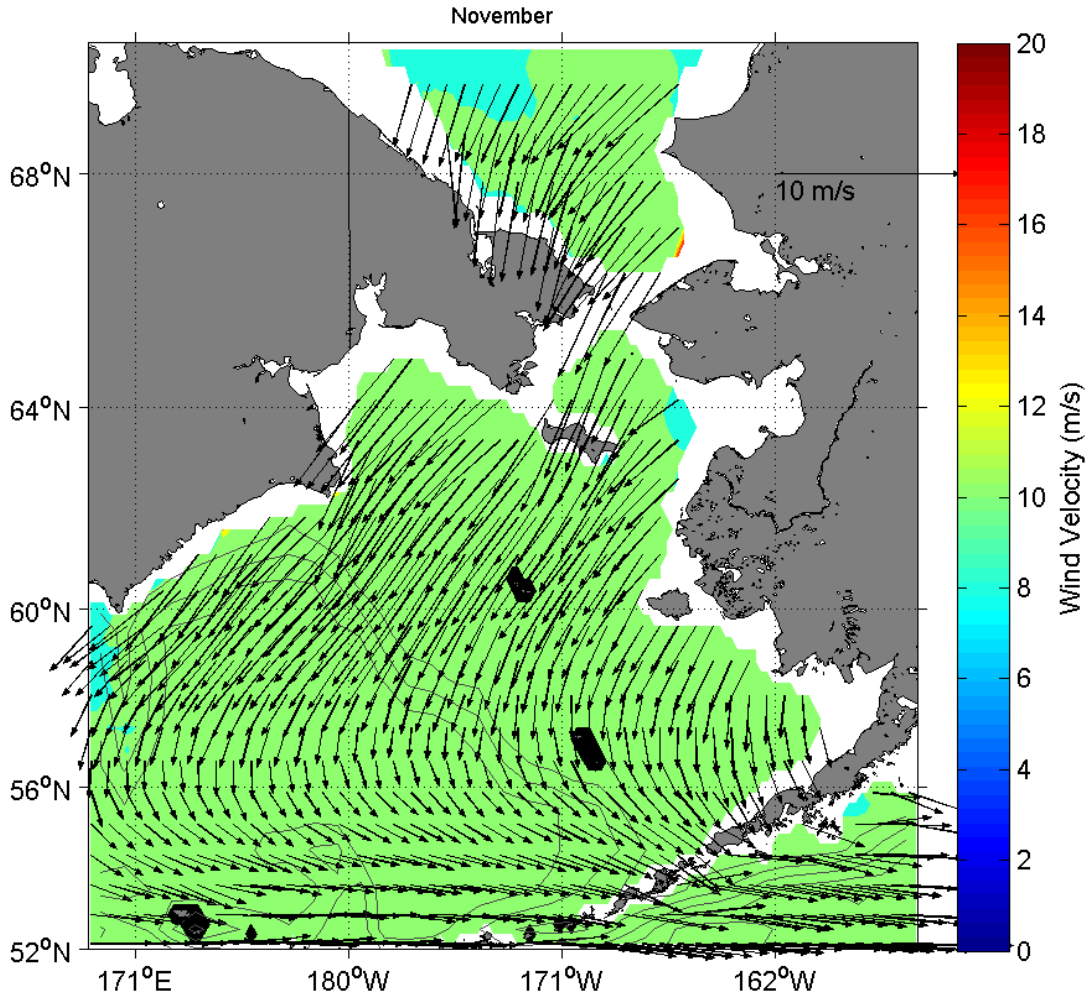

Figure C-11. Monthly mean winds for November. Every third vector is plotted. Means are based upon data collected every 12 hours.

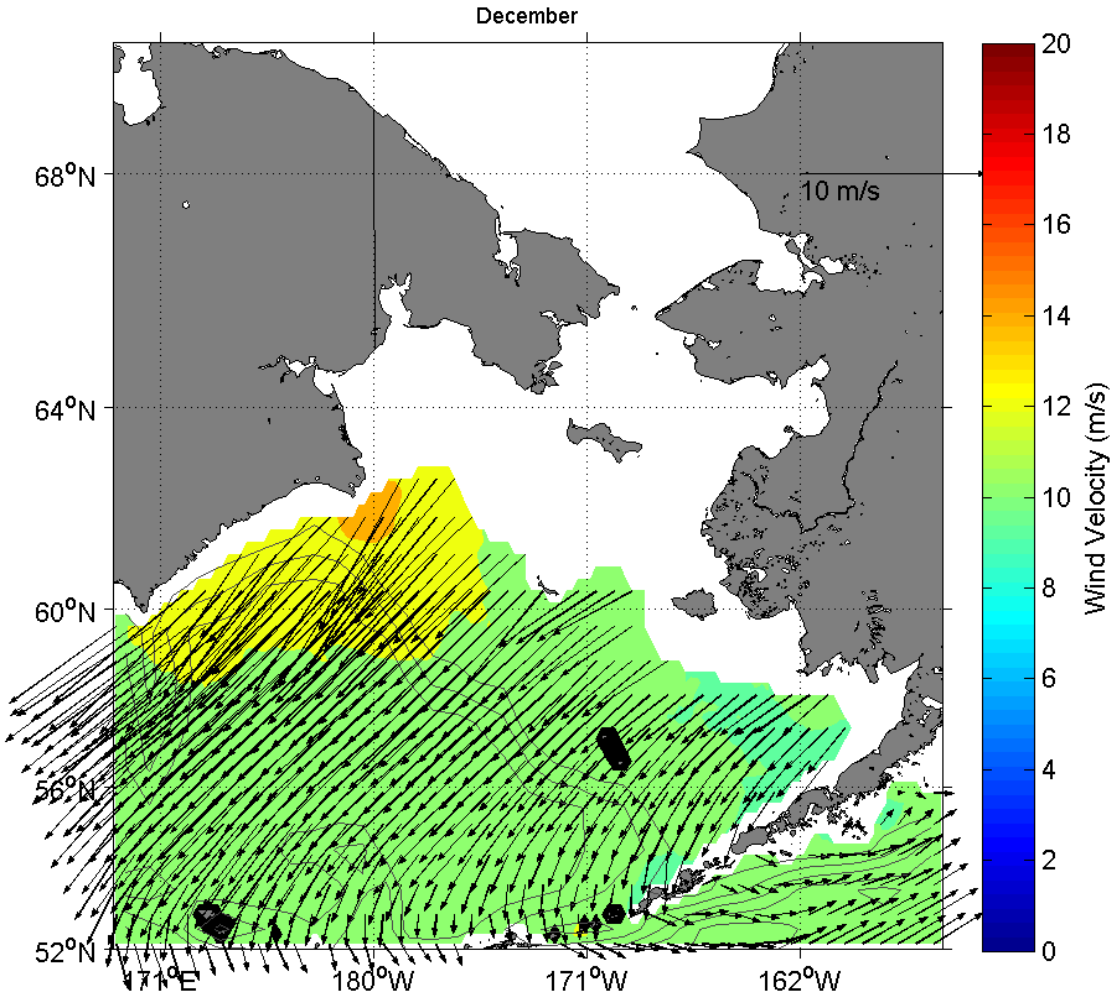

Figure C-12. Monthly mean winds for December. Every third vector is plotted. Means are based upon data collected every 12 hours.

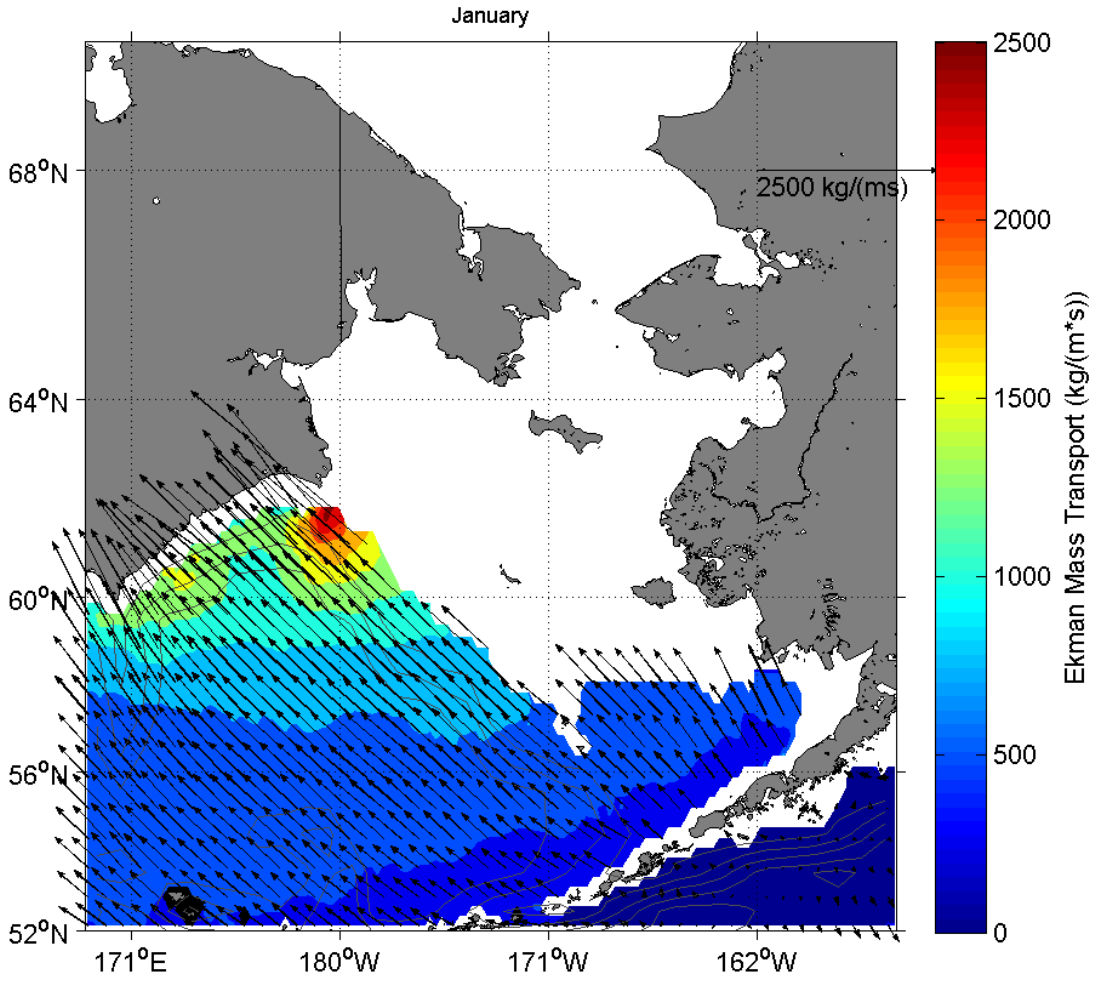

Figure C-13. Monthly mean Ekman transport for January. Every third vector is plotted. Means are based upon data collected every 12 hours.

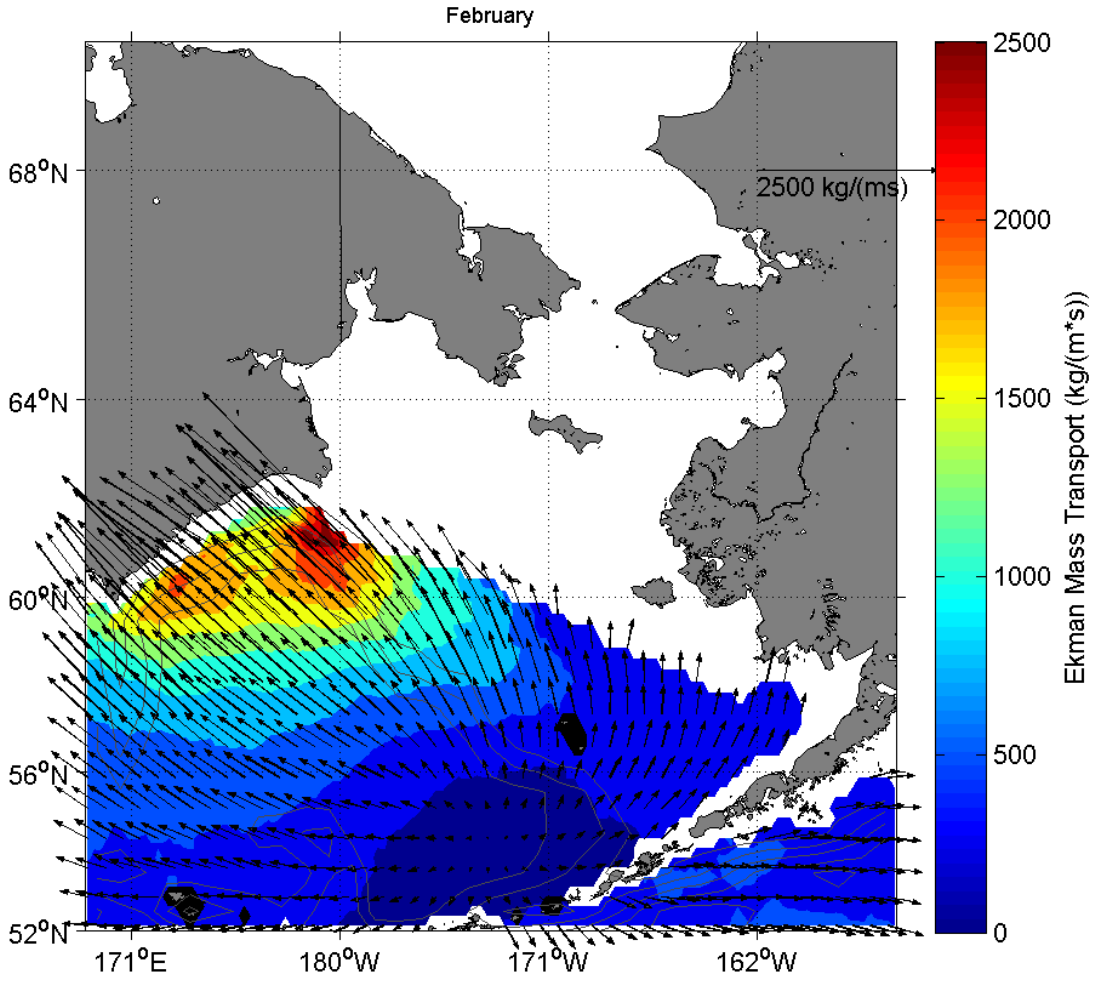

Figure C-14. Monthly mean Ekman transport for February. Every third vector is plotted. Means are based upon data collected every 12 hours.

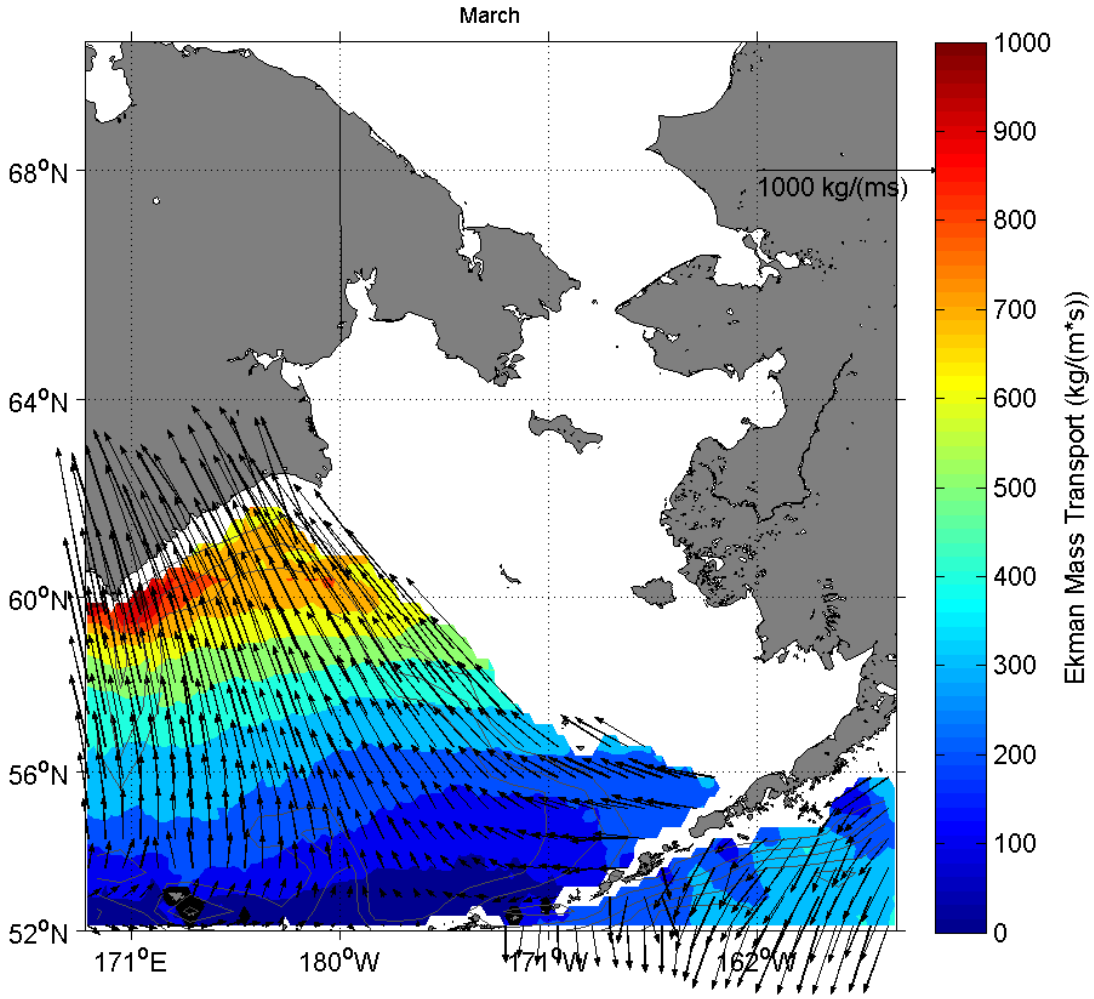

Figure C-15. Monthly mean Ekman transport for March. Every third vector is plotted. Means are based upon data collected every 12 hours.

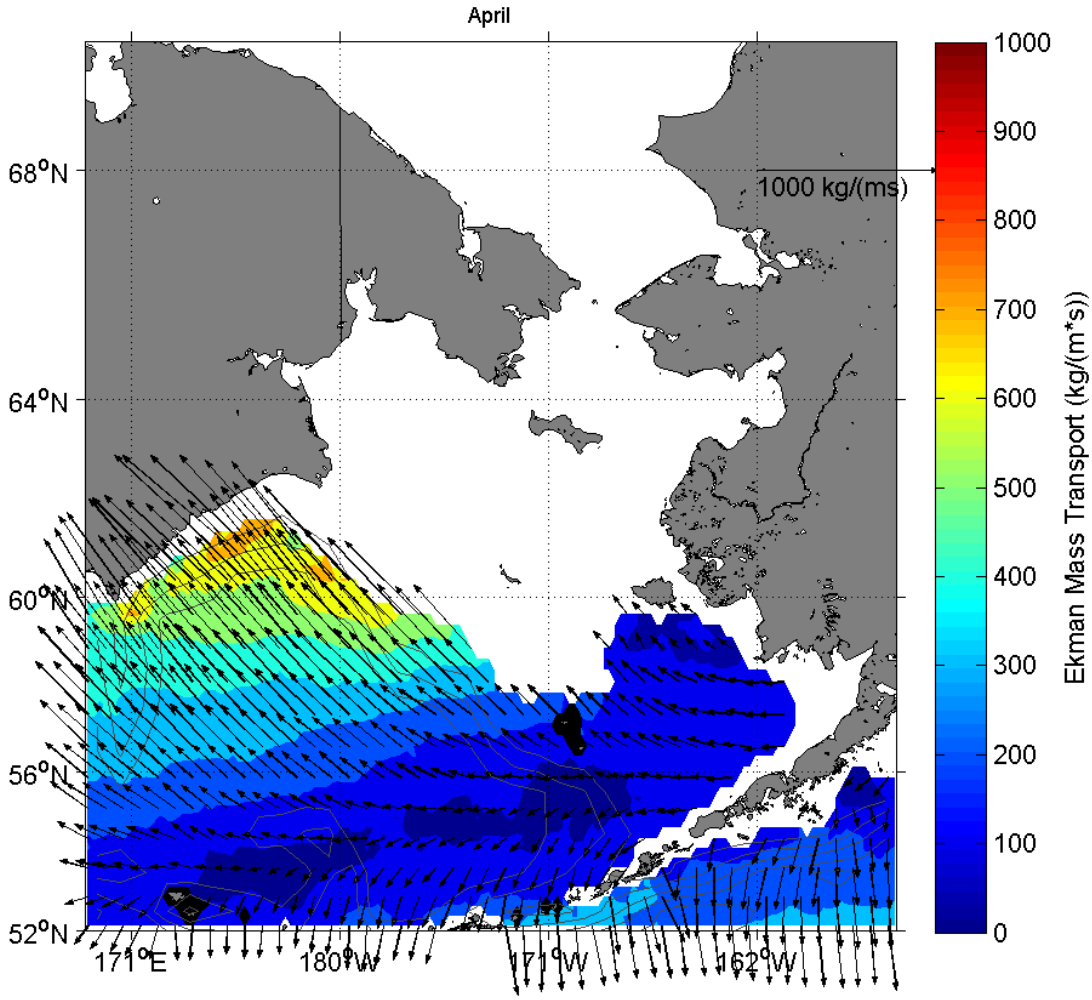

Figure C-16. Monthly mean Ekman transport for April. Every third vector is plotted. Means are based upon data collected every 12 hours.

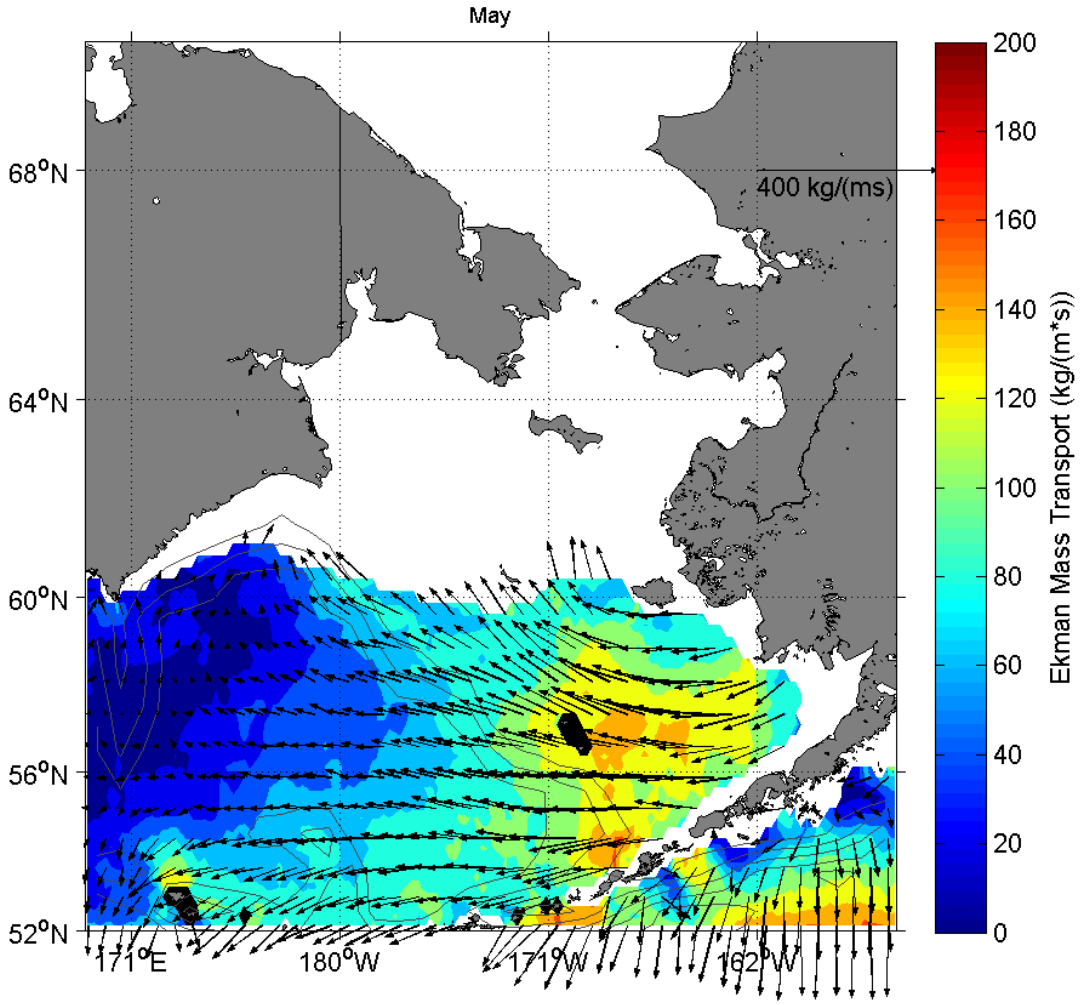

Figure C-17. Monthly mean Ekman transport for May. Every third vector is plotted. Means are based upon data collected every 12 hours.

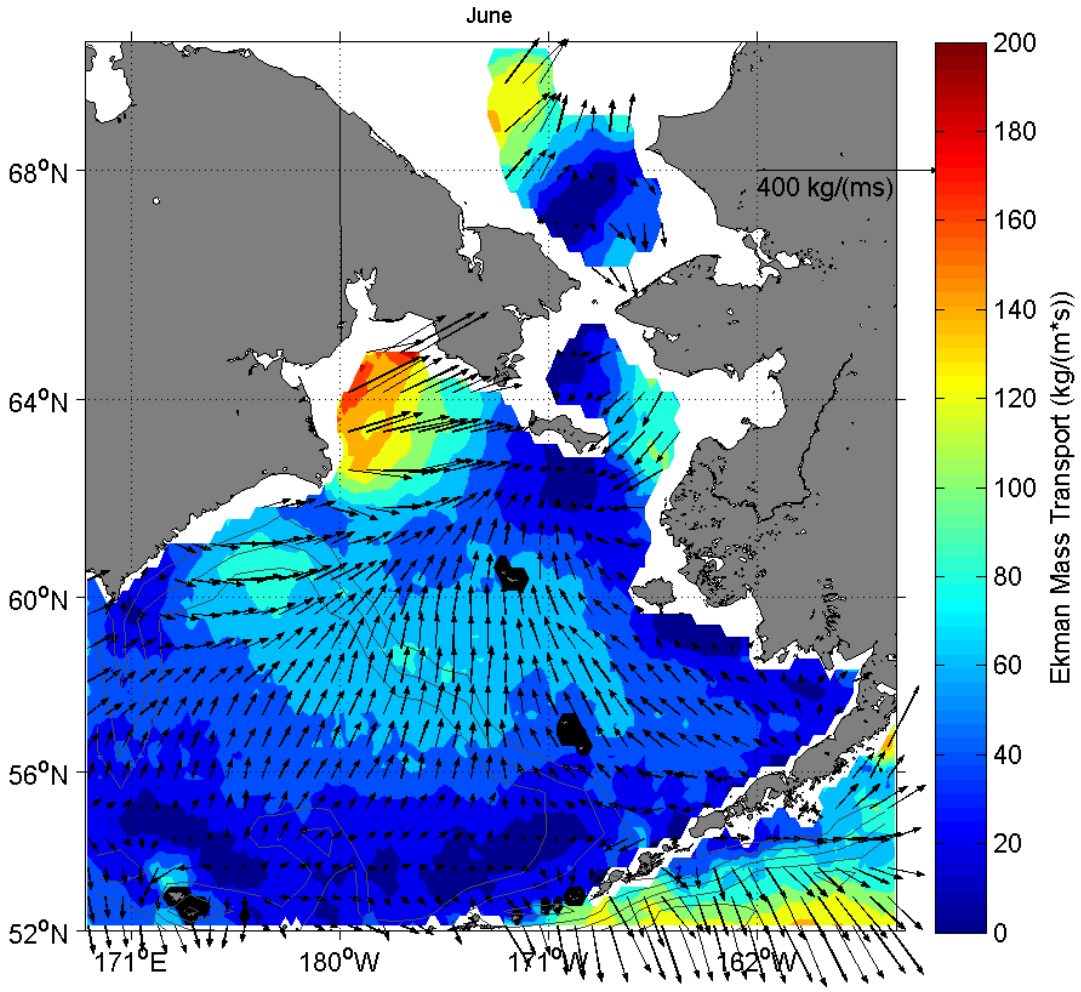

Figure C-18. Monthly mean Ekman trans**port for June.** Every third vector is plotted. Means are based upon data collected every 12 hours.

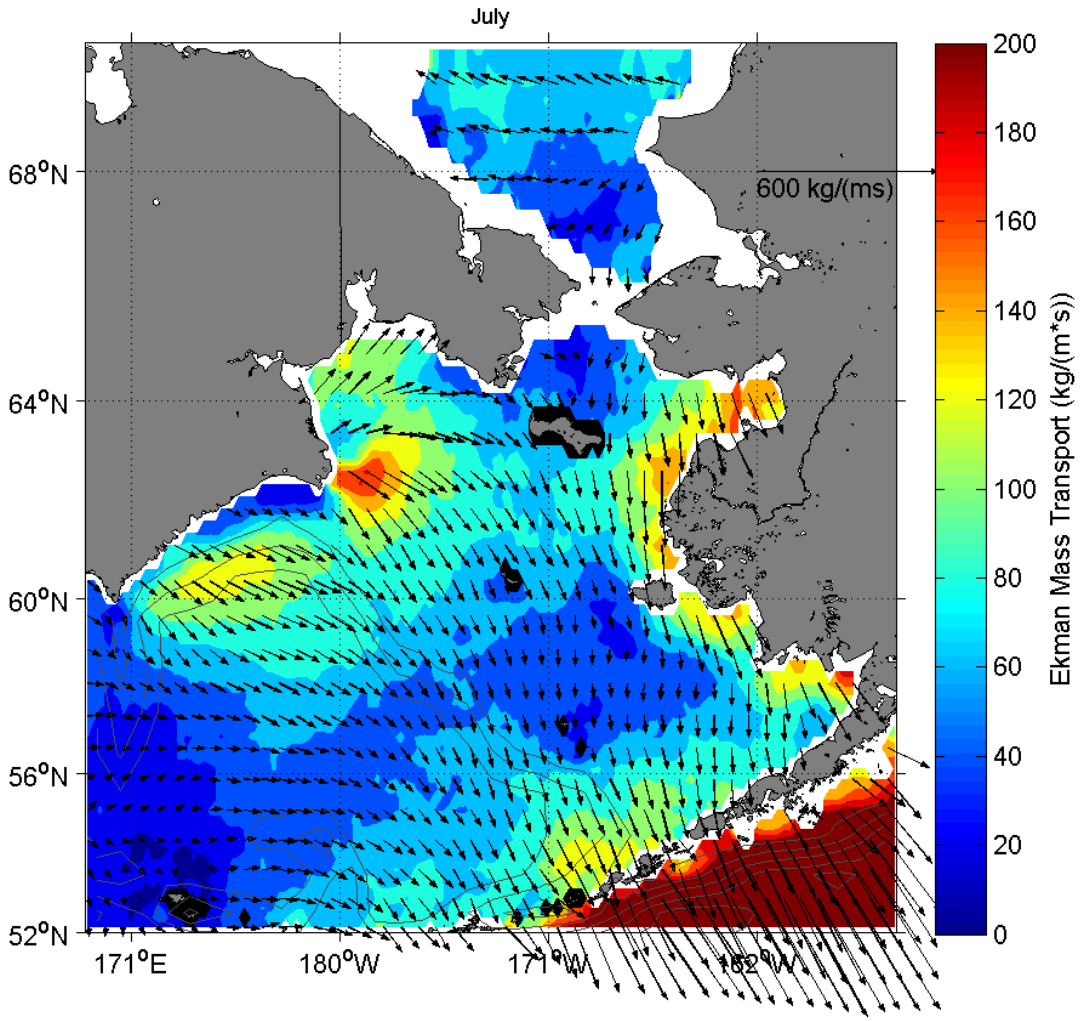

Figure C-19. Monthly mean Ekman transport for July. Every third vector is plotted. Means are based upon data collected every 12 hours.

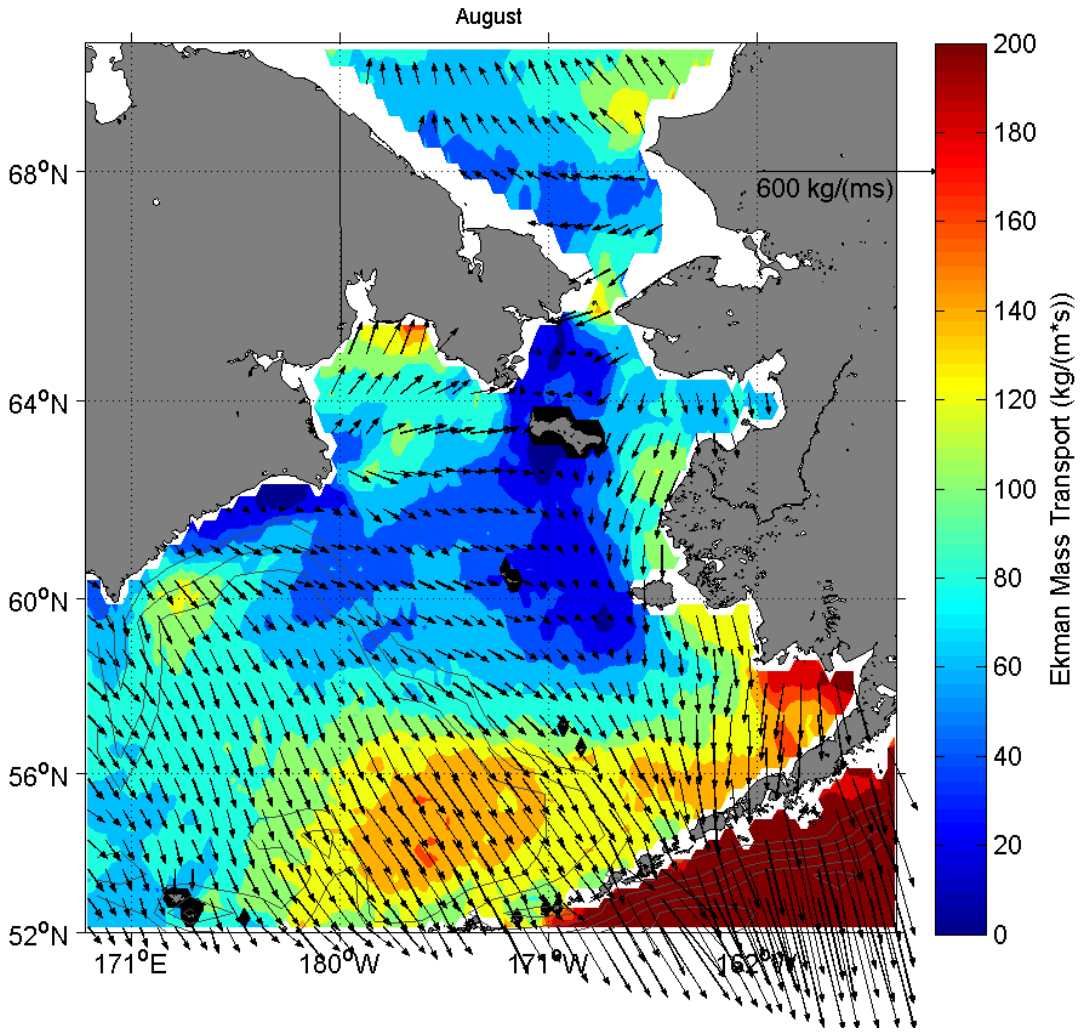

Figure C-20. Monthly mean Ekman transport for August. Every third vector is plotted. Means are based upon data collected every 12 hours.

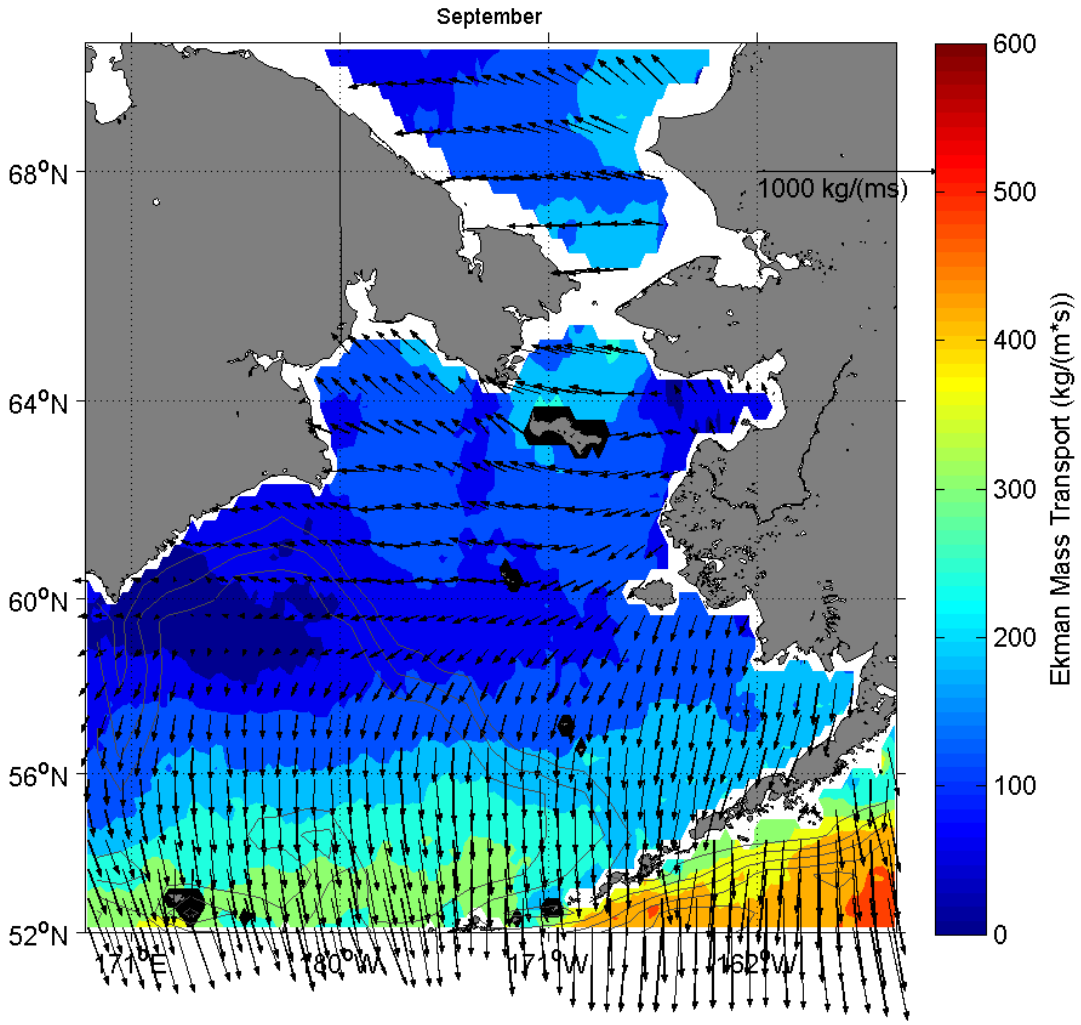

Figure C-21. Monthly mean Ekman transport for September. Every third vector is plotted. Means are based upon data collected every 12 hours.

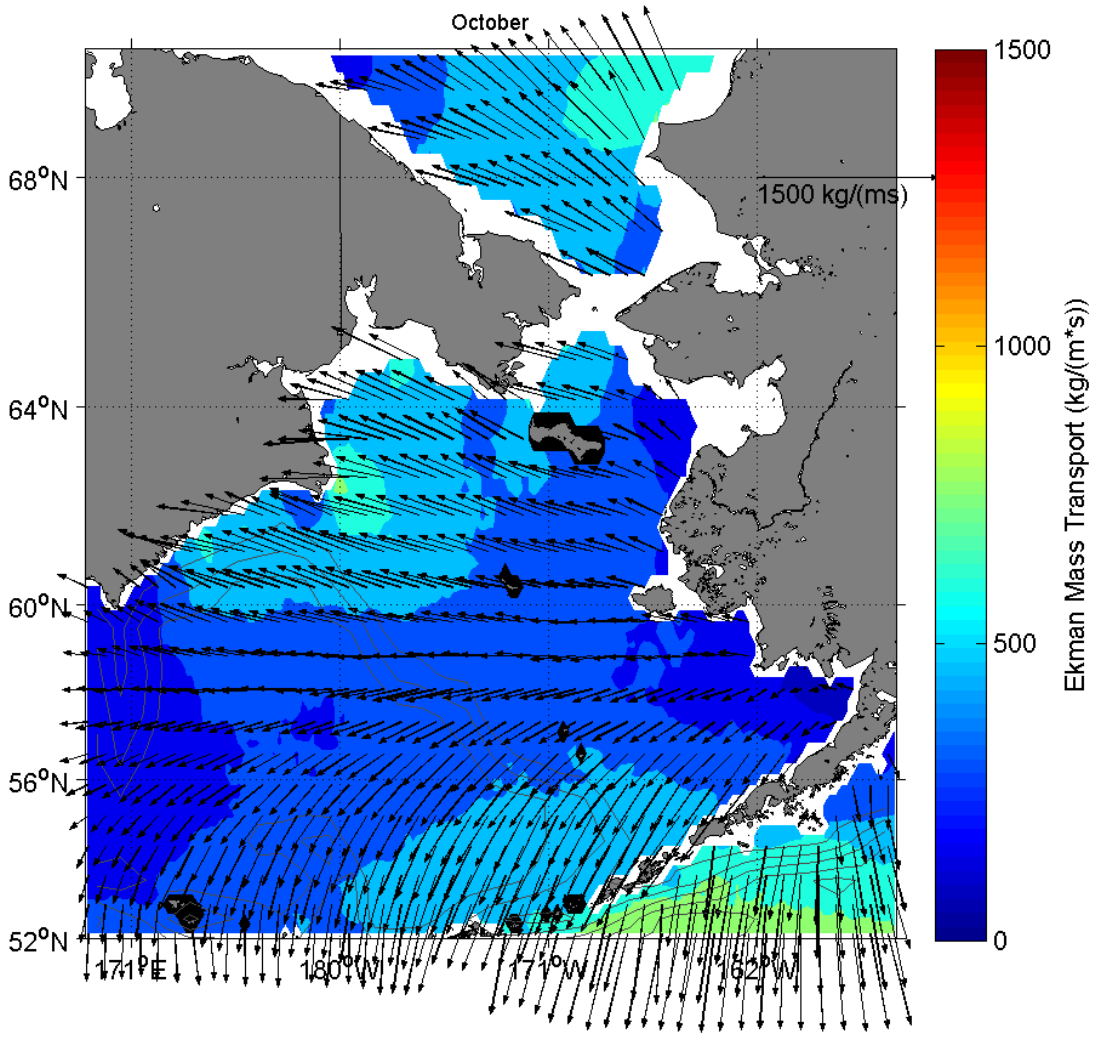

Figure C-22. Monthly mean Ekman transport for October. Every third vector is plotted. Means are based upon data collected every 12 hours.

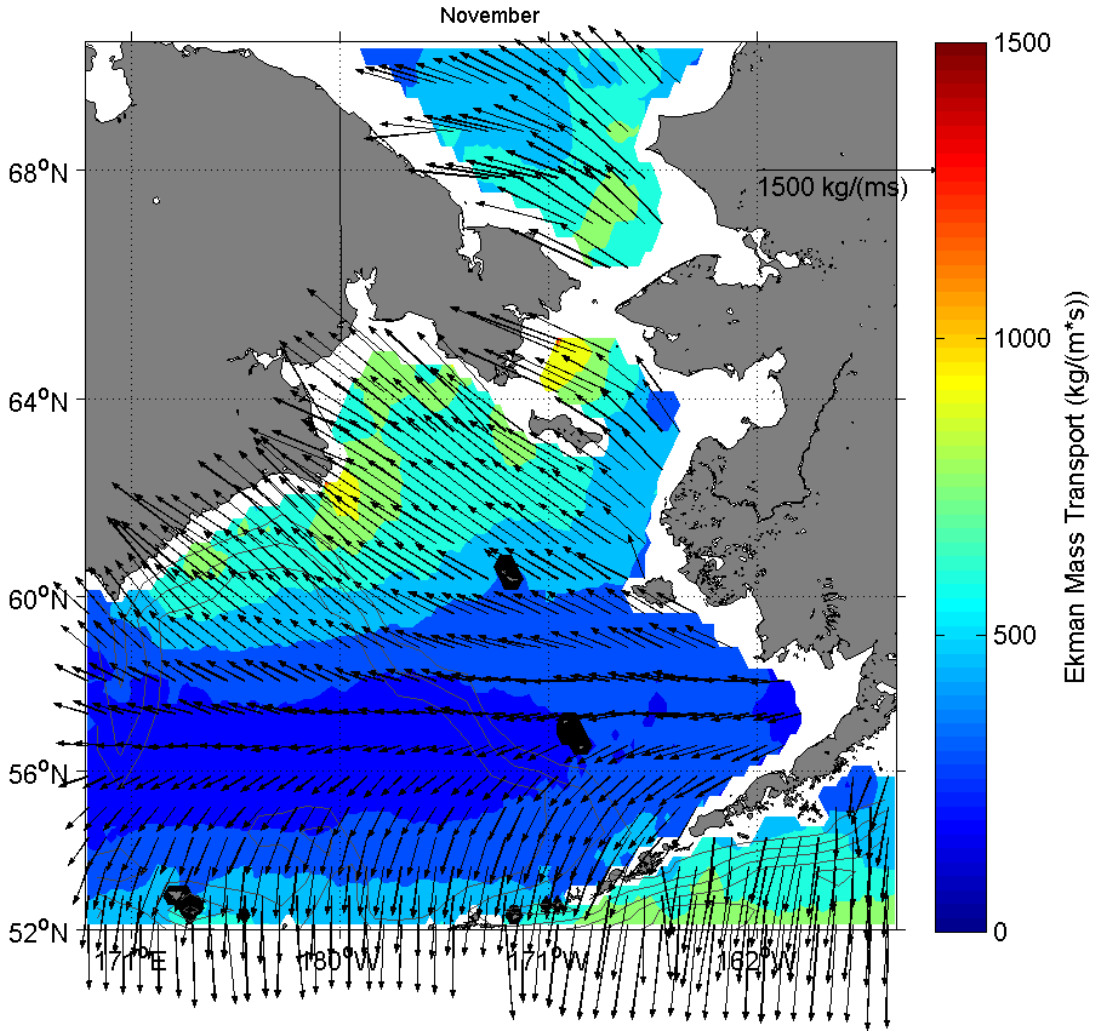

Figure C-23. Monthly mean Ekman transport for November. Every third vector is plotted. Means are based upon data collected every 12 hours.

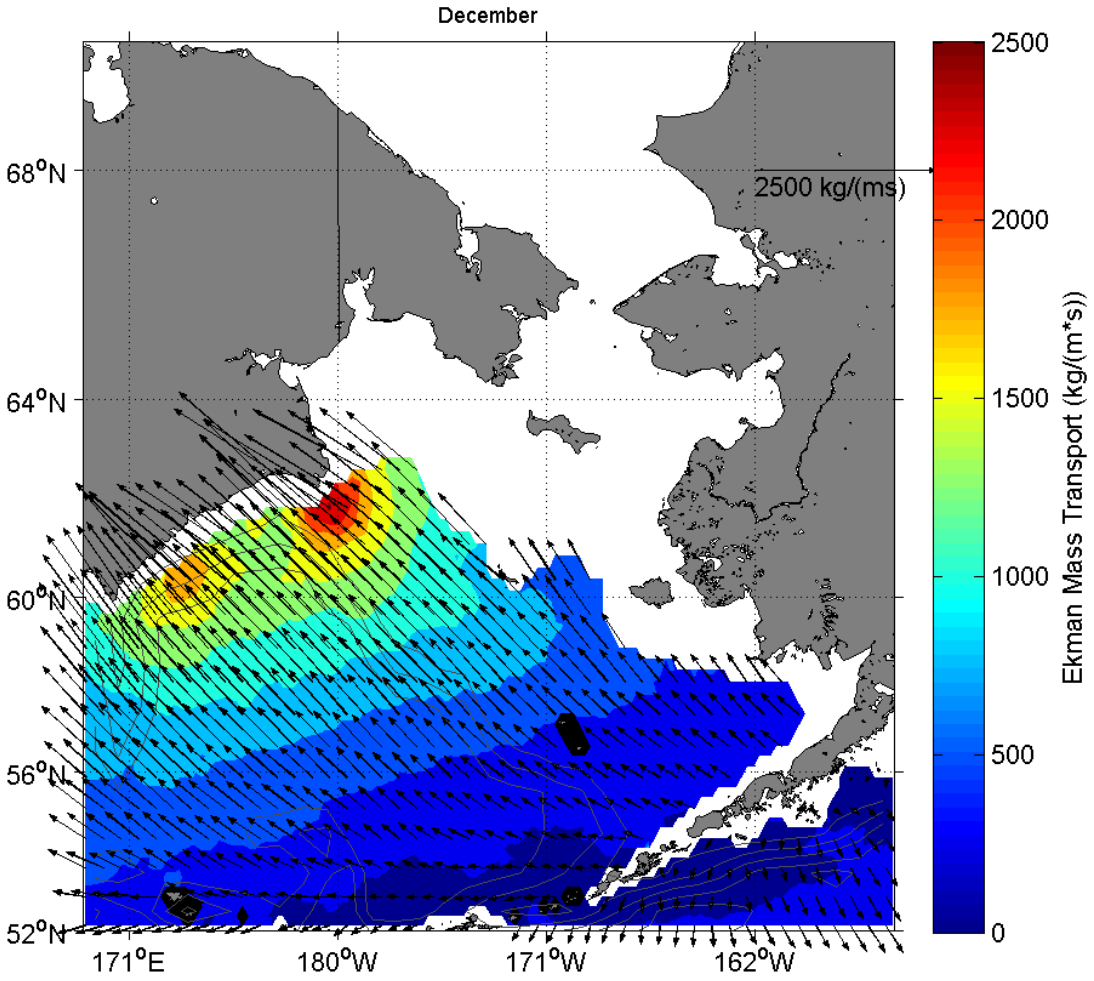

Figure C-24. Monthly mean Ekman transport for December. Every third vector is plotted. Means are based upon data collected every 12 hours.

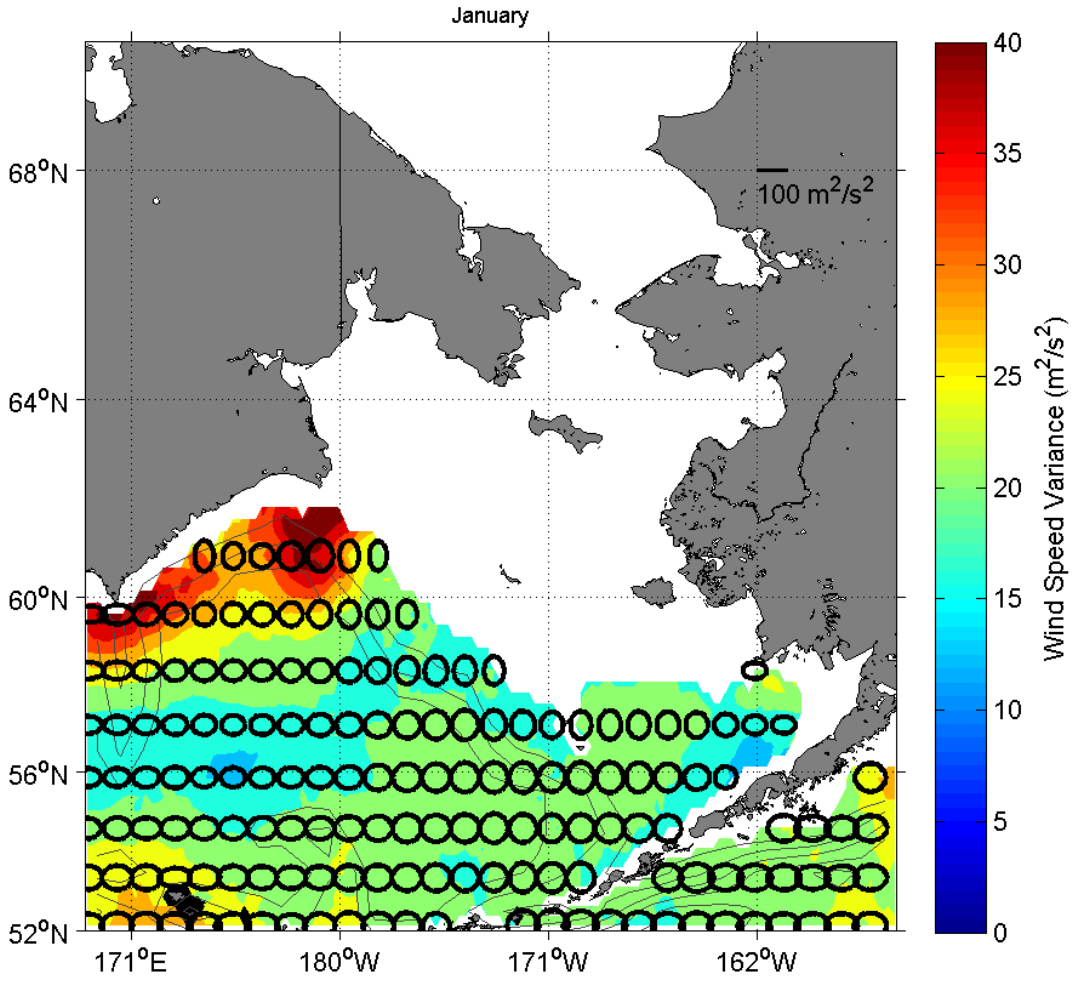

Figure C-25. Monthly variance of zonal (U) and meridional **(V) wind components for January.** Every fifth ellipse is plotted. Variances are based upon data collected every 12 hours. The lengths of the zonal axes are scaled by the variances of the zonal components of the wind. The lengths of the meridional axes are scaled by the variances of the meridional components of the wind.

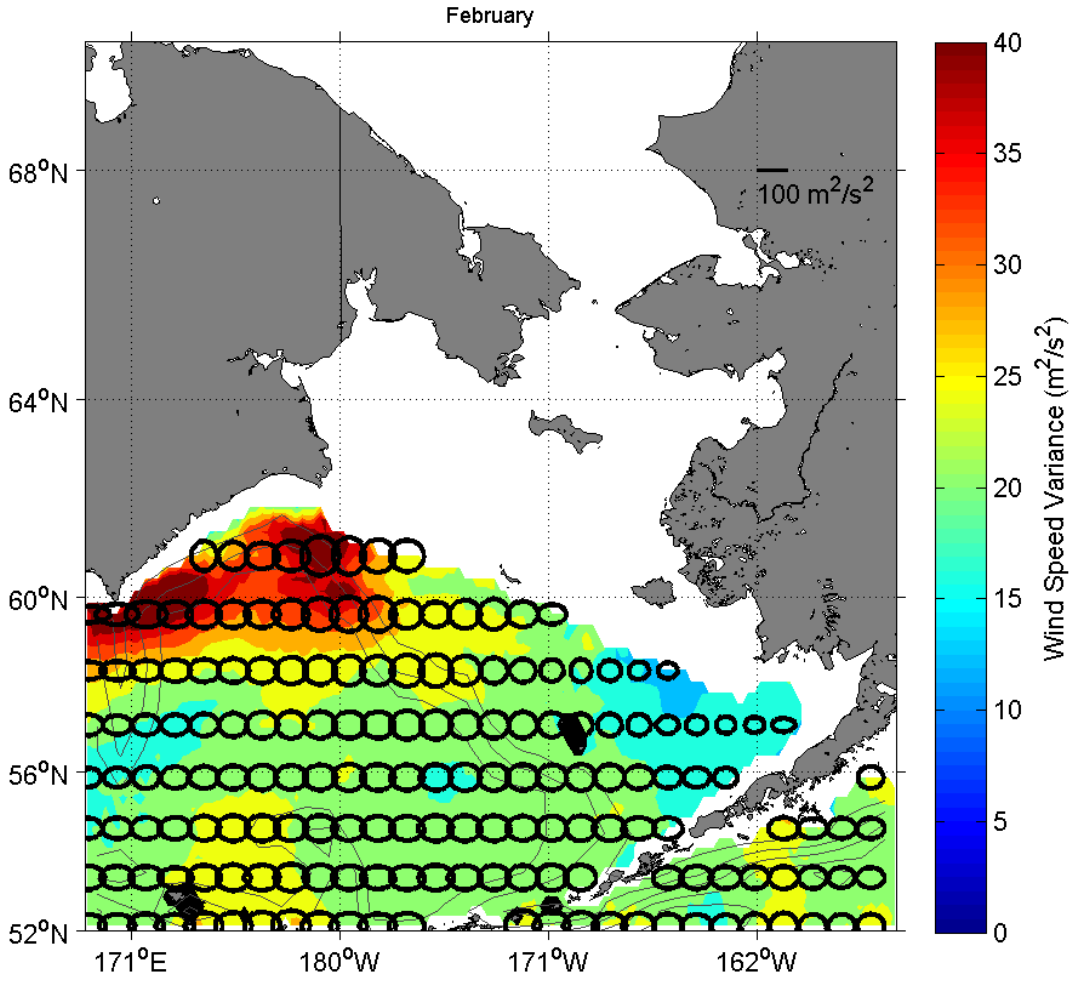

Figure C-26. Monthly variance of zonal (U) and meridional (V) wind components for February. Every fifth ellipse is plotted. Variances are based upon data collected every 12 hours. The lengths of the zonal axes are scaled by the variances of the zonal components of the wind. The lengths of the meridional axes are scaled by the variances of the meridional components of the wind.

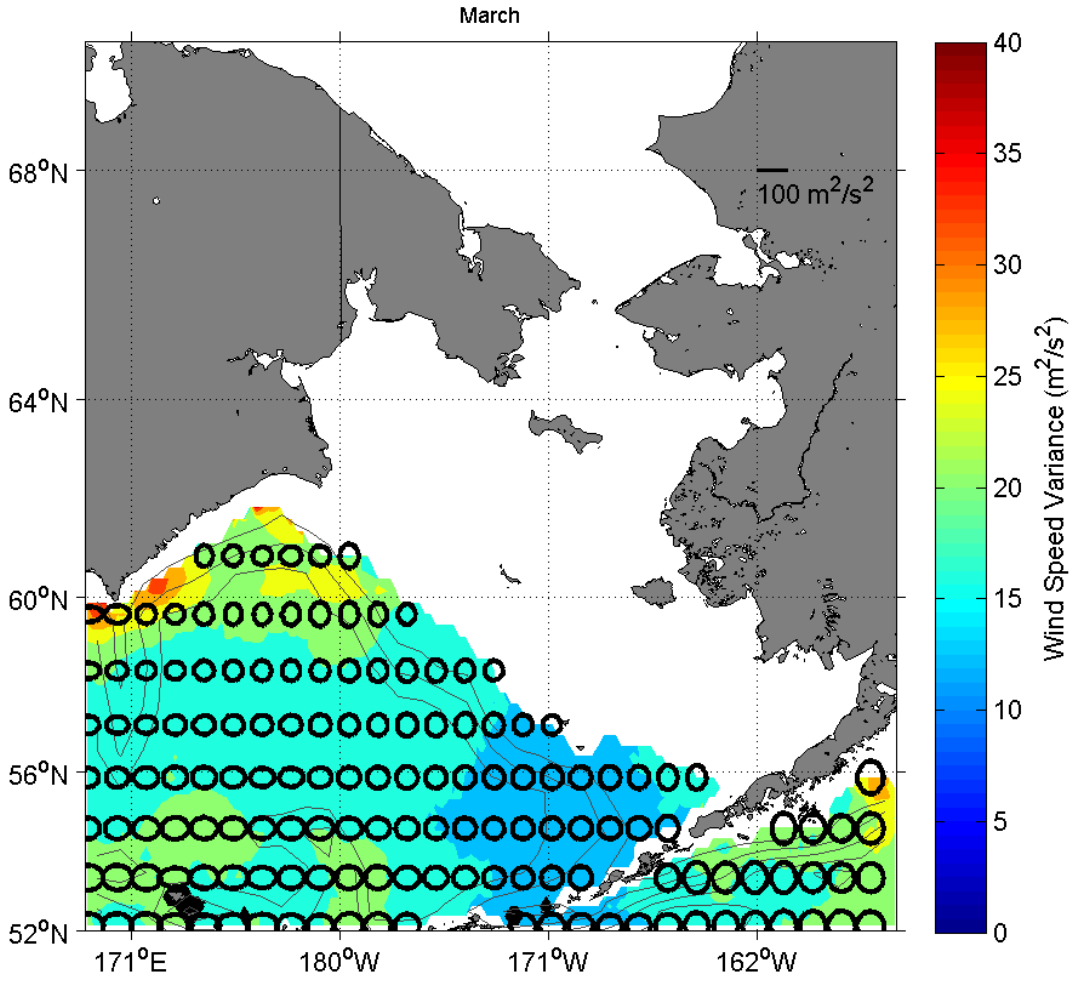

Figure C-27. Monthly variance of zonal (U) and mer**idional (V) wind components for March.** Every fifth ellipse is plotted. Variances are based upon data collected every 12 hours. The lengths of the zonal axes are scaled by the variances of the zonal components of the wind. The lengths of the meridional axes are scaled by the variances of the meridional components of the wind.

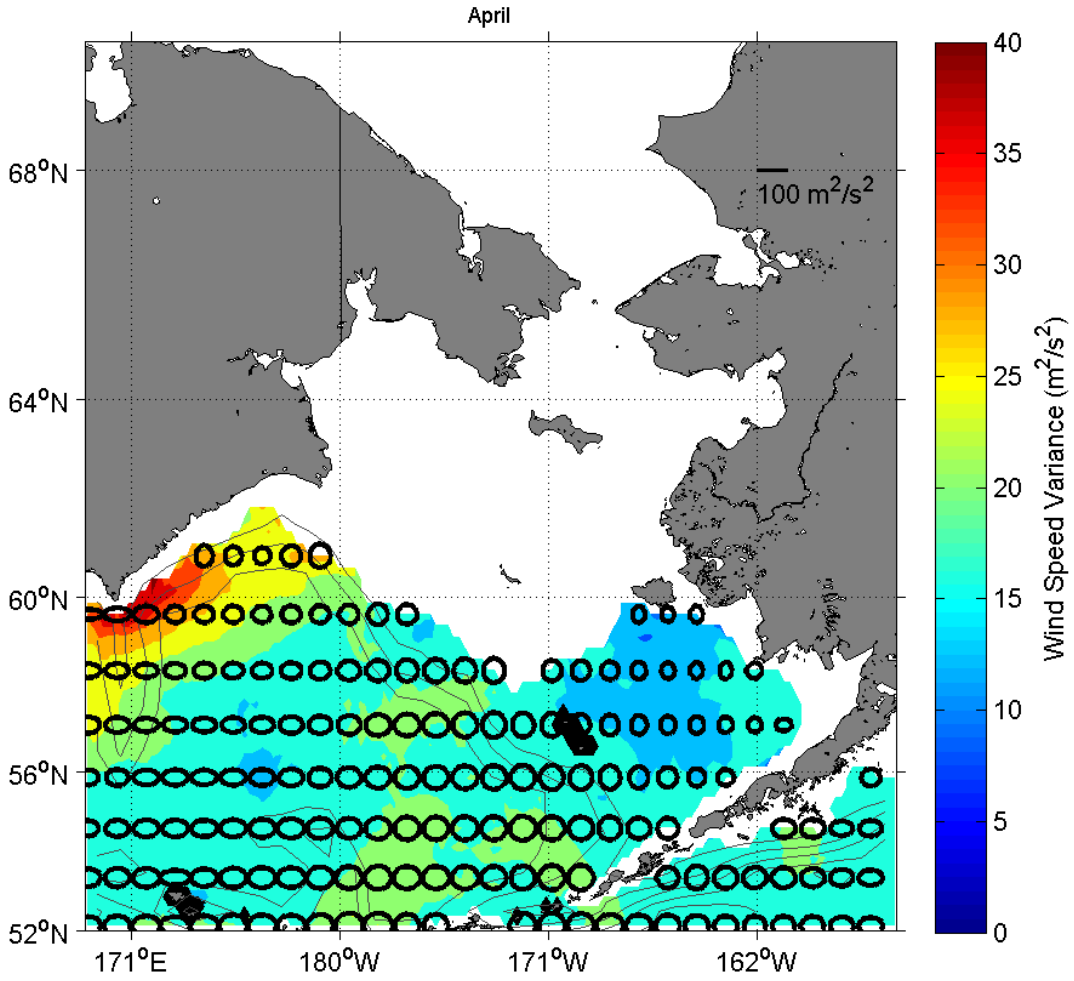

Figure C-28. Monthly variance of zonal (U) and meridional (V) wind components for April. Every fifth ellipse is plotted. Variances are based upon data collected every 12 hours. The lengths of the zonal axes are scaled by the variances of the zonal components of the wind. The lengths of the meridional axes are scaled by the variances of the meridional components of the wind.

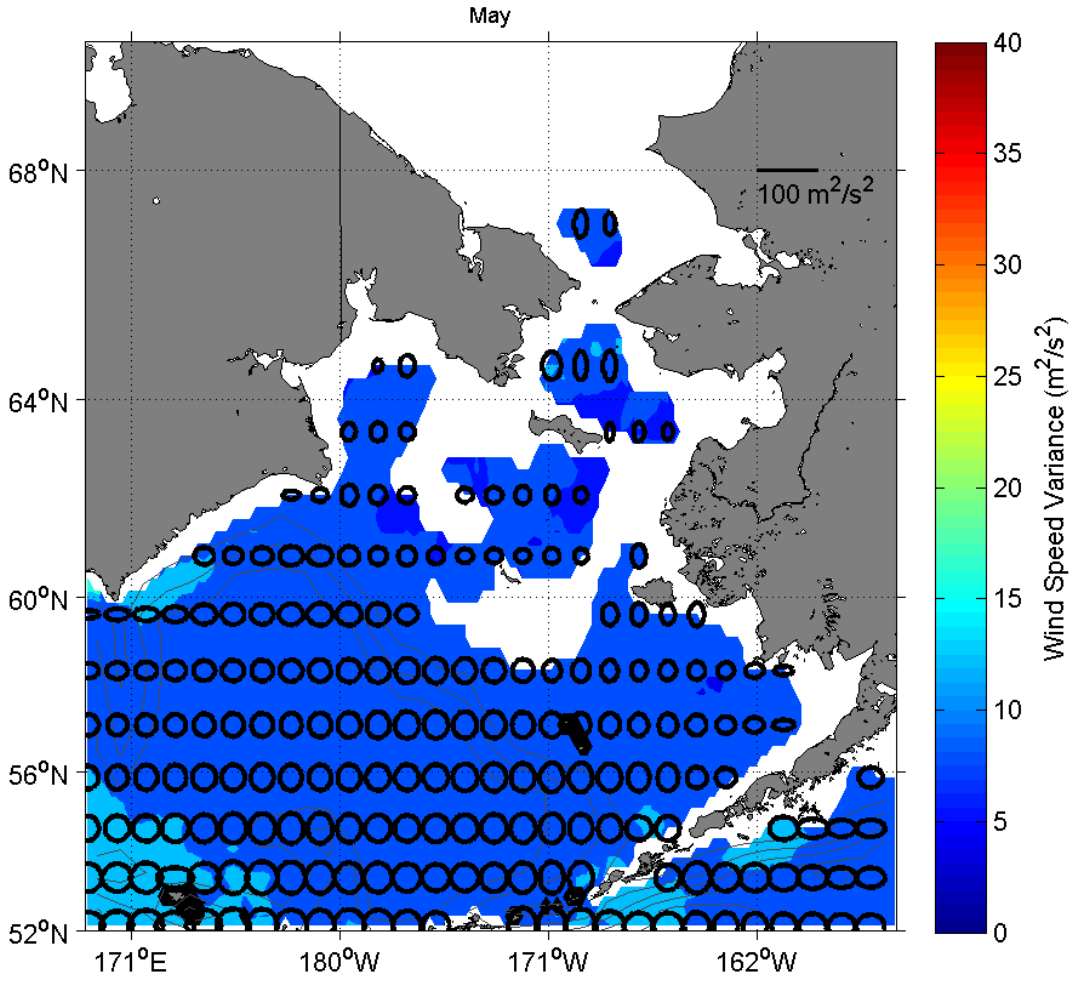

Figure C-29. Monthly variance of zonal (U) and mer**idional (V) wind components for May.** Every fifth ellipse is plotted. Variances are based upon data collected every 12 hours. The lengths of the zonal axes are scaled by the variances of the zonal components of the wind. The lengths of the meridional axes are scaled by the variances of the meridional components of the wind.

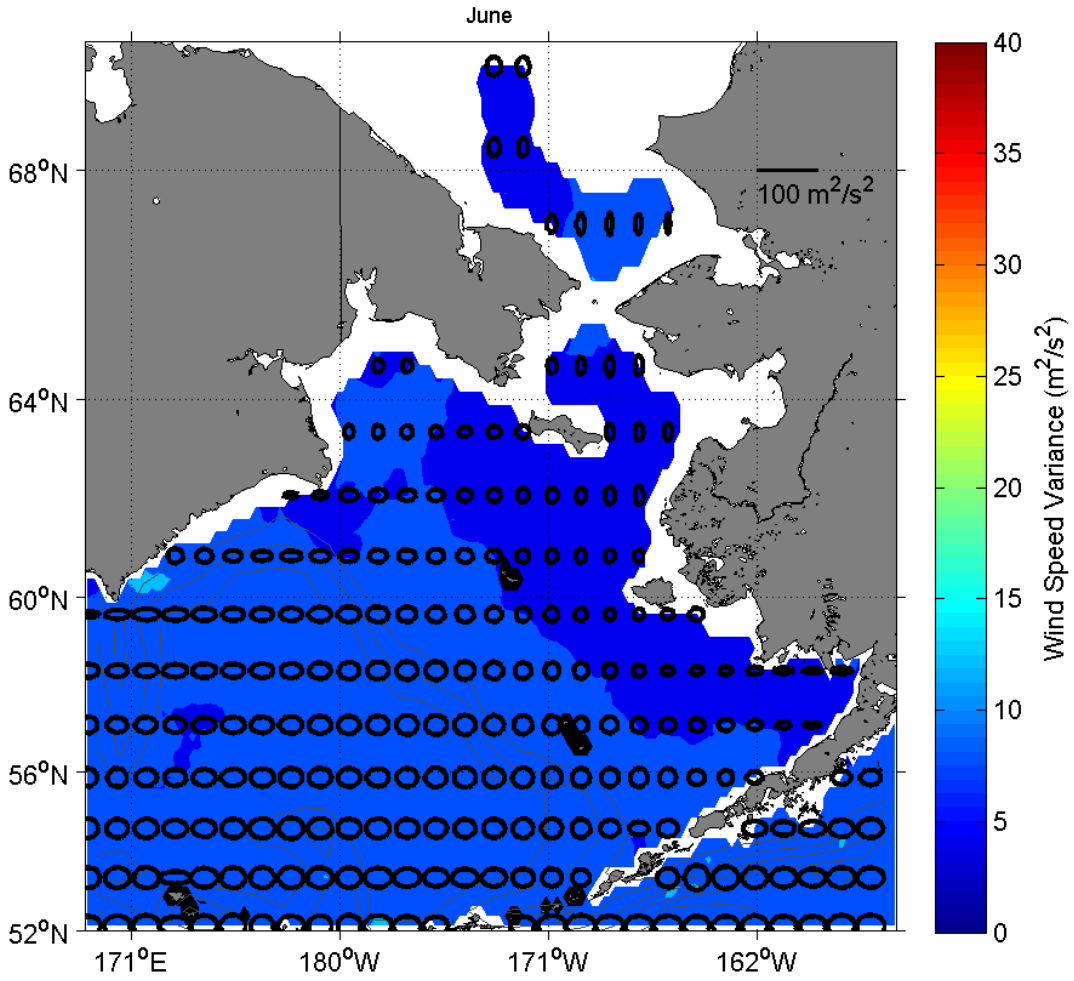

Figure C-30. Monthly variance of zonal (U) and meridional (V) wind components for June. Every fifth ellipse is plotted. Variances are based upon data collected every 12 hours. The lengths of the zonal axes are scaled by the variances of the zonal components of the wind. The lengths of the meridional axes are scaled by the variances of the meridional components of the wind.

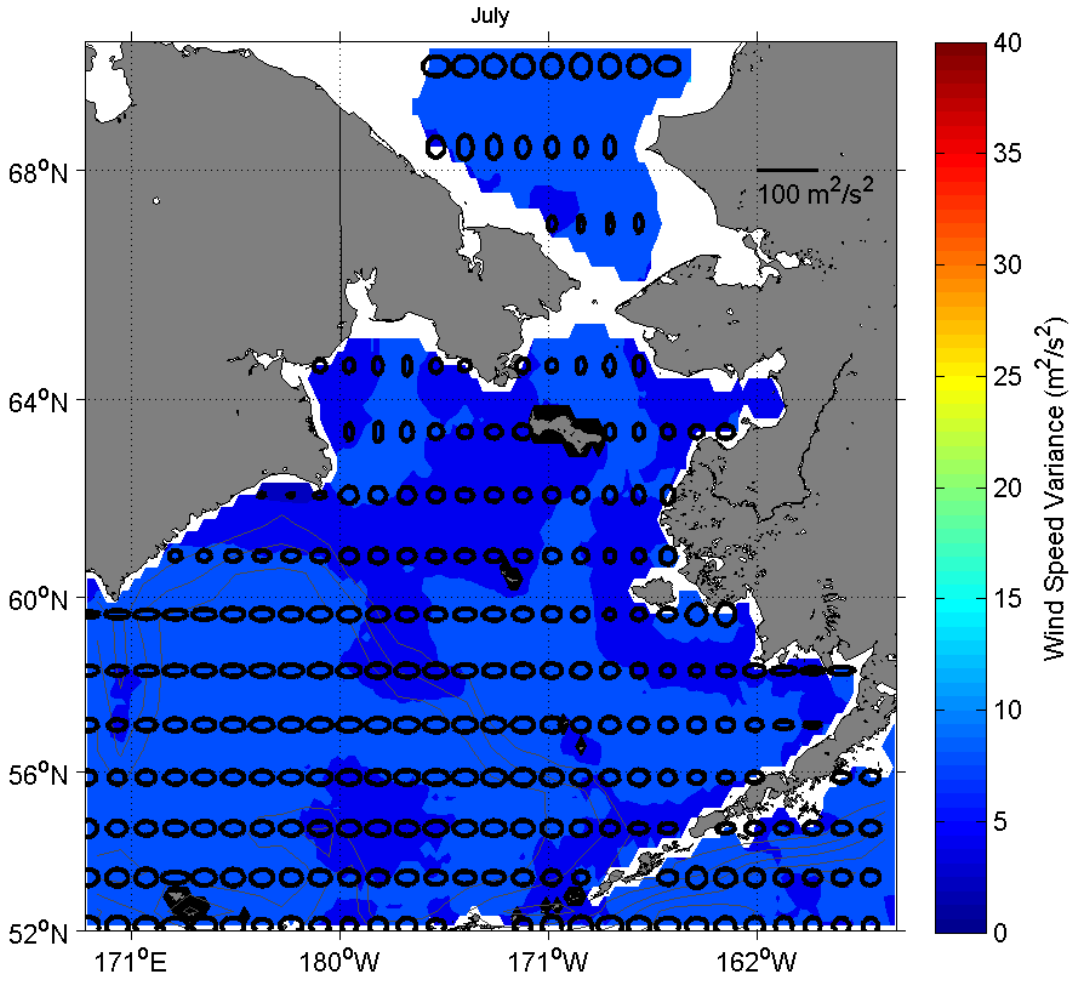

Figure C-31. Monthly variance of zonal (U) and meridi**onal (V) wind components for July.** Every fifth ellipse is plotted. Variances are based upon data collected every 12 hours. The lengths of the zonal axes are scaled by the variances of the zonal components of the wind. The lengths of the meridional axes are scaled by the variances of the meridional components of the wind.

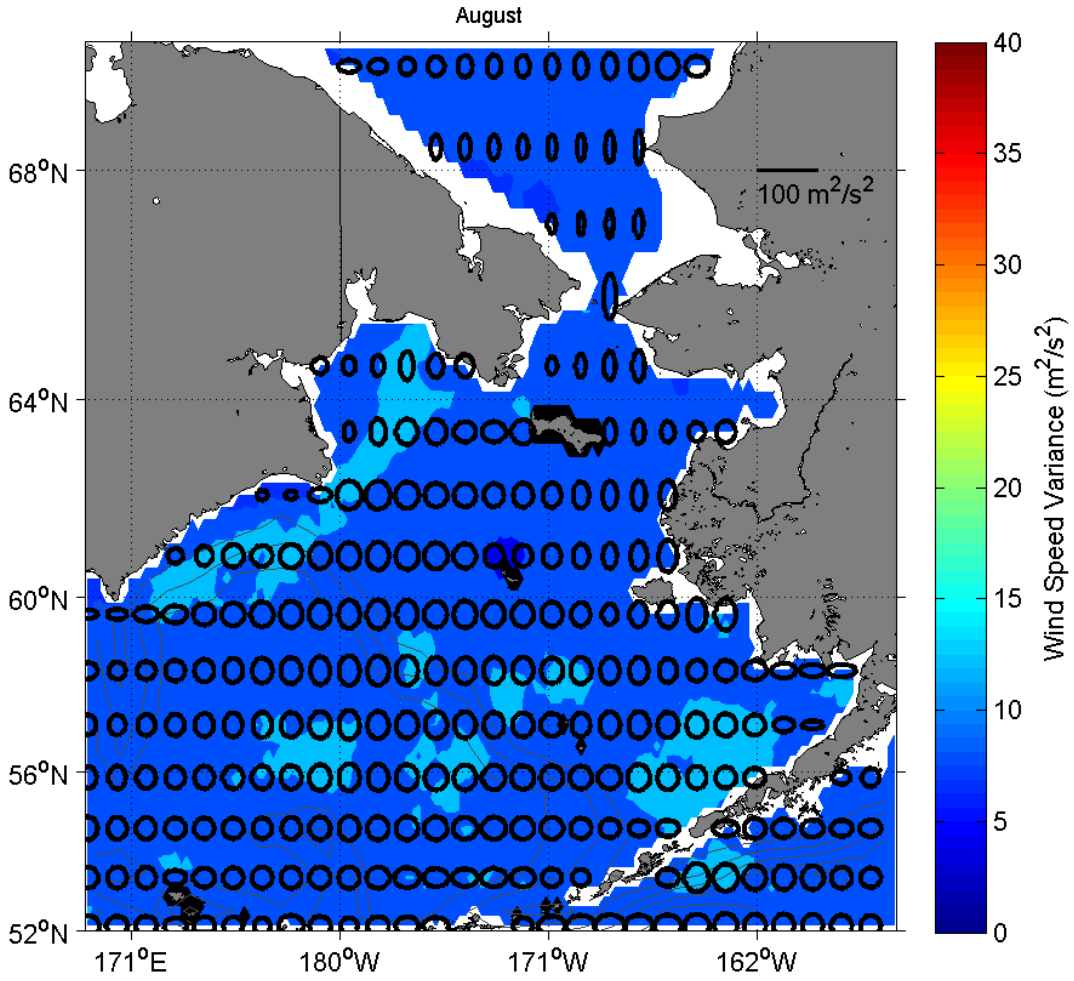

Figure C-32. Monthly variance of zonal (U) and meridional (V) wind components for August. Every fifth ellipse is plotted. Variances are based upon data collected every 12 hours. The lengths of the zonal axes are scaled by the variances of the zonal components of the wind. The lengths of the meridional axes are scaled by the variances of the meridional components of the wind.

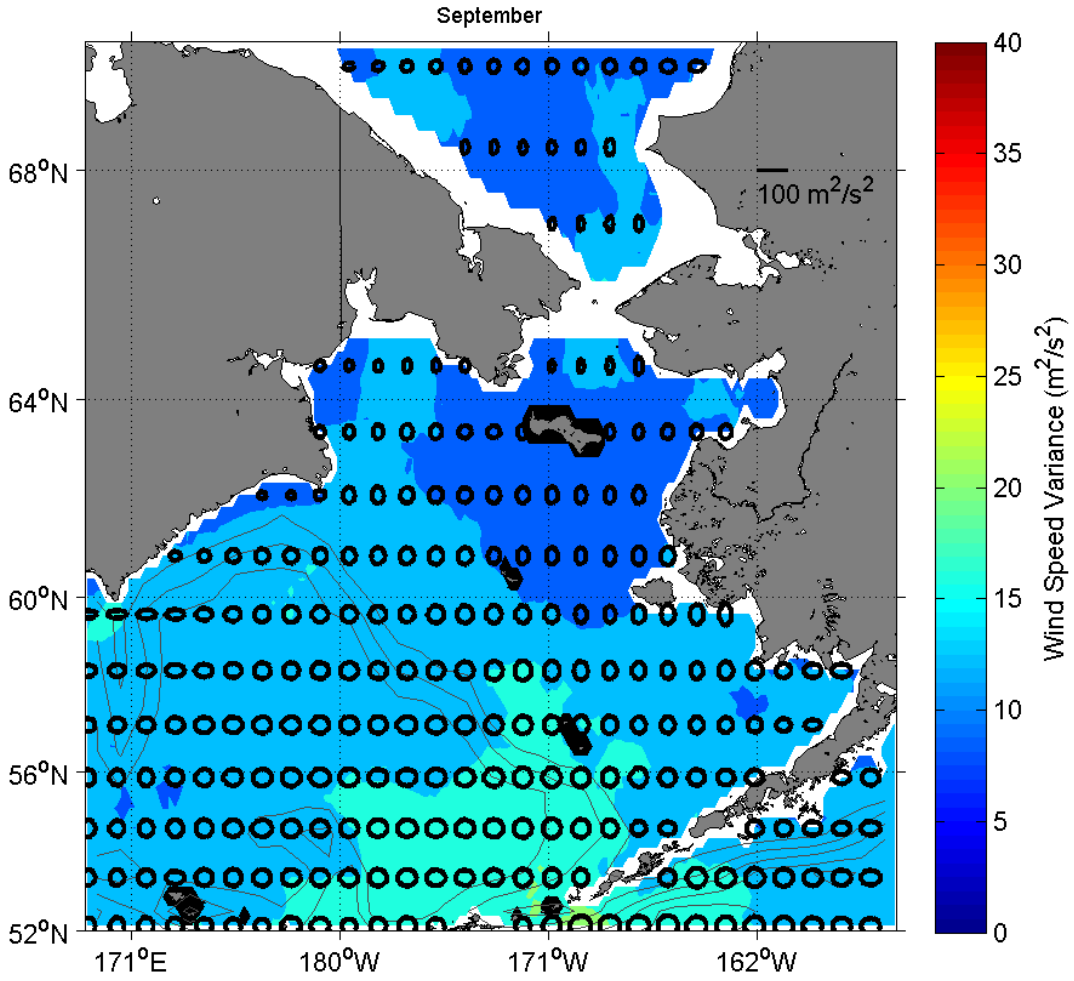

Figure C-33. Monthly variance of zonal (U) and meridi**onal (V) wind components for September.** Every fifth ellipse is plotted. Variances are based upon data collected every 12 hours. The lengths of the zonal axes are scaled by the variances of the zonal components of the wind. The lengths of the meridional axes are scaled by the variances of the meridional components of the wind.

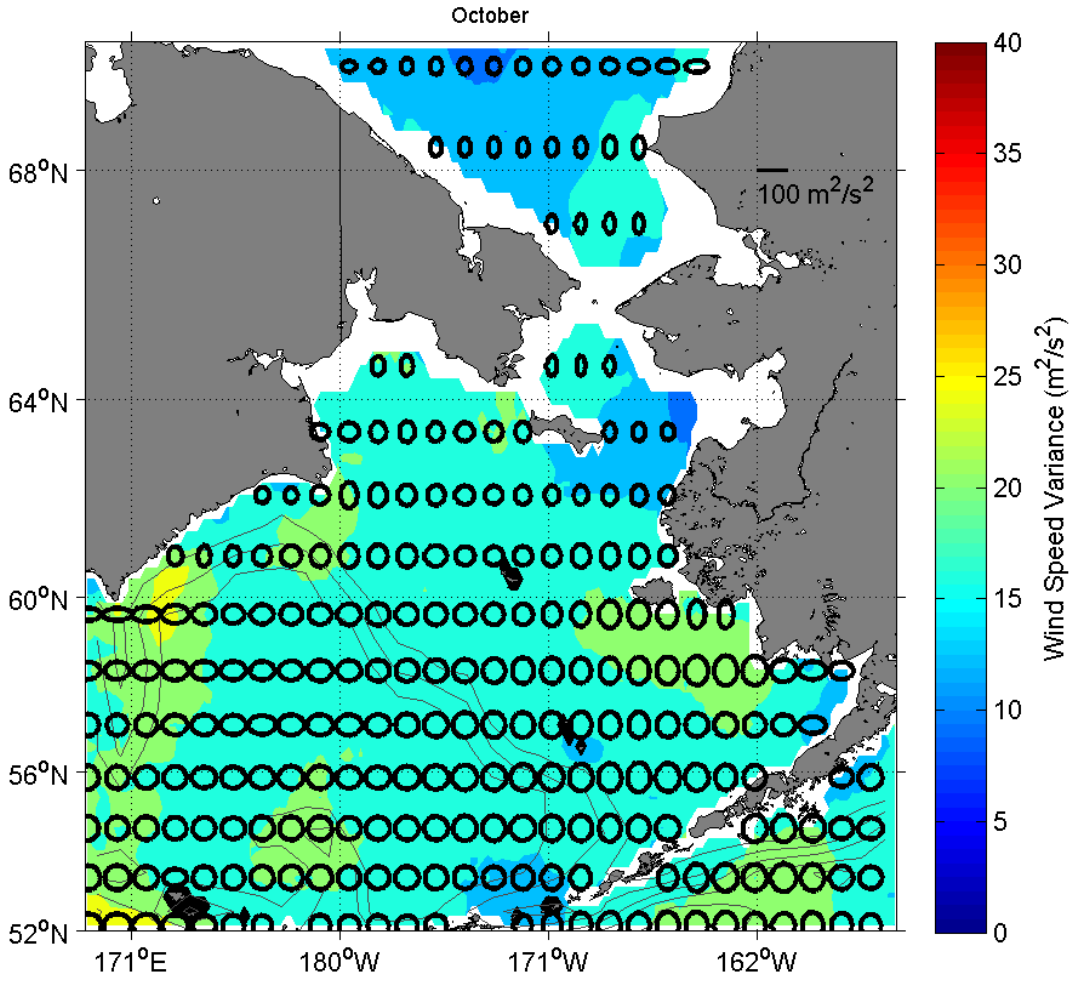

Figure C-34. Monthly variance of zonal (U) and meridional (V) wind components for October. Every fifth ellipse is plotted. Variances are based upon data collected every 12 hours. The lengths of the zonal axes are scaled by the variances of the zonal components of the wind. The lengths of the meridional axes are scaled by the variances of the meridional components of the wind.

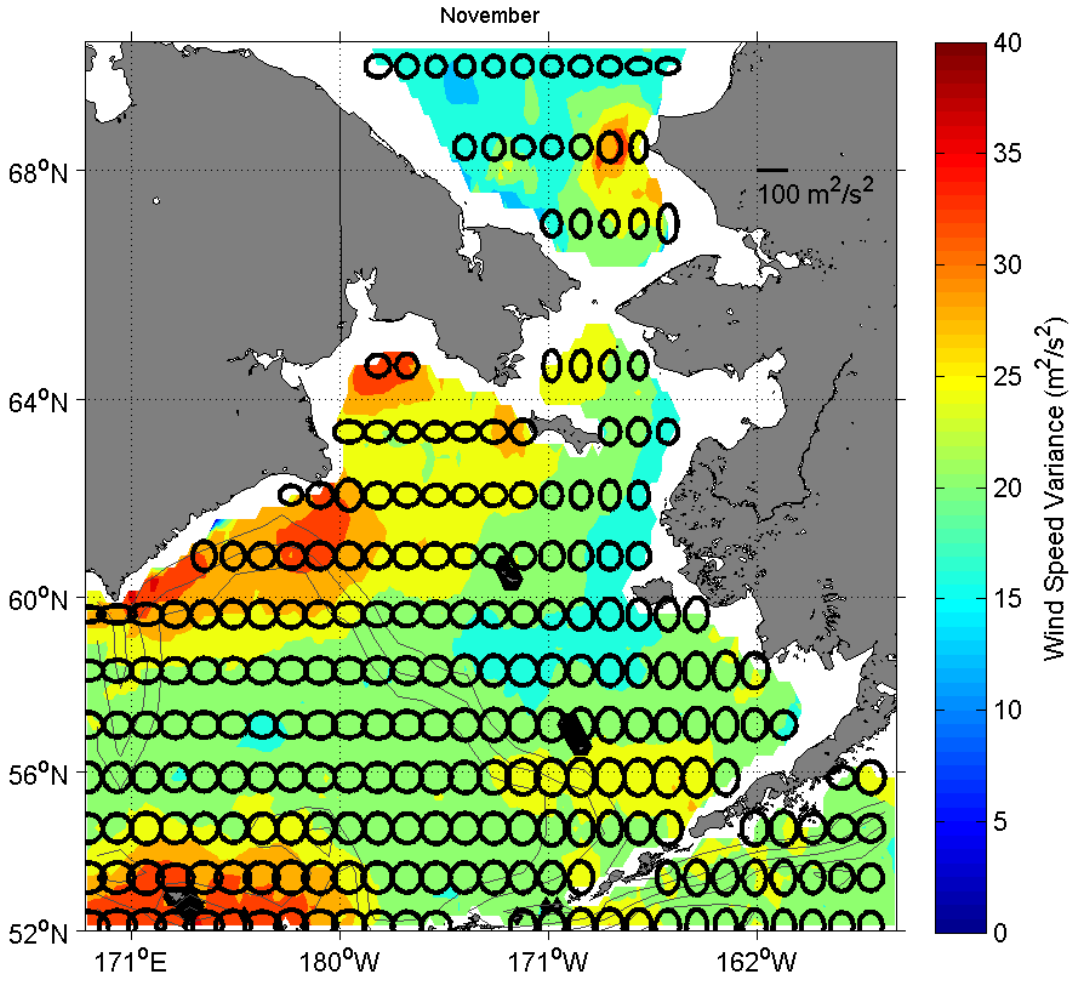

Figure C-35. Monthly variance of zonal (U) and **meridional (V) wind components for November.** Every fifth ellipse is plotted. The lengths of the zonal axes are scaled by the variances of the zonal components of the wind. The lengths of the meridional axes are scaled by the variances of the meridional components of the wind.

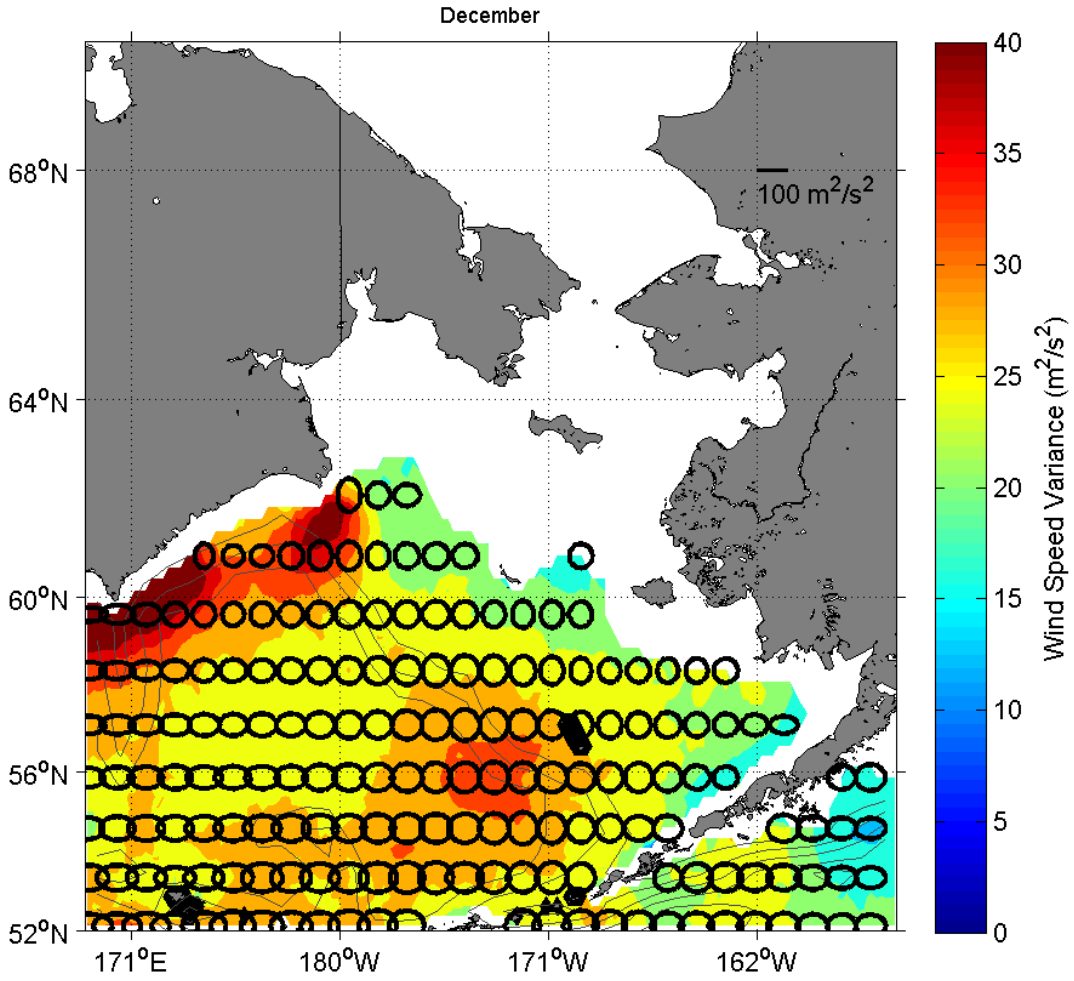

Figure C-36. Monthly variance of zonal (U) and meridional (V) wind components for December. Every fifth ellipse is plotted. Variances are based upon data collected every 12 hours. The lengths of the zonal axes are scaled by the variances of the zonal components of the wind. The lengths of the meridional axes are scaled by the variances of the meridional components of the wind.

Appendix D

Seasonal Anomalies of Surface Ekman Cross-shelf Transport (1948-2007)

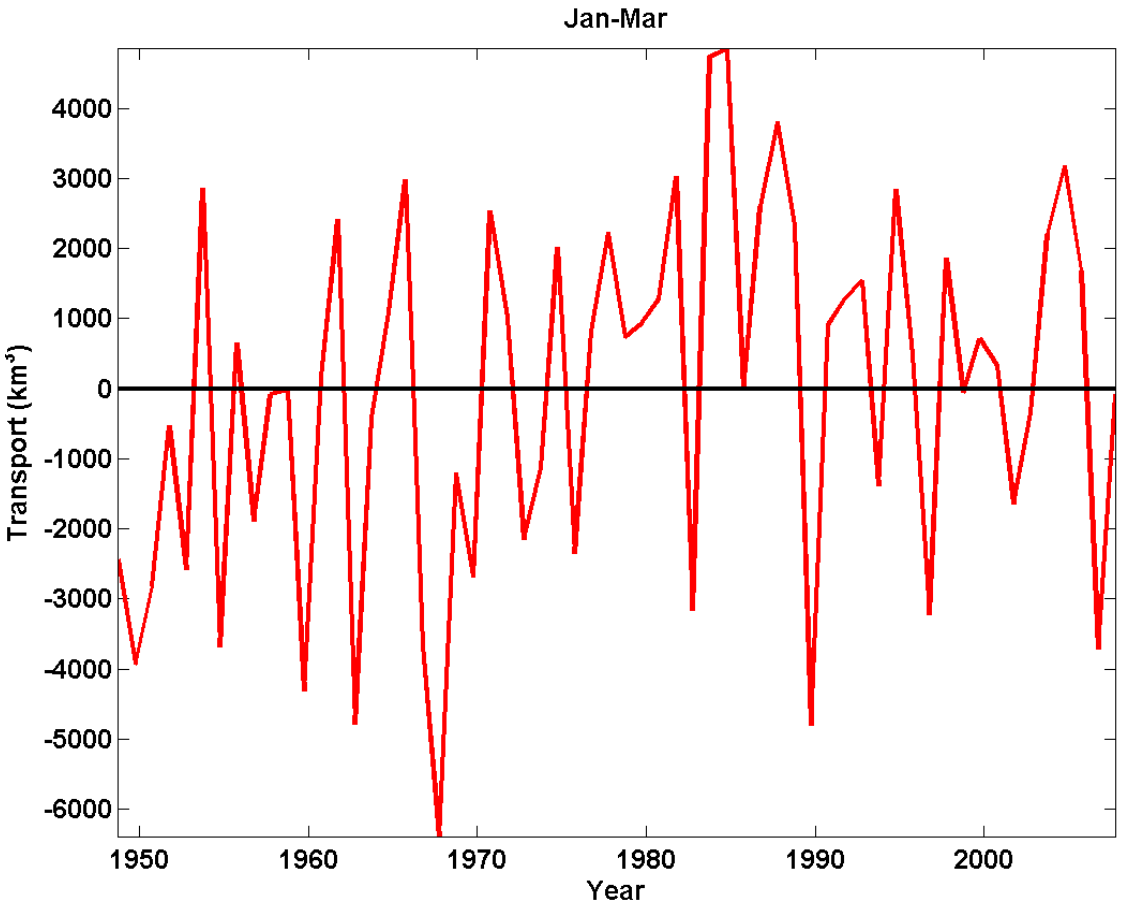

Figure D-1. Anom**alies of surface Ekman cross-shelf transport during January through March from 1948 to 2007.** The overall mean of surface Ekman cross-shelf transport for these months during this time period has been subtracted.

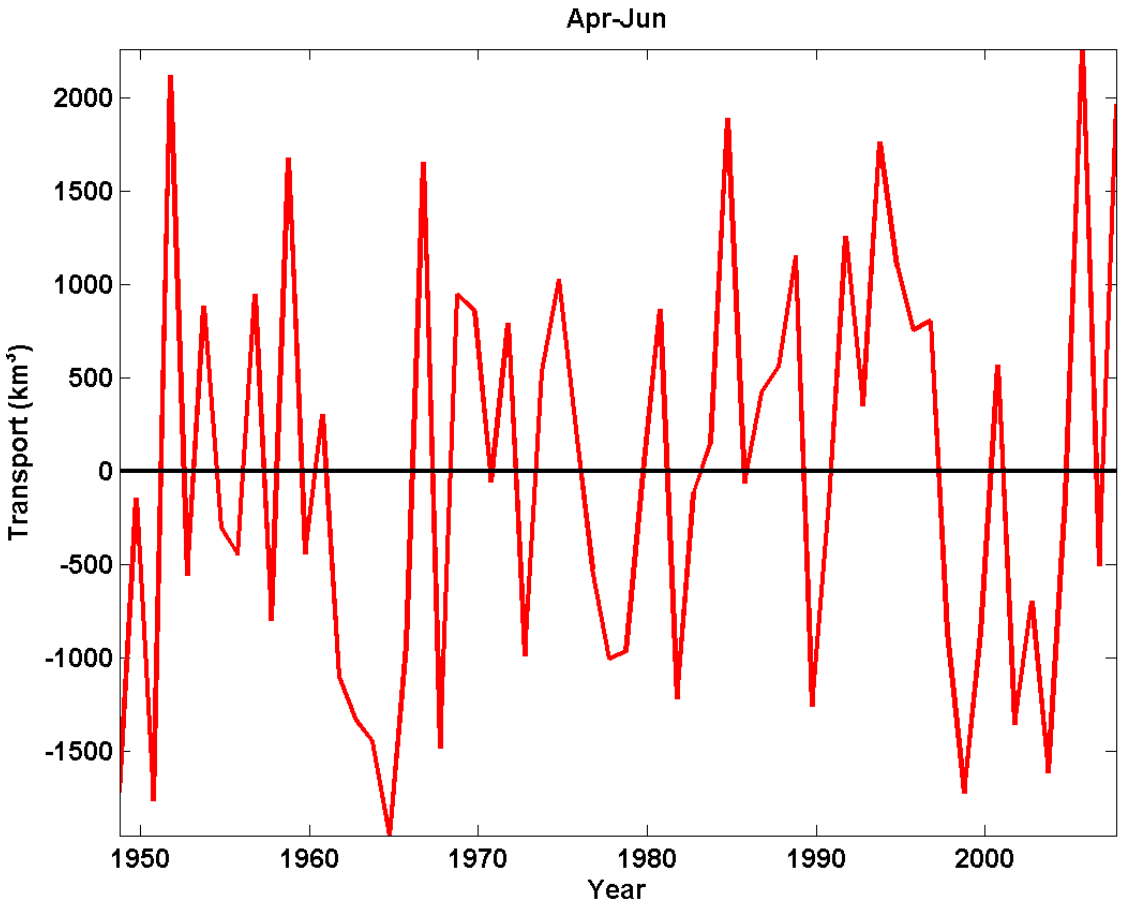

Figure D-2. Anomalies of surface Ekman **cross-shelf transport during April through June from 1948 to 2007.** The overall mean of surface Ekman cross-shelf transport for these months during this time period has been subtracted.

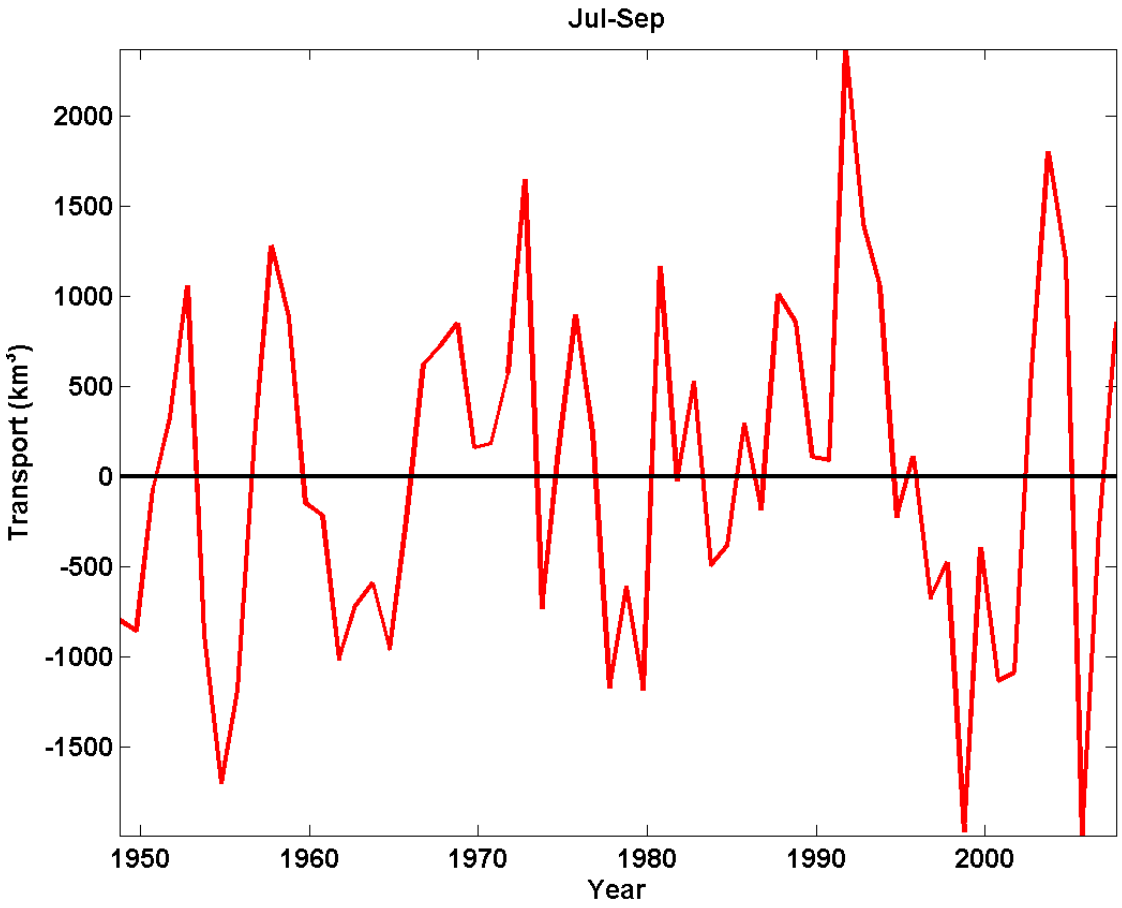

Figure D-3. Anomalies of surface Ekman cross-shelf transport **during July through September from 1948 to 2007.** The overall mean of surface Ekman cross-shelf transport for these months during this time period has been subtracted.

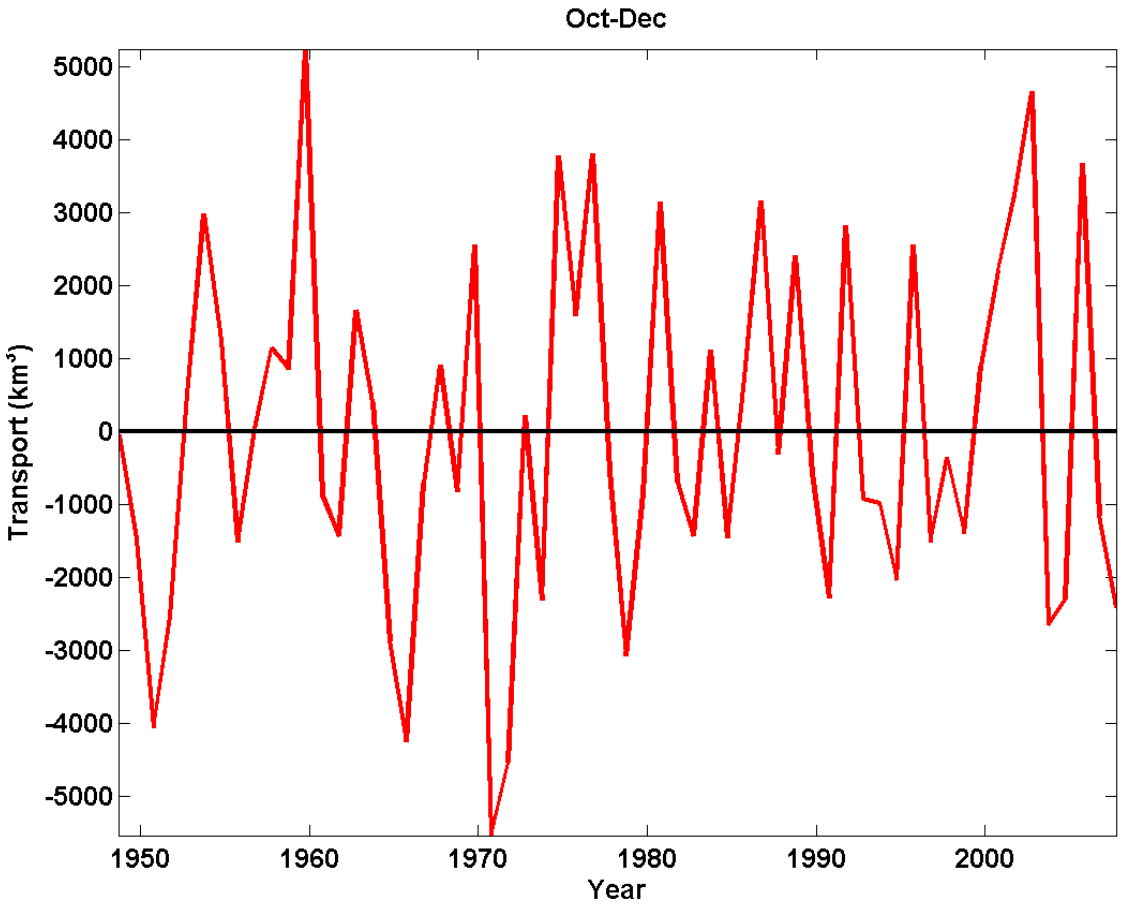

Figure D-4. Anomalies of surface Ekman cross-shelf transport during October thro**ugh December from 1948 to 2007.** The overall sum of surface Ekman cross-shelf transport for these months during this time period has been subtracted.

Table D-1. Cross-correlations between monthly mean values of surface Ekman cross-shelf transport and climate indices.

PDO					
Onshore Flow	Lat (Degrees North)	Lon (Degrees West)	Correlation	Lags (Months)	p-value
	60	180	0.32	1	<<0.05*
	57.5	185	0.30	1	<<0.05*
	55	190	0.24	1	<<0.05*
Offshore Flow	60	180	0.24	1	<<0.05*
	57.5	185	0.18	1	<<0.05*
	55	190	0.16	1	<<0.05*
Net Flow	60	180	0.34	1	<<0.05*
	57.5	185	0.30	1	<<0.05*
	55	190	0.24	1	<<0.05*
Onshore Flow	Total Shelbreak		0.36	1	<<0.05*
Offshore Flow			0.33	1	<<0.05*
Net Flow			0.22	1	<<0.05*
PNA					
Onshore Flow	Lat (Degrees North)	Lon (Degrees West)	Correlation	Lags (Months)	p-value
	60	180	0.23	0	<<0.05*
	57.5	185	0.23	0	<<0.05*
	55	190	0.16	0	<<0.05*
Offshore Flow	60	180	0.40	0	<<0.05*
	57.5	185	0.36	0	<<0.05*
	55	190	0.27	0	<<0.05*
Net Flow	60	180	0.29	0	<<0.05*
	57.5	185	0.35	0	<<0.05*
	55	190	0.27	0	<<0.05*
Onshore Flow	Total Shelbreak		0.35	0	<<0.05*
Offshore Flow			0.24	0	<<0.05*
Net Flow			0.38	0	<<0.05*
AO					
Onshore Flow	Lat (Degrees North)	Lon (Degrees West)	Correlation	Lags (Months)	p-value
	60	180	0.11	-269	0.01*
	57.5	185	0.13	-257	<<0.05*
	55	190	0.11	-6	<<0.05*
Offshore Flow	60	180	0.14	-59	<<0.05*
	57.5	185	0.11	-107	<<0.05*
	55	190	0.10	-105	0.01*
Net Flow	60	180	0.11	-234	0.01*
	57.5	185	0.11	-258	0.01*
	55	190	0.10	-164	0.01*
Onshore Flow	Total Shelbreak		0.12	-258	0.01*
Offshore Flow			0.13	-257	<<0.05*
Net Flow			0.11	74	<<0.05*

Table D-1 (Continued)

ALPI					
Onshore Flow	Lat (Degrees North)	Lon (Degrees West)	Correlation	Lags (Years)	p-value
	60	180	0.25	0	<<0.05*
	57.5	185	0.26	-24	0.07
	55	190	0.26	-5	<<0.05*
Offshore Flow	60	180	0.27	0	<<0.05*
	57.5	185	0.23	7	0.05
	55	190	0.27	7	<<0.05*
Net Flow	60	180	0.28	0	<<0.05*
	57.5	185	0.24	7	<<0.05*
	55	190	0.27	7	<<0.05*
Onshore Flow	Total Shelbreak		0.28	0	<<0.05*
Offshore Flow			0.28	0	<<0.05*
Net Flow			0.26	7	<<0.05*
NP					
Onshore Flow	Lat (Degrees North)	Lon (Degrees West)	Correlation	Lags (Years)	p-value
	60	180	0.31	4	<<0.05*
	57.5	185	0.32	12	<<0.05*
	55	190	0.28	-16	<<0.05*
Offshore Flow	60	180	0.25	1	<<0.05*
	57.5	185	0.23	-16	0.08
	55	190	0.31	-1	<<0.05*
Net Flow	60	180	0.32	4	<<0.05*
	57.5	185	0.28	12	<<0.05*
	55	190	0.30	-16	<<0.05*
Onshore Flow	Total Shelbreak		0.30	8	<<0.05*
Offshore Flow			0.29	8	<<0.05*
Net Flow			0.22	-16	0.09
WP (Winter)					
Onshore Flow	Lat (Degrees North)	Lon (Degrees West)	Correlation	Lags (Years)	p-value
	60	180	0.24	-35	0.15
	57.5	185	0.18	-24	0.17
	55	190	0.28	-24	0.07
Offshore Flow	60	180	0.32	-35	0.08
	57.5	185	0.40	-24	<<0.05*
	55	190	0.37	-24	<<0.05*
Net Flow	60	180	0.29	-35	0.11
	57.5	185	0.32	-24	<<0.05*
	55	190	0.39	-24	<<0.05*
Onshore Flow	Total Shelbreak		0.26	-35	0.13
Offshore Flow			0.23	-35	0.16
Net Flow			0.38	-24	<<0.05*

Table D-1 (Continued)

WP (Spring)					
Onshore Flow	Lat (Degrees North)	Lon (Degrees West)	Correlation	Lags (Years)	p-value
	60	180	0.27	9	<<0.05*
	57.5	185	0.23	9	0.06
	55	190	0.23	9	0.06
Offshore Flow	60	180	0.31	-2	<<0.05*
	57.5	185	0.38	9	<<0.05*
	55	190	0.30	5	<<0.05*
Net Flow	60	180	0.30	9	<<0.05*
	57.5	185	0.34	9	<<0.05*
	55	190	0.30	9	<<0.05*
Onshore Flow	Total Shelbreak		0.40	9	<<0.05*
Offshore Flow			0.33	9	<<0.05*
Net Flow			0.37	9	<<0.05*

Note: Mean annual transports are used in for calculation of cross-correlation between the flows and the ALPI as this is an annual index. P-values with an asterisk indicate significant correlations at the 95% confidence level.

Appendix E

CEOF Analysis of NCEP Data

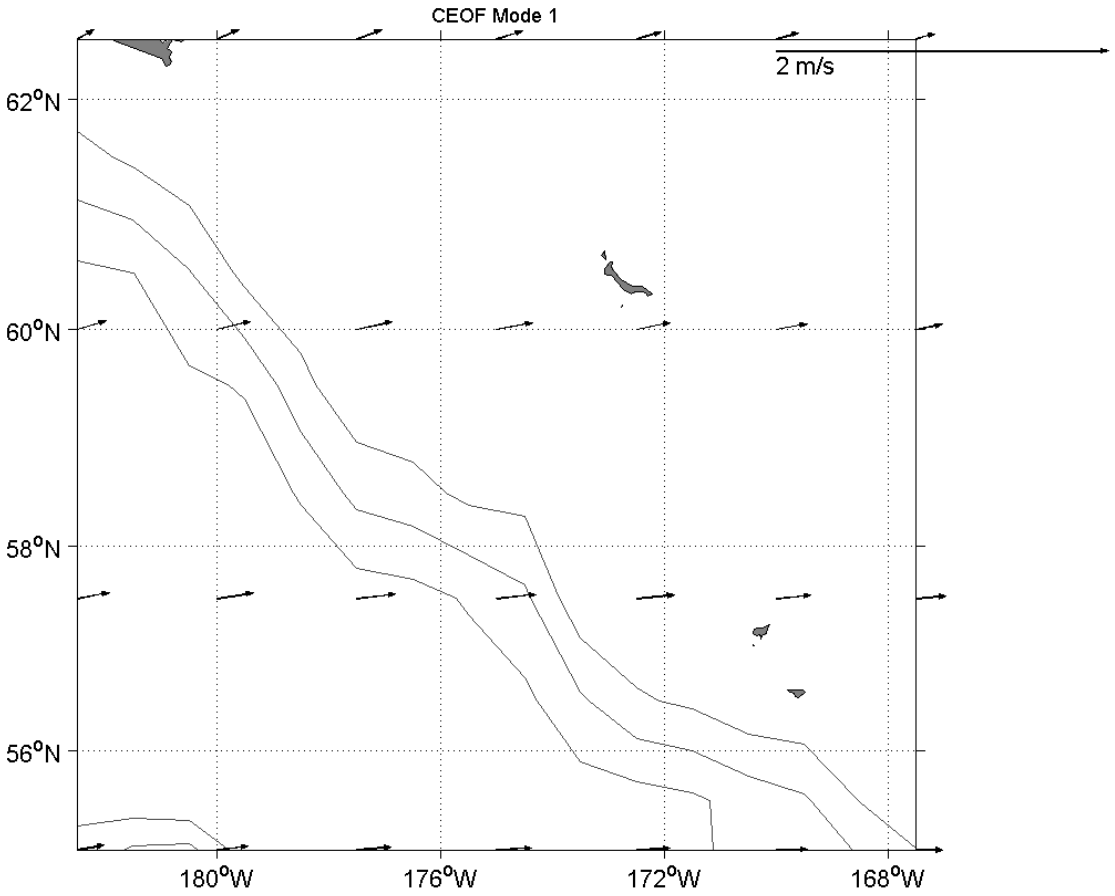

Figure E-1. Mode 1 for NCEP 6-hourly data from 1948-2007. The same small domain and method used to calculate CEOFs for the QuikSCAT data was used. This mode accounts for 61.3% of the variance.

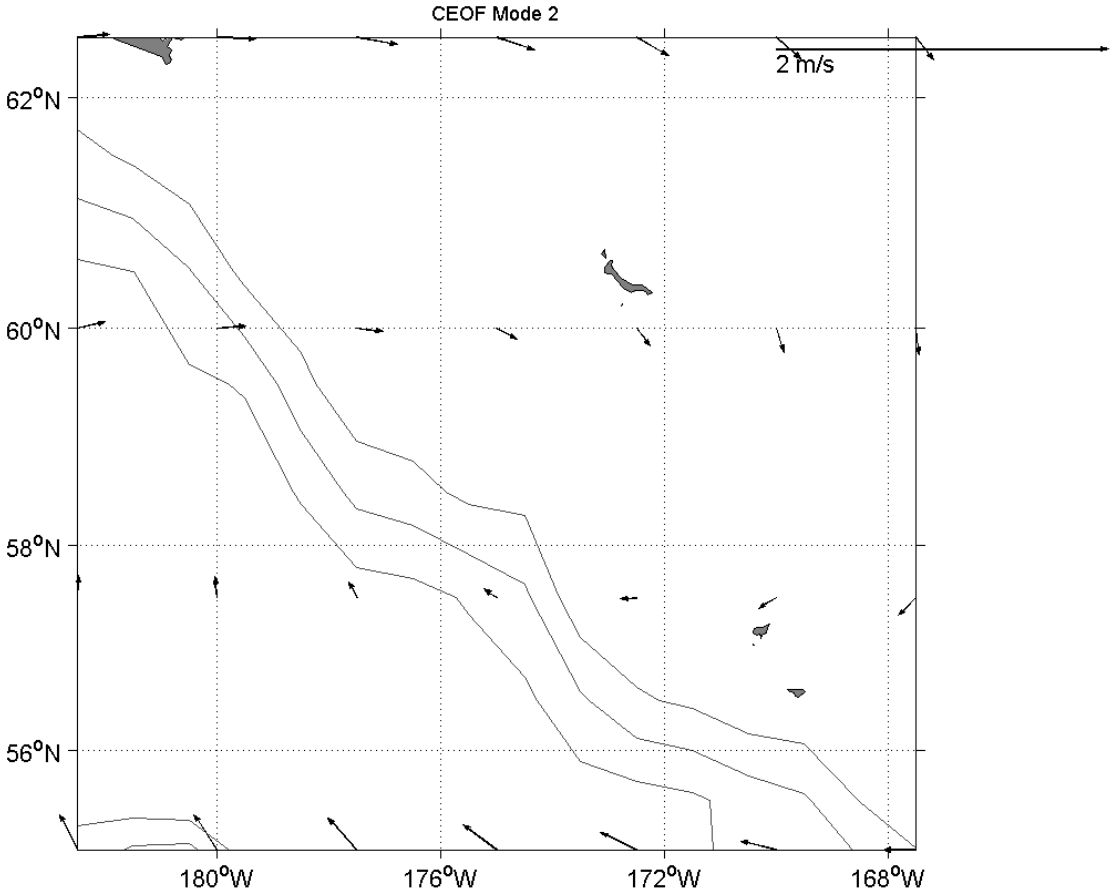

Figure E-2. Mode 2 for NCEP 6-hourly data from 1948-2007. The same small domain and method used to calculate CEOFs for the QuikSCAT data was used. This mode accounts for 16.6% of the variance.

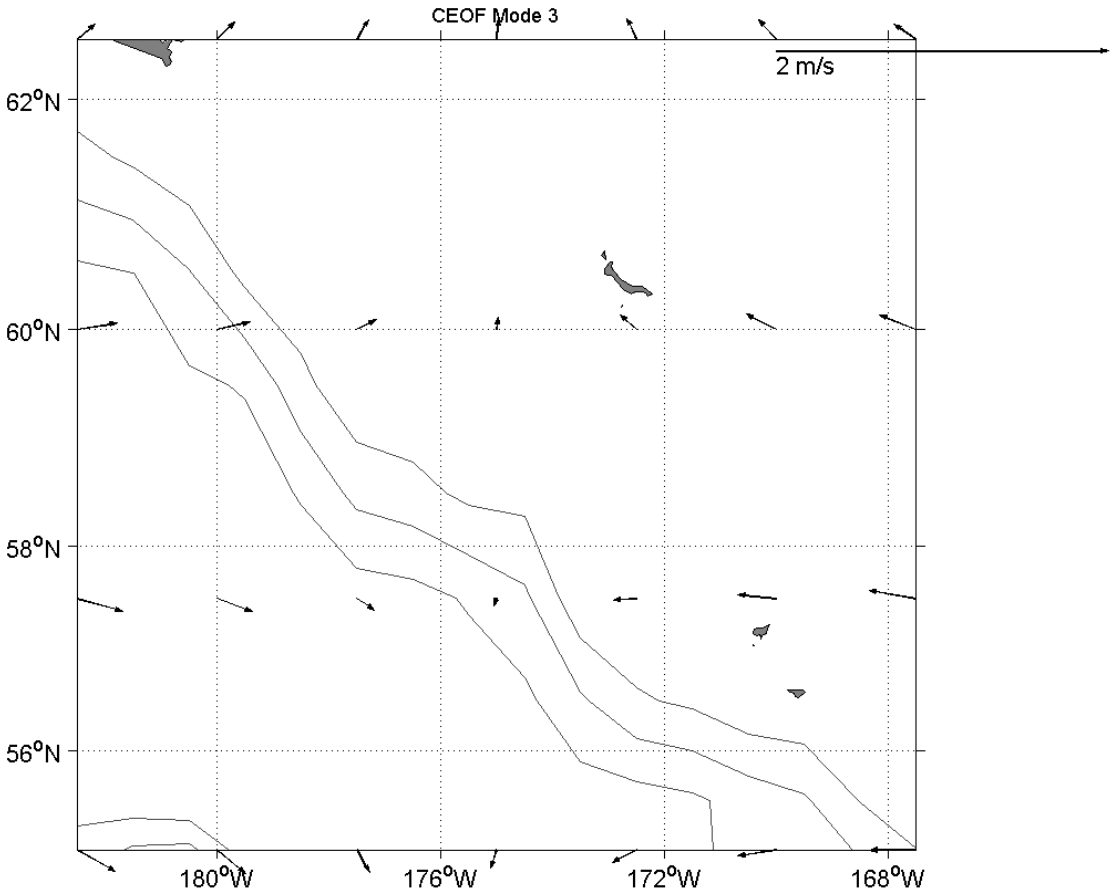

Figure E-3. Mode 3 for NCEP 6-hourly data from 1948-2007. The same small domain and method used to calculate CEOFs for the QuikSCAT data was used. This mode accounts for 12.0% of the variance.

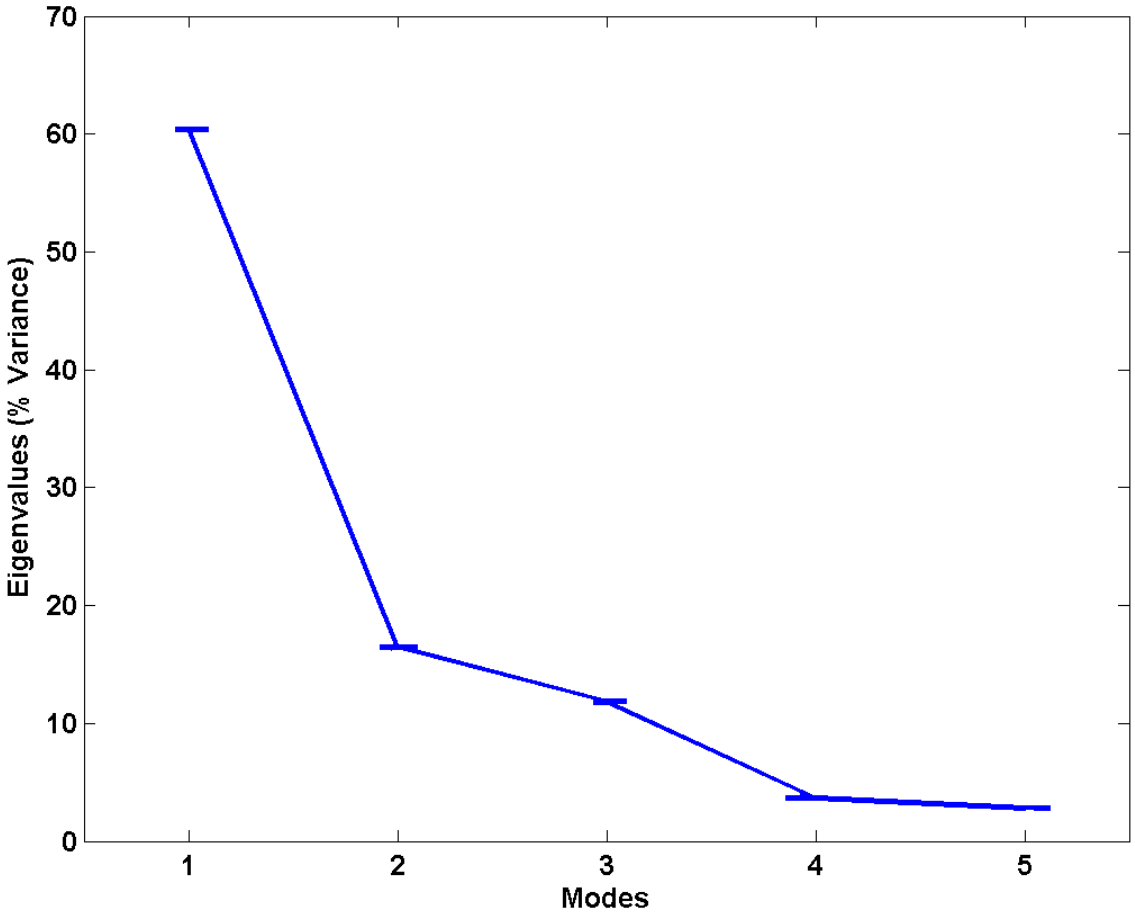

Figure E-4. Eigenvalues for the first five modes of the NCEP CEOFs. The first five modes are significant. These modes are based upon the winds calculated every six hours from 1948-2007. They are also calculated for the smaller domain over the Bering Sea shelf and deeper basin.

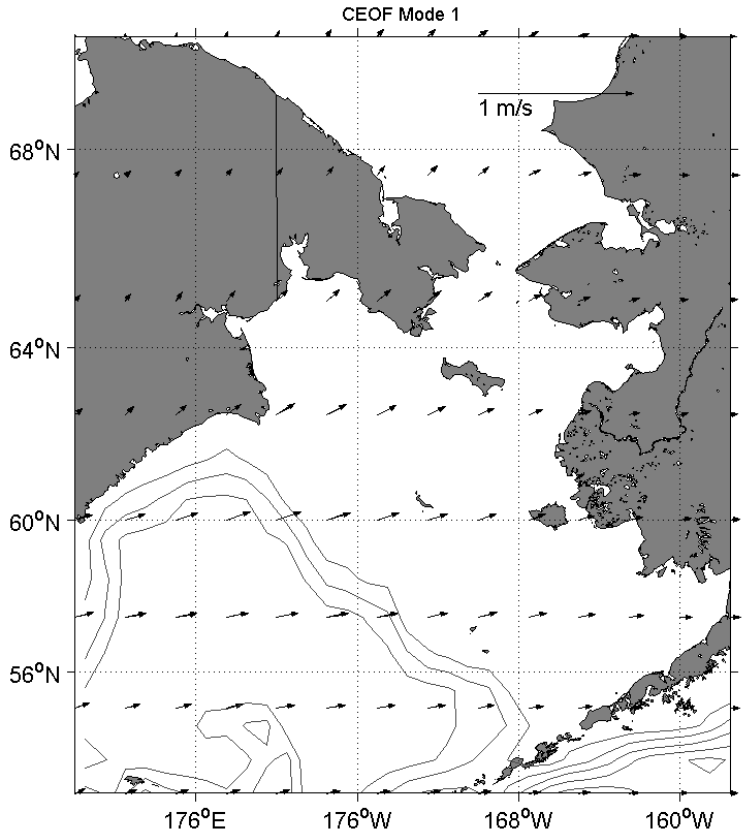

Figure E-5. Mode 1 for NCEP monthly data from 1948-2007.

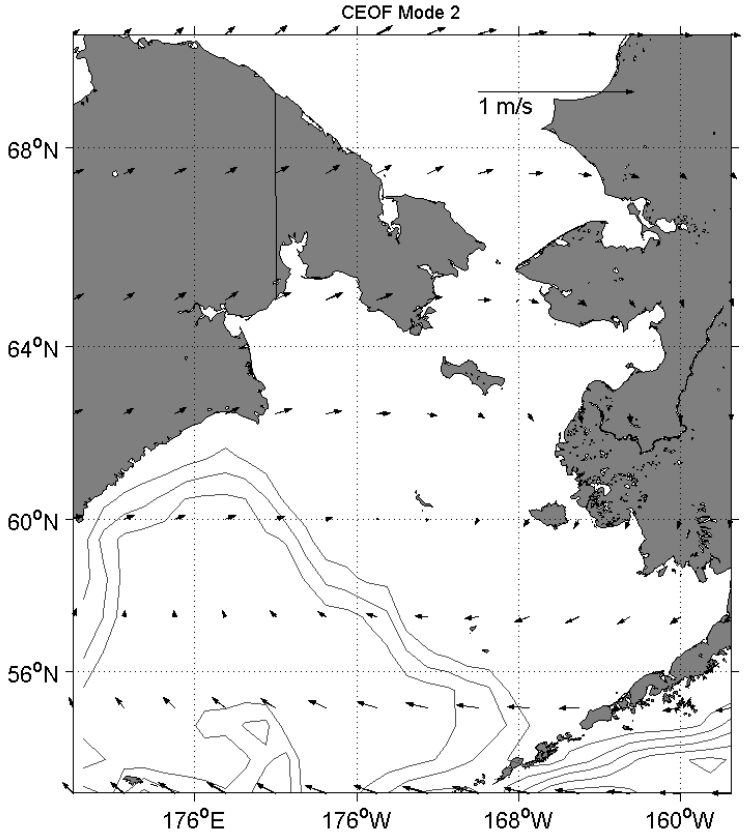

Figure E-6. Mode 2 for NCEP monthly data from 1948-2007.

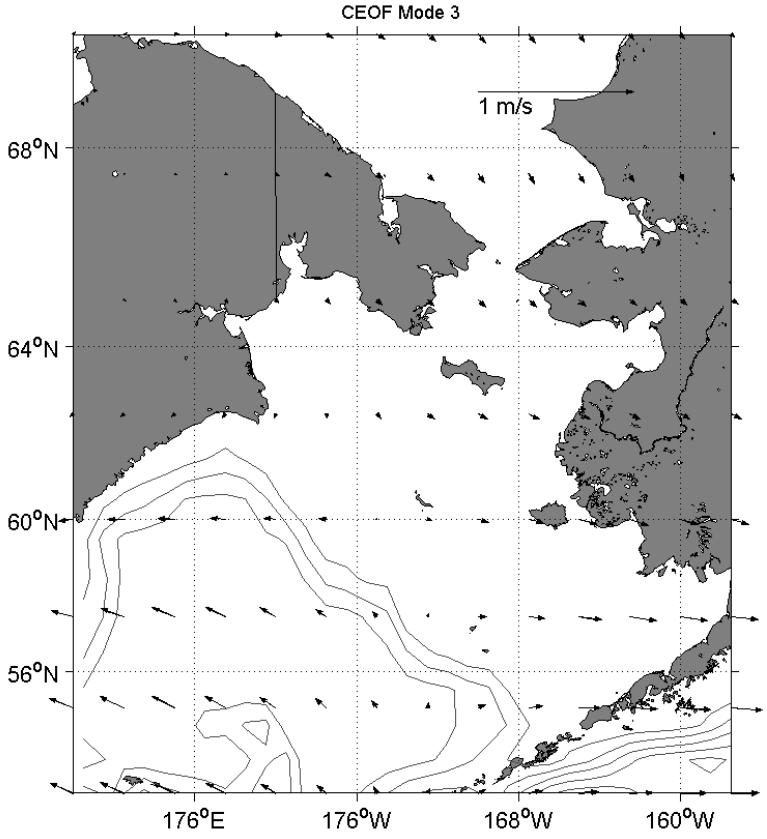

Figure E-7. Mode 3 for NCEP monthly data from 1948-2007.

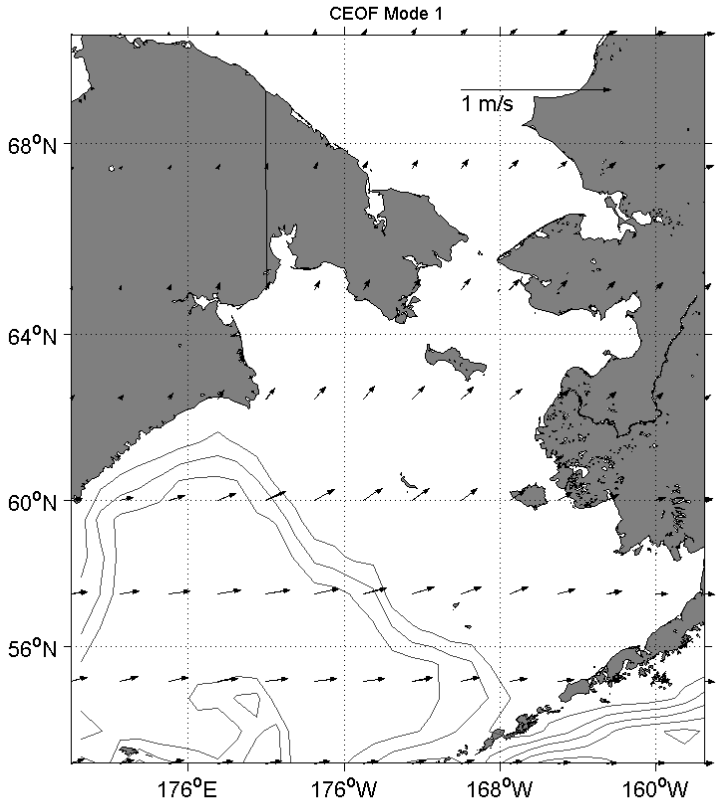

Figure E-8. Mode 1 for NCEP yearly data from 1948-2007.

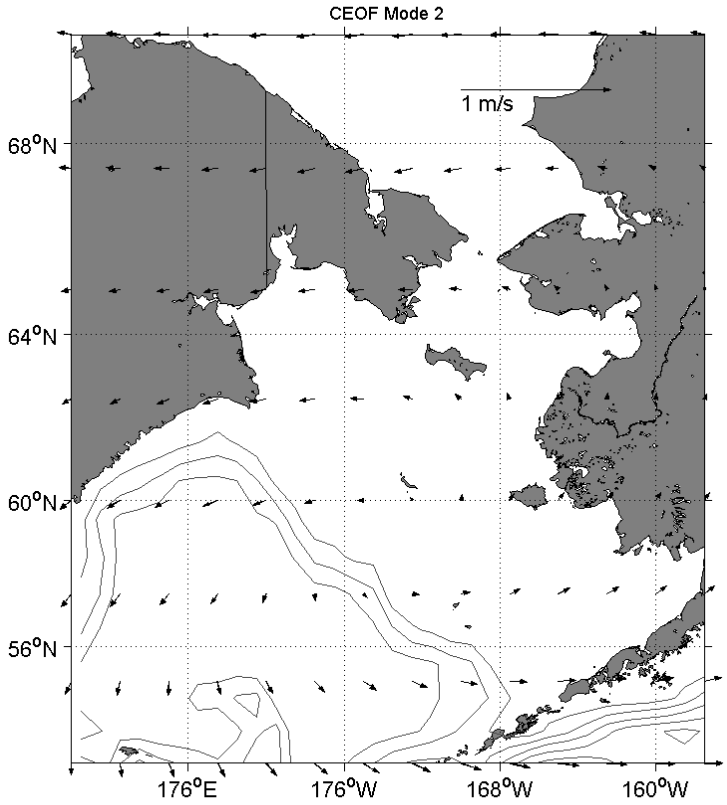

Figure E-9. Mode 2 for NCEP yearly data from 1948-2007.

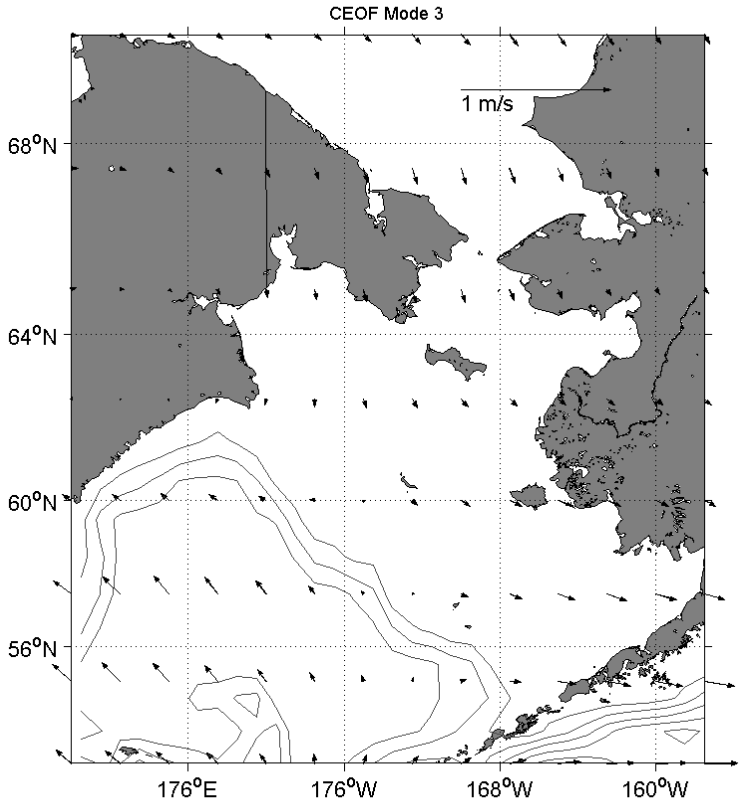

Figure E-10. Mode 3 for NCEP yearly data from 1948-2007.

Table E-1. Cross-correlation analyses between CEOF amplitudes and climate indices.

	PDO			**PNA**		
	Correlation Coefficient	Lags	p-value	Correlation Coefficient	Lags	p-value
Mode 1						
Real Component	0.19	30	<<0.05*	0.10	-32	0.01*
Imaginary Component	0.38	1	<<0.05*	0.37	0	<<0.05*
Magnitude	0.20	-34	<<0.05*	0.11	313	0.01*
Phase	0.25	1	<<0.05*	0.28	0	<<0.05*
Phase Speed	0.08	366	0.07	0.11	-168	0.01*
Mode 2						
Real Component	0.20	141	<<0.05*	0.11	-168	0.01*
Imaginary Component	0.23	1	<<0.05*	0.20	0	<<0.05*
Magnitude	0.17	-12	<<0.05*	0.09	-53	0.01*
Phase	0.16	0	<<0.05*	0.16	0	<<0.05*
Phase Speed	0.08	-102	<<0.05*	0.09	-60	0.01*
Mode 3						
Real Component	0.37	1	<<0.05	0.25	0	<<0.05*
Imaginary Component	0.13	-82	<<0.05*	0.16	0	<<0.05*
Magnitude	0.17	193	<<0.05*	0.09	231	0.02*
Phase	0.14	26	<<0.05*	0.10	-189	0.01*
Phase Speed	0.07	340	0.10	0.10	122	0.01*
Mode 4						
Real Component	0.17	9	<<0.05*	0.10	-246	0.02*
Imaginary Component	0.20	6	<<0.05*	0.11	199	0.01*
Magnitude	0.19	-70	<<0.05*	0.12	231	0.01*
Phase	0.14	8	<<0.05*	0.11	-45	<<0.05*
Phase Speed	0.09	66	<<0.05*	0.12	0	<<0.05*
	AO			**ALPI**		
	Correlation Coefficient	Lags	p-value	Correlation Coefficient	Lags	p-value
Mode 1						
Real Component	0.30	0	<<0.05*	0.28	-20	0.04
Imaginary Component	0.13	-258	<<0.05*	0.29	0	<<0.05*
Magnitude	0.15	-245	<<0.05*	0.28	19	<<0.05*
Phase	0.11	-221	0.01*	0.27	-7	<<0.05*
Phase Speed	0.09	-193	0.02*	0.22	-23	0.01*
Mode 2						
Real Component	0.13	-189	<<0.05*	0.22	6	0.05
Imaginary Component	0.12	-233	0.01*	0.25	-24	0.08
Magnitude	0.12	-65	<<0.05*	0.19	-4	0.08
Phase	0.11	-19	<<0.05*	0.26	-7	0.03*
Phase Speed	0.09	-26	0.01*	0.30	-6	0.02*
Mode 3						
Real Component	0.13	-295	0.01*	0.32	0	0.01*
Imaginary Component	0.12	78	<<0.05*	0.42	-2	<<0.05*
Magnitude	0.12	-293	0.01*	0.27	-2	0.02*
Phase	0.10	-209	0.01*	0.38	-2	<<0.05*
Phase Speed	0.09	-96	0.01*	0.36	11	0.01*
Mode 4						
Real Component	0.13	123	<<0.05*	0.29	-1	0.01*
Imaginary Component	0.13	-38	<<0.05*	0.26	6	0.03*
Magnitude	0.13	114	<<0.05*	0.29	19	0.03*
Phase	0.13	-38	<<0.05*	0.23	6	0.05
Phase Speed	0.10	-36	0.01*	0.35	-19	0.01*

Table E-1 (Continued)

	NP			WP Winter		
	Correlation Coefficient	Lags	p-value	Correlation Coefficient	Lags	p-value
Mode 1						
Real Component	0.25	-12	0.05	0.31	-13	0.02*
Imaginary Component	0.32	12	0.02*	0.35	-24	0.03*
Magnitude	0.24	6	0.05	0.31	-9	0.02*
Phase	0.30	12	0.03*	0.33	-24	0.03*
Phase Speed	0.20	20	0.13	0.17	10	0.13
Mode 2						
Real Component	0.25	-14	0.06	0.38	-2	<<0.05*
Imaginary Component	0.31	-3	0.01*	0.31	-39	0.12
Magnitude	0.32	-4	0.01*	0.23	-10	0.06
Phase	0.32	-25	0.04*	0.34	-4	0.01*
Phase Speed	0.22	10	0.08	0.20	-33	0.18
Mode 3						
Real Component	0.33	-3	0.01*	0.22	-4	0.06
Imaginary Component	0.37	-3	<<0.05*	0.24	-24	0.10
Magnitude	0.26	-6	0.03*	0.21	7	0.08
Phase	0.24	-3	0.04*	0.21	5	0.07
Phase Speed	0.30	30	0.07	0.20	-14	0.11
Mode 4						
Real Component	0.40	-1	<<0.05*	0.20	-16	0.11
Imaginary Component	0.38	2	<<0.05*	0.26	-5	0.03*
Magnitude	0.27	-4	0.03*	0.29	-10	0.03*
Phase	0.24	4	0.04*	0.21	-2	0.07
Phase Speed	0.25	36	0.15	0.15	-8	0.15
	WP Spring					
	Correlation Coefficient	Lags	p-value			
Mode 1						
Real Component	0.37	-2	<<0.05*			
Imaginary Component	0.45	9	<<0.05*			
Magnitude	0.23	16	0.08			
Phase	0.30	9	0.02*			
Phase Speed	0.08	0	0.29			
Mode 2						
Real Component	0.26	19	0.06			
Imaginary Component	0.25	0	0.03*			
Magnitude	0.31	0	0.01*			
Phase	0.21	-25	0.13			
Phase Speed	0.10	-8	0.24			
Mode 3						
Real Component	0.13	29	0.26			
Imaginary Component	0.27	5	0.03*			
Magnitude	0.31	-4	0.01*			
Phase	0.25	5	0.04*			
Phase Speed	0.09	12	0.27			
Mode 4						
Real Component	0.34	0	0.01*			
Imaginary Component	0.22	-13	0.08			
Magnitude	0.23	-18	0.09			
Phase	0.20	-22	0.14			
Phase Speed	0.09	18	0.29			

Note: Significant correlations are indicated by an asterisk next to each p-value.

Appendix F

Monthly Means and Errors of Surface Ekman Convergence and Divergence within the Small Domain (Figure 8) over the Bering Sea Shelf

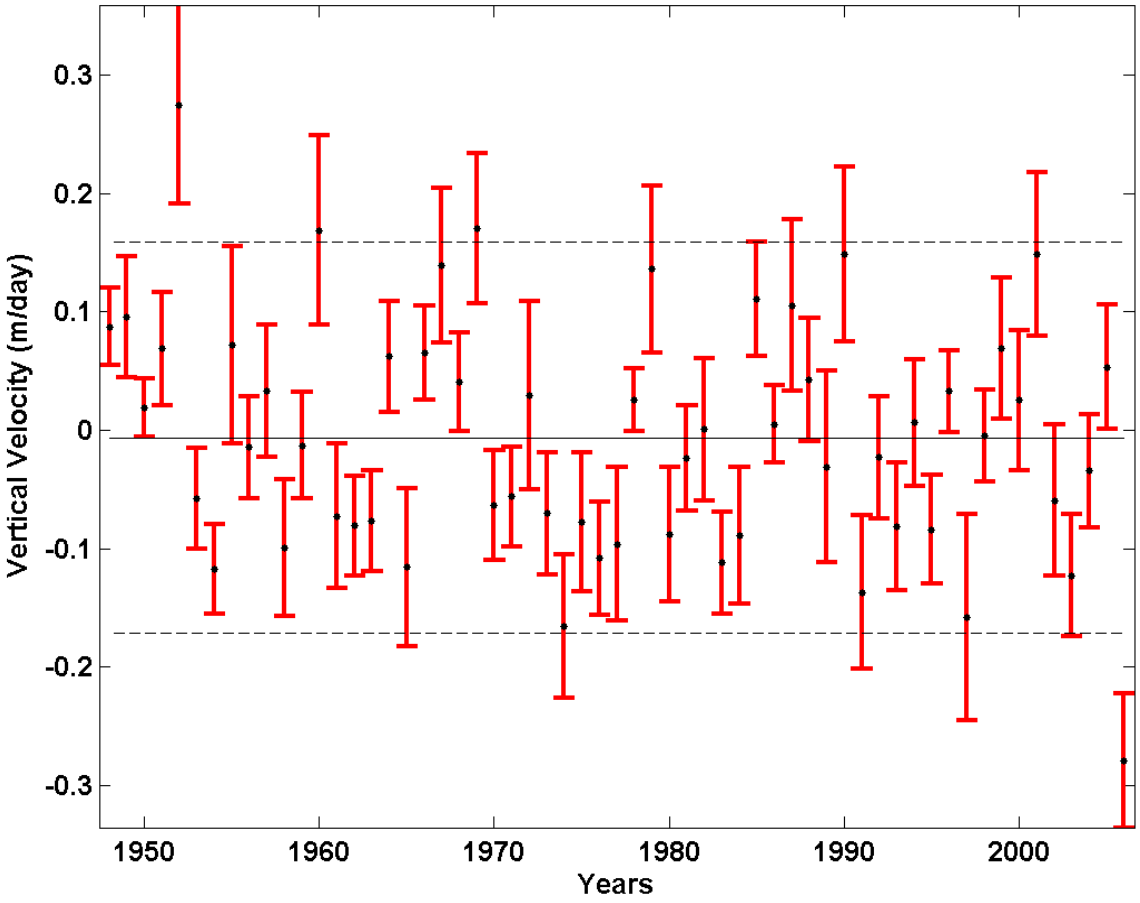

Figure F-1. The monthly means and errors of Ekman suction and pumping within the small domain over the Bering Sea shelf for January. Positive values indicate surface Ekman suction and negative values indicate Ekman pumping. NCEP wind data computed every six hours from 1948-2007 is used in the plot. The monthly means are indicated by black dots. The error bars for each mean are calculated at the 95% confidence level and are shown in red. The overall mean for the month and the errors at the 95% confidence level are shown in black.

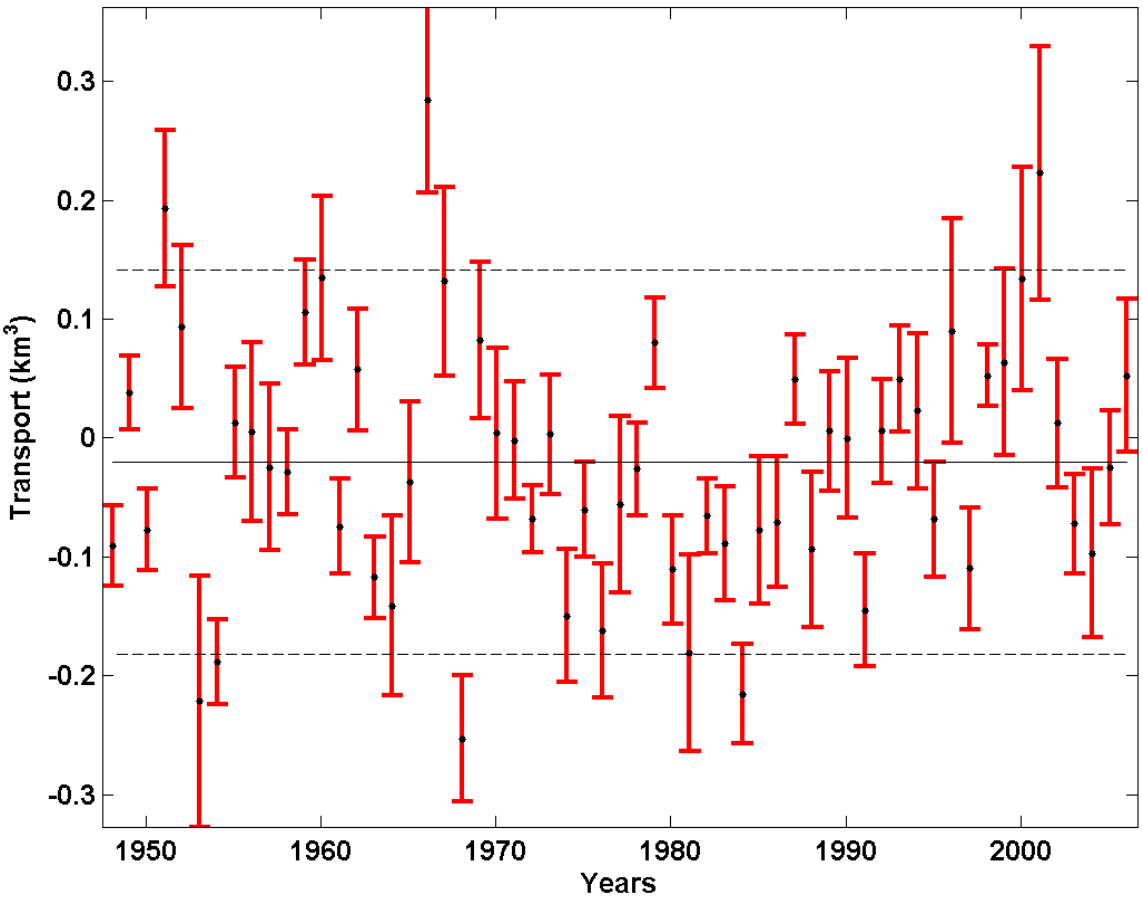

Figure F-2. The monthly means and errors of Ekman suction and pumping within the small domain over the Bering Sea shelf for February. Positive values indicate surface Ekman suction and negative values indicate Ekman pumping. NCEP wind data computed every six hours from 1948-2007 is used in the plot. The monthly means are indicated by black dots. The error bars for each mean are calculated at the 95% confidence level and are shown in red. The overall mean for the month and the errors at the 95% confidence level are shown in black.

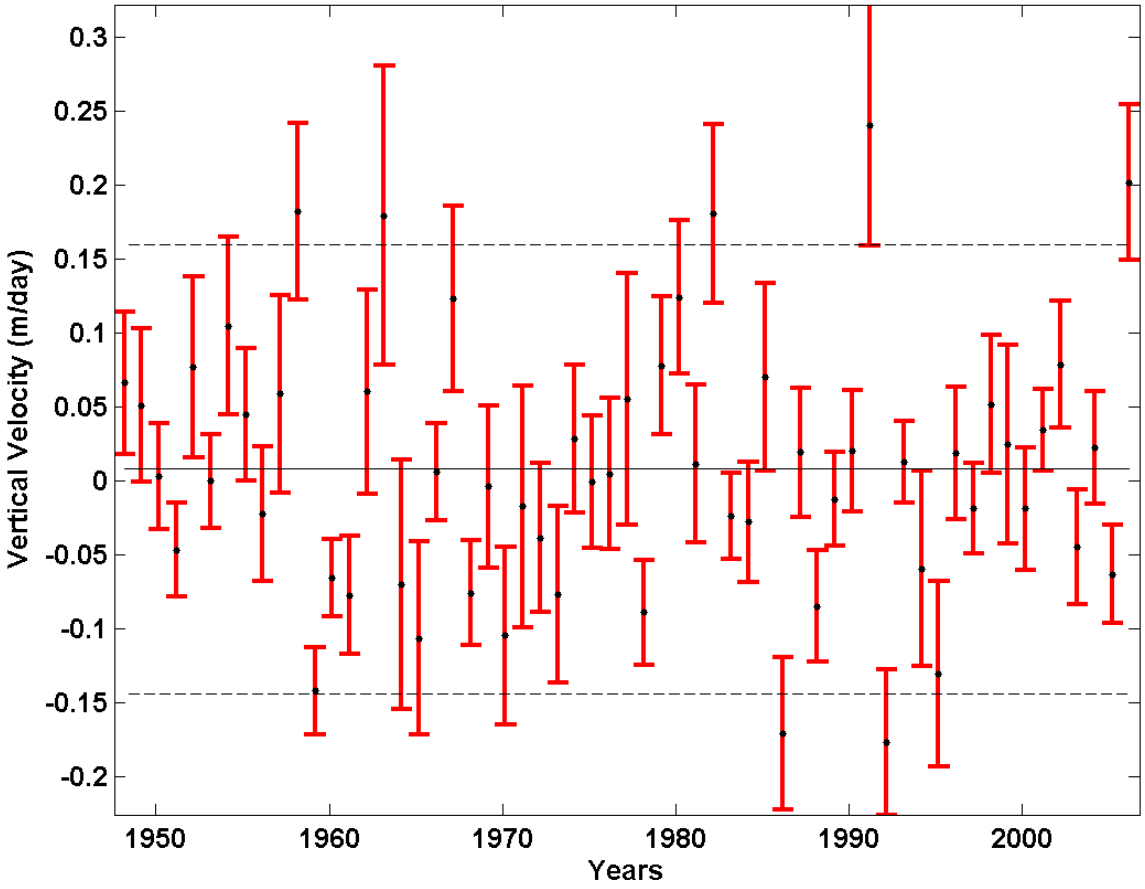

Figure F-3. The monthly means and errors of Ekman suction and pumping within the small domain over the Bering Sea shelf for March. Positive values indicate surface Ekman suction and negative values indicate Ekman pumping. NCEP wind data computed every six hours from 1948-2007 is used in the plot. The monthly means are indicated by black dots. The error bars for each mean are calculated at the 95% confidence level and are shown in red. The overall mean for the month and the errors at the 95% confidence level are shown in black.

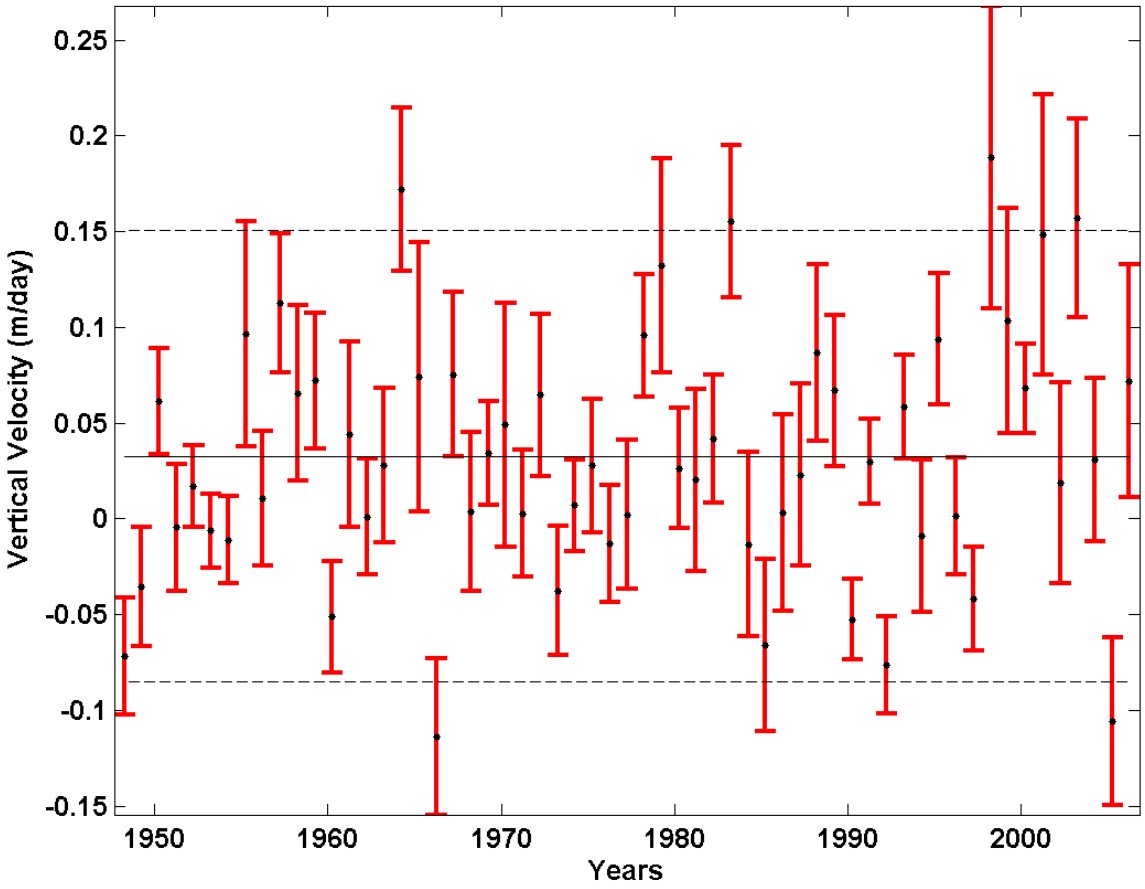

Figure F-4. The monthly means and errors of Ekman suction and pumping within the small domain over the Bering Sea shelf for April. Positive values indicate surface Ekman suction and negative values indicate Ekman pumping. NCEP wind data computed every six hours from 1948-2007 is used in the plot. The monthly means are indicated by black dots. The error bars for each mean are calculated at the 95% confidence level and are shown in red. The overall mean for the month and the errors at the 95% confidence level are shown in black dashed lines.

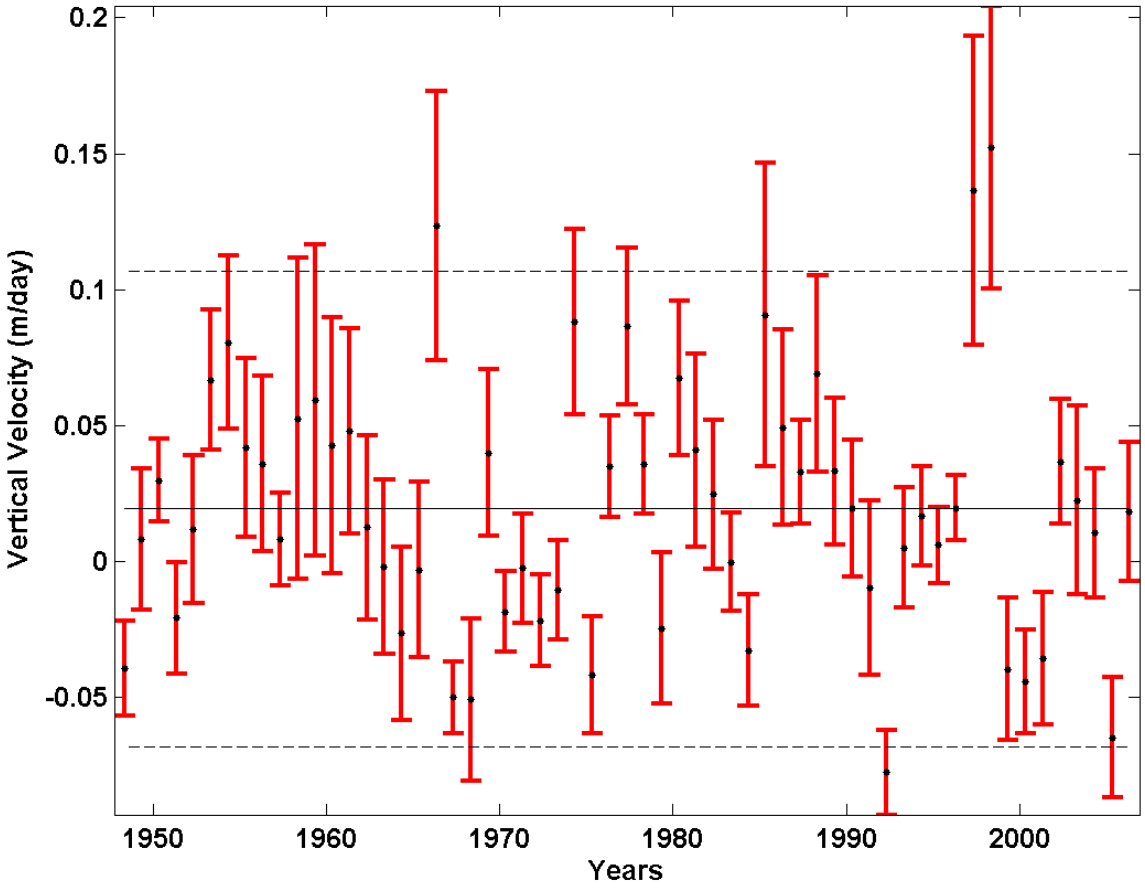

Figure F-5. The monthly means and errors of Ekman suction and pumping within the small d**omain over the Bering Sea shelf for May.** Positive values indicate surface Ekman suction and negative values indicate Ekman pumping. NCEP wind data computed every six hours from 1948-2007 is used in the plot. The monthly means are indicated by black dots. The error bars for each mean are calculated at the 95% confidence level and are shown in red. The overall mean for the month and the errors at the 95% confidence level are shown in black.

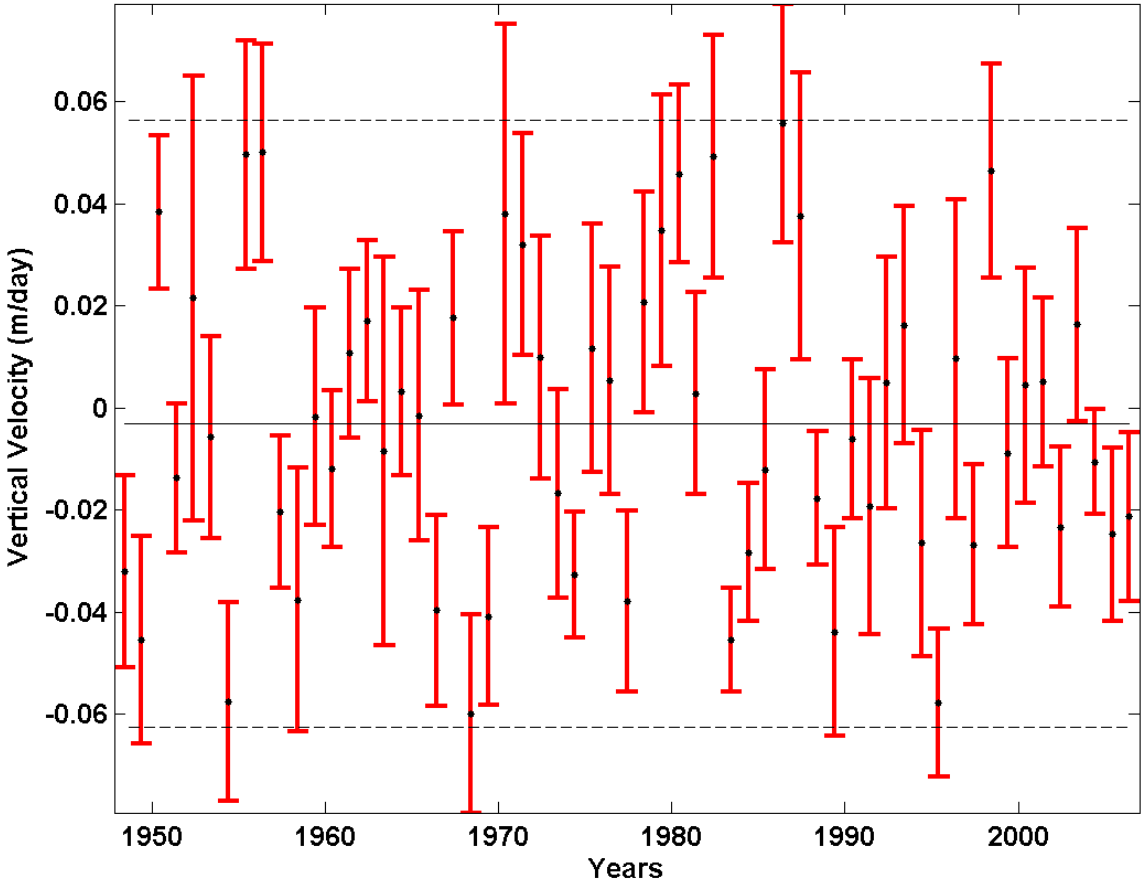

Figure F-6. The monthly means and errors of Ekman suction and **pumping within the small domain over the Bering Sea shelf for June.** Positive values indicate surface Ekman suction and negative values indicate Ekman pumping. NCEP wind data computed every six hours from 1948-2007 is used in the plot. The monthly means are indicated by black dots. The error bars for each mean are calculated at the 95% confidence level and are shown in red. The overall mean for the month and the errors at the 95% confidence level are shown in black.

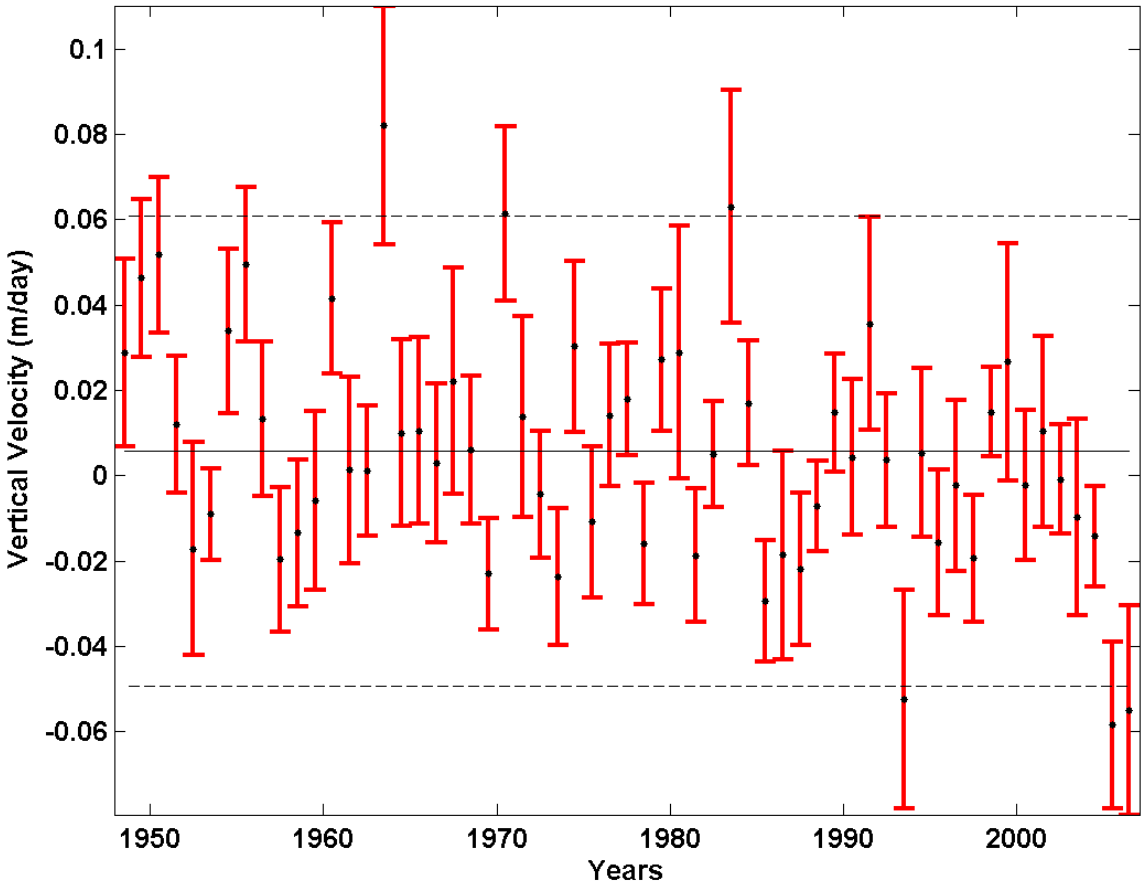

Figure F-7. The monthly means and errors of Ekman suction and pumping within the small domain over the Bering Sea shelf for July. Positive values indicate surface Ekman suction and negative values indicate Ekman pumping. NCEP wind data computed every six hours from 1948-2007 is used in the plot. The monthly means are indicated by black dots. The error bars for each mean are calculated at the 95% confidence level and are shown in red. The overall mean for the month and the errors at the 95% confidence level are shown in black.

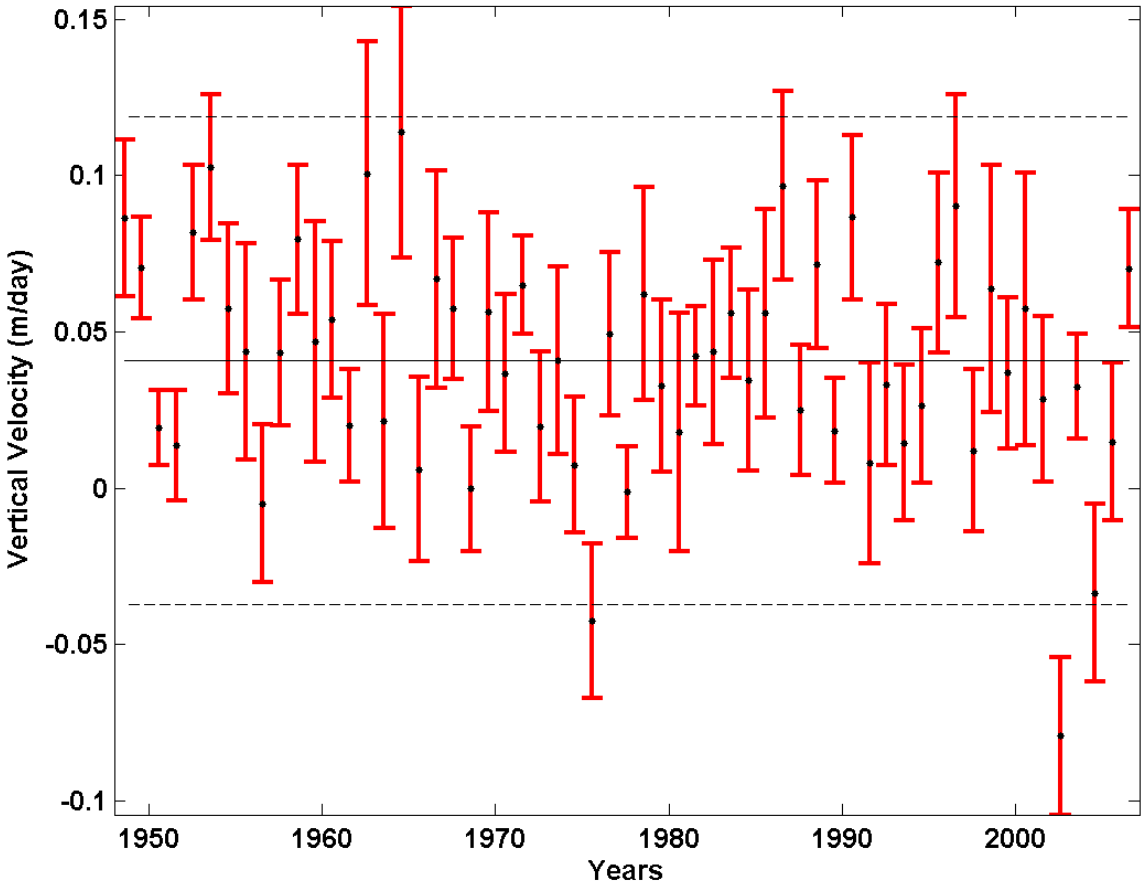

Figure F-8. The monthly means and errors of Ekman suction and pumping within the small domain over the Bering Sea shelf for August. Positive values indicate surface Ekman suction and negative values indicate Ekman pumping. NCEP wind data computed every six hours from 1948-2007 is used in the plot. The monthly means are indicated by black dots. The error bars for each mean are calculated at the 95% confidence level and are shown in red. The overall mean for the month and the errors at the 95% confidence level are shown in black.

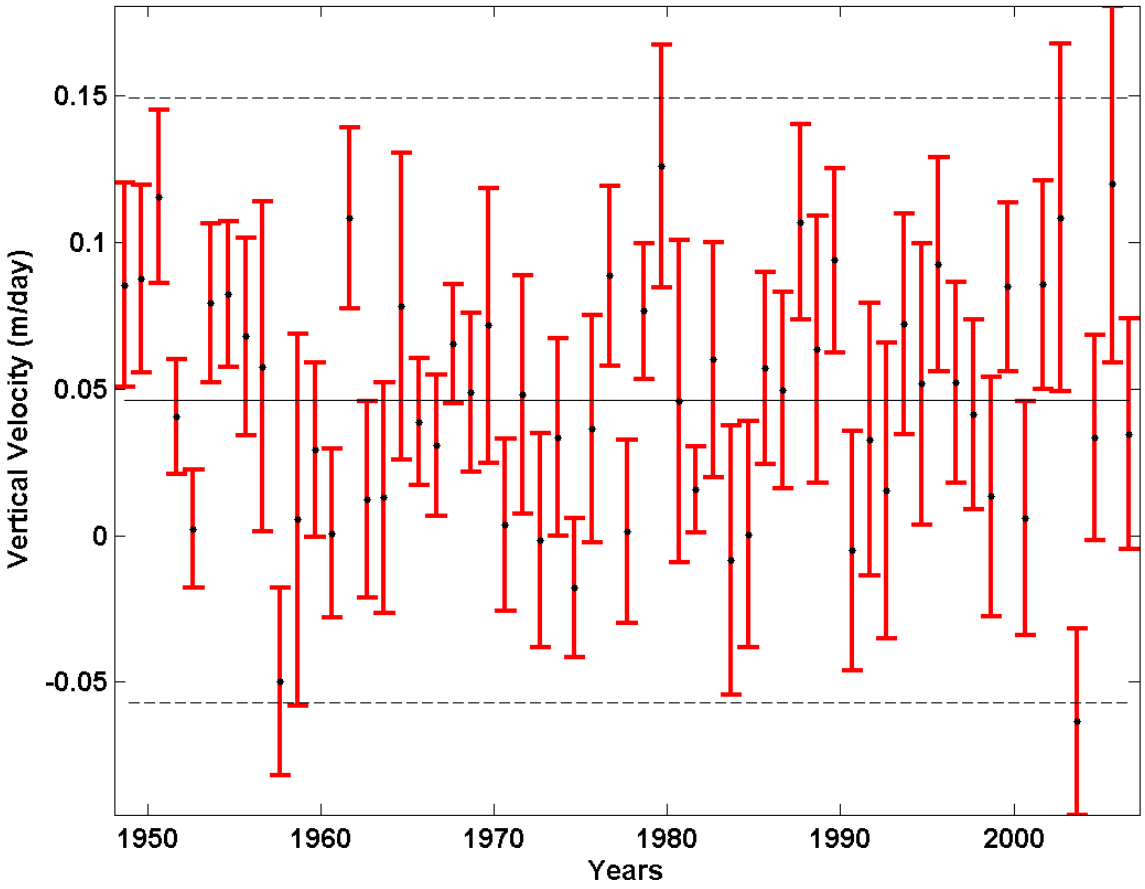

Figure F-9. The monthly means and errors of Ekman suction and pumping within the small domain over the Bering Sea shelf for September. Positive values indicate surface Ekman suction and negative values indicate Ekman pumping. NCEP wind data computed every six hours from 1948-2007 is used in the plot. The monthly means are indicated by black dots. The error bars for each mean are calculated at the 95% confidence level and are shown in red. The overall mean for the month and the errors at the 95% confidence level are shown in black.

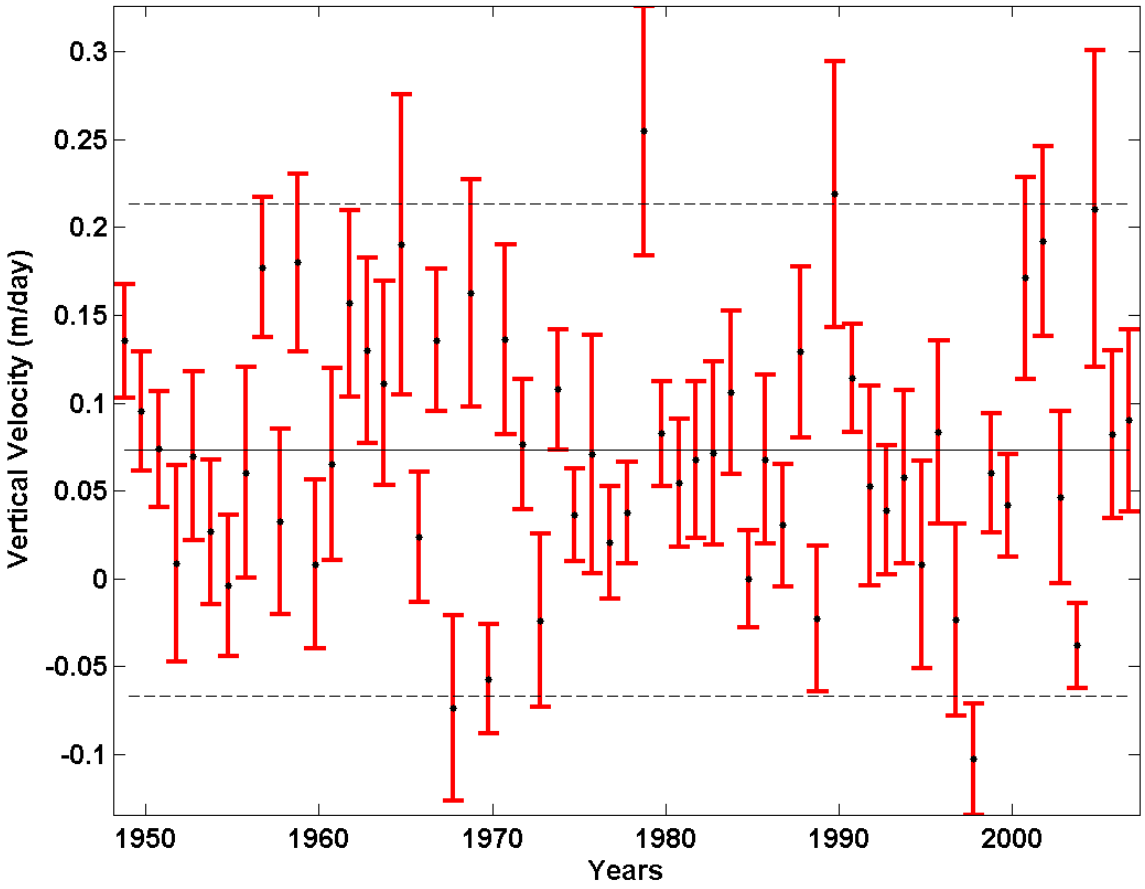

Figure F-10. The monthly means and errors of Ekman suction and pumping within the small domain over the Bering Sea shelf for October. Positive values indicate surface Ekman suction and negative values indicate Ekman pumping. NCEP wind data computed every six hours from 1948-2007 is used in the plot. The monthly means are indicated by black dots. The error bars for each mean are calculated at the 95% confidence level and are shown in red. The overall mean for the month and the errors at the 95% confidence level are shown in black.

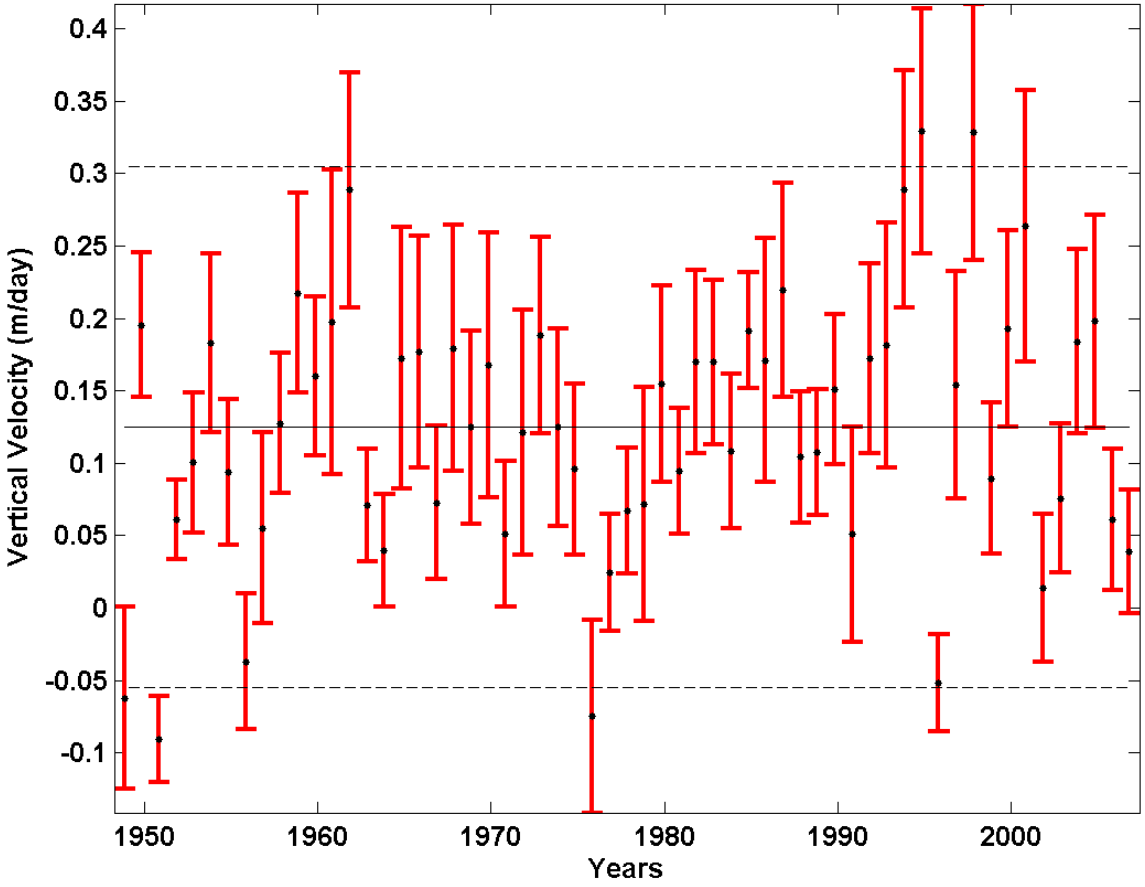

Figure F-11. The monthly means and errors of Ekman suction and pumping within the small domain over the Bering Sea shelf for Nov**ember.** Positive values indicate surface Ekman suction and negative values indicate Ekman pumping. NCEP wind data computed every six hours from 1948-2007 is used in the plot. The monthly means are indicated by black dots. The error bars for each mean are calculated at the 95% confidence level and are shown in red. The overall mean for the month and the errors at the 95% confidence level are shown in black.

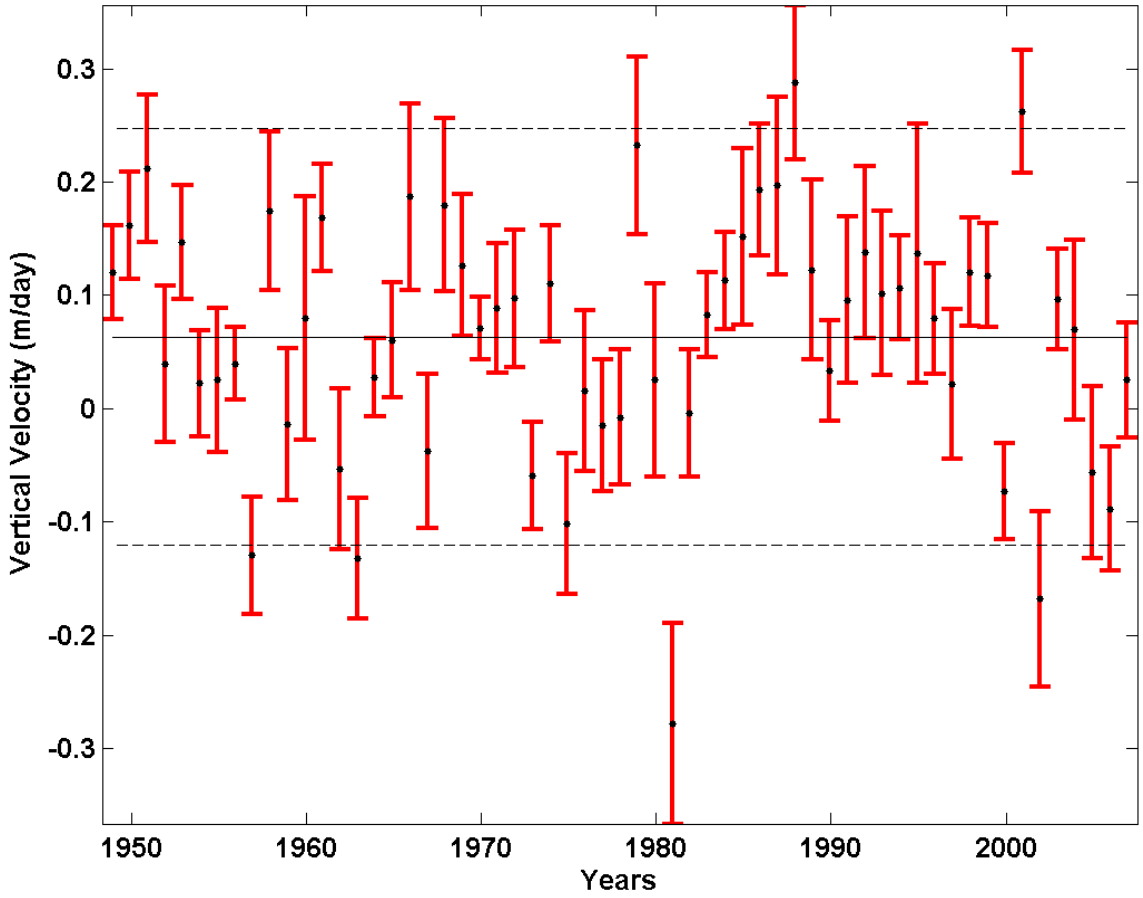

Figure F-12. The monthly means and errors of Ekman suction and pumping within the small domain **over the Bering Sea shelf for December.** Positive values indicate surface Ekman suction and negative values indicate Ekman pumping. NCEP wind data computed every six hours from 1948-2007 is used in the plot. The monthly means are indicated by black dots. The error bars for each mean are calculated at the 95% confidence level and are shown in red. The overall mean for the month and the errors at the 95% confidence level are shown in black.

Appendix G

Price-Weller-Pinkel (PWP) Model Results

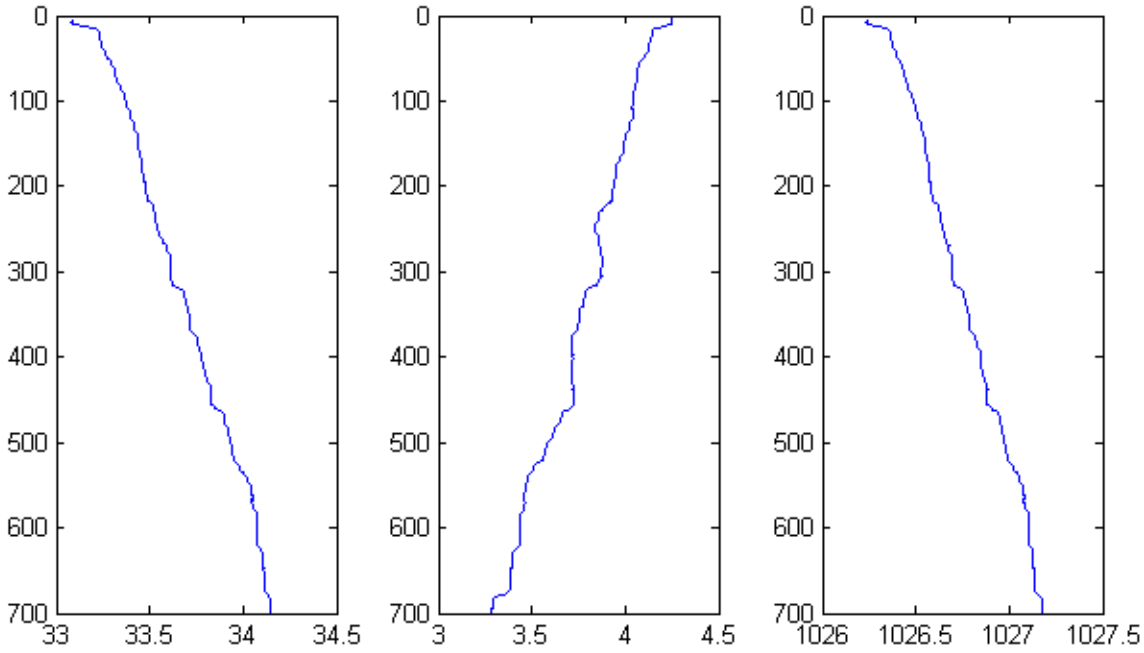

Figure G-1**. The initial vertical profile used.** The data are taken from a CTD deployment at 53.72 ºN, 167.73 ºW on March 11, 2001. The left panel is salinity, the middle panel is temperature, and the right panel is density. This profile is statically stable and was used for all of the model runs.

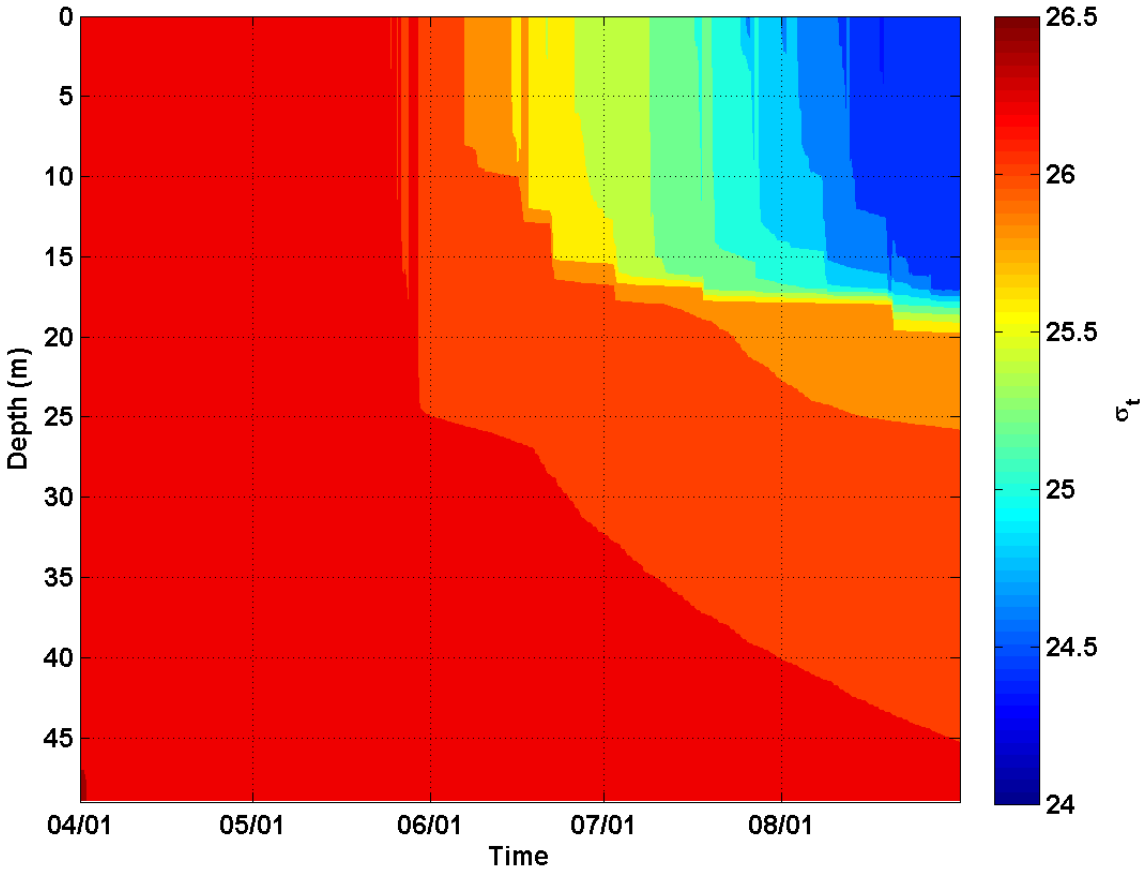

Figure G-2. PWP model output for the model run which used QuikSCAT wind measurements from April 2001 through August 2001. The wind measurements were taken from a grid point near the Pribilof Islands (54.1250 ºN, 168.8750 ºW). The winds were interpolated to one hour intervals so the water column profiles were calculated after each one hour time step.

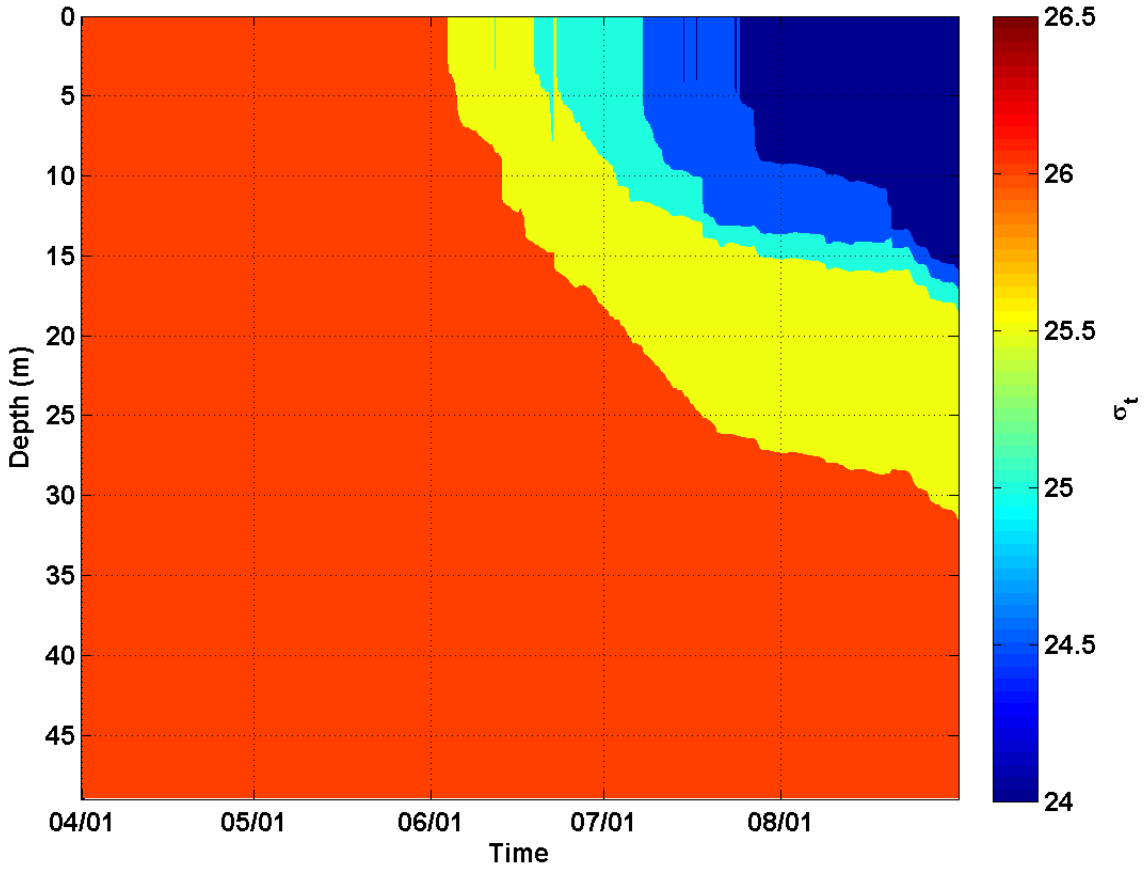

Figure G-3. PWP model output for the model run which used QuikSCAT wind measurements from April 2001 through August **2001 and calculated values of wind-stress-curl.** The wind measurements were taken from a grid point near the Pribilof Islands (54.1250 ºN, 168.8750 ºW). The winds were interpolated to one hour intervals so the water column profiles were calculated after each one hour time step.

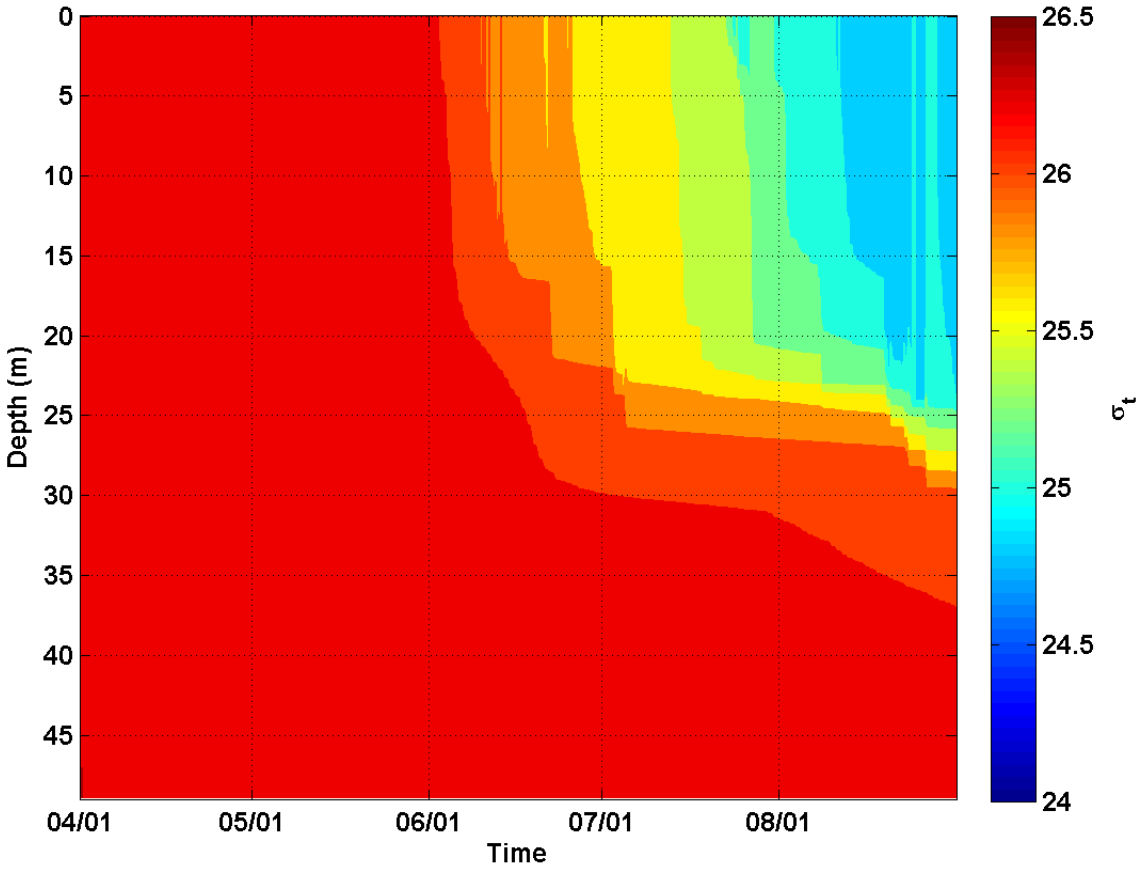

Figure G-4. PWP model output for the model run which used NCEP wind measurements from April 2001 through August 2001. The wind measurements were taken from a grid point near the Pribilof Islands (55.00 ºN, 167.50 ºW). The winds were interpolated to one hour intervals so the water column profiles were calculated after each one hour time step.

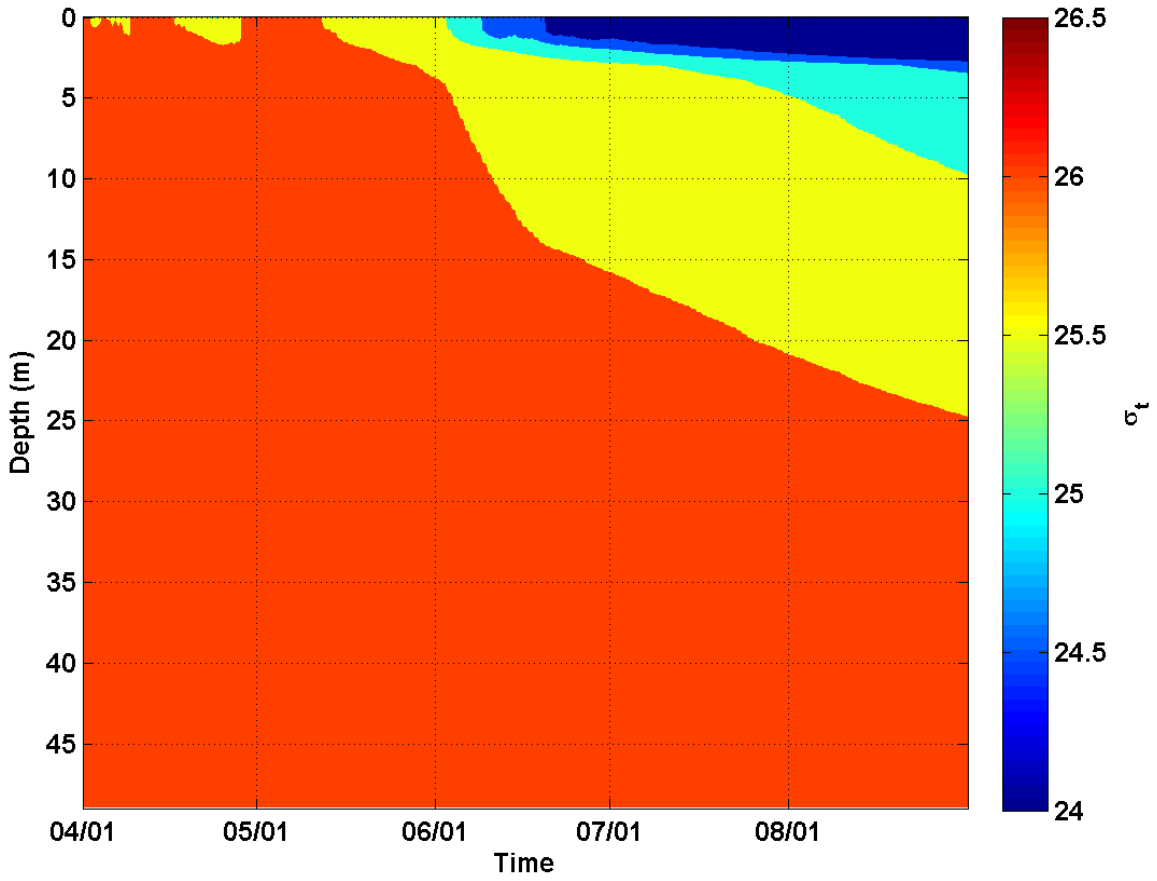

Figure G-5. PWP model output for the model run which used no wind measurements from April 2001 through August 2001. The flux data were taken from a grid point near the Pribilof Islands (55.00 ºN, 167.50 ºW). The water column profiles were calculated after each one hour time step.

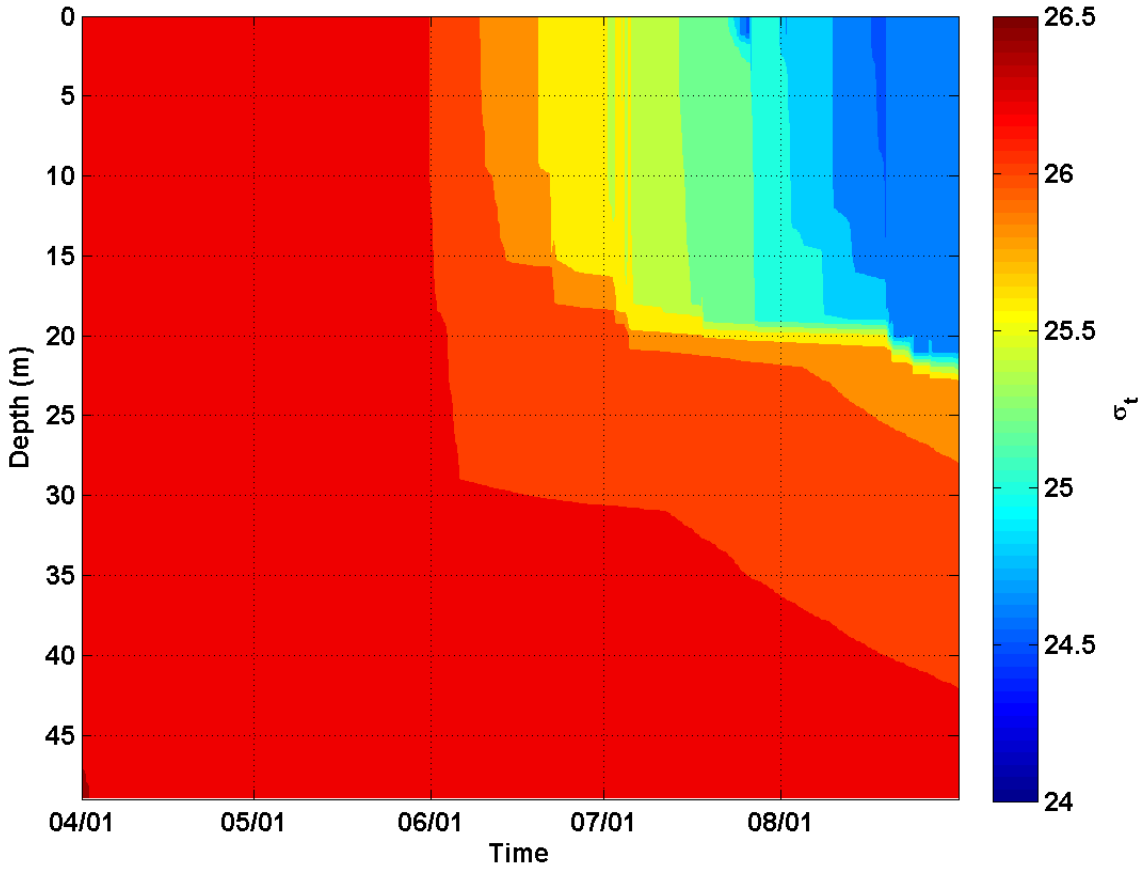

Figure G-6. PWP model output for the model run which used under-sampled NCEP wind measurements from Apr**il 2001 through August 2001.** The wind measurements were taken from a grid point near the Pribilof Islands (55.00 ºN, 167.50 ºW) and only from the 06:00 and 18:00 hrs sampling times. These are roughly the same times as the QuikSCAT wind measurements. The winds were interpolated to one hour intervals so the water column profiles were calculated after each one hour time step.

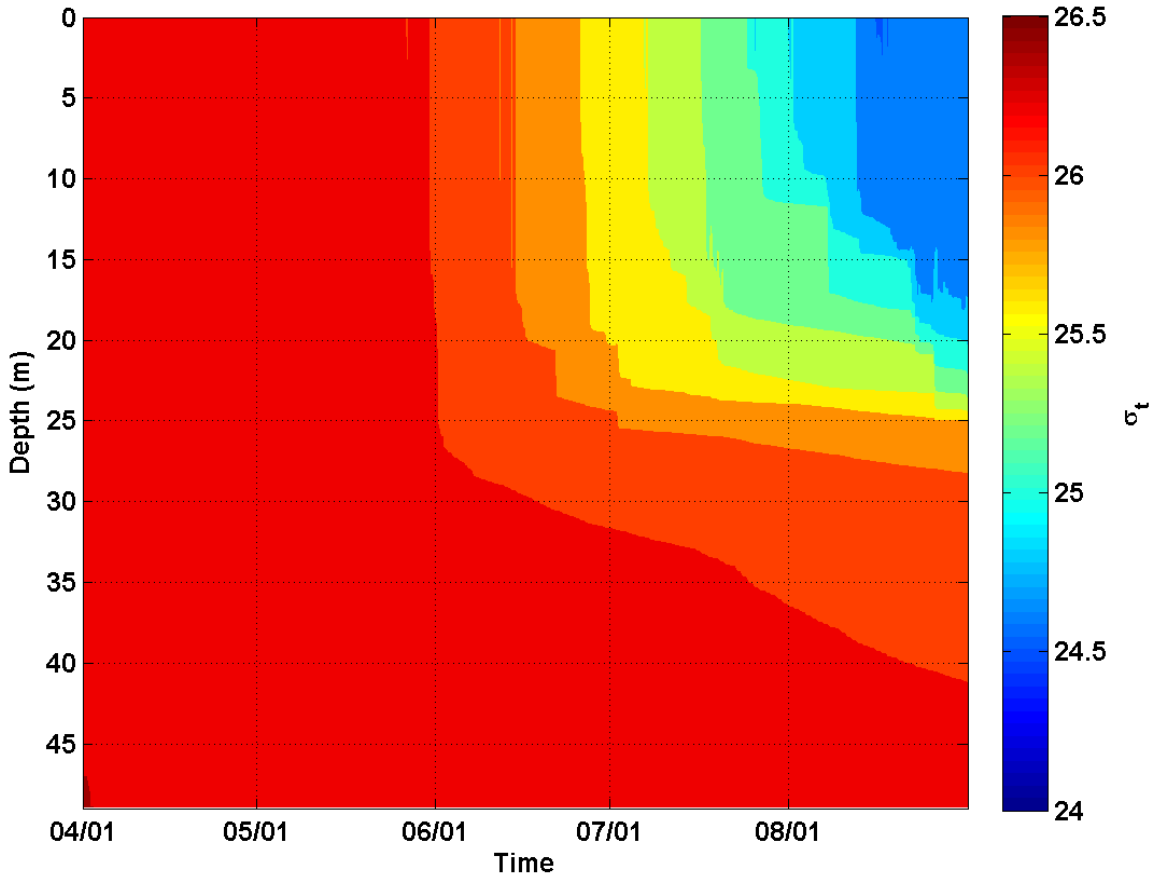

Figure G-7. PWP model output for the model run which used NWS wind measurements from April 2001 through August 2001. The wind measurements were taken from station PASN on St. Paul Island (57.1667 ºN, 170.2167 ºW). The winds were interpolated to one hour intervals so the water column profiles were calculated after each one hour time step.

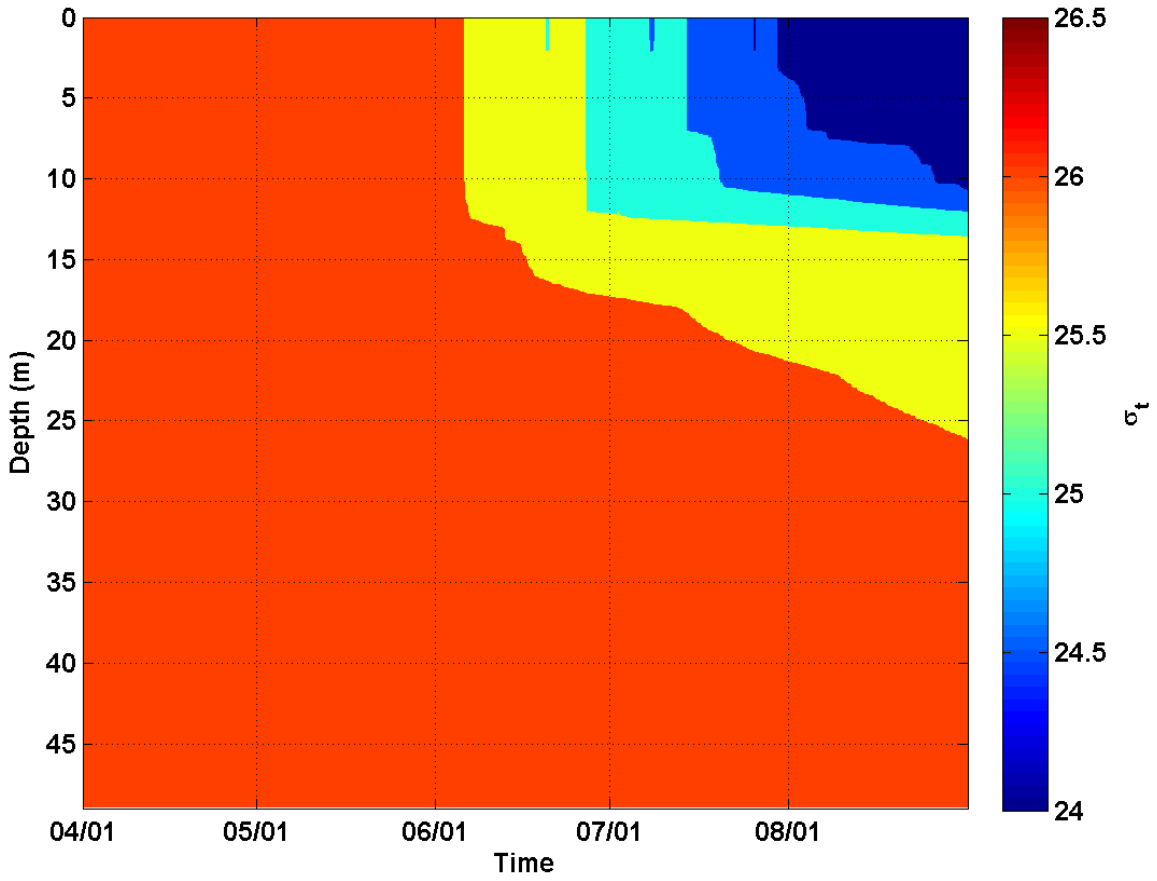

Figure G-8. PWP model output for the m**odel run which used NWS wind measurements from April 2001 through August 2001.** The wind measurements were taken from station PASN on St. Paul Island (57.1667 ºN, 170.2167 ºW) and low-pass filtered at 20 hours. The winds were then interpolated to one hour intervals so the water column profiles were calculated after each one hour time step.

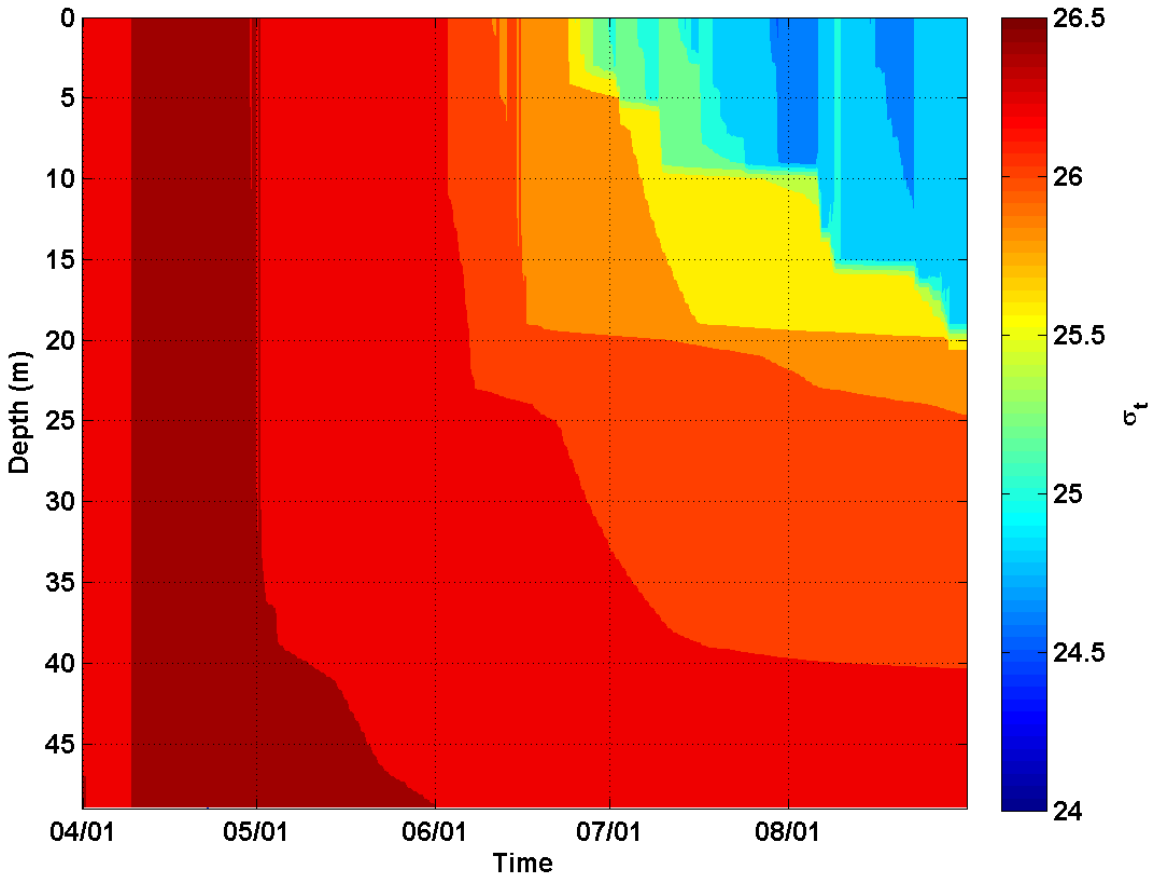

Figure G-9. PWP model output for the model run which used QuikSCAT wind measurements from April 2005 through August 2005. The wind measurements were taken from a grid point over the central shelf (58.1250 ºN, 172.8750 ºW). The winds were interpolated to one hour intervals so the water column profiles were calculated after each one hour time step.

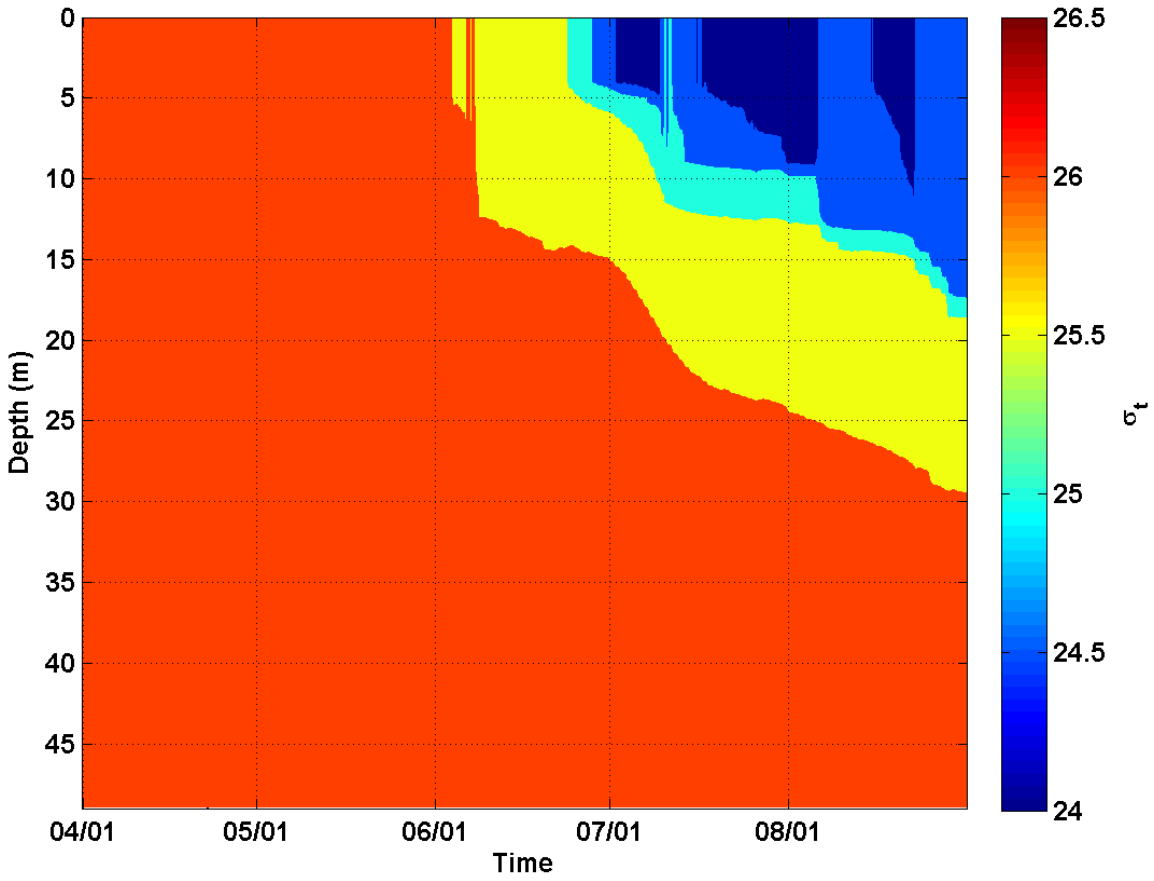

Figure G-10. PWP model output for the model run which used QuikSCAT wind measurements from April 2005 through August 2005 and calculated values of wind-stress-curl. The wind measurements were taken from a grid point over the central shelf (58.1250 ºN, 172.8750 ºW). The winds were interpolated to one hour intervals so the water column profiles were calculated after each one hour time step.

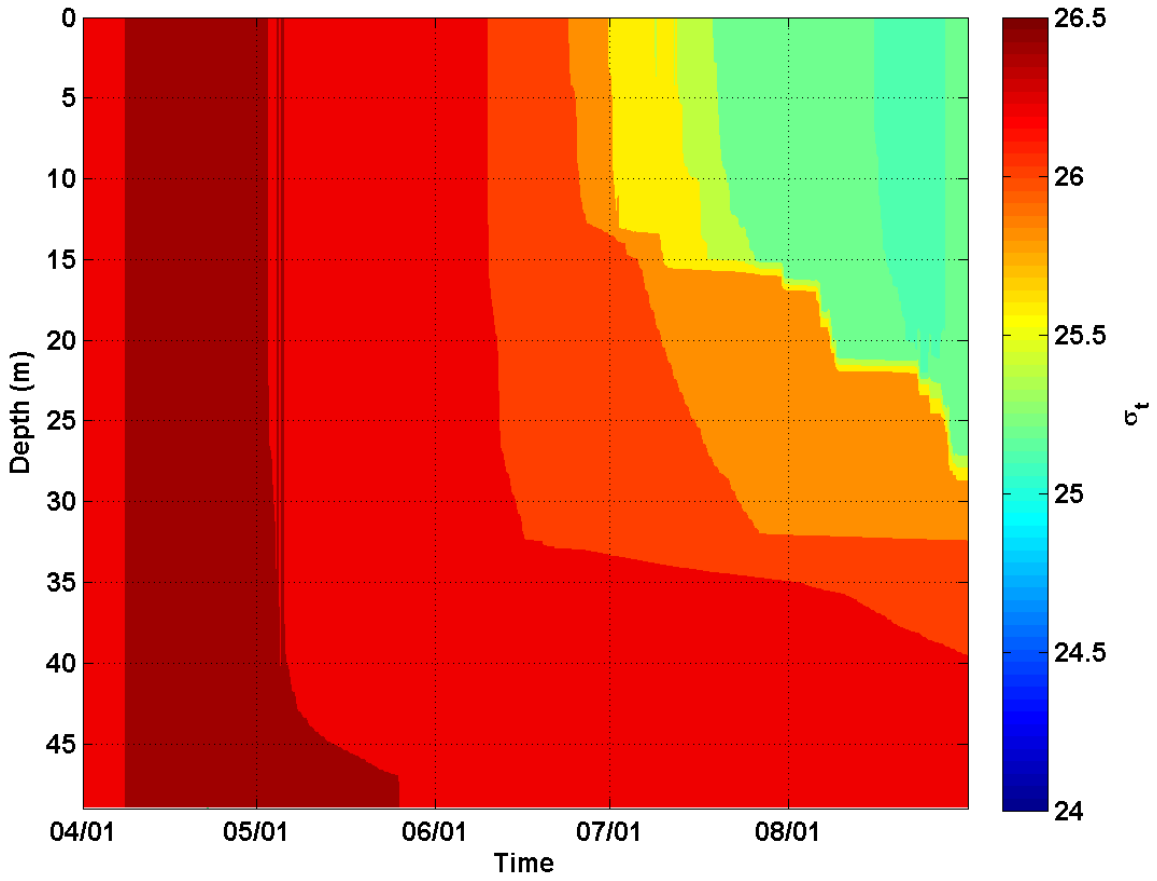

Figure G-11. PWP model output for the model run which used NCEP wind measurements from April 2005 through August 2005. The wind measurements were taken from a grid point over the central shelf (58.1250 ºN, 172.8750 ºW). The winds were interpolated to one hour intervals so the water column profiles were calculated after each one hour time step.

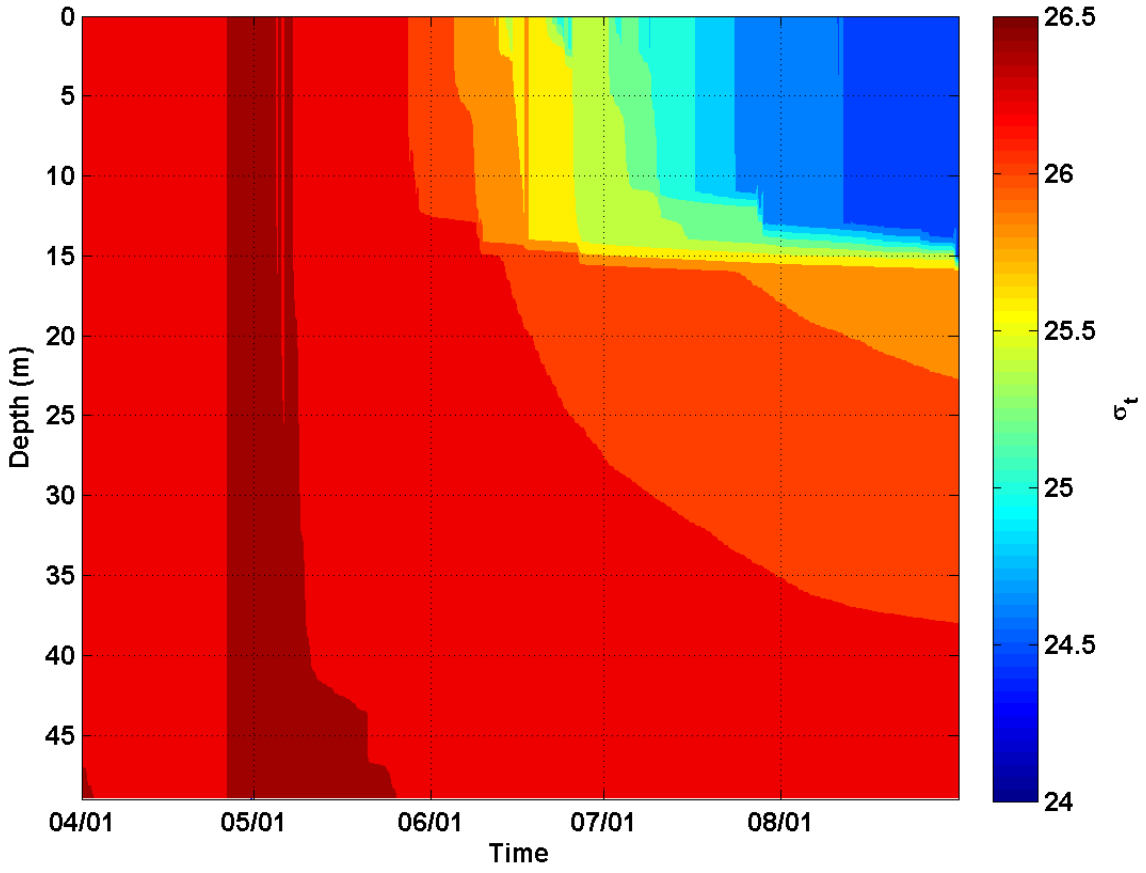

Figure G-12. PWP model output for the model run which used QuikSCAT wind measurements **from April 2006 through August 2006.** The wind measurements were taken from a grid point over the southeastern shelf (57.1250 ºN, 167.8750 ºW). The winds were interpolated to one hour intervals so the water column profiles were calculated after each one hour time step.

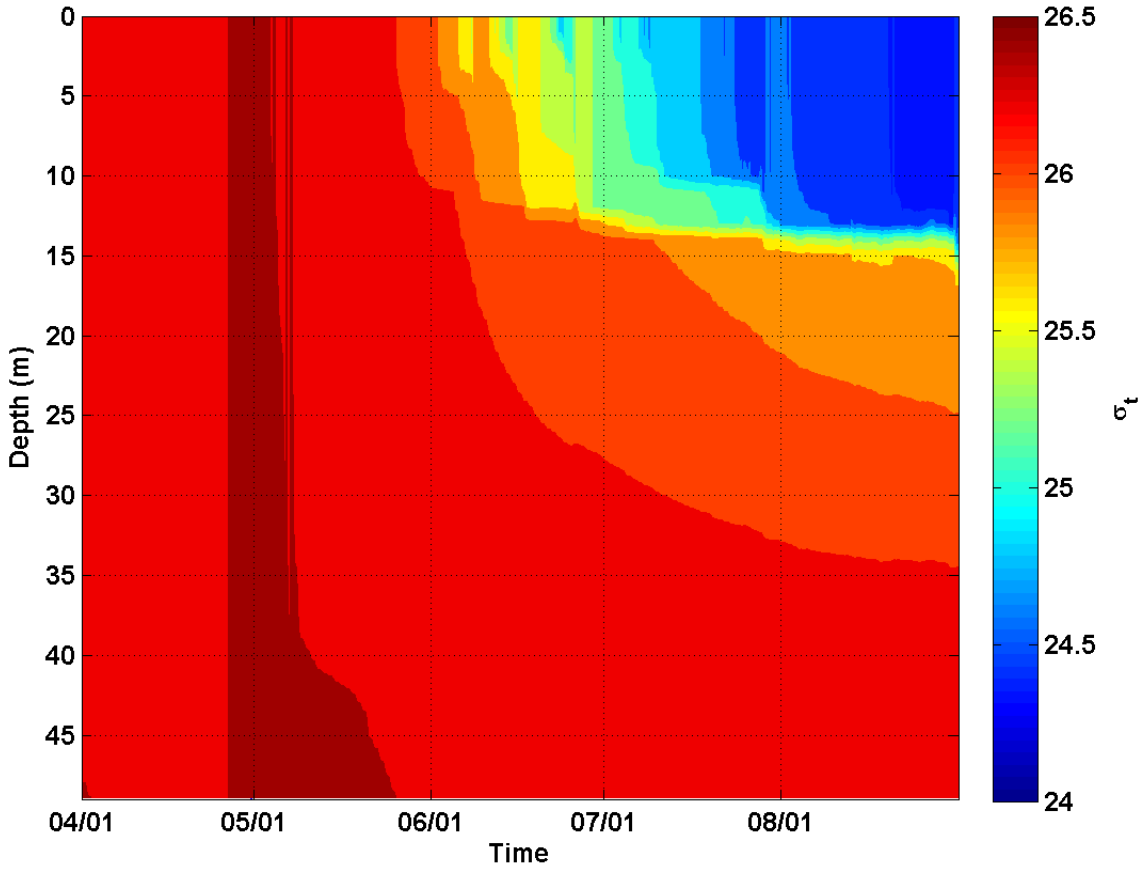

Figure G-13. PWP model output for the model run which used QuikSCAT wind measurements from April 2006 through August 2006 and calculated values of wind-stress-curl. The wind measurements were taken from a grid point over the southeastern shelf (57.1250 ºN, 167.8750 ºW). The winds were interpolated to one hour intervals so the water column profiles were calculated after each one hour time step.

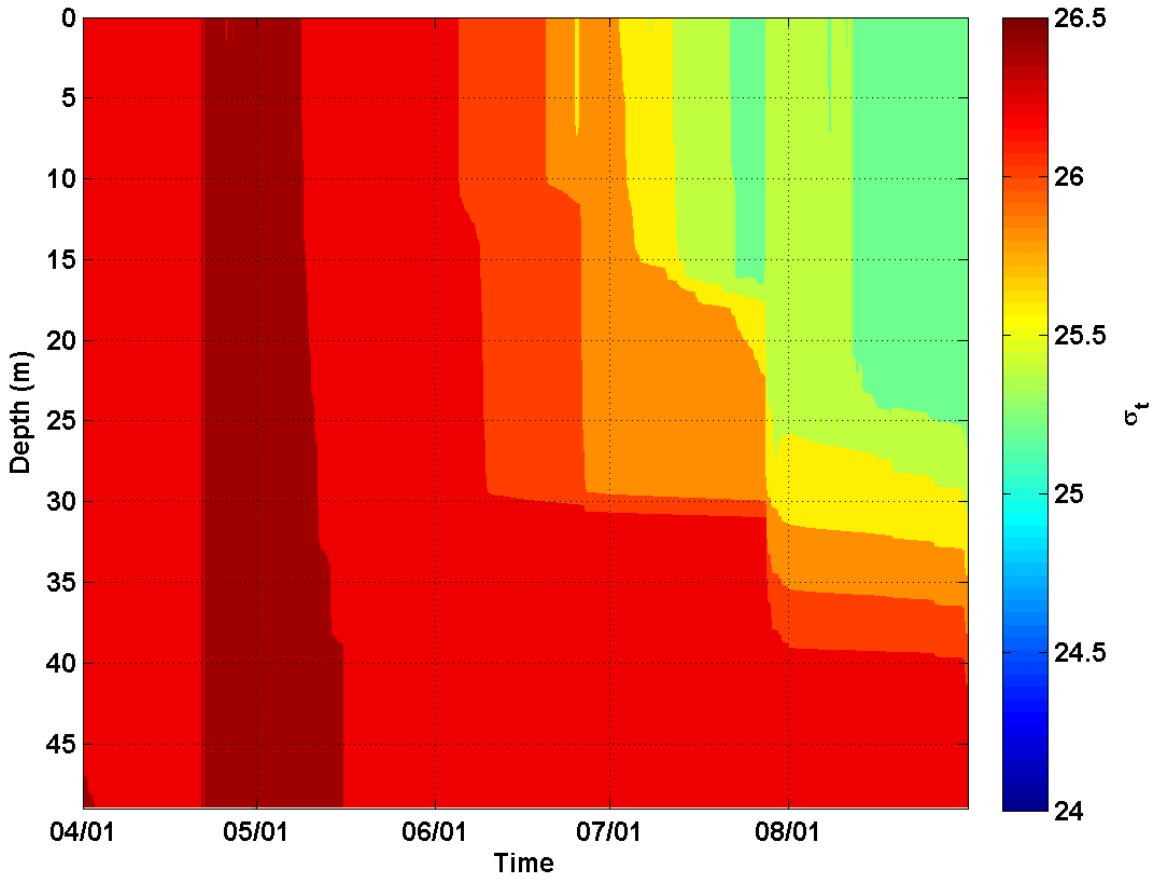

Figure G-14. PWP model output for the model run which used NCEP wind measurements from A**pril 2006 through August 2006.** The wind measurements were taken from a grid point over the southeastern shelf (57.1250 ºN, 167.8750 ºW). The winds were interpolated to one hour intervals so the water column profiles were calculated after each one hour time step.

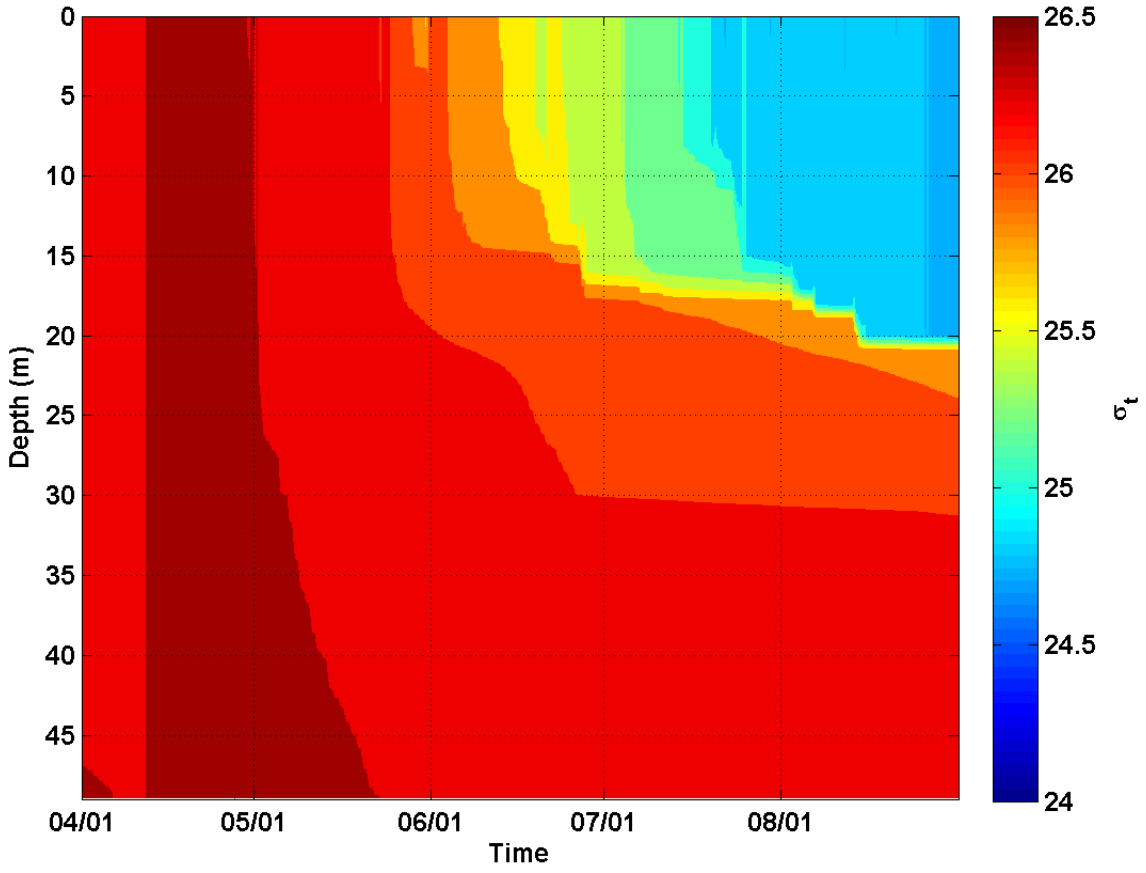

Figure G-15. PWP model output for the model run which used six-hourly NCEP wind measurements from April 2004 through August 2004. The wind measurements were taken from a grid point over the northwestern shelf (62.1250 ºN, 175.8750 ºW). The winds were interpolated to one hour intervals so the water column profiles were calculated after each one hour time step.

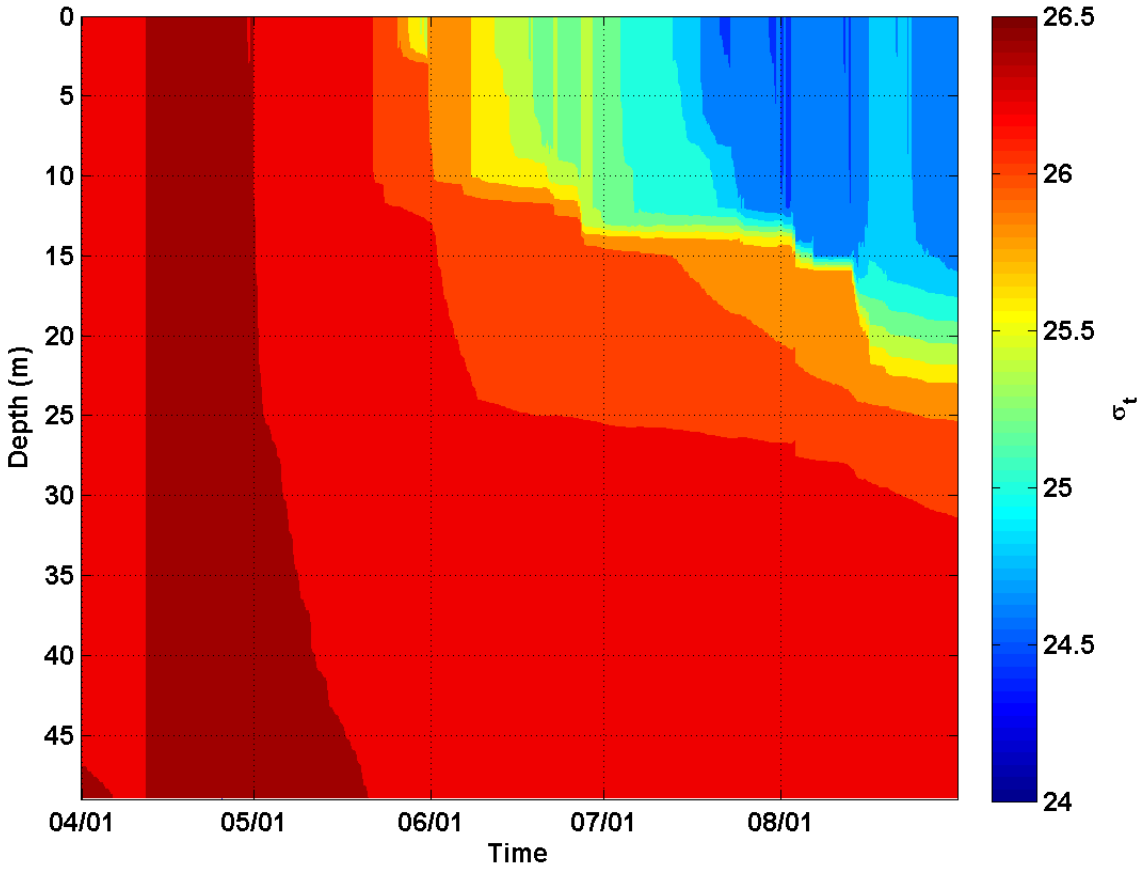

Figure G-16. PWP model output for the model run which used six-hourly NCEP wind measurements from April 2004 through August 2004 and calculated values of wind-stress-curl. The wind measurements were taken from a grid point over the northwestern shelf (62.1250 ºN, 175.8750 ºW). The winds were interpolated to one hour intervals so the water column profiles were calculated after each one hour time step.